POLITECNICO DI MILANO
PhD in Electrical Engineering
Energy Department

ADVANCED CONTROL STRATEGIES FOR POWER CONVERTERS IN AC MICROGRIDS

Modelling, analysis, design and testing.

Candidate:
Alberto Bolzoni

Supervisor: Prof. R. Perini
Tutor: Prof. S. Leva
Head of the PhD program: Prof. Gabriele D'Antona

April 2019 - XXXI cycle

Contents

List of Figures

List of Tables

Abstract

The main topic of this thesis regards the analysis and development of control strategies for power converters in microgrid applications, mainly referring to three-phase AC systems; the thesis is divided into two parts, each followed by a specific bibliographic section to allow an easier identification of the references. A preliminary chapter precedes Part I and serves as an introductory framework for the rest of the work.

In the first chapter, the topic of microgrids is presented from the normative perspective, identifying the major technical trends and the on-going standardization process. Furthermore, it introduces the characteristics of the main control architecture later developed in the work: two main schemes (each corresponding to a part of the thesis) are analysed and extended.

The first part refers to the *droop control*: this architecture allows the regulation of the voltage amplitude and frequency in a distributed way. The dynamical model of the droop is developed and analysed in chapter two: the focus is to identify rigorous analytical design procedures to increase the converter stability and to correctly set the control parameters.

Chapter three deals with the introduction of *virtual impedance*: this technique represents a modification of the traditional droop scheme and enhances the converter dynamical behaviour both in grid-connected and island mode. The stability conditions for the virtual impedance loop are identified and the design procedure is validated experimentally. The analysis illustrates a strong stability sensitivity with respect to the converter external output impedance. In this perspective, a couple of real-time identification algorithms for the converter output interface reconstruction have been developed, based on the system response to some harmonic disturbances. The introduced algorithms are illustrated and tested in chapter four: they can be used as input for possible adaptive schemes inside the converter control.

The second part of the thesis deals with the *grid-following* architecture, typically adopted for non-dispatchable units. Moreover, the traditional scheme has been modified in order to transiently emulate the presence of a physical machine connected to the network: the introduced changes allow the provision of a transitory frequency support (*synthetic inertia*), which damp the network frequency overshoot during power imbalances and improves the grid regulation performances.

Chapter five introduces the dynamical model of the converter under grid-following regulation and defines the design rules of the internal controllers. Furthermore, it identifies the case studies used for the analytical and numerical development of the second part of the thesis.

A key aspect related to the experimental implementation of synthetic inertia schemes regards the possibility to estimate the angular quantities in a fast and clean way, even under disturbed network conditions. In chapter six, several architectures are tested and compared experimentally: the goal is to develop an advanced algorithm able to reconstruct the derivative angular frequency of the fundamental harmonic, keeping into

account all the physical disturbances that are naturally present in any real power network.

Chapter seven analyses a derivative current-based inertia scheme: the mathematical modelling of the system allows to identify the stability conditions for the control as a function of the external regulation properties of the network. The effectiveness of the proposed technique is validated experimentally.

A second possible synthetic inertia scheme is analysed in the last chapter; in this case, the emulation of the synchronous machine behaviour is obtained acting on the DC voltage of the converter with a proportional-based regulation. Again, the mathematical model is analysed and later experimentally tested.

Four final Appendices are reported at the end. The first one includes the explicit representation of the state-space models developed in the main chapters of the work, reported in appendix for compactness. The second and third include some mathematical procedures used for the definition of the internal converter controllers or for the results reconstruction; even though the reported analysis are necessary for a correct regulation of the system and for dynamical performances identification, still the adopted methodologies are well-developed and documented in literature. In the final appendix, an extensive description of the experimental system used for models validation is provided.

Chapter 1

General context

1.1 Chapter introduction

This section has the objective of introducing the main control architectures analysed in the rest of the thesis. Moreover, the chapter provides a technical definition of the concepts of *microgrid* and *smart-grid*, referring to the available standards published in literature: even though the analysis does not have the presumption to enter into all the details of the normative scenario, still it provides a useful overview of the incoming standardization process.

1.2 Introduction to microgrids systems

Even though the scientific literature of the last years has significantly explored the topic of microgrids, it may be hard to find a univocal technical definition for these systems. The description of a microgrid is often associated to the one of *smart-grid*: even if in some cases a certain superposition may exist, it is necessary to define the technical borders of each concept and avoid misunderstandings.

1.2.1 Smart-grid definition

The concept of smart-grid has a data-oriented characterization and refers to the massive presence of ICT [1] infrastructures used for the optimal management of electrical networks. This definition takes into account the possibility to operate a system in an economic way thanks to the coordination of flexibility sources (e.g. storage units, electrical vehicles, controllable loads), knowing their actual state from standardized communication protocols; in this perspective, no constraints are introduced as regards the electrical characterization of the control system of each single element nor on its operational conditions (island or grid-connected). The concept of smart-grid takes its origin from IEEE 2030 [1] and IEC 81950 [2] which are, in practice, communication standards.

An example on the introduction of communication schemes for optimized grid management is related to Demand-Side-Response schemes, which consist in the provision of frequency regulation services by means of non-essential-load modulation, actuated by the Transmission System Operator (TSO). This concept, already applied for several years by most of the European TSO, has recently evolved in the perspective of the participation of flexible-load resources to the Ancillary Service Market [3].

[1] Information and Communication Technologies

1.2.2 Microgrid definition

A microgrid is an electrical concept: it stands for an autonomous power system able to operate independently of an external network or connected to the main system in the Point of Common Coupling (PCC); by definition, the microgrid is able to maintain a stable supply of the local loads both in grid-connected and island conditions by means of distributed or centralized controllers. Because of the required operational flexibility, microgrids are typically characterized by a high percentage of units interconnected by fully-controllable electronic converters: this allows an easy implementation of stable regulation schemes for the network.

From the point of view of the available standards, the concept of microgrid has a direct application on the series IEEE 1547 [4] which clarifies the electrical behaviour of distributed generation units at the interface of an external system. In particular, IEEE 1547.4 specifically clarifies the conditions of independent converters operated in island, together with the corresponding procedures for connection / disconnection to the public mains.

At a European level, the technical specifications for distributed generation interface to traditional electrical networks have been initially promoted by ENTSO-E and subsequently approved by the European Commission by means of the decree 631/2016 and 1447/2016 [5] - [6]. The application of the general guidelines into specific technical constraints is taken into account by the grid code of each country; even though single-unit island operations were already available for specific stand-alone photovoltaic applications [7], the concept of microgrid is not fully regulated in most of the national network standards.

As concern the Italian situation, the first technical specifications for the connection of distributed resources to the public network has been introduced in the grid code attachment A70 [8]. The document clarifies the characteristics that must be imposed by the control system of the interface converter in renewable sources, even though it does not provide any direct indication related to the operations of autonomous systems in island conditions; furthermore, the proposed protection settings in [8] are designed in order to avoid that the public network remains permanently supplied during unintentional island conditions. As far as concern private systems operated autonomously, the scenario remains unclear. Nonetheless, new versions of the technical standards CEI 0-16 and CEI 0-21 [9] - [10], recently approved by the Italian Authority, allow some behind-the-meter operations of the storage units and seem to represent an evolution towards a more mature microgrid scenario.

Significant differences exist also as regards the regulation services provision to the public network from electronic-interfaced sources: referring for example to the primary frequency regulation (also labelled Frequency Containment Regulation FCR), it is possible to identify a wide range of regulation settings. Some of them are suitable both for traditional synchronous generators and power electronics units, like in the Italian case [11] - [12]; others [13] - [14] impose technical constraints that can be met exclusively by digitally-controlled converters.

Given the high variety of standardization approaches as well as the proposition of new regulation services [15], this thesis proposes to develop rigorous analytical models associated to the most used architectures available in literature. The focus of the analysis will be mainly electrical (thus the decision to refer to the term microgrid instead of *smart-grid*): main characteristics of the major control strategies for power converters in isolated electrical systems will be analysed and extended, with a focus on the mathematical stability conditions. New design technique and control schemes will be proposed to enhance the dynamical performances of the electronic converter and of the whole system.

1.3 Microgrid control: converter level

At the converter level, the three main architectures proposed in literature for voltage-source inverters are explained in [16] and reported in Fig. 1.1.

- The control architecture reported in Fig.1.1(a) goes under the name of $V\omega$ scheme. In this configuration, the converter imposes both the magnitude and the angular frequency of the three-phase voltage set at the interface with the external system,

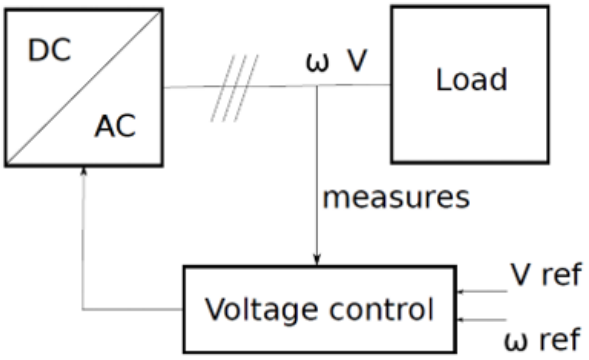

(a) Grid-forming architecture

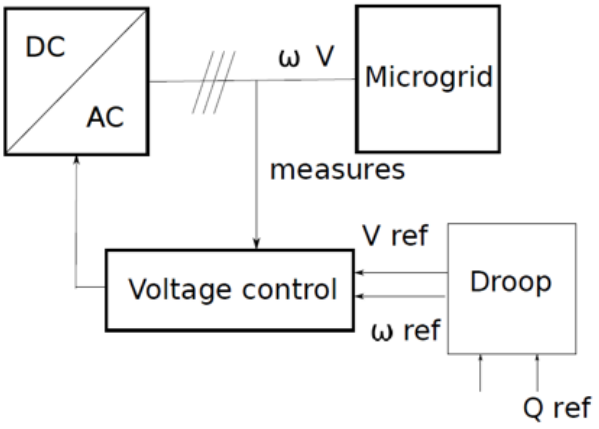

(b) Grid-supporting architecture

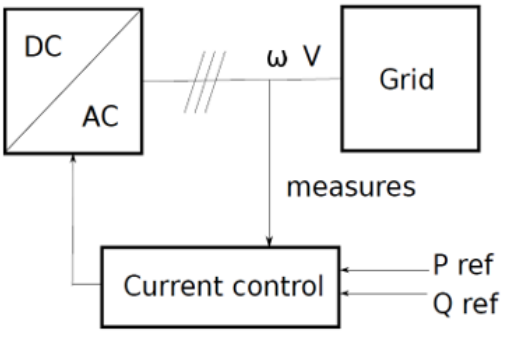

(c) Grid-following architecture

FIGURE 1.1: Typical control architectures for grid converters.

behaving according to power systems slack-bus model. Even though this configuration allows to maintain the system in nominal conditions indefinitely, nevertheless this architecture cannot be applied to multiple converters operated in parallel as the power sharing between units would be undetermined. This control is generally regarded as grid-forming architecture and it generates a three-phase balanced voltage set independently of external system conditions.

- A second very well-known control for grid-converters is the droop regulation (Fig. 1.1(b)). In this scheme, the angular frequency and magnitude of the three-phase voltage set at the converter interface are determined by the average active and reactive power injection of each unit. This allows to equally share the load between parallel-connected converters both at steady-state and during transients. This scheme is a *grid-supporting* architecture: all the units regulated by means of this strategy contribute to the provision of primary voltage and frequency regulation, proportionally to their nominal rating.
- The third architecture regulates the active and reactive power injections from each unit (Fig. 1.1(c)) to almost constant set-points, thus goes under the name of PQ scheme or *grid-following* architecture. It allows to maintain constant injections independently of the external system condition, even though it does not provide any contribution to the system regulation.

In this thesis, the last two architectures will be considered and analysed. Starting from the base configuration already available in literature, several changes are introduced in order to improve the regulation performances of the converters and to extend the functionalities associated to these controls, both in grid-connected and island mode.

As for the droop regulation scheme, a rigorous dynamical model is developed: differently from the available literature, the model is able to take into account all the major dynamical interactions that occur inside the control. Moreover, the base droop architecture is extended in order to adaptively take into account the changes associated to the modification of converter output impedance, which plays a major role in the definition of stability. These aspects are covered in the first part of the thesis.

As for the grid-following architecture several schemes aimed at the provision of transitory active power injection are proposed, in order to improve the microgrid behaviour during frequency transients: this approach goes under the name of synthetic inertia and it is developed in the second part of the thesis.

1.4 Microgrid control: system level

At a system level, two different control approaches can be identified: *Centralized control* and *Hierarchical control*.

1.4.1 Centralized control

The *centralized control* is generally exploited for systems with a limited number of interconnected units. The control approach is quite simple, as all the computation burden associated to the grid stability and its management is taken into account by a single regulation unit, typically a micro-controller or an industrial computer. As all the information has to be acquired and elaborated in real-time by a single intelligence, the number of converters that can be physically interfaced to the system is contained by the computation power of the controller. Moreover, the possibility to regulate the system with a centralized control approach is dependant on the communication interfaces

availability between the central controller and the peripheral units: this makes the system intrinsically susceptible to instability in case of fault on the data infrastructure.

1.4.2 Hierarchical control

A second, more advanced, architecture goes under the name of *hierarchical scheme* [17] and it is realized by means of several regulation levels (typically three, as in traditional power systems), each of them with its own peculiar characteristics. The first level corresponds to the primary regulation and it is carried out by distributed controllers, each managing a single interconnected converter; in this way, the management and regulation of the fast dynamics is independent of the communication infrastructures availability. The system stability under the changes of the local load and production is obtained by means of grid supporting droop schemes reported in Fig.1.1(b).

A secondary-level control, based on the communication between adjacent units, contributes to restoring nominal conditions for the system after a transient, changing the reference values for distributed controllers. As only a limited number of information is exchanged on the communication platform, the characteristics of the data network are typically less stringent with respect to the ones of the centralized control.

The tertiary level determines the nominal set-points of the secondary control and it is responsible of the microgrid coordination with the external utility networks.

1.5 Conclusion

This brief introductory chapter has described the area of interest of the thesis. The concept of microgrid is reported referring to its electrical characteristics and technical standards typically adopted in the practical applications; additionally, the major features of the analysed architectures are taken into account, providing a general frame for the analysis performed in the following chapters.

Norms and standards

[1] IEEE-SCC21, *IEEE Std 2030-2011 - "Guide for Smart Grid Interoperability of Energy Technology and Information Technology Operation with the Electric Power System (EPS), End-Use Applications, and Loads"*, Sept 2011.

[2] International Electrotechnical Commission IEC, *"Communication networks and systems for power utility automation - IEC 61850 series"*, 2014.

[3] 'ARERA Italian Energy Authority', *"Apertura del Mercato per il Servizio di Dispacciamento (MSD) alla Domanda Elettrica", Decree 300 - 2017*, 2017.

[4] IEEE-SCC21, *"Standard for Interconnecting Distributed Resources with Electric Power Systems"*, July 2018.

[5] ENTSO-E, *"Establishing a network code on requirements for grid connection of generators"*. Official Journal of the European Union, 2016. approved by European Commission, decree 2016 / 361.

[6] ENTSO-E, *"Establishing a Network Code on requirements for grid connection of HVDC systems"*. Official Journal of the European Union, 2016. Approved by European Commission, decree 2016 / 1447.

[7] International Electrotechnical Commission IEC, *"Photovoltaic (PV) stand-alone systems - Design verification", IEC 62124*, 2005.

[8] Terna, *"Allegato A70 - Regolazione Tecnica dei requisiti di sistema della Generazione Distribuita" (Italian grid code)*. Available at: www.terna.it, 2012. Attachment to the Italian grid code.

[9] Comitato Elettrotecnico Italiano CEI, *"Reference technical rules for the connection of active and passive consumers to the HV and MV electrical networks of distribution company", CEI 0-16*, 2016. Attachment to the Italian grid code.

[10] Comitato Elettrotecnico Italiano CEI, *"Reference technical rules for the connection of active and passive users to the LV electrical Utilities", CEI 0-21*, 2012. Attachment to the Italian grid code.

[11] Terna, *"Allegato A15 - Partecipazione alla Regolazione di Frequenza e Frequenza-Potenza" (Italian grid code)*. Available at: www.terna.it, 2008. Attachment to the Italian grid code.

[12] Terna, *"Allegato A73 - Specifiche tecniche per la verifica e la valorizzazione del servizio di Regolazione Primaria di Frequenza" (Italian grid code)*. Available at: www.terna.it, 2008. Attachment to the Italian grid code.

[13] National Grid, *"Enhanced Frequency Response - Invitation to tender for pre-qualified parties"*, 2016.

[14] National Grid, *"Testing guidance for providers of Enhanced Frequency Response Balancing service"*, 2016.

[15] ENTSO-E, ENTSO-E guidance document for national implementation for Network Codes on grid connection, *"Need for synthetic inertia (SI) for frequency regulation"*, 2016.

[16] J. Rocabert, A. Luna, F. Blaabjerg, and P. Rodríguez, "Control of power converters

in ac microgrids," *IEEE Transactions on Power Electronics*, vol. 27, pp. 4734–4749, Nov 2012.

[17] J. M. Guerrero, J. C. Vasquez, J. Matas, L. G. de Vicuna, and M. Castilla, "Hierarchical control of droop-controlled ac and dc microgrids—a general approach toward standardization," *IEEE Transactions on Industrial Electronics*, vol. 58, pp. 158–172, Jan 2011.

Part I

Mathematical model of droop controlled converters

Introduction to part I

In this part of the thesis, the structure of droop-controlled converters will be analysed. Droop converters are responsible of grid voltage and frequency management according to a distributed-regulation scheme; these units are generally controlled with a nested-loop architecture, whose reference is modulated according to the average power injection to guarantee equal load sharing between parallel-connected units.

The dynamical model of the droop converter will be analysed in detail; furthermore, different changes with respect to the classical architecture have been introduced in order to improve the dynamic performances of the converter in a vast range of operating conditions. These include the possibility to modify the equivalent output impedance of the converter and to estimate on-line the interface impedance. The equivalent final structure of the system is reported in Figure 1.2; each of the following chapters in Part I will be devoted to the analysis of a single aspect of the reported architecture.

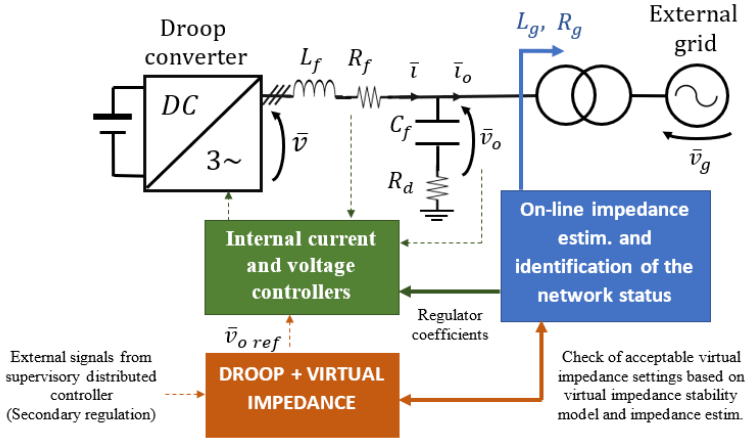

FIGURE 1.2: Proposed Enhanced Droop architecture

Chapter 2

Model of the converter under droop regulation

2.1 Chapter introduction

In this chapter, the dynamical model associated to droop-controlled converters will be derived. Even if the basic concepts of droop regulation for active and reactive power are already available in literature, here the attempt is to obtain a complete description of the control dynamics which include enough structure to take into account also the secondary effects associated to the internal control loops.

2.2 Nomenclature

Physical circuit

- R_f, L_f, C_f, R_d: parameters associated to the LC filter [p.u.];
- R_g, L_g: parameters of the interface impedance [p.u.];
- $T_g = L_g/(R_g\omega_b)$: output impedance time constant [s];
- ω_{pcc}: angular frequency at the point of common coupling [p.u.];
- V_{pcc}: voltage amplitude at the point of common coupling [p.u.];

Droop parameters

- ω: inverter angular frequency [p.u.];
- m, n (m_d, n_d): linear and derivative coefficients of the droop control [p.u.];
- ω^*, V^*: no-load angular frequency and voltage in the droop control of the inverter [p.u.];
- $p_o(t)$, $q_o(t)$ (P_o, Q_o): instantaneous (average) real, reactive powers;
- T_p: time constant of the filter for average power calculation [s];
- m_{rest}, n_{rest}: droop coefficients of the characteristic imposed by the external network [p.u.];
- ω^*_{rest}, V^*_{rest}: no-load angular frequency and voltage of the external regulation [p.u.];
- p_{rest}, q_{rest}: instantaneous real and reactive powers provided by the rest of the network;
- T_{rest}: time constant of the primary regulation performed by other converters [s];

Current and voltage controllers

- H_I: grid-current compensation gain in the voltage loop;
- H_V: capacitor-voltage compensation gain in the voltage loop;
- $T_{iV} = k_{pV}/k_{iV}$: integral time of the PI voltage regulator;
- ω_{cI}, ω_{cV}: cut-off angular frequency of the current and voltage loops [rad/s];

Operators and base frequency

- $p = d/dt$: time derivative operator;
- $s = j\omega_s$: complex Laplace operator and frequency response notation [rad/s];
- ω_b: base angular frequency [rad/s].

2.3 Droop equation from power decoupling: traditional derivation

The droop equations derivation as typically reported in literature is based on the concept of power decoupling. This property is generally considered a positive feature in power systems as it allows independent regulation of frequency and voltage amplitude, reducing the coupling phenomena between active and reactive powers: the traditional form of the droop equations is generally obtained focusing on this perspective.

Consider the circuit reported in Fig.2.1: the converter is interfaced to an external grid modelled as the series connection of a sinusoidal voltage source with an ohmic-inductive impedance. This is the lumped-parameter model typically used in power systems applications. Considering the voltage level, it is possible to neglect the shunt capacitances, and calculate the exchanged active and reactive powers with simple formulations. Phasor domain is considered for the analysis.

Define $\bar{V_1} = V_1 \angle \psi_1$ the source phasor-voltage and $\bar{V_2} = V_2 \angle \psi_2$ the equivalent phasor voltage of the grid. The equivalent branch impedance between nodes 1 and 2 can be expressed as $\bar{Z}_g = R_g + j\omega L_g$ and its characteristic angle $\theta = atan\left(\frac{\omega L_g}{R_g}\right)$.

The typical approach used to derive the droop equations starts from the calculation of the average active and reactive power exchange between the converter and the network (represented by the voltage sources $\bar{V_1}$ and $\bar{V_2}$, interfaced by the equivalent impedance $\bar{Z}_g$). The current can be obtained from a simple Kirchhoff equation (2.1), while (2.2) allows to obtain the expression of the complex power injected by the converter.

$$\bar{I} = \frac{\bar{V_1} - \bar{V_2}}{\bar{Z}_g} \tag{2.1}$$

$$\bar{S_o} = \bar{V_1} \cdot \underline{I} = \frac{V_1^2 - V_1 V_2 e^{j(\psi_1 - \psi_2)}}{Z_g e^{-j\theta}} \tag{2.2}$$

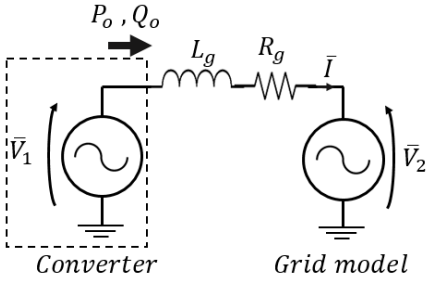

FIGURE 2.1: Simplified equivalent model of the converter interface. The model comprises two sinusoidal voltage sources for converter and grid respectively ($\bar{V_1}$ and $\bar{V_2}$); an ohmic-inductive interface impedance $\bar{Z}_g$ is considered.

Introducing the angular difference $\delta = \psi_1 - \psi_2$, (2.2) can be rewritten to highlight the active and reactive powers separately:

$$P_o = Re(\bar{S}_o) = \frac{V_1}{Z_g} \cdot (V_1 cos(\theta) - V_2 cos(\delta + \theta)) \tag{2.3}$$

$$Q_o = Im(\bar{S}_o) = \frac{V_1}{Z_g} \cdot (V_1 sin(\theta) - V_2 sin(\delta + \theta)) \tag{2.4}$$

The dependency of the active and reactive powers on the magnitudes $[V_1, V_2]$ and phase difference δ is associated to the characteristic angle θ of the impedance $\bar{Z}_g$. In case the interface impedance shows a predominantly inductive behaviour ($\theta \to \frac{\pi}{2}$) the equations in (2.3) simplify to:

Inductive network

$$P_o = Re(\bar{S}_o) = \frac{V_1 V_2 sin(\delta)}{\omega L_g} \tag{2.5}$$

$$Q_o = Im(\bar{S}_o) = \frac{V_1}{\omega L_g} \cdot (V_1 - V_2 cos(\delta)) \tag{2.6}$$

Alternatively, if we consider the case of a mainly resistive impedance ($\theta \to 0$) the following simplification holds:

Resistive network

$$P_o = Re(\bar{S}_o) = \frac{V_1}{R_g} \cdot (V_1 - V_2 cos(\delta)) \tag{2.7}$$

$$Q_o = Im(\bar{S}_o) = -\frac{V_1 V_2 sin(\delta)}{R_g} \tag{2.8}$$

The two formulations reported in (2.5)-(2.6) and (2.7)-(2.8), for inductive and resistive networks respectively, represent the typical conditions under which power decoupling holds. As the load angle δ typically has a limited value, it is possible to derive approximate proportional relations between δ, voltage magnitudes $[V_1, V_2]$ and exchanged active and reactive powers P_o - Q_o.

Inductive network

$$P_o = \frac{V_1 V_2 \delta}{\omega L_g} \tag{2.9}$$

$$Q_o = \frac{V_1}{\omega L_g} \cdot (V_1 - V_2) \tag{2.10}$$

Resistive network

$$P_o = \frac{V_1}{R_g} \cdot (V_1 - V_2) \tag{2.11}$$

$$Q_o = -\frac{V_1 V_2 \delta}{R_g} \tag{2.12}$$

The droop control emulates the linear dependency between active / reactive injections, angular quantities (load angle δ or angular frequency ω) and voltage magnitude difference ΔV.

Even though some authors have proposed different types of relationships for the droop structure [1]-[2], nevertheless the most typical control schemes introduce a linear dependency between state variables.

Two configurations are generally taken into account:

- linear dependency between active power P_o and angular frequency ω, as well as between reactive power Q_o and voltage difference ΔV (2.13) - (2.14);
- linear dependency between active power P_o and voltage difference ΔV, as well as between reactive injection Q_o and angular frequency ω (2.16) - (2.15).

$$\omega = \omega^* - m \cdot P_o \tag{2.13}$$
$$v_o^{ref} = V^* - n \cdot Q_o \tag{2.14}$$

$$\omega = \omega^* - m \cdot Q_o \tag{2.15}$$
$$v_o^{ref} = V^* - n \cdot P_o \tag{2.16}$$

The terms ω^* and V^* are the no-load frequency and the voltage amplitude references; these values are typically chosen depending on the nature of the energy source on the primary side of the converter, the network standards and the set-up imposed by the system secondary control [3] - [4] - [5].

Droop slopes take into account the load-ability of the unit and the maximum allowed range of variation for the frequency and voltage magnitude. For inductive droop characteristics, the slopes m and n can be obtained as:

$$m = \frac{\omega_{Max} - \omega_{min}}{P_{Max} - P_{min}} \tag{2.17}$$
$$n = \frac{V_{Max} - V_{min}}{Q_{Max} - Q_{min}} \tag{2.18}$$

The case expressed by (2.13) - (2.14) is the most used scheme [6]-[7]-[8], as it emulates the characteristics of primary voltage and frequency regulation typically adopted for traditional generators in predominantly-inductive transmission networks [9]-[10]. Even though the characteristics of this type of regulation suit very well for high-voltage distribution because of the inductive nature of the system, they may not be the perfect solution for low or medium-voltage microgrids in which the power decoupling is less evident.

The modification of the droop equations according to (2.15)-(2.16), in order to adapt them to the case of predominantly resistive networks, may be reasonable only for some specific cases: we have to take into account that the determination of the equivalent external impedance seen by the converter depends on a multitude of physical factors (e.g. voltage level, presence or absence of the interface transformer, loading conditions of the system, number and nature of active loads connected to the network). Thus both solutions proposed in (2.13)-(2.14) and (2.15)-(2.16) suffer from the inherent time variability of the external network impedance.

In this thesis, inductive droop (2.13)-(2.14) is taken into account: nevertheless, several changes to improve its control performances even with a predominantly resistive impedance will be analysed; moreover, it will be investigated the possibility to estimate the equivalent impedance seen by the converter, in order to develop robust and adaptive control schemes for the converter.

2.4 Structure of the system

Consider the model of a single converter controlled by means of a droop scheme. The unit may be connected to an external strong power system which is imposing amplitude and angular frequency of the three-phase voltages at the interface (Fig. 2.2(a)) or it is supplying a microgrid where active and reactive primary regulation is carried out in a distributed way (Fig. 2.2(b)). Table 2.1 includes the base system used for per-unit transformation, as well as the characteristics of the considered study case for each converter.

The design of the LCL filter is carried out according to [11]; the filter includes a damping resistor R_d, designed in order to avoid parallel resonance.

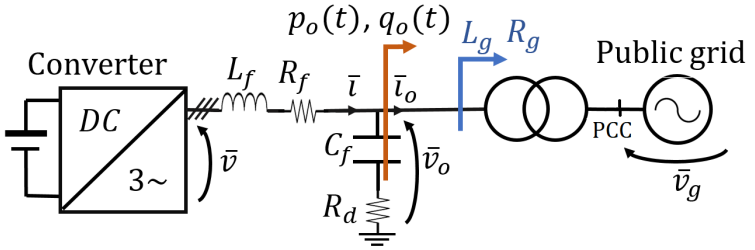

(a) Operation of the converter in grid-connected mode.

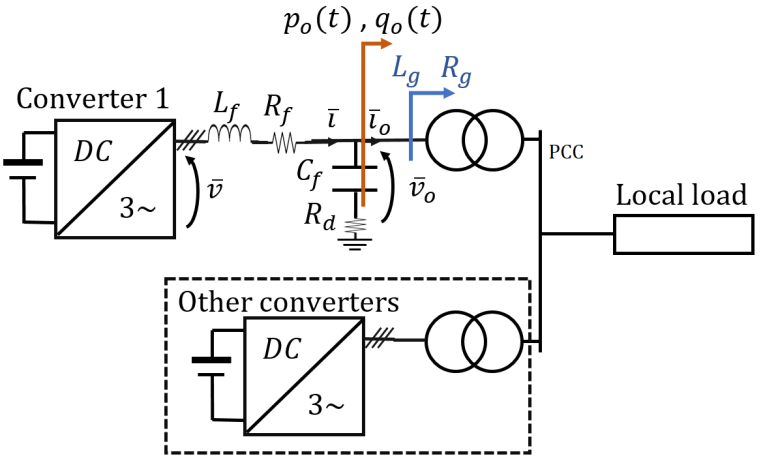

(b) Operation of the converter in island mode.

FIGURE 2.2: Operations of the converter interfaced to a public network (a) or in island mode (b).

TABLE 2.1: System parameters

Quantity	*Value*
Base system V_b [V], A_b [kVA], ω_b [rad/s]	200; 2.4; 2π 50
R_f, L_f, C_f, R_d [p.u.]	0.0073, 0.045, 0.052, 0.63
R_g, L_g [p.u.]	0.049, 0.024
Current loop cut-off ang. freq. [rad/s] ω_{cI}	$2\pi \cdot 350$
Current loop phase margin	70 deg.
Voltage loop cut-off ang. freq. [rad/s] ω_{cV}	$2\pi \cdot 50$

As regards the proportional droop parameters as defined in (2.17) - (2.18), the values in Table 2.2 are considered. A first order filter with time constant T_p is used for the extraction of average power components according to the droop equations (2.13) - (2.14).

The external system is represented by the three-phase voltage source $\bar{v}_g$ and the equivalent ohmic-inductive impedance (R_g, L_g).

2.5 Non-linear model of the converter

Consider the per-unit (p.u.) dynamical equations of the filter in the $\alpha\beta$ frame. The operator $p = \frac{d}{dt}$ represents the time derivative; as it is homogeneous with $[s^{-1}]$, it is divided by the base angular frequency ω_b.

$\alpha\beta$ **frame**

$$\bar{v} - \bar{v}_o = R_f\,\bar{i} + L_f \frac{p}{\omega_b}\bar{i} \tag{2.19}$$

$$C_f\,\frac{p}{\omega_b}\,\bar{v}_o = (\bar{i} - \bar{i}_o) + R_d\,C_f\,\frac{p}{\omega_b}\,(\bar{i} - \bar{i}_o) \tag{2.20}$$

$$\bar{v}_o - V_{pcc}e^{j\,\delta} = R_g\,\bar{i}_o + L_g\,\frac{p}{\omega_b}\,\bar{i}_o \tag{2.21}$$

For the control, a rotating dq frame aligned to reference voltage $\bar{v}_{o\,ref}$ is considered (thus $\bar{v}_{o\,ref} = v_{od\,ref} + j\cdot 0$). The expressions of the filter equations in the dq frame can be obtained from the substitution $\frac{p}{\omega_b} \to \frac{p}{\omega_b} + j\omega$, where ω is the rotating control frame angular frequency expressed in per-unit.

dq **frame**

$$\bar{v} - \bar{v}_o = R_f\,\bar{i} + L_f \frac{p}{\omega_b}\bar{i} + j\,\omega\,L_f\,\bar{i} \tag{2.22}$$

$$C_f\,\frac{p}{\omega_b}\,\bar{v}_o + j\,\omega\,C_f\,\bar{v}_o = (1 + j\omega R_d C_f)\,(\bar{i} - \bar{i}_o) + R_d\,C_f\,\frac{p}{\omega_b}\,(\bar{i} - \bar{i}_o) \tag{2.23}$$

$$\bar{v}_o - V_{pcc}e^{j\,\delta} = R_g\,\bar{i}_o + L_g\,\frac{p}{\omega_b}\,\bar{i}_o + j\,\omega\,L_g\,\bar{i}_o \tag{2.24}$$

The representation of the control scheme on synchronous axes is reported in Fig. 2.3. The converter regulation is realized by means of three nested loops, respectively associated to the control of the filter current $\bar{i}$, the capacitor voltage $\bar{v}_o$ and the droop control, which defines the instantaneous voltage reference based on the absorbed active and reactive powers.

TABLE 2.2: Droop parameters

Quantity	*Value*
Droop coefficients m , n [p.u.]	0.010 , 0.017
Time constant T_p for average power calculation [s]	0.10

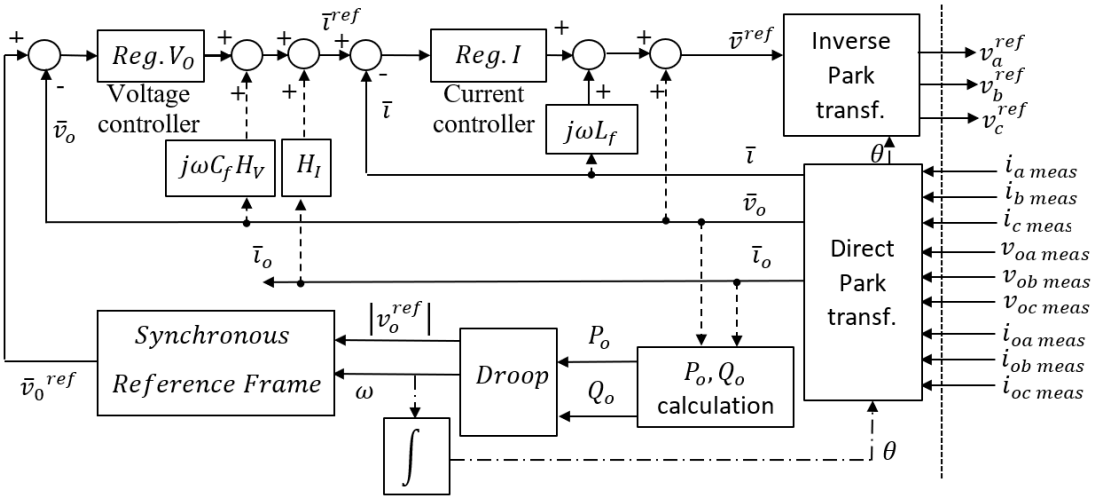

FIGURE 2.3: Control system of the converter under study.

The dynamical equations associated to the internal current and voltage loops can be expressed as:

$$\bar{v}^{ref} = (k_{pI} + k_{iI}/p)\left(\bar{i}^{ref} - \bar{i}\right) + \bar{v}_o + j\,\omega\,L_f\,\bar{i} \tag{2.25}$$

$$\bar{i}^{ref} = (k_{pV} + k_{iV}/p)\left(\bar{v}_o^{ref} - \bar{v}_o\right) + H_I(p)\,\bar{i}_o + H_V(p)\,j\omega C_f\,\bar{v}_o \tag{2.26}$$

Two additional complex state variables $\bar{E}_i$ and $\bar{E}_v$ model the effect of the integral regulators in the current and voltage loop:

$$p\bar{E}_i = \left(\bar{i}^{ref} - \bar{i}\right) \tag{2.27}$$

$$p\bar{E}_v = \left(\bar{v}_o^{ref} - \bar{v}_o\right) \tag{2.28}$$

$H_I(p)$ and $H_V(p)$ represent the transfer functions associated to the feed-forward compensation of the output current $\bar{i}_o$ and capacitor voltage $\bar{v}_o$. A typical simplification assumes the functions $H_I(p)$ and $H_V(p)$ as constant coefficients; this choice significantly reduces the complexity of the control system and the number of state variables in the dynamical model. In the next section, it will be shown that there is a strong correlation between the desired characteristics of the voltage $\bar{v}_o$ control loop and the feed-forward term H_I.

Neglecting the internal switching dynamic of the converter, it is possible to assume $\bar{v} \cong \bar{v}^{ref}$.

As for the voltage reference definition $\bar{v}_o^{ref}$, a typical inductive droop is taken into account; derivative coefficients are also introduced in the traditional droop equations in order to improve the dynamical behaviour of the converter [12] - [13]: nevertheless, in the consulted literature, a rigorous design procedure for the derivative droop coefficients has not been clearly identified. In section 2.8 a straightforward method able to predict the effects of derivative droop coefficients on the system dynamics will be developed.

The magnitude and angular frequency of the voltage reference $\bar{v}_o^{ref}$ can thus be expressed as:

$$\omega = \omega^* - (m + m_d p)\ P_o = \omega^* - \frac{(m + m_d p)\,(v_{od}\, i_{od} + v_{oq}\, i_{oq})}{1 + T_p\, p} \tag{2.29}$$

$$v_{od}^{ref} = V^* - (n + n_d p)\ Q_o = V^* - \frac{(n + n_d p)\,(v_{oq}\, i_{od} - v_{od}\, i_{oq})}{1 + T_p\, p} \tag{2.30}$$

$$v_{oq}^{ref} = 0 \tag{2.31}$$

Depending on the characteristics of the external system, the load angle δ, which expresses the angular difference between converter-controlled and grid voltages, and the corresponding amplitude V_{pcc} in (2.24) are determined by the following equations:

Grid-connected mode

$$p\delta = \omega_b \cdot (\omega_{pcc} - \omega) \tag{2.32}$$

$$\omega_{pcc} = \text{ constant} \qquad V_{pcc} = \text{ constant} \tag{2.33}$$

Island conditions mode (see Fig. 2.4)

$$p\delta = \omega_b \cdot (\omega_{pcc} - \omega) \tag{2.34}$$

$$\omega_{pcc} = \omega_{rest}^* - \frac{m_{rest}}{1 + p\, T_{rest}} \cdot p_{rest} \tag{2.35}$$

$$V_{pcc} = v_{rest} - \left|\bar{Z}_{rest} \cdot \bar{i}_{rest}\right| \cong \left(V_{rest}^* - \frac{n_{rest}}{1 + p\, T_{rest}} \cdot q_{rest}\right) - \left|\bar{Z}_{rest} \cdot \frac{(p_{rest} - j q_{rest})}{V_{pcc}}\right| \cong \tag{2.36}$$

$$\cong \left(V_{rest}^* - \frac{n_{rest}}{1 + p\, T_{rest}} \cdot q_{rest}\right) - \frac{\left(R_{rest} \cdot p_{rest} + \omega^0 L_{rest} \cdot q_{rest}\right)}{V_{pcc}} \tag{2.37}$$

where (neglecting the active and reactive losses into the network):

$$p_{rest} + p_o \cong p_{load} \qquad q_{rest} + q_o \cong q_{load} \tag{2.38}$$

Equation (2.37) takes into account:

- the equivalent impedance $\bar{Z}_{rest} = R_{rest} + j\omega^0 L_{rest}$ seen from the load to the equivalent high-power external grid. The circuital representation of the model is provided in Fig.2.4, and the voltage drop associated to the external regulation system is modelled according to the simplified steady state approximation typically used in power systems [14].
- the primary voltage regulation performed by the rest of the system, according to the typically used proportional scheme [15].

The reference circuit used for the identification of converters contribution to the definition of the reactive voltage at the Point of Common Coupling is given by Fig. 2.4.

The local load is modelled as a constant power absorption; moreover it is assumed that the voltage drop associated to the regulation system shows a predominantly inductive nature, thus changing (2.37) into (2.39).

$$V_{\text{pcc}} \cong \left(V_{rest}^* - \left(\frac{n_{rest}}{1 + sT_{rest}} + \omega^0 L_{rest}/V_{pcc}^0\right) \cdot q_{rest}\right) \tag{2.39}$$

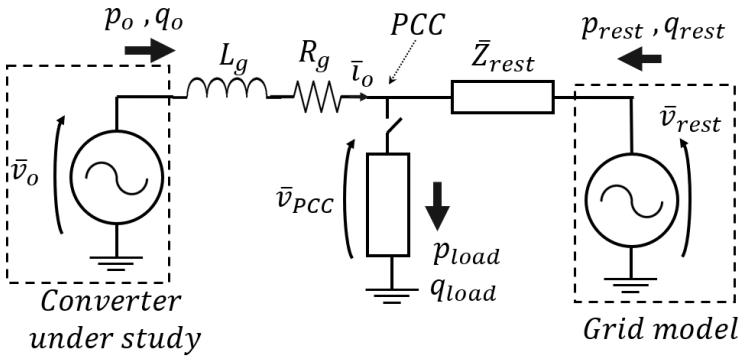

FIGURE 2.4: Physical representation of the circuit used for the analysis of the converter behaviour in island mode.

The explicit form of the state space model used for numeric stability evaluation of the droop-controlled converter is reported in Appendix A: all the already introduced equations are grouped there, highlighting the typical state space form typically used in control theory.

2.6 Controllers design

Assume that the desired cut-off frequencies for the current and voltage loops are respectively ω_{cI} and ω_{cV} (Table 2.1); it is decided to use typical linear PI controllers for the regulation of the system, with constant feed-forward compensations. Under these hypotheses, the dynamic of the regulator is linear and it can be analysed in the Laplace domain.

As regards the current loop, the design process is straightforward and does not present any significant theoretical complexity. The proposed procedure and the numerical results are included in Appendix B.

As for the voltage loop, the situation is more complex: according to [16] and [12], the coefficient H_I associated to the grid current compensation into the voltage loop has to be chosen lower than one in order to maintain stable operations for the system. The consistency of this hypothesis will be verified, together with its effect in terms of regulation properties for the voltage loop.

Consider the voltage loop control on synchronous dq axes, as reported in Fig. 2.5. The loop is controlled by means of a traditional PI controller; feed-forward compensations of the external current $\bar{i}_o$ and of the capacitor voltage $\bar{v}_o$ coupling term are taken into account by H_I and H_V.

Similarly to the procedure reported in Appendix B for the current loop, the starting point for the design of the voltage regulator is the identification of an equivalent load

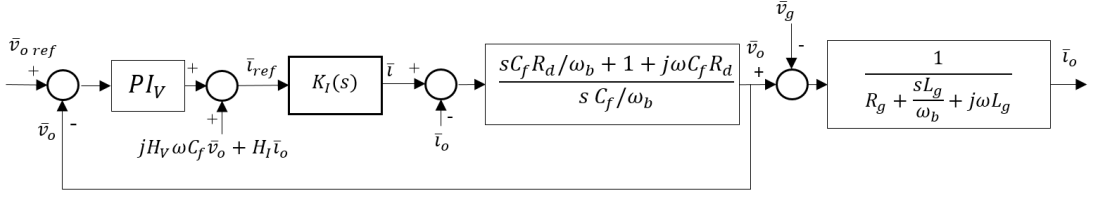

FIGURE 2.5: Equivalent block diagram associated to the voltage control.

function $G_V(s)$ which includes the dynamical characteristics of the system under control. The following procedure will be carried out:

- in this section, a simplified design model for the voltage loop is proposed: the objective is to derive analytical expressions for the PI coefficients k_{pV} and k_{iV};
- in the next section, a numerical model will be developed in order to verify the consistency of the introduced simplifications.

2.6.1 Identification of a simplified load function $G_V(s)$.

Starting from the model in Fig. 2.5, the following hypotheses are introduced:

- a non-ideal feed-forward term $H_I = 0.95$ is considered;
- all the coupling terms are neglected, both as regards capacitor and interface impedance;
- the effect of the external grid voltage $\bar{v}_g$ is neglected in the design of the voltage loop.

From the model reported in Fig. 2.6(a) and 2.6(b), it follows the identification of the equivalent load function $G_V(s)$ on a synchronous control system obtained as:

$$G_V(s) = K_I(s) \cdot F_c(s) \cdot \frac{1}{1 + (1 - H_I K_I(s)) \cdot F_c(s) \cdot Y_g(s)} \tag{2.40}$$

where $K_I(s)$ represents the internal current loop according to the equation (B.17) in Appendix B; $F_c(s)$ and $Y_g(s)$ take into account the capacitor and interface impedance respectively.

$$F_c(s) = \frac{1 + sC_f R_d/\omega_b}{sC_f/\omega_b} \tag{2.41}$$

$$Y_g(s) = \frac{1}{R_g + sL_g/\omega_b} \tag{2.42}$$

The equivalent Bode diagram of the transfer function $G_V(s)$ as obtained in (2.40) is plotted in Figure (2.7); physical values used for the calculation are the ones reported in Table 2.1. The profile associated to the load function shows a non-monotonic behaviour and a resonance peak close to the desired cut-off angular frequency ω_{cV}, thus the regulator coefficients definition has to be carried out carefully.

2.6.2 Design approach 1

A first approach consists in the application of the same formulations (2.43)-(2.44) used for the current controller (Appendix B). These expressions allow to identify the proportional and integral coefficients of the PI, as functions of the desired cut-off angular frequency ω_{cV} and phase margin ϕ_{mV} for the voltage loop; $G_V(s)$ is the load function as reported in (2.40).

$$k_{pV} = \frac{\cos(-\arg(G_V(j\omega_{cV})) - \pi + \phi_{mV})}{|G_V(j\omega_{cV})|} \tag{2.43}$$

$$k_{iV} = -\omega_{cV} \frac{\sin(-\arg(G_V(j\omega_{cV})) - \pi + \phi_{mV})}{|G_V(j\omega_{cV})|} \tag{2.44}$$

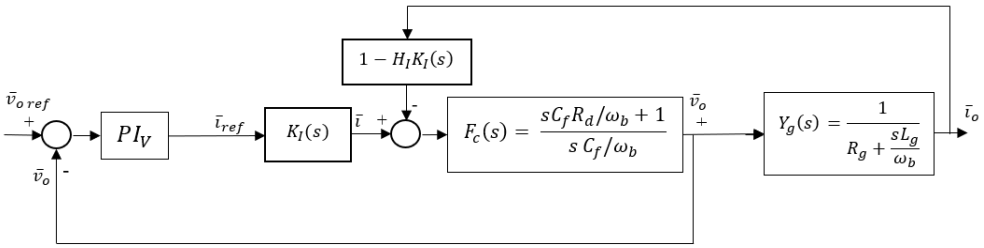

(a) Simplified voltage control scheme - step 1

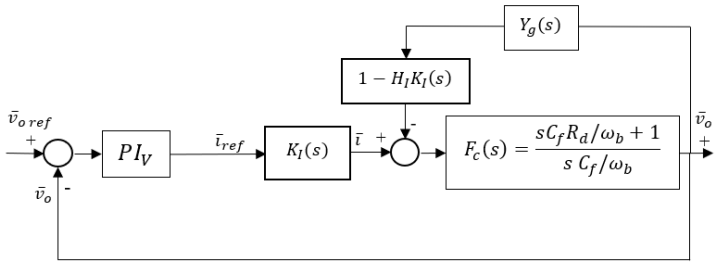

(b) Simplified voltage control scheme - step 2

FIGURE 2.6: Simplified schemes for the identification of the loop function $G_V(s)$. Coupling terms and external grid voltage $\bar{v}_g$ are neglected into the derivation of the model.

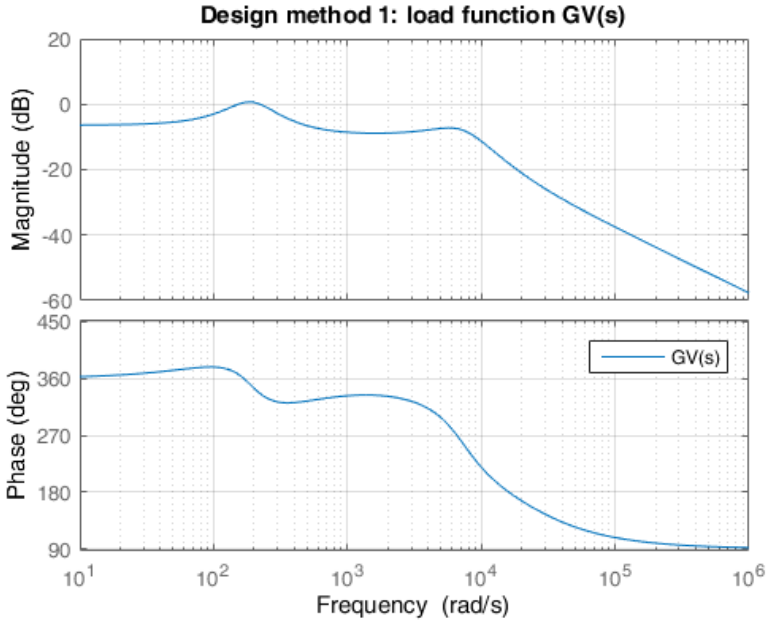

FIGURE 2.7: Equivalent simplified load function $G_V(s)$ of the voltage regulator. Coupling terms are not taken into account during the design phase.

Once defined the desired cut-off ω_{cV} according to Table 2.1, one can choose $\phi_{mV} = 90$ degrees, obtaining $k_{pV} = 1.74$ pu and $k_{iV} = 610.$ pu/s.; the open and closed-loop functions for this case are reported in Fig. 2.8.

In Fig. 2.9, the values of the parameters k_{pV} and k_{iV} as a function of the desired phase margin ϕ_{mV} are plotted. Nevertheless it is difficult to have a clear understanding of what is physically happening inside the control and which is an acceptable phase margin for the loop. Moreover (2.43) and (2.44) require the phase evaluation of a high-order transfer function $G_V(j\omega_{cV})$ where the position of the poles cannot be calculated in an analytical form; thus the implementation of (2.43) and (2.44) requires a significant computational effort, that may be hardly obtainable with standard micro-controllers.

In this perspective, a simplified low-order evaluation of the equivalent load function $G_V(s)$ is proposed. This allows to derive analytical expressions for the regulator coefficients k_{pV} and k_{iV} that can be calculated also when the control device shows a low computational power.

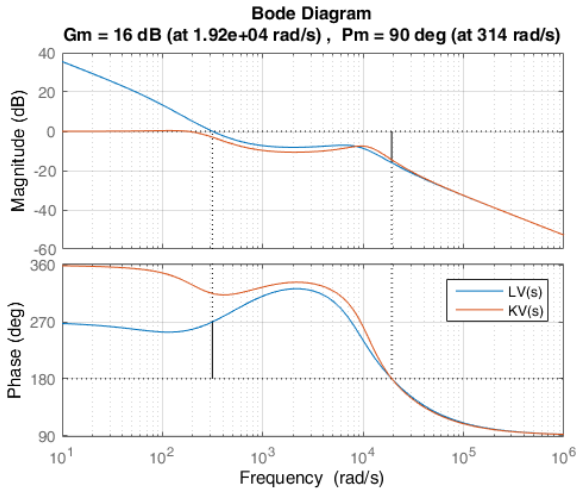

FIGURE 2.8: Open $L_V(s)$ and closed loop function $K_V(s)$ associated to the voltage loop, designed according to the Method 1.

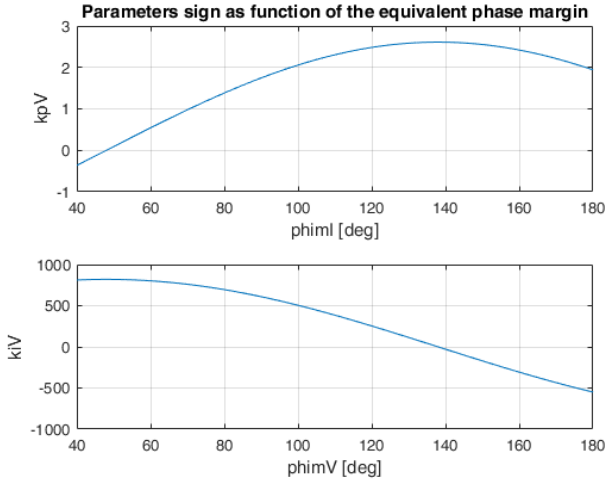

FIGURE 2.9: Values of the regulator coefficients k_{pV}-k_{iV} as function of the phase margin under design Method 1 ($\omega_{cV} = 2\pi \cdot 50$ rad/s.)

2.6.3 Design approach 2

Consider the expression of the equivalent load function $G_V(s)$ as identified in (2.40). The idea behind this design method is to express voltage controller parameters as a direct function of the physical characteristics of the system, in a form which is readily implementable on a low-computational-power controller.

$$G_V(s) = \frac{\left(\frac{1}{1+s/\omega_{cI}}\right)\cdot\left(\frac{1+sC_fR_d/\omega_b}{sC_f/\omega_b}\right)}{1+\left(1-H_I\cdot\left(\frac{1}{1+s/\omega_{cI}}\right)\right)\cdot\left(\frac{1+sC_fR_d/\omega_b}{sC_f/\omega_b}\right)\cdot\left(\frac{1}{sL_g/\omega_b+R_g}\right)} \tag{2.45}$$

The calculation of the denominator in (2.45) would lead to a third order polynomial; even though it can be solved analytically, it is not easy to manage the expressions of the obtained roots.

Nevertheless, a single approximation in (2.45) allows to reduce the system order while keeping most of the information related to the dynamical effect of the terms inside the control: considering the Bode diagram associated to the non-ideal current feed-forward $(1-H_IK_I(s))$ as reported in Fig. 2.10, it is easy to recognize that the dominant behaviour in the frequency range of interest can be approximated as the combination of a gain with a low-frequency zero. Thus:

$$(1-H_IK_I(s)) = \left(1-H_I\cdot\left(\frac{1}{1+s/\omega_{cI}}\right)\right) = \tag{2.46}$$

$$= \left(\frac{1+s/\omega_{cI}-H_I}{1+s/\omega_{cI}}\right) = \tag{2.47}$$

$$= (1-H_I)\cdot\frac{1+\frac{s}{\omega_{cI}\cdot(1-H_I)}}{1+s/\omega_{cI}} \cong \tag{2.48}$$

$$\cong (1-H_I)\cdot\left(1+\frac{s}{\omega_{cI}\cdot(1-H_I)}\right) \quad \text{for } \omega_s \le \omega_{cI}\ (s=j\omega_s) \tag{2.49}$$

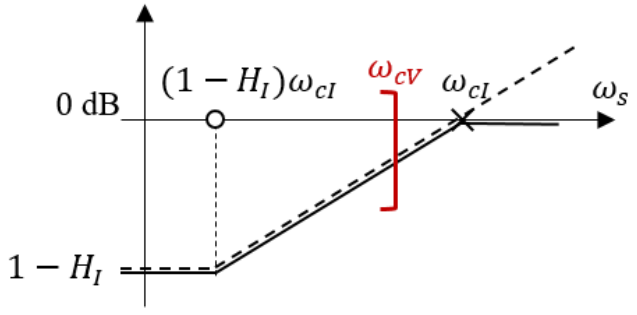

FIGURE 2.10: Approximation of the dynamic behaviour of the non-ideal feed-forward current compensation.

Introducing the approximation (2.49) in (2.45) leads to the following expression for the load function $G_V(s)$:

$$G_V(s) = \left(\frac{1}{1+s/\omega_{cI}}\right) \cdot \frac{(1+sC_fR_d/\omega_b)\cdot(sL_g/\omega_b+R_g)}{\frac{s^2}{\omega_b^2}\cdot a + \frac{s}{\omega_b}\cdot b + c} = \tag{2.50}$$

$$= \left(\frac{1}{1+s/\omega_{cI}}\right) \cdot \frac{R_g\,(1+s/\omega_Z)\,(1+sT_g)}{(1-H_I)\,(1+s/\omega_{p1})\,(1+s/\omega_{p2})} \tag{2.51}$$

$$a = \left(L_gC_f + C_fR_d\frac{\omega_b}{\omega_{cI}}\right) \qquad b = \left(R_gC_f + (1-H_I)\,R_dC_f + \frac{\omega_b}{\omega_{cI}}\right) \tag{2.52}$$

$$c = (1-H_I) \qquad \omega_Z = \frac{\omega_b}{C_fR_d} \tag{2.53}$$

The formulation in (2.50) is significant as it allows to analytically keep into account the predominant dynamics and to understand the influence of each element in the stability of the open loop function $L_V(s)$:

- the current controller produces a pole ω_{cI} at high frequency, typically outside the desired pass-band of the voltage loop ω_{cV} ($\omega_{cI} \cong 7\,\omega_{cV}$);
- the combination of the capacitor C_f with the damping resistor R_d produces a zero at high frequency ($\omega_Z \cong 30\omega_b \cong 10^4$ rad/s);
- the interaction of the grid with the control system introduces a zero in $\tau_g^{-1} = \omega_b \cdot \frac{R_g}{L_g}$ and a couple of poles (ω_{p1} - ω_{p2}) that can be obtained from the resolution of the second order polynomial. Given the value of the difference $1 - H_I$ sufficiently small ($H_I = 0.95$), the two pulsations ω_{p1} and ω_{p2} are real for all the possible combinations of the output impedance parameters, as the polynomial discriminant is positive (Fig. 2.11).

Figure 2.12 represents the asymptotic behaviour of the load function $G_V(s)$: in the low frequency range $\omega_s < \omega_{cV}$, the function resembles the one reported in Fig. 2.7, even

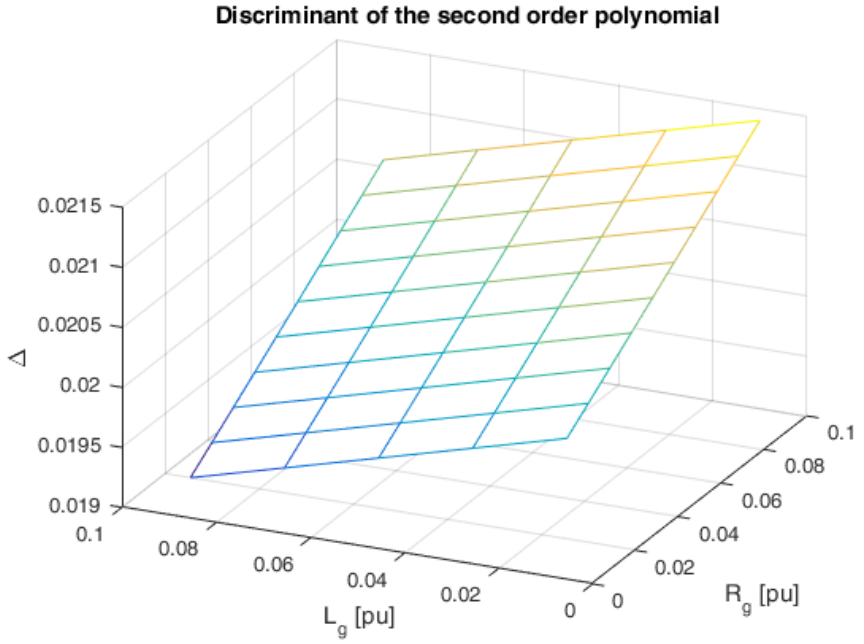

FIGURE 2.11: Sign of the discriminant for the second-order polynomial in (2.50) under typical values of the output-impedance parameters R_g and L_g.

though some differences exist in the high frequency range.

The voltage regulator can be designed imposing its zero T_{iV}^{-1} far below the desired cut-off frequency ω_{cV} and then imposing the loop pass-band for the system by acting on the proportional term k_{pV}. Consider $T_{iV}^{-1} = \frac{k_{iV}}{k_{pV}} = 10$ rad/s: as the zero of the controller T_{iV}^{-1} occurs before the expected cut-off angular frequency of the voltage loop ω_{cV}, the PI behaves almost as a pure proportional term k_{pV} close to ω_{cV}. Thus it is possible to derive the simplified expression of the proportional and integral terms as:

$$k_{pV} \cdot |G_V(j\omega_{cV})| \cong 1 \tag{2.54}$$

$$k_{pV} = \frac{L_g C_f + R_d C_f \omega_b/\omega_{cI}}{\omega_b^2} \cdot \frac{\sqrt{\omega_{p1}^2 + \omega_{cV}^2}\sqrt{\omega_{p2}^2 + \omega_{cV}^2}\sqrt{1 + (\omega_{cV}/\omega_{cI})^2}}{\sqrt{1 + (\omega_{cV} C_f R_d/\omega_b)^2}\sqrt{R_g^2 + (\omega_{cV} L_g/\omega_b)^2}} \tag{2.55}$$

$$k_{iV} = k_{pV} \cdot T_{iV}^{-1} \tag{2.56}$$

The simplified equations in (2.55)-(2.56) can be used as base scheme for the adaptive voltage regulation, in coordination with the impedance estimation algorithm. For the moment, constant coefficients are considered based on the case study reported in Table 2.1. The values of the proportional and integral terms obtained from (2.55)-(2.56) are the following: $k_{pV} = 2.84$ p.u. and $k_{iV} = 28.4$ p.u./s.

Open and closed-loop transfer functions for the voltage control loop in these conditions are reported in Fig. 2.13. Even though in this case the cut-off frequency does not coincide exactly with the desired one ω_{cV}, still the system shows a good phase margin and the definition of the parameters can be easily performed also in real-time with a low-computational-power micro-controller.

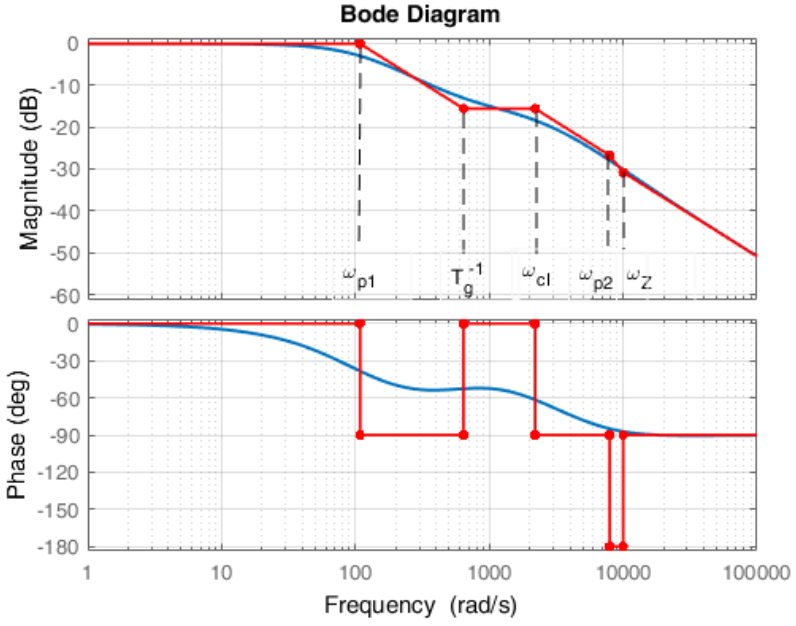

FIGURE 2.12: Asymptotic approximated behaviour of the load function $G_V(s)$. Even though for high frequency the function is different from the exact one reported in Fig. 2.7, still it is able to predict the main tendency of the system in the desired frequency range $\omega_s < \omega_{cV}$.

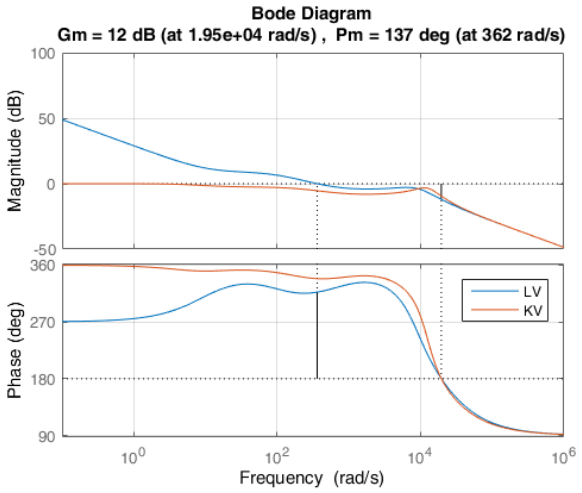

FIGURE 2.13: Open $L_V(s)$ and closed loop function $K_V(s)$ associated to the voltage loop, designed according to the Method 2.

2.7 Effect of the compensations terms on the voltage control loop

Following the procedure presented in [17], it is possible to derive a frequency based characterization of the voltage loop, which allows to study the effect of the feed-forward compensation terms. The proposed approach refers to the complex coefficients transfer functions notation as developed in [18]-[19].

Even though similar analyses have been performed to study the instability of constant-power control schemes (grid-following architecture) in [20]-[21], also including the effect of the phase synchronization [22]-[23], it has rarely been used for the analysis of droop-controlled converters.

The procedure develops in three main steps:

- identification of the transfer functions of each subsystem referred to its proper reference frame ($\alpha\beta$ for the physical circuit, dq for the synchronous control);
- combination of the functional blocks into a unique reference frame (in this case, $\alpha\beta$);
- application of the Generalized Nyquist Criterion [18] for stability evaluation.

2.7.1 Block identification

Consider the blocks related to the voltage loop as reported in Fig. 2.14(a).

- The control acts on the synchronous axes dq quantities and a PI controller is used for the regulation. As the internal current loop is characterized by a faster dynamic behaviour, it can be approximated as the first-order transfer function reported in Appendix B, equation (B.17). On the left side of the picture, it is included the model of the voltage control PI_{Vo}, designed in the previous section, whose expression in the dq frame is:

$$PI_{Vo\,dq} = \frac{sk_{pV} + k_{iV}}{s} \tag{2.57}$$

- The model includes the feed-forward current compensation associated to H_I and the one of the voltage coupling term defined by H_V; both act on dq axes. The

scope of this analysis is to assess their influence on the performance and on the stability of the voltage control.

- The control system acquires the quantities referred to the $\alpha\beta$ frame and later rotate them to synchronous axes; anti aliasing filter $AF(s)$ are included for correct modelling of the high-frequency behaviour. A fourth-order Butterworth filter with a cut-off frequency $\omega_{filt} = 2\pi \cdot 2500$ rad/s is taken into account, coherently with the one installed on the experimental set-up.

$$AF(s) = \frac{\omega_{filt}^2}{s^2 + 2\xi_1\omega_{filt}\, s + \omega_{filt}^2} \cdot \frac{\omega_{filt}^2}{s^2 + 2\xi_2\omega_{filt}\, s + \omega_{filt}^2} \tag{2.58}$$

- On the right side, the dynamical model of the physical system on fixed axes $\alpha\beta$ is depicted. The dynamics of the capacitor filter C_f with its damping resistor R_d and the one of the grid interface impedance are reported; these are respectively defined by the transfer functions $F_c(s)$ and $Y_g(s)$ in Fig.2.14(a).

2.7.2 Graphical resolution of the control system

The procedure allows to determine the behaviour of the voltage regulator, highlighting its dynamical characteristics for positive and negative sequences under possible non-ideal compensations associated to the coupling terms. Moreover, it should be considered that the model as reported in Fig. 2.14(a) does not include approximations, except for the one associated to the internal dynamic of the current loop.

Starting from the model in Fig.2.14(a), it is possible to derive Fig. 2.14(b) and 2.14(c): these modifications preserve the analytical equivalence of the dynamical models, even though the topologies may seem to be different.

Once determined Fig.2.14(c), it is necessary to identify a procedure to transform the transfer function $H_I \cdot K_I(s)$ (referred to the dq frame) into an equivalent block referred to the fixed system $\alpha\beta$. The procedure based on the complex-coefficients transfer matrices [24]-[25] allows to derive the α and β components of the equivalent dynamical model as a function of the original transfer functions in the dq domain, under positive and negative sequences separately. The method significantly simplifies when the control system is identically designed in the d and q axes, which is the case of Fig. 2.14(a) - 2.14(c).

Under this condition, the equivalent $\alpha\beta$ model can be easily obtained by means of an angular frequency shift expressed by (2.59), as reported in [26] and [27]. Analogously, the reverse transformation is given by (2.60); ω stands for the per-unit angular frequency of the synchronous rotating system, while ω_b is the base angular frequency.

$$F_{\alpha\beta}(s) = F_{dq}(s - j\omega\omega_b) \tag{2.59}$$

$$F_{dq}(s) = F_{\alpha\beta}(s + j\omega\omega_b) \tag{2.60}$$

This allows to build the scheme reported in Fig.2.15(a). The topology change from Fig.2.14(c) to Fig.2.15(a) allows to identify an equivalent loop which comprises the capacitor transfer function $F_c(s)$, the grid admittance $Y_g(s)$ and a weighting function $W(s)$ (2.61), which takes into account the combination of the grid current $\bar{i}_o$ and of its compensation inside the control scheme:

$$W(s) = H_I\, K_{I\,\alpha\beta}(s)\, AF(s) \tag{2.61}$$

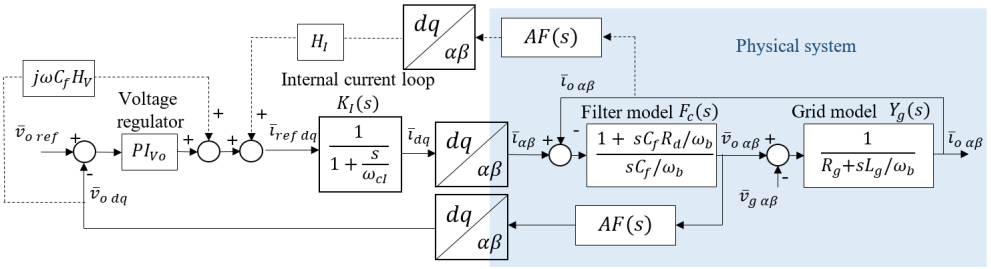

(a) Equivalent voltage control scheme - Step 1

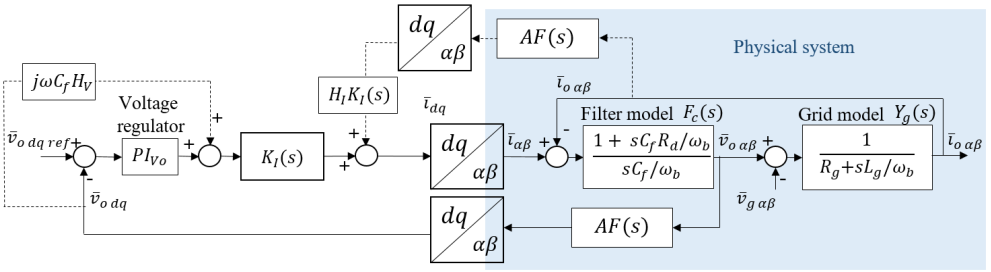

(b) Equivalent voltage control scheme - Step 2

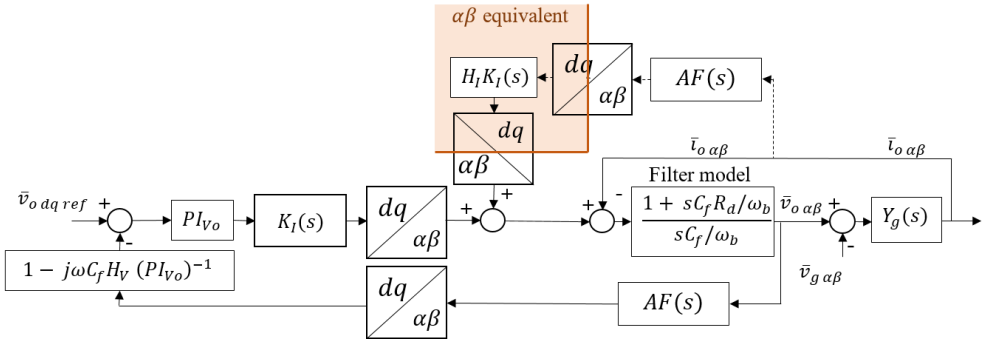

(c) Equivalent voltage control scheme - Step 3

FIGURE 2.14: Analytical derivation of the equivalent voltage control diagram - steps 1-3

The term $K_{I\,\alpha\beta}(s)$ in (2.61) corresponds to the internal current control model as seen by the $\alpha\beta$ frame and it is obtained applying (2.59) to (B.17). The result is a complex coefficients transfer function:

$$K_{I\,\alpha\beta}(s) = K_I(s - j\omega\omega_b) = \frac{1}{1 + s/\omega_{cI} - j\omega\omega_b/\omega_{cI}} \tag{2.62}$$

A further elaboration of the system in Fig.2.15(a) allows to reconstruct the behaviour of the voltage regulator as seen from the $\alpha\beta$ frame. To do so, it is useful to identify a fictitious reference voltage $\bar{v}^{ref}_{o\,\alpha\beta}$ expressed as an $\alpha\beta$ space vector, as shown in Fig.2.15(b).

The elaboration of Fig. 2.15(b) into Fig. 2.15(c) represents the final stage of the analysis. Once obtained the equivalent $\alpha\beta$ sub-blocks by means of the technique already exploited in (2.62), it is possible to obtain a model which links the fictitious capacitor voltage reference $\bar{v}^{ref}_{o\,\alpha\beta}$ and the actual one $\bar{v}_{o\,\alpha\beta}$ in a unique complex coefficient model referred to the $\alpha\beta$ frame.

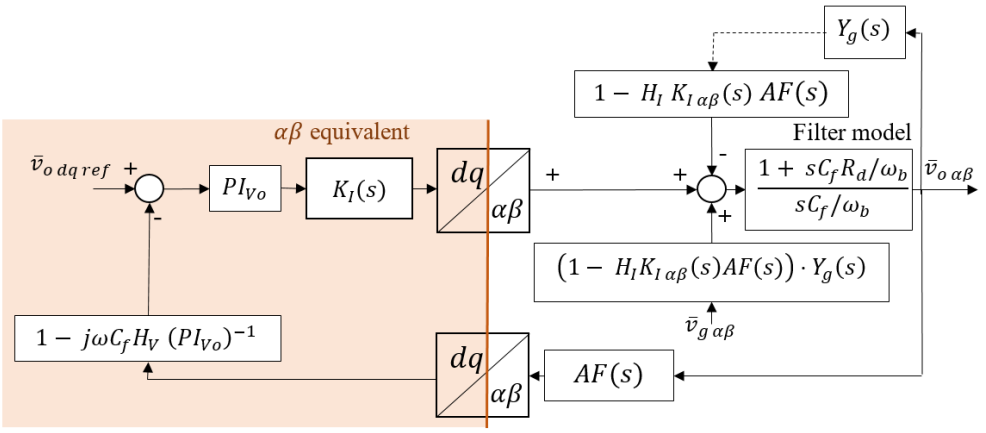

(a) Equivalent voltage control scheme - Step 4

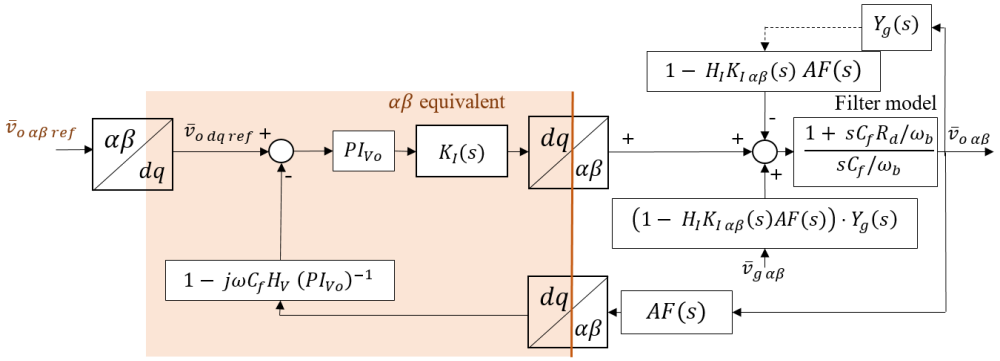

(b) Equivalent voltage control scheme - Step 5

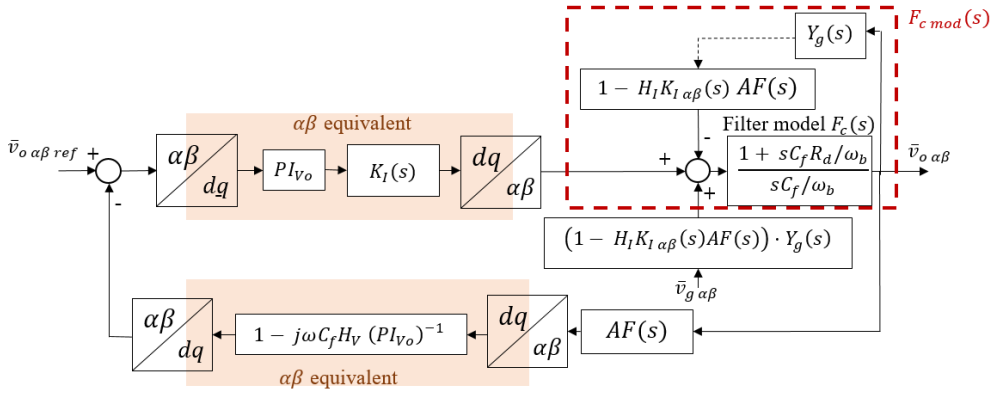

(c) Equivalent voltage control scheme - Step 6

FIGURE 2.15: Analytical derivation of the equivalent voltage control diagram - steps 4-5

Even though the procedure may seem to be excessively complex, it reconstructs in a numerical way the characteristics of the voltage regulator and assesses the consistency of any approximation related to the effect of feed-forward terms.

This allows to express the equivalent controlled voltage $\bar{v}_o$ as:

$$\bar{v}_{o\,\alpha\beta} = K_{V\,\alpha\beta}(s) \cdot \bar{v}^{ref}_{o\,\alpha\beta} \quad (\bar{v}_{g\,\alpha\beta} = 0) \tag{2.63}$$

in which:

$$L_{V\,\alpha\beta}(s) = PI_{Vo\,\alpha\beta}(s) \cdot K_{I\,\alpha\beta}(s) \cdot F_{c\,mod}(s) \cdot \left(1 - j\omega C_f H_V (PI_{\alpha\beta})^{-1}\right) \cdot AF(S) \tag{2.64}$$

$$K_{V\,\alpha\beta}(s) = \frac{PI_{Vo\,\alpha\beta}(s) \cdot K_{I\,\alpha\beta}(s) \cdot F_{c\,mod}(s)}{1 + L_{V\,\alpha\beta}(s)} \tag{2.65}$$

Transfer function $F_{c\,mod}(s)$ in (2.65) stands for the dynamical effect of the capacitor, modified by the non-ideal compensation of the grid current $\bar{i}_o$. It can be obtained as:

$$F_{c\,mod}(s) = \frac{F_c(s)}{1 + F_c(s) \cdot Y_g(s)\,(1 - H_I\,K_{I\,\alpha\beta}(s)\,AF(s))} \tag{2.66}$$

$$\text{where } F_c(s) = \frac{1 + sC_f R_d/\omega_b}{sC_f/\omega_b} \tag{2.67}$$

Transfer function $K_{V\,\alpha\beta}(s)$ takes into account the ability of the control to impose the reference $\bar{v}^{ref}_{o\,\alpha\beta}$ to the capacitor bank; $L_{V\,\alpha\beta}(s)$ determines the stability conditions for the control and keeps into account all the effects associated to axes coupling and partial compensations.

2.7.3 Effect of the output current feed-forward coefficient H_I

Consider the Bode diagrams associated to the open-loop function $L_{V\,\alpha\beta}(s)$ under different values of the feed-forward compensation H_I; all the results reported here are obtained by means of a self-developed Matlab library that allows to perform frequency shift operations (2.59) - (2.60) in an automated way and, lately, to analyse the dynamical behaviour of the system under positive and negative sequences.

The loop stability is studied referring to the generalized Nyquist stability criterion for complex coefficients transfer functions as reported in [18]. Since the loop transfer function $L_{V\,\alpha\beta}(s)$ is obtained as a product of sub-blocks with negative real-part poles, the stability is guaranteed provided that the loop function does not perform rotations around the point $(-1; 0)$ in the complex plane [28]. The technique is very powerful as it allows to keep into account in a numerical way all the effects associated to the system sub-block, while keeping a simple formal representation.

Figure (2.18(a)) considers the case in which no compensation of the external current $\bar{i}_o$ is introduced ($H_I = 0$). In the negative frequencies range, the loop function $L_{V\,\alpha\beta}(s)$ does not show any intersection with the 0dB axis, thus all negative sequence components show a stable behaviour. As for the positive sequences, the Bode diagram of the loop function $L_{V\,\alpha\beta}(s)$ in Fig.2.18(a) shows an ideally-infinite gain in correspondence to the fundamental component of the system; the phase profile does not intersect the boundaries $(-\pi, \pi)$. In order to have a physical interpretation of this condition, consider the Nyquist diagram reported in Fig. 2.16 which is associated to the frequency response profile in Fig.2.18(a). The magnitude diagram intersects the 0dB axis twice even though

no rotations are performed around the point (-1;0); the resulting system is thus stable. The same condition occurs when $H_I = 0.95$ (Fig. 2.18(b)).

On the other hand, consider the simplified representation of the Nyquist diagram in case $H_I = 1$ in Fig. 2.17; the main tendency of the diagram can be reconstructed from the frequency response in 2.18(c). As for the negative sequence, no stability issues are highlighted as the magnitude profile does not intersect the 0dB axis. Nevertheless, the positive sequence response produces a rotation around the point $(-1; 0)$, which determines the instability of the system.

Once assessed the stability of the system for $H_I < 1$, it is interesting to evaluate the performances of the closed-loop control, according to the function $K_1(s)$ in the cases $H_I = 0$ or $H_I = 0.95$ (Fig. 2.19(a) and Fig. 2.19(b) respectively). Predictably, the second case allows a higher regulation capability as it produces a flatter behaviour of the closed-loop function around the nominal angular frequency of the system. The frequency range in which the magnitude is close to 0dB stands for the regulation pass-band of the voltage control, referred to the $\alpha\beta$ frame.

This analysis allows to highlight the following characteristics associated to the compensation terms in the control:

- current feed-forward coefficient H_I plays a major role in the stability of the converter; a design value $H_I = 0.95$ guarantees stable operations and a good regulation pass-band of the voltage control loop;

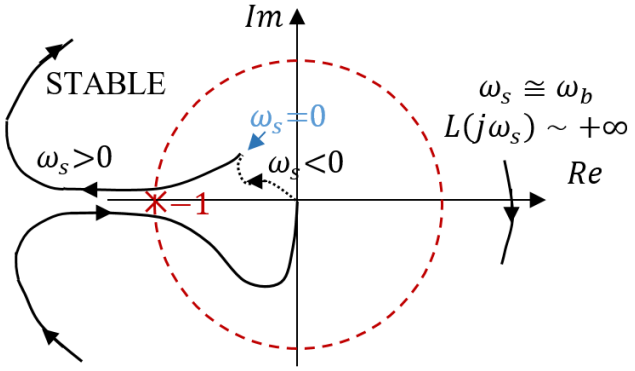

FIGURE 2.16: Generalized Nyquist digram in stable condition.

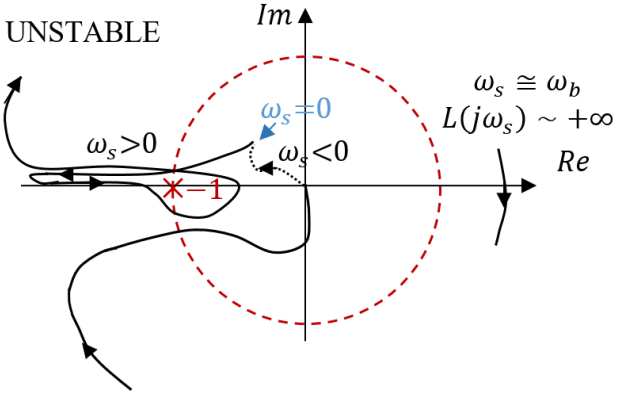

FIGURE 2.17: Generalized Nyquist digram in unstable condition.

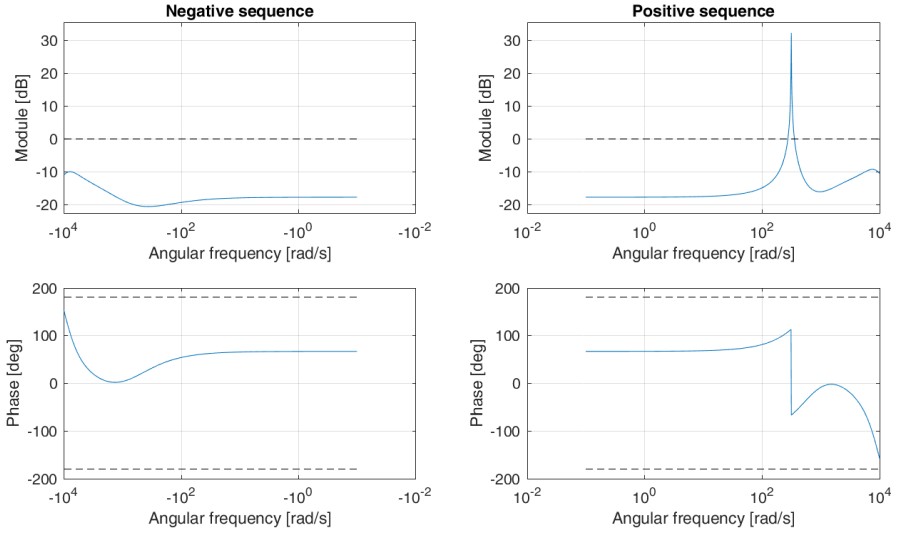

(a) $H_I = 0$

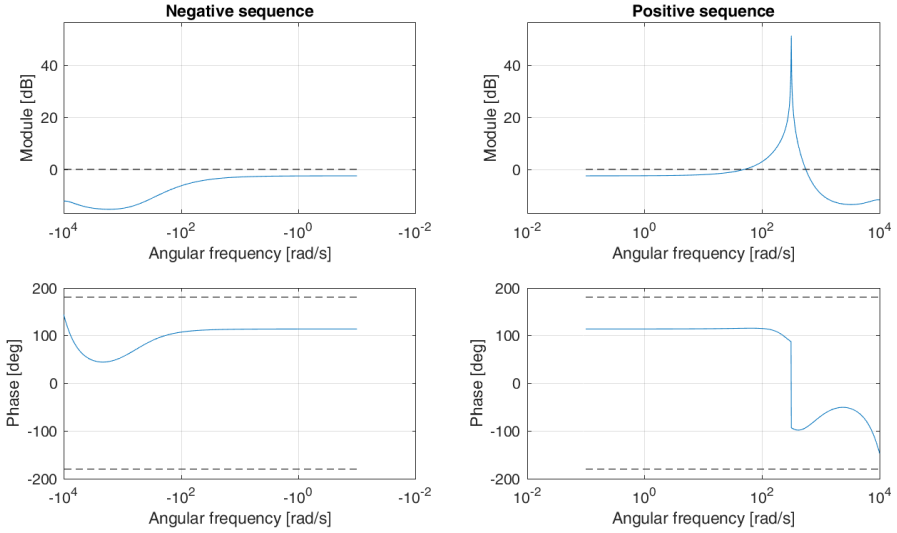

(b) $H_I = 0.95$

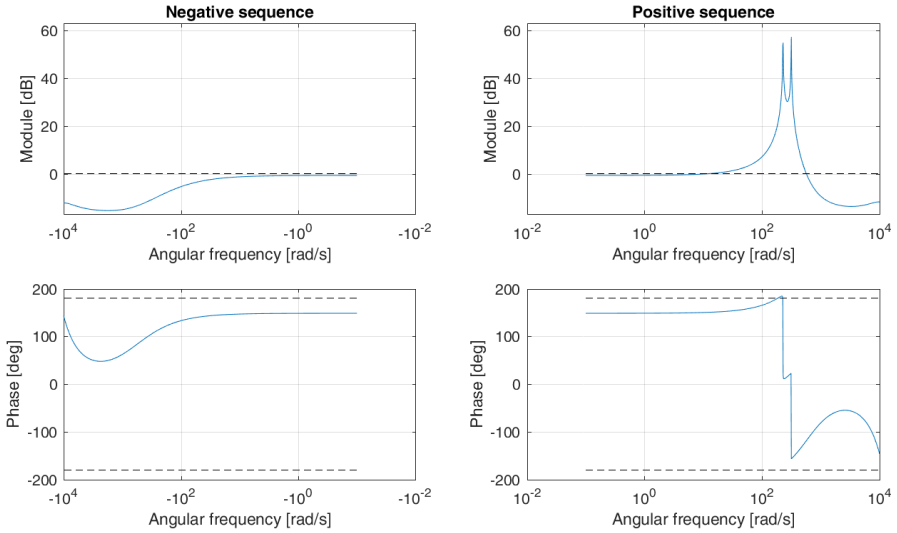

(c) $H_I = 1$

FIGURE 2.18: Frequency response of the open-loop transfer function $L_{V\,\alpha\beta}(s)$ under different values of the feed-forward current coefficient H_I. The diagrams are used to reconstruct the Nyquist representations in Fig.2.16-2.17

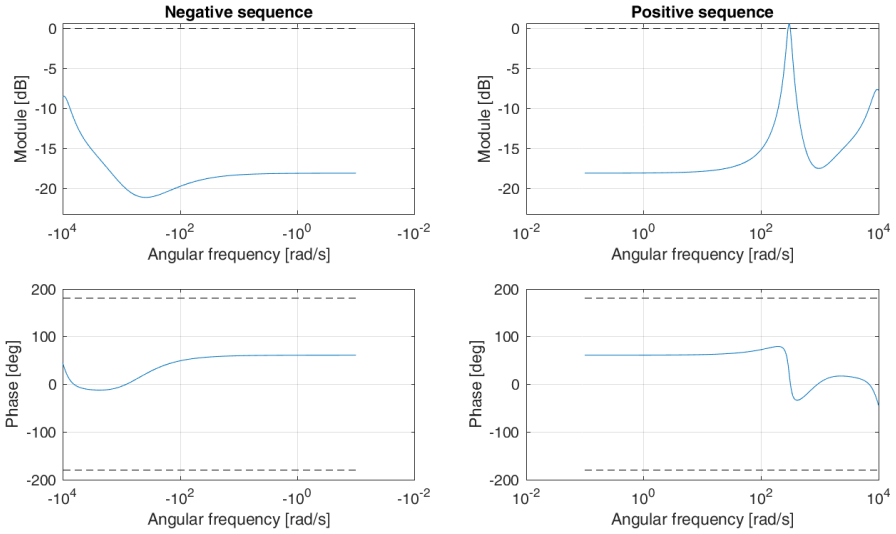

(a) $H_I = 0$

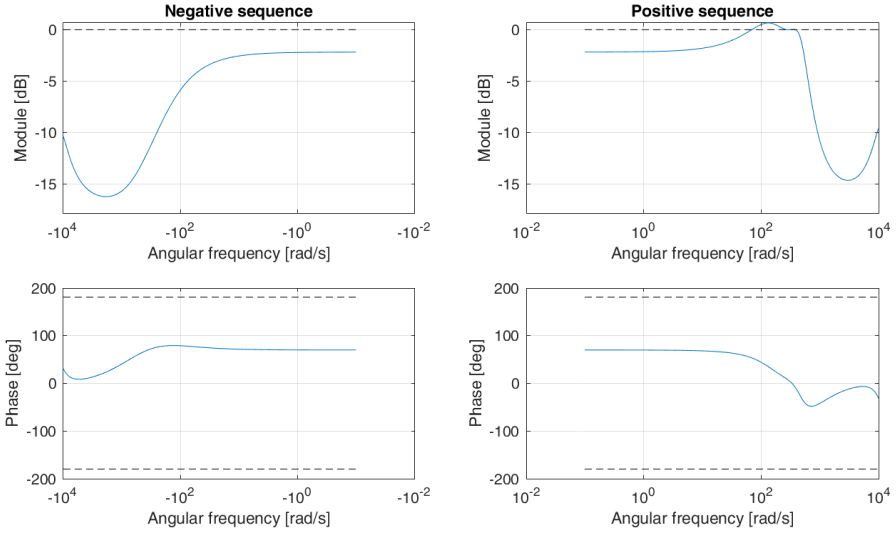

(b) $H_I = 0.95$

FIGURE 2.19: Frequency response of the closed-loop transfer function $K_{V\,\alpha\beta}(s)$ under different values of the feed-forward current coefficient H_I. When $H_I = 0$ (a), the closed-loop function has a magnitude profile much lower than $0\,dB$ for $\omega_s \neq \omega_b$, which indicates poor regulation performances. On the other hand $H_I = 0.95$ (b) guarantees a significant regulation pass-band.

- performing the same analysis on the voltage de-coupling coefficient H_V, it is possible to see that it does not significantly affect the system stability; a value $H_V = 1$ can be chosen.

In the next section, a simplified model for the design of the derivative droop coefficients will be taken into account: the assumptions introduced in the model derivation are the ones just mentioned and, thus, their consistency is supported by the mathematical analysis carried out previously.

2.8 Linearised model

2.8.1 Derivation of the complete linearised model

Consider the linearisation procedure applied to equations (2.22) -(2.38), together with the simplifying hypotheses derived in section 2.7.3 and in [29]. In this context, a microgrid supplied by several converters is taken into account; local loads are modelled as constant absorptions characterized by the active / reactive powers p_{load} and q_{load}. The system under study is a microgrid supplied by several droop-controlled inverters (Figure 2.2(b)); the case of a single converter connected to a very strong grid (Figure 2.2(a)) can be easily obtained from the developed procedure imposing $m_{rest} = n_{rest} = 0$.

The variational method is applied to derive the stability conditions for the droop derivative terms. Each state variable $x(t)$ is linearised in $x(t) = \left(X^0 + \Delta x(t)\right)$ and the dynamical dependencies between the variations are taken into account. The introduced hypotheses are the following:

- the time-derivatives of the steady-state components are obviously equal to zero;
- second-order differential terms are neglected with respect to first order ones, as the product of variations are negligible when the small-signal model is considered;
- steady-state phasor equalities are simplified within the model, leading to a pure variational system;
- the Laplace complex angular frequency s is introduced instead of the derivative operator p in the linearised model.

The application of this procedure to (2.22) -(2.38) leads to the linearised model in (2.68) - (2.76).

$$\Delta\bar{v} = \Delta\bar{v}_o + (R_f + L_f\, s/\omega_b)\ \Delta\bar{i} + jL_f\left(\omega^0\Delta\bar{i} + \Delta\omega\,\bar{I}\right) \tag{2.68}$$

$$\left(C_f\,\frac{s}{\omega_b} + j\omega^0 C_f\right)\Delta\bar{v}_o + j\Delta\omega\, C_f\bar{V}_o =$$

$$= \left(1 + j\omega^0 R_d C_f + R_d\, C_f\,\frac{s}{\omega_b}\right)(\Delta\bar{i} - \Delta\bar{i}_o) + jC_f R_d\Delta\omega\left(\bar{I} - \bar{I}_o\right) \tag{2.69}$$

$$\Delta\bar{v}_o = jV_{pcc}\, e^{j\delta^0}\,\Delta\delta + \Delta V_{pcc}\, e^{j\delta^0} + (R_g + L_g\, s/\omega_b)\ \Delta\bar{i}_o + jL_g\left(\omega^0\Delta\bar{i}_o + \Delta\omega\,\bar{I}_o\right) \tag{2.70}$$

$$\Delta\bar{v}^{ref} = (k_{pI} + k_{iI}/s)\left(\Delta\bar{i}^{ref} - \Delta\bar{i}\right) + \Delta\bar{v}_o + j\,\omega^0\, L_f\,\Delta\bar{i} + j\,\Delta\omega\, L_f\,\bar{I} \tag{2.71}$$

$$\Delta\bar{i}^{ref} = (k_{pV} + k_{iV}/s)\left(\Delta\bar{v}_o^{ref} - \Delta\bar{v}_o\right) + H_i\,\Delta\bar{i}_o + j\omega^0 C_f H_V\Delta\bar{v}_o + j\Delta\omega^0 C_f H_V\bar{V}_o \tag{2.72}$$

$$\Delta\omega = \Delta\omega^* - \frac{m + s\, m_d}{1 + s\, T_p}\cdot\Delta p_o = \Delta\omega^* - \frac{m + s\, m_d}{1 + s\, T_p}\cdot(\Delta v_{od}\, I_{od} + V_{od}\,\Delta i_{od} + \Delta v_{oq}\, I_{oq}) \tag{2.73}$$

$$\Delta v_{od}^{ref} = \Delta V^* - \frac{n + s\, n_d}{1 + s\, T_p}\cdot\Delta q_o = \Delta V^* - \frac{n + s\, n_d}{1 + s\, T_p}\cdot(\Delta v_{oq}\, I_{od} - \Delta v_{od}\, I_{oq} - V_{od}\,\Delta i_{oq}) \tag{2.74}$$

$$\Delta v_{oq}^{ref} = 0 \tag{2.75}$$

$$\frac{s}{\omega_b}\Delta\delta = \Delta\omega_{pcc} - \Delta\omega \tag{2.76}$$

$$\Delta\omega_{pcc} = \Delta\omega^*_{rest} - \frac{m_{rest}}{1 + sT_{rest}}\,\Delta p_{rest} \tag{2.77}$$

$$\Delta V_{pcc} \cong \Delta V^*_{rest} - \left(\frac{n_{rest}}{1 + sT_{rest}} + \omega^0 L_{rest}/V^0_{pcc}\right)\Delta q_{rest} \quad (R_{rest} \cong 0) \tag{2.78}$$

$$\Delta p_{rest} + \Delta p_o \cong \Delta p_{load} \tag{2.79}$$

$$\Delta q_{rest} + \Delta q_o \cong \Delta q_{load} \tag{2.80}$$

The numerical resolution of the Equations (2.68)-(2.80) allows to calculate the eigenvalues of the system at equilibrium. Even though the eigenvalues calculation represents a strong numerical tool for the identification of the stability properties of the converter, still sometimes it is hard to interpret the results and to derive simple design guidelines for the controllers. Thus, in the following it will be developed a simplified model that takes into account the dominant dynamics associated to the droop control: the aim is to provide an intuitive understanding of how each control element affects the system stability.

In particular, the simplified model will be exploited for the identification of suitable design criteria for the derivative droop coefficients.

2.8.2 Reduced order model

Consider a reduced-order model obtained from the application of reasonable simplifications to the complete linearised system (2.68)-(2.80). The hypotheses introduced in this context are the following:

- the internal current loop of the system, designed according to Appendix B, has a fast response; thus it can be assumed as an ideal unitary gain and its internal dynamics are neglected;

- As the effect of the damping resistor R_d is typically associated to the high-frequency behaviour, it will be neglected in this simplified model developed for derivative droop coefficients design that mainly affect the dominant low angular frequency dynamics of the system.
- provided that the voltage control regulator is designed taking into account the effects of the non-ideal compensation H_I, it can be approximated as an equivalent first order low-pass filter with a pass-band equal to the desired cut-off frequency ω_{cV}.

The application of these simplifying hypotheses to (2.68)-(2.80) leads to the reduced order system reported in (2.81)-(2.88).

$$\Delta\bar{v}_o = jV_{pcc}\,e^{j\delta^0}\,\Delta\delta + \Delta V_{pcc}\,e^{j\delta^0} + (R_g + L_g\,s/\omega_b)\;\Delta\bar{i}_o + jL_g\left(\omega^0\Delta\bar{i}_o + \Delta\omega\,\bar{I}_o\right) \quad (2.81)$$

$$\Delta\bar{v}_o = \frac{1}{1+s/\omega_{cV}}\cdot\Delta\bar{v}_o^{ref} = K_V(s)\,\Delta\bar{v}_o^{ref} \quad (2.82)$$

$$\Delta\omega = \Delta\omega^* - \frac{m + s\,m_d}{1+s\,T_p}\cdot(\Delta v_{od}\,I_{od} + V_{od}\,\Delta i_{od} + \Delta v_{oq}\,I_{oq}) \quad (2.83)$$

$$\Delta v_{od}^{ref} = \Delta V^* - \frac{n + s\,n_d}{1+s\,T_p}\cdot(\Delta v_{oq}\,I_{od} - \Delta v_{od}\,I_{oq} - V_{od}\,\Delta i_{oq}) \quad (2.84)$$

$$\Delta v_{oq}^{ref} = 0 \quad (2.85)$$

$$\frac{s}{\omega_b}\Delta\delta = \Delta\omega_{pcc} - \Delta\omega \quad (2.86)$$

$$\Delta\omega_{pcc} = \Delta\omega_{rest}^* - \frac{m_{rest}}{1+sT_{rest}}\;(\Delta p_{load} - \Delta p_o) \quad (2.87)$$

$$\Delta V_{pcc} = \Delta V_{rest}^* - \left(\frac{n_{rest}}{1+sT_{rest}} + \omega^0 L_{rest}/V_{pcc}^0\right)\cdot\;(\Delta q_{load} - \Delta q_o) \quad (2.88)$$

Moreover, the steady state load angle δ^0 is typically small, thus the projection of (2.81) on direct and quadrature axes leads to:

$$\begin{aligned}\Delta v_{od} &= -\sin(\delta^0)V_{pcc}\Delta\delta + \Delta V_{pcc}\cos(\delta^0) + (R_g + L_g\,s/\omega_b)\;\Delta i_{od} - L_g\left(\omega^0\Delta i_{oq} + \Delta\omega\,I_{oq}\right) \cong \\ &\cong \Delta V_{pcc} + (R_g + L_g\,s/\omega_b)\;\Delta i_{od} - L_g\left(\omega^0\Delta i_{oq} + \Delta\omega\,I_{oq}\right)\end{aligned} \quad (2.89)$$

$$\begin{aligned}\Delta v_{oq} &= \cos(\delta^0)V_{pcc}\Delta\delta + \Delta V_{pcc}\sin(\delta^0) + (R_g + L_g\,s/\omega_b)\;\Delta i_{oq} + L_g\left(\omega^0\Delta i_{od} + \Delta\omega\,I_{od}\right) \cong \\ &\cong V_{pcc}\Delta\delta + (R_g + L_g\,s/\omega_b)\;\Delta i_{oq} + L_g\left(\omega^0\Delta i_{od} + \Delta\omega\,I_{od}\right)\end{aligned} \quad (2.90)$$

The combination of (2.89) - (2.90) with the system of equations given by (2.82)-(2.88) is the starting point of the analysis: defining the equivalent impedance time constant $T_g = L_g/\left(R_g\omega_b\right)$ and the corresponding admittance function as $Y_g(s) = \frac{1}{R_g(1+sT_g)}$, the linearised system reported in Fig. 2.20 can be obtained.

The complete linearised system is composed of four dynamically-coupled sub-blocks, which determine the stability conditions for the converter both in grid-connected or island mode. The blocks physically correspond to the direct and quadrature axes, as well as to the mathematical implementation of the active and reactive droop equations.

The system in Fig. 2.20 takes into account the dominant dynamics of the system and the dependency with respect to the steady state current conditions. As a first assumption, it is possible to assume that the converter is operated in no-load conditions (Fig. 2.21): starting from this common frame, the behaviour of the system in grid-connected and during island operations will be analysed separately.

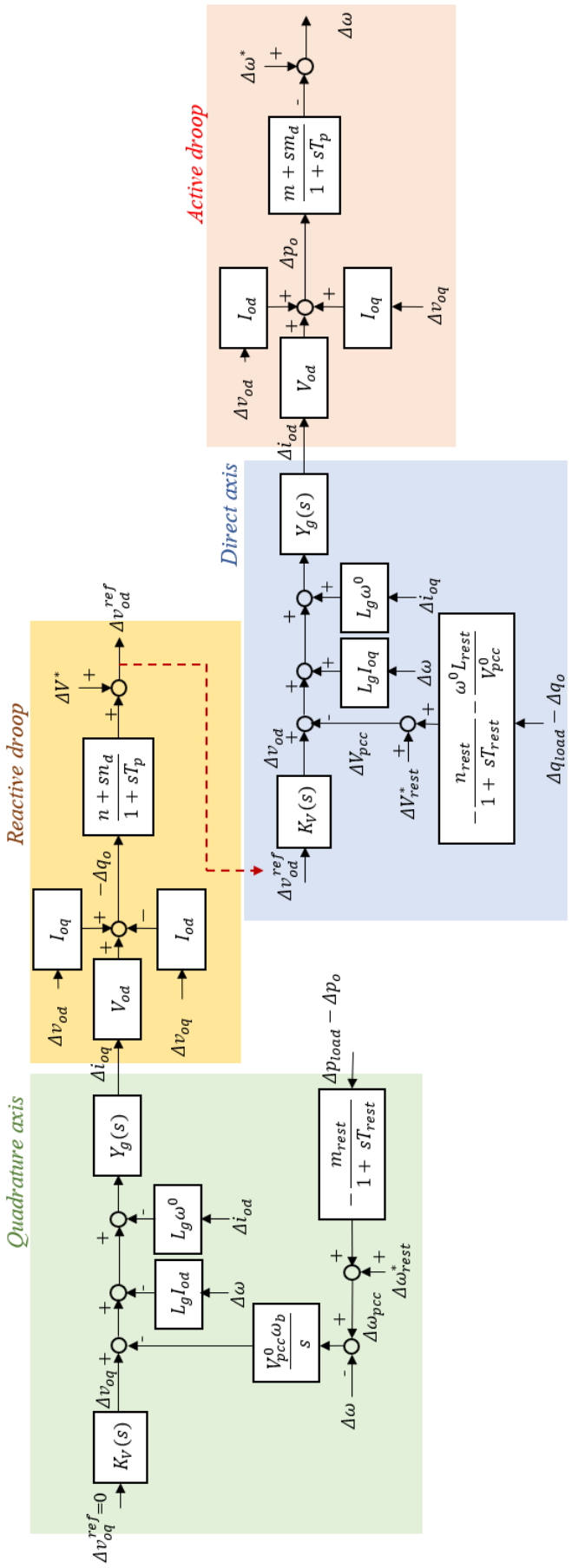

FIGURE 2.20: Complete representation of the linearised droop system. The model is composed of four different sub-block respectively associated to the direct and quadrature components, as well as of the active and reactive droop equations that produce the axis coupling.

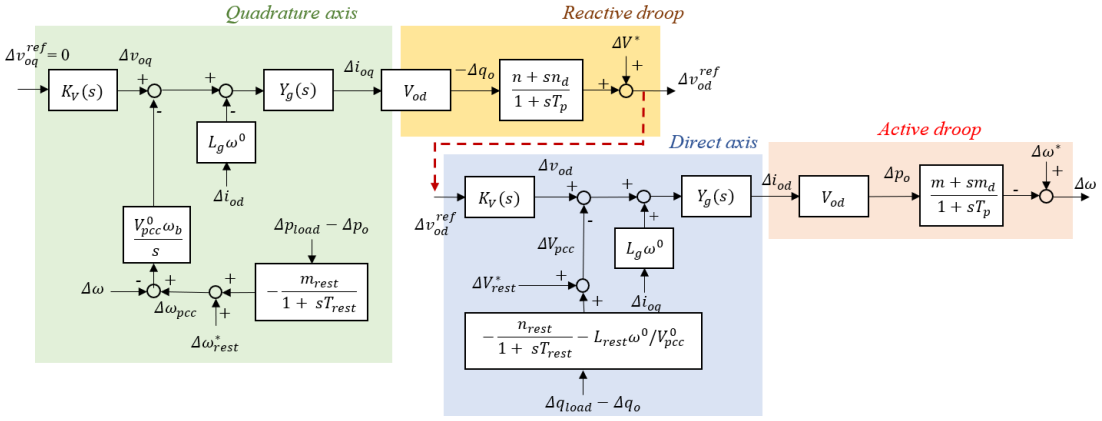

FIGURE 2.21: No-load model of the converter for the design of derivative droop coefficients.

2.9 Model of the converter in grid-connected mode.

The graphical model reported in Fig. 2.21 can be adapted to the analysis of grid-connected mode conditions. The graphical elaboration of the system is carried out in Fig. 2.22.

Two different aspects will be considered in the analysis:

- the prediction of the steady state response of the system after changes in the frequency and voltage droop intersections ($\Delta\omega^*$, ΔV^*);
- the design of the derivative droop coefficients m_d and n_d in a straightforward way.

Even though several authors have proposed the introduction of derivative coefficients to stabilize the dynamics associated to the droop control both recently [6] and in the past [12] - [13], still it is difficult to find a model that really tries to understand in deep the dynamic effect of these regulation terms. Elaborating the models is [29] - [16], the architecture here proposed seems to predict very well the dynamical characteristics of the control.

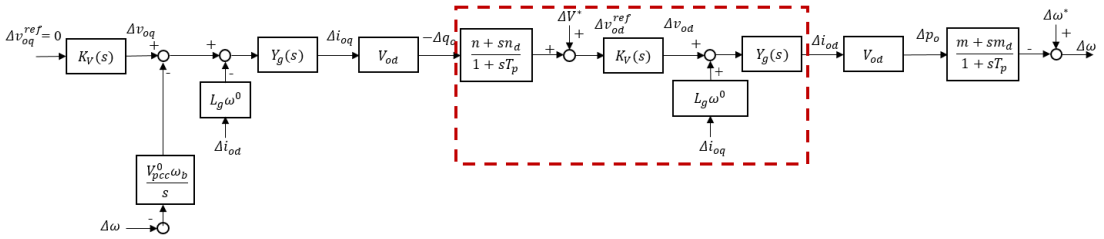

(a) Step 1

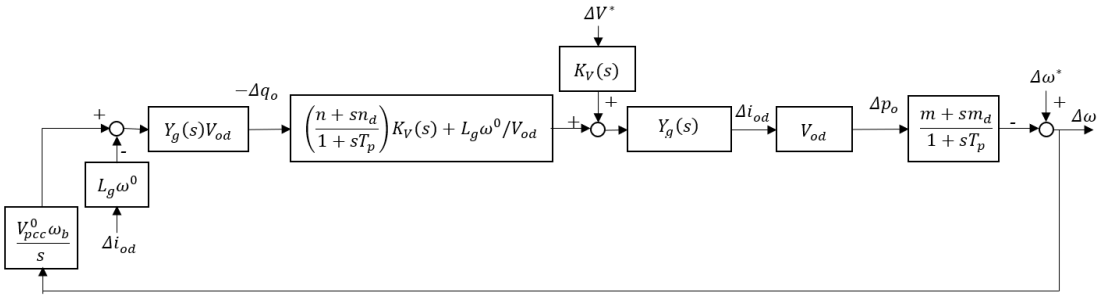

(b) Step 2

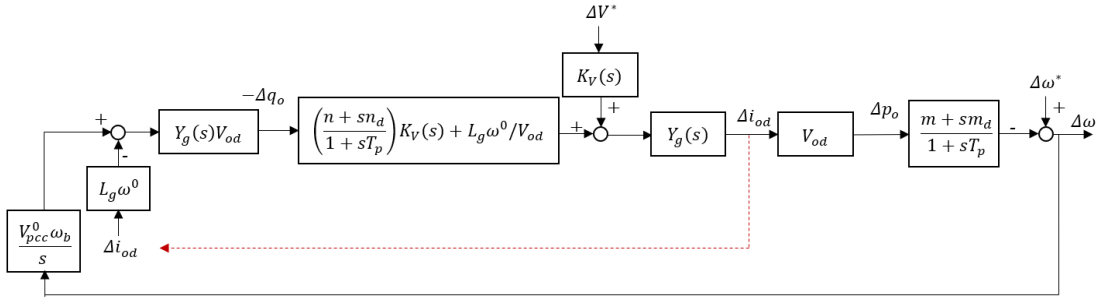

(c) Step 3

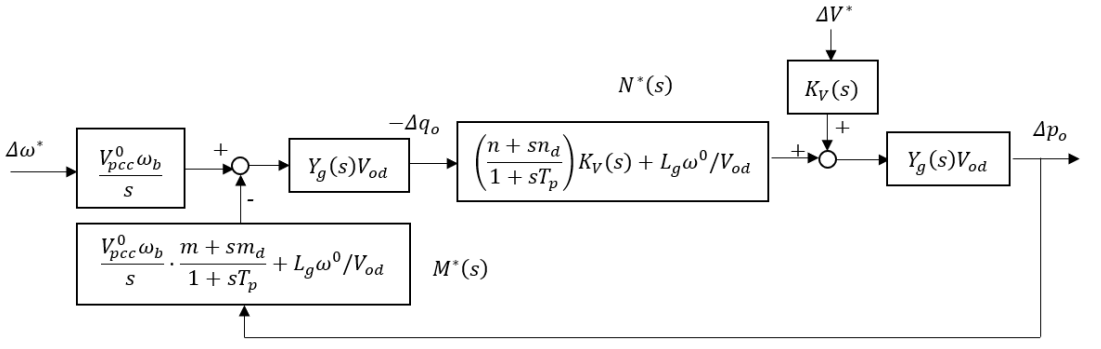

(d) Step 4

FIGURE 2.22: No-load model of the converter in grid-connected mode.

2.9.1 Derivative coefficients design

Consider the model reported in Fig. 2.22(d); the expressions of the transfer functions involved in the determination of the loop stability are the following:

$$Y_g(s) = \frac{1}{R_g + sL_g/\omega_b} = \frac{1/R_g}{1+sT_g} \tag{2.91}$$

$$K_V(s) = \frac{1}{1+s/\omega_{cV}} \tag{2.92}$$

$$N^*(s) = \left[\frac{n+sn_d}{1+sT_p}\cdot K_V(s) + L_g\omega^0/V_{od}\right] = \tag{2.93}$$

$$= \frac{n + \frac{\omega^0 L_g}{V_{o\,d}} + s\left(n_d + \frac{T_p L_g \omega^0}{V_{od}} + \frac{L_g\omega^0}{\omega_{cV}V_{od}}\right) + s^2\frac{T_p L_g\omega^0}{\omega_{cV}V_{od}}}{(1+sT_p)\cdot\left(1+\frac{s}{\omega_{cV}}\right)} \tag{2.94}$$

$$M^*(s) = \left[\frac{V^0_{pcc}\omega_b}{s}\frac{m+s\,m_d}{1+sT_p} + L_g\omega^0/V_{od}\right] = \tag{2.95}$$

$$= \frac{V^0_{pcc}\omega_b}{s}\cdot\frac{m+s\left(m_d + \frac{L_g\omega^0}{V_{od}V^0_{pcc}\omega_b}\right) + s^2\frac{T_pL_g\omega^0}{V_{od}V^0_{pcc}\omega_b}}{1+sT_p} = \tag{2.96}$$

$$= \frac{V^0_{pcc}\omega_b}{s}\cdot m\cdot\frac{1+\frac{2\xi_M}{\omega_{n\,M}}s + \frac{s^2}{\omega^2_{n\,M}}}{1+sT_p} \tag{2.97}$$

According to the scheme in Fig. 2.22(d), the loop function is given by (2.98). Initially the sub-functions will be analysed separately and then will be combined together in the loop $L_{\text{droop}}(s)$ for stability evaluation.

$$L_{\text{droop}}(s) = Y_g^2(s)V_{od}^2M^*(s)N^*(s) \tag{2.98}$$

As a first step, consider the function $N^*(s)$; it shows:

- a low frequency pole in T_p^{-1} associated to the average reactive power calculation;
- a high frequency pole in ω_{cV} associated to the effects of the internal voltage controller;
- a couple of zeros, whose angular frequencies depend on the control characteristics and on the equivalent inductance L_g seen at the interface point.

As ω_{cV} typically shows a higher values with respect to the droop dynamics, the asymptotic behaviour $\omega_{cV}\to\infty$ can be invoked to derive the approximated positions of the zeros; in particular it is possible to see that the system shows a low-frequency zero and a high frequency one close to ω_{cV}. Thus the function $N^*(s)$ can be approximated as

$$N^*(s) \cong \frac{\left(n + L_g\omega^0/V_{od}\right)\cdot(1+s\tau^*_N)}{1+sT_p} \tag{2.99}$$

where the zero is placed at the angular frequency:

$$\tau^{*\,-1}_N = \frac{\left(n + L_g\omega^0/V_{od}\right)}{(n_d + T_pL_g\omega^0/V_{od})} \tag{2.100}$$

Figure 2.23 shows the asymptotic behaviour of the transfer function $N^*(s)$ under different values of the derivative parameter n_d: a positive n_d moves the zero of the transfer function to lower angular values, while a negative n_d shifts the zero position towards faster dynamics. Even though $n_d = 0$, the zero introduced by the function is still placed close to the pole in T_p^{-1}: this reduces the sensitivity of the loop function $L_{\text{droop}}(s)$ with respect to the derivative voltage droop coefficient n_d.

Consider now the behaviour associated to $M^*(s)$, as defined in (2.96). For $m_d = 0$, the Bode diagram shows:

- a couple of low-angular-frequency poles (one in the origin and one in T_p^{-1});
- a couple of complex conjugate zeros, whose natural frequency and damping are respectively given by (2.101) and (2.102).

The introduction of a positive coefficient m_d linearly increases the damping associated to the zeros in $M^*(s)$, while keeping a constant natural frequency $\omega_{n\,M}^*$. The corresponding Bode diagram is reported in Fig. 2.24.

$$\omega_{nM}^* = \sqrt{\frac{mV_{od}V_{pcc}^0\omega_b}{T_pL_g\omega^0}} \tag{2.101}$$

$$\xi_M^* = \frac{1}{m}\left(m_d + \frac{L_g\omega_0}{V_{od}V_{pcc}^0\omega_b}\right)\cdot 0.5\cdot\omega_{n\,M}^* \tag{2.102}$$

Once identified the general behaviour of the single sub-functions, all the dynamics are combined together in order to identify the stability properties of the loop $L_{\text{droop}}(s)$ (2.98). Consider the initial case in which both the derivative terms m_d and n_d are equal to zero. Referring to the numerical values reported in Tables 2.1 and 2.2, Fig. 2.25 holds.

The dominant dynamics of the open-loop function $L_{\text{droop}}(s)$ in (2.98) lead to the asymptotic Bode diagram reported in Fig. 2.25. It is possible to identify:

- a pole in the origin;

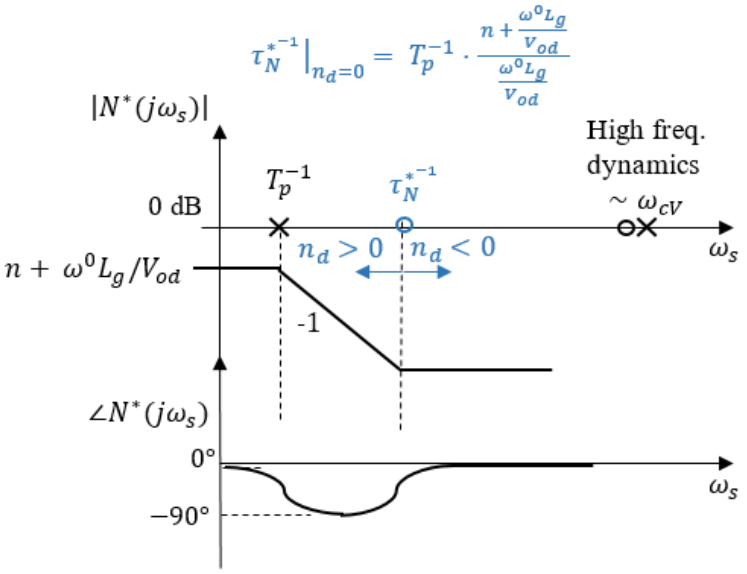

FIGURE 2.23: Asymptotic behaviour of the transfer function $N^*(s)$

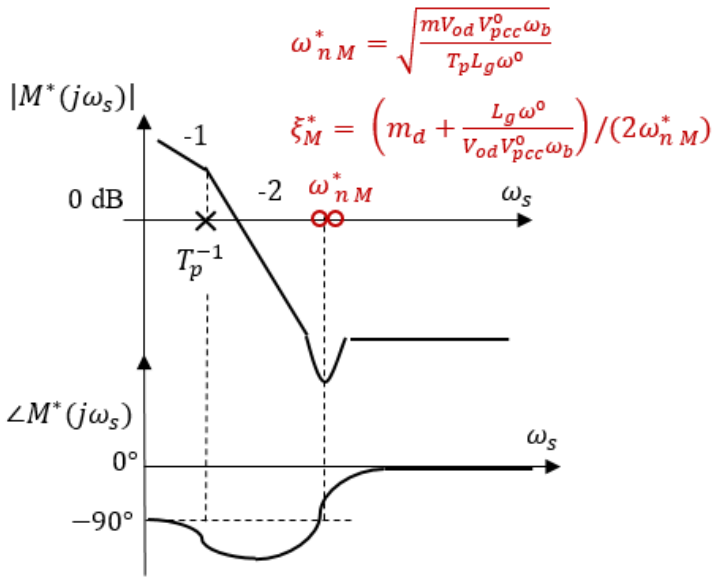

FIGURE 2.24: Asymptotic behaviour of the transfer function $M^*(s)$

- a couple of real poles in $T_p^{-1} = 10$ rad/s;
- a zero introduced by the voltage droop in $\tau^{*\,-1}_N(n_d = 0) = 17$ rad/s;
- a couple of low-damped complex conjugate zeros introduced by the frequency droop, with $\omega^*_{\mathrm{n\,M}} = 36$ rad/s and $\xi^*_M = 0.14$;
- a couple of real poles associated to the equivalent grid admittance $T_g^{-1} = \frac{\omega_b R_g}{L_g}$. The position of these poles exclusively depends on the relative value of the per-unit resistance, per-unit inductance and on the base angular frequency ω_b. In order to assess the effect of these dynamics on the system stability, it is possible to consider a variation range that includes grids characterized by a strong inductive nature, as well as more resistive ones. For low voltage grids the characteristic impedance ratio ranges in $R_g/L_g \in [0.25; 4]$ p.u., thus $T_g^{-1} \in [80; 1250]$ rad/s: thus these poles are typically much faster than the cut-off angular frequency associated to the droop feedback.

It is possible to see that the open loop function is characterized by a low stability margin because of the combination of the slow-frequency poles which are only partially compensated by the zeros in the loop. Even though the pole T_g^{-1} of the transfer function $Y_g(s)$ can be generally neglected, the ratio L_g/R_g affects the stability as it influences the $L_{droop}(s)$ gain (Fig. 2.25(a)). Higher values of L_g/R_g produce an increase of the pass-band and thus a higher leading contribution to the phase-margin from the zeros: this has a positive effect on system stability.

Furthermore, stability can be improved introducing the droop derivative coefficients m_d and n_d: the idea is to compensate the delay of the couple of real poles in T_p^{-1} by acting on the positions of the zeros associated to the frequency and voltage droop, that can be modified by m_d and n_d. Thus the design can be performed imposing that:

- the zeros in $\tau^{*\,-1}_N$ is moved left-ward to have $\tau^{*\,-1}_N \cong T_p^{-1}$: this can be done acting on the coefficient n_d.
- the introduction of a strong derivative action on the frequency droop by means of $m_d > 0$ increases the damping ξ^*_M and produces a left-side movement of one

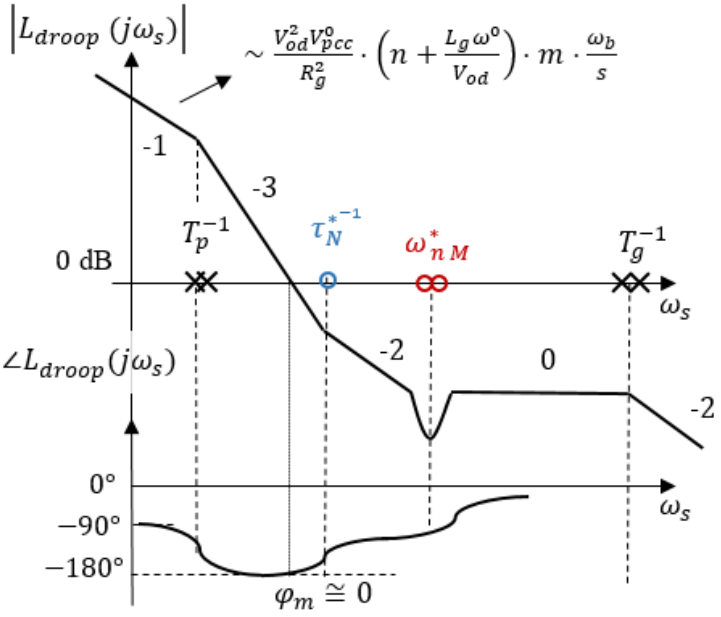

(a) Singularities identification

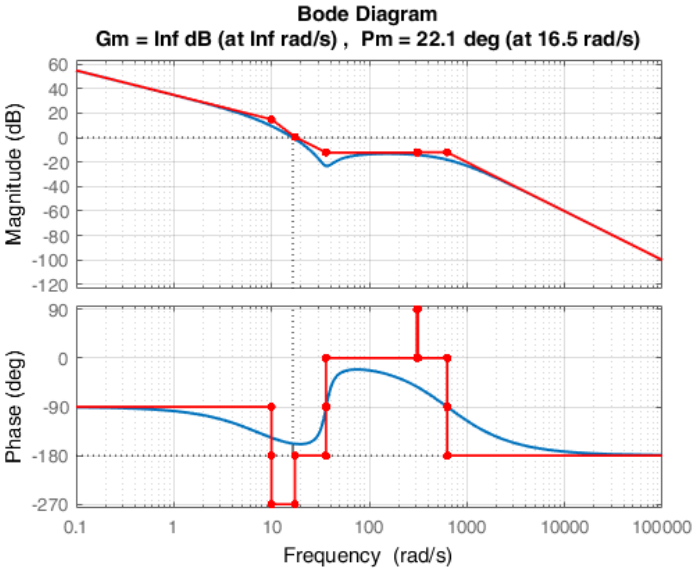

(b) Exact plot (MATLAB)

FIGURE 2.25: Asymptotic behaviour of $L_{\text{droop}}(s)$ with $m_d = 0$ and $n_d = 0$.

frequency droop zero; the other moves right-ward and does not affect the system stability.

The combination of these two effects almost entirely compensates the delay introduced by the poles in T_p^{-1} and significantly increases the system phase margin. The proposed design idea is illustrated in Fig. 2.26.

According to the proposed design concept, the values of the derivative droop coefficients can be derived as follows:

- in order to make ${\tau^*}_N^{-1} \cong T_p^{-1}$, it has to be chosen $n_d = n \cdot T_p$;
- In order to provide sufficient stability, the damping has to be chosen $\xi_M^* > 1$ to have real zeros. Analysing the damping function in (2.102), it is possible to see that the term associated to the inductance L_g is practically very small, as it is divided by the base angular frequency ω_b. Thus for $m_d \neq 0$ equation (2.102) can be approximated as:

$$\xi_M^* \cong \frac{m_d}{m} \cdot 0.5 \cdot \omega_{n\,M}^* \tag{2.103}$$

The correctness of the proposed results has been verified considering the correspondence of the reduced-order stability limits with the ones obtainable in a numerical way from the eigenvalues of the complete model of the system. Figure 2.27 shows the influence of the derivative term on the eigenvalues of the complete full-order model, as a proof of the validity of the developed analysis. The stability limit of the full system is reached for $m_d = 0$ (and $n_d = 0$ in this numerical model); the result is coherent with the characteristics of the approximated loop function of the droop $L_{\text{droop}}(s)$ that in the same conditions shows a limited even though positive phase margin (Fig. 2.25(b)). Moreover, the analysis of the participation factors [30] associated to the slow dynamics of the system reveals a strong dependence with respect to the state variables involved in the definition of the loop $L_{\text{droop}}(s)$.

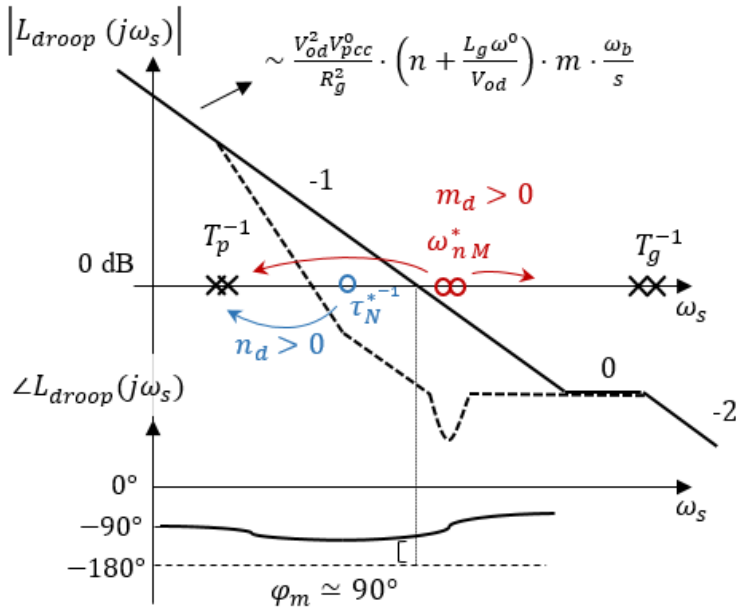

FIGURE 2.26: Asymptotic behaviour of the transfer function $L_{\text{droop}}(s)$ when derivative terms m_d and n_d are introduced. Dashed lines indicate the base case without derivative coefficients already introduced in Fig.2.25(a).

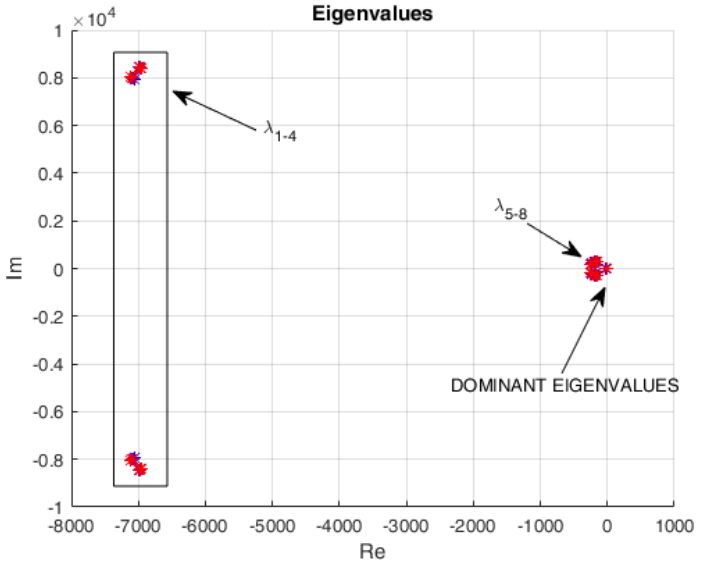

(a) Fast dyanamics

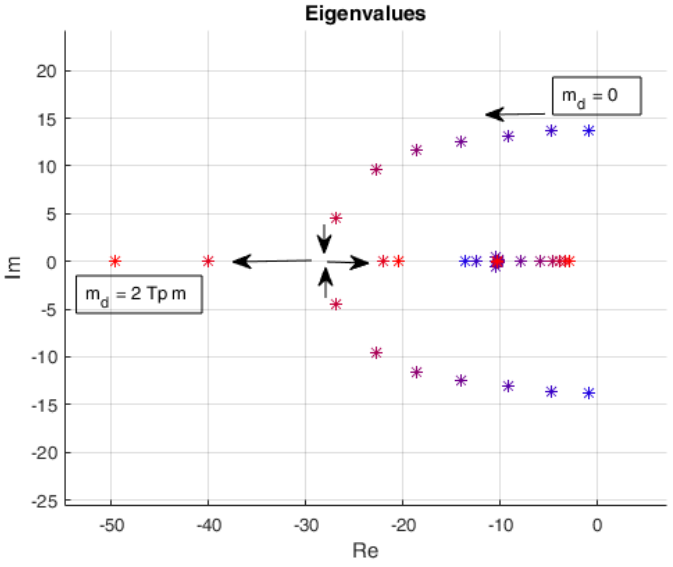

(b) Dominant eigenvalues

FIGURE 2.27: System eigenvalues under different values of the frequency droop derivative coefficient $m_d \in (0; 2 \cdot T_p \cdot m)$ with steps of $\Delta m_d = 0.25 T_p m$. The eigenvalues evolution shows the strong stabilization effect introduced by m_d; voltage derivative term n_d has been taken equal to zero. Eigenvalues in blue stand for the lower values of the m_d interval, while red ones are associated to the higher values.

A similar analysis has been done for the voltage droop derivative coefficient n_d, even though the improvements in terms of system stability are less effective. This is reasonable since the zero in τ^{*-1}_N introduced by the reactive droop is naturally close to the poles in T_p^{-1} even with $n_d = 0$, as it is possible to see in Fig. 2.28.

2.9.2 Steady state conditions

The Laplace final-value theorem applied to the diagram in Fig. 2.22(d) and the feedback resolution allow to identify the steady-state variations of the output quantities (active / reactive powers Δp_o-Δq_o) after a step-step change of the control variables (frequency / voltage droop intersection $\Delta\omega^*$-ΔV^*).

The active power steady state variation after a step change of the frequency droop intersection $\Delta\omega^*$ is given by:

$$\Delta p_o(\infty) = \lim_{s\to 0} s \cdot \frac{V^0_{pcc}\omega_b}{s} \cdot Y_g^2(s)V_{od}^2 \cdot N^*(s) \cdot \frac{1}{1 + Y_g^2(s)V_{od}^2 N^*(s)M^*(s)} \cdot \frac{\Delta\omega^*}{s} \tag{2.104}$$

where:

$$N^*(s) = \left[\frac{n + L_g\omega^0/V_{od} + s(n_d + T_p L_g\omega^0/V_{od})}{1 + sT_p}\right] \tag{2.105}$$

$$M^*(s) = \left[\frac{V^0_{pcc}\omega_b}{s}\frac{m + s\,m_d}{1 + s\,T_p} + L_g\omega_0/V_{od}\right] \tag{2.106}$$

$$Y_g(s) = \frac{1/R_g}{1 + sT_g} \tag{2.107}$$

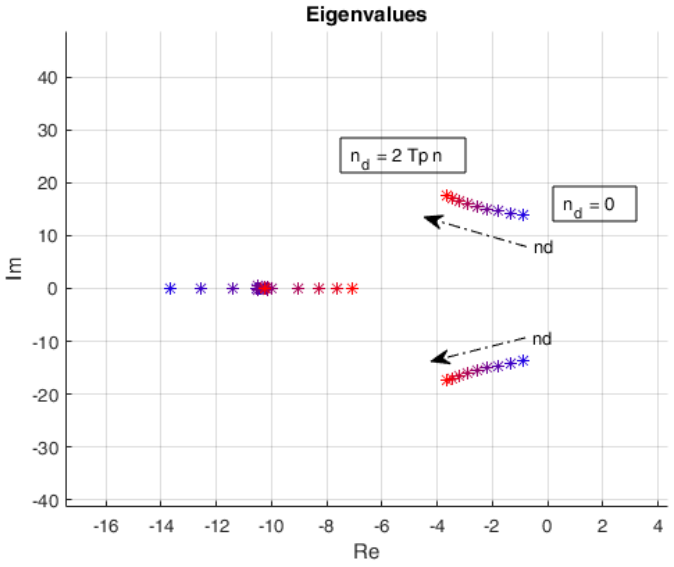

FIGURE 2.28: System eigenvalues under different values of the voltage droop derivative coefficient $n_d \in (0; 2\cdot T_p \cdot n)$ with steps of $\Delta n_d = 0.25 T_p n$. The term n_d has a stabilizing effect, even though it shows a lower effectiveness if compared to m_d as it is possible to see by comparison with Fig.2.27; the frequency derivative term m_d has been taken equal to zero. Eigenvalues in blue stand for the lower values of the n_d interval, while red ones are associated to the higher values.

Considering that:

$$N^*(0) = n + L_g\omega^0/V_{od} \tag{2.108}$$

$$M^*(0) \simeq \frac{V_{pcc}\omega_b m}{s} \tag{2.109}$$

$$Y_g(0) = 1/R_g \tag{2.110}$$

Equation (2.104) becomes:

$$\Delta p_o(\infty) = \lim_{s\to 0} \frac{V_{pcc}^0\omega_b}{s} \cdot \frac{n + L_g\omega^0/V_{od}}{R_g^2} \cdot V_{od}^2 \cdot \frac{1}{1 + \frac{V_{od}^2}{R_g^2} \cdot (n + L_g\omega^0/V_{od}) \cdot \frac{V_{pcc}\omega_b m}{s}} \cdot \Delta\omega^* = \tag{2.111}$$

$$= \lim_{s\to 0} \frac{V_{pcc}^0\omega_b}{s} \cdot \frac{1}{\frac{V_{pcc}\omega_b m}{s}} \cdot \Delta\omega^* = \frac{\Delta\omega^*}{m} \tag{2.112}$$

Equation (2.112) shows that a change in the frequency droop reference produces a proportional variation of the injected active power by means of the inverse of the coefficient m, as desired. Nevertheless, it is also interesting to analyse if a step change in $\Delta\omega^*$ affects the reactive term Δq_o.

$$\Delta q_o(\infty) = \lim_{s\to 0} -s \cdot \frac{V_{pcc}\omega_b}{s} \cdot Y_g(s)V_{od} \cdot \frac{1}{1 + {Y_g}^2(s)V_{od}^2 N^*(s)M^*(s)} \cdot \frac{\Delta\omega^*}{s} = \tag{2.113}$$

$$= -\lim_{s\to 0} \frac{V_{pcc}\omega_b}{s} \cdot \frac{V_{od}}{R_g} \cdot \frac{1}{1 + \frac{V_{od}^2}{R_g^2} \cdot (n + L_g\omega^0/V_{od}) \cdot \frac{V_{pcc}\omega_b m}{s}} \cdot \Delta\omega^* = \tag{2.114}$$

$$= -\frac{R_g}{(V_{od}n + L_g\omega^0) \cdot m} \cdot \Delta\omega^* \tag{2.115}$$

Equation (2.115) shows that a step variation of the frequency droop intersection causes an undesired change of the reactive power injected by the converter. This behaviour is stronger when the grid shows a highly resistive nature, while it is attenuated in case of strong inductive network or when a high reactive droop term n is introduced. Furthermore the sign of the variation is the opposite of the one associated to active power: thus a positive change of $\Delta\omega^*$ produces an increase of the active power injection and a decrease of the reactive power one.

It is also interesting to analyse the system response under a step change of ΔV^*.

$$\Delta p_o(\infty) = \lim_{s\to 0} s \cdot Y_g(s)V_{od} \cdot \frac{1}{1 + {Y_g}^2(s)V_{od}^2 N^*(s)M^*(s)} \cdot \frac{\Delta V^*}{s} = \tag{2.116}$$

$$= \lim_{s\to 0} \frac{V_{od}}{R_g} \cdot \frac{1}{1 + \frac{V_{od}^2}{R_g^2} \cdot (n + L_g\omega^0/V_{od}) \cdot \frac{V_{pcc}\omega_b m}{s}} \cdot \Delta V^* = 0 \tag{2.117}$$

$$\Delta q_o(\infty) = \lim_{s\to 0} sM^*(s) \cdot {Y_g}^2(s){V_{od}}^2 \cdot \frac{1}{1 + {Y_g}^2(s)V_{od}^2 N^*(s)M^*(s)} \cdot \frac{\Delta V^*}{s} = \tag{2.118}$$

$$= \frac{1}{n + L_g\omega^0/V_{od}} \cdot \Delta V^* \tag{2.119}$$

A variation of the voltage droop reference ΔV^* does not affect active power injection, while it produces a change of the reactive power. Nevertheless, the variation Δq_o is also

influenced by the external inductance of the system, according to (2.119).

To summarize, it is possible to identify some operative considerations:

- active power injection are exclusively influenced by the frequency droop parameters (m and $\Delta\omega^*$), while for reactive power the perfect decoupling cannot be obtained solely by means of a proportional voltage droop control; in this perspective, next chapter will show how it is possible to improve the steady state reactive decoupling introducing an additional *virtual-impedance* loop.
- From (2.115), the positive decoupling effect of a high L_g/R_g ratio can be highlighted, that allows to reduce the undesired reactive power variation caused by the frequency droop modification $\Delta\omega^*$; this is coherent if we consider the intrinsic similarity of the droop control with the inductive power-flow equations reported in the first section of the chapter.

Furthermore, the proposed procedure and the identification of the loop system in Fig.2.20 are very powerful since it can be exploited for the analysis of any type of droop regulation [31]-[32]-[3] and for the determination of their stability properties.

2.9.3 Model verification

The simulated transients reported in Fig. 2.29(a)-2.29(d) are exploited to verify the correctness of the dynamical model introduced in Fig. 2.22(d), both in terms of the steady state behaviour as well as regarding the dynamical improvement introduced by the derivative droop coefficients.

A single converter is simulated in grid-connected mode; the interface impedance is defined by $R_g = 0.55$ and $L_g = 0.53$ per-unit. Two different transients are studied, respectively associated to the changes of the intersections in the angular frequency ($\Delta\omega^* = 0.0025$) and voltage droop ($\Delta V^* = 0.004$); both the transients are reported both in case of normal droop and after the introduction of the derivative terms m_d-n_d. The design of the derivative droop coefficients is carried out referring to the procedure reported in the previous sections and the following values are obtained: $n_d = n \cdot T_p$, $m_d = 0.4 \cdot m \cdot T_p$, that according to (2.103) produce an equivalent damping $\xi_M^* = 0.7$ for the complex conjugate poles in $M^*(s)$ and the compensation of the slow pole in T_p^{-1} in $N^*(s)$.

A first consideration regards the higher stability properties associated to the introduction of the derivative coefficients: the absence of the derivative terms (Fig. 2.29(a) and Fig. 2.29(c)) produces transitory behaviours characterized by significant oscillatory dynamics, which are an indication of the low phase margin in the global system, coherently to the behaviour already highlighted in Fig. 2.27. As a consequence of the same changes in the droop intersections, the derivative terms (Fig.2.29(b) and Fig.2.29(d)) guarantee more regular transients with practically no overshoots. This confirms the validity and the general correctness of the proposed design method for the derivative droop terms, as reported in Section 2.9.1.

A second consideration regards the correctness of the converter behaviour at steady state. According to the model reported in Fig. 2.22(d) and the equations (2.112)-(2.115)-(2.117)-(2.119), the changes in the active and reactive injections can be expressed as a functions of the frequency and voltage droop changes, as well as of the characteristics of the interface impedance. In Table 2.3 this comparisons is carried out. The results obtained from the the system simulation match wit the theoretical ones associated to the analytical resolution of the model derived in Fig. 2.22(d). The correspondence of the theoretical results with the numerical ones represents an intrinsic verification of the

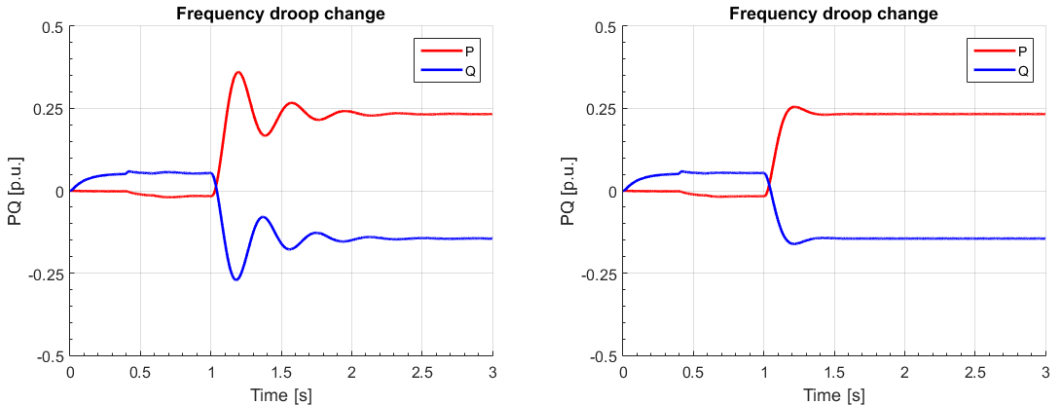

(a) Frequency droop change - no derivative coeff. (b) Frequency droop change - derivative coeff.

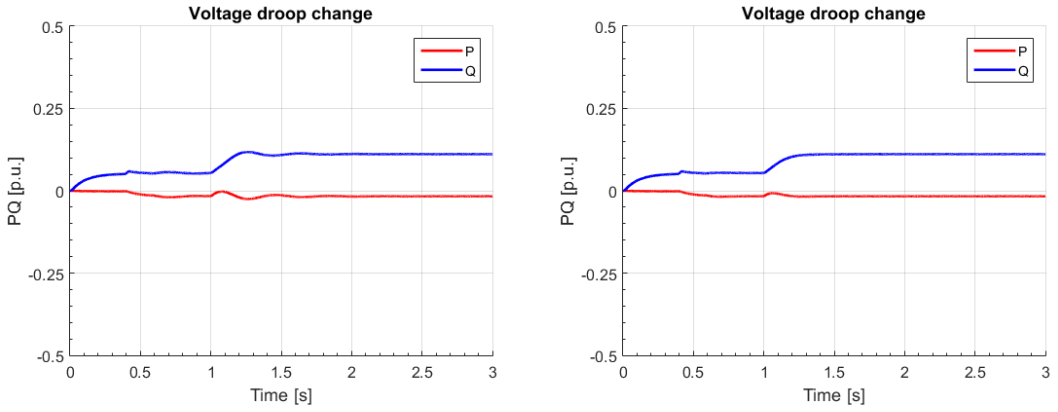

(c) Voltage droop change - no derivative coeff. (d) Voltage droop change - derivative coeff.

FIGURE 2.29: Simulated verification of the dynamical model. The following changes are considered intersections in the angular frequency $\Delta\omega^* = 0.0025$ and voltage droop $\Delta V^* = 0.004$. The changes are considered separately, without and with the derivative droop coefficients m_d-n_d.

derived dynamical model and thus validates its exploitation for the prediction of the converter stability characteristics.

2.10 Model of the converter in island operations.

The model in Fig. 2.21 can be also used to predict the behaviour of the converter when interfaced to an external microgrid operated in island. In particular, it can be exploited to determine the power sharing under step changes associated to the variation

TABLE 2.3: Droop model verification

Droop change	*Power change*	*Theoretical*	*Simulated*	*Mismatch*
$\Delta\omega^* = 0.0025$	$\Delta p_o(\infty)$	0.25 p.u.	0.25 p.u.	< 0.01 p.u.
	$\Delta q_o(\infty)$	-0.20 p.u.	-0.20 p.u.	< 0.01 p.u.
$\Delta V^* = 0.004$	$\Delta p_o(\infty)$	0 p.u.	0 p.u.	< 0.01 p.u.
	$\Delta p_o(\infty)$	0.07 p.u.	0.06 p.u.	0.01 p.u.

of the local load Δp_{load} - Δq_{load}; voltage and frequency droop intersections are assumed constant both for the single converter and for the entire microgrid ($\Delta\omega^* = 0$, $\Delta V^* = 0$, $\Delta\omega^*_{rest} = 0$, $\Delta V^*_{rest} = 0$).

The same procedure carried out for the grid-connected case is taken into account; the graphical elaboration of the block diagram is reported in Figure 2.30 and 2.31. The internal dynamic of the voltage loop has been neglected as its effects, according to the analysis related to the function $N^*(s)$ reported in the previous section, are mainly associated to high frequency behaviour ($K_V(s) = 1$).

The final model as reported in Fig. 2.31(b) allows to identify the power sharing between the unit under test and the external regulation system, that may also represent the equivalent characteristic of other droop-controlled converters which are performing the regulation on the grid.

Again, the steady-state power injection from the converter can be studied referring to the Laplace final-value theorem in Fig. 2.31(b) and subsequent resolution of the feedbacks. Thus the following expressions are obtained:

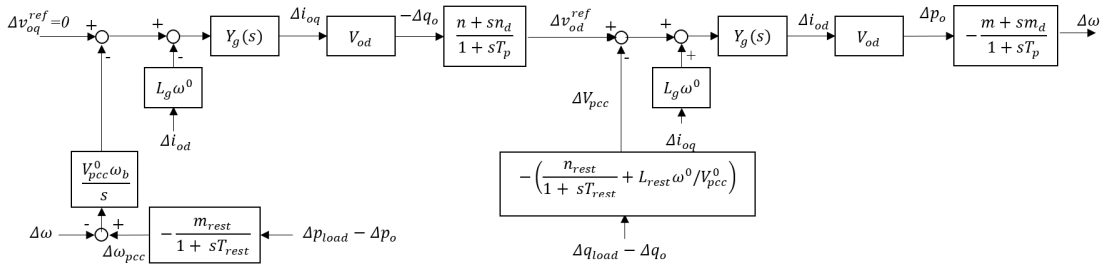

(a) Step 1

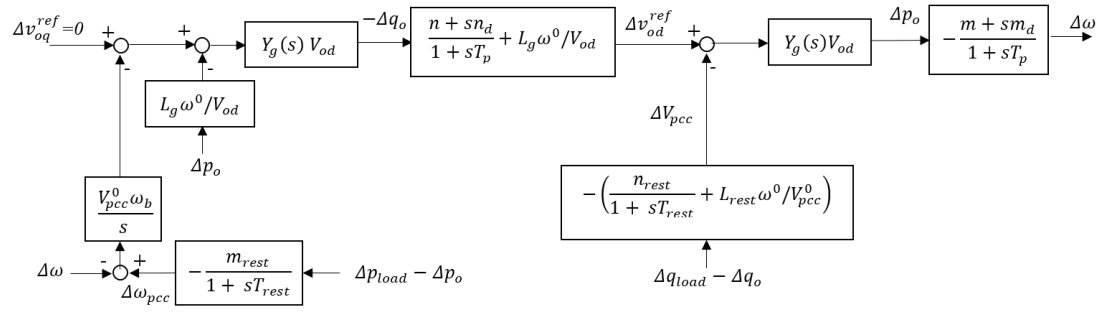

(b) Step 2

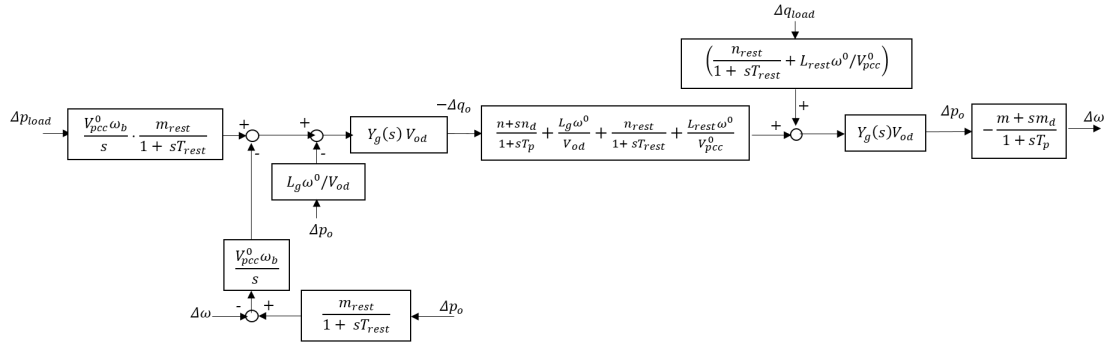

(c) Step 3

FIGURE 2.30: Model of the converter in grid-connected mode. Steps 1-3

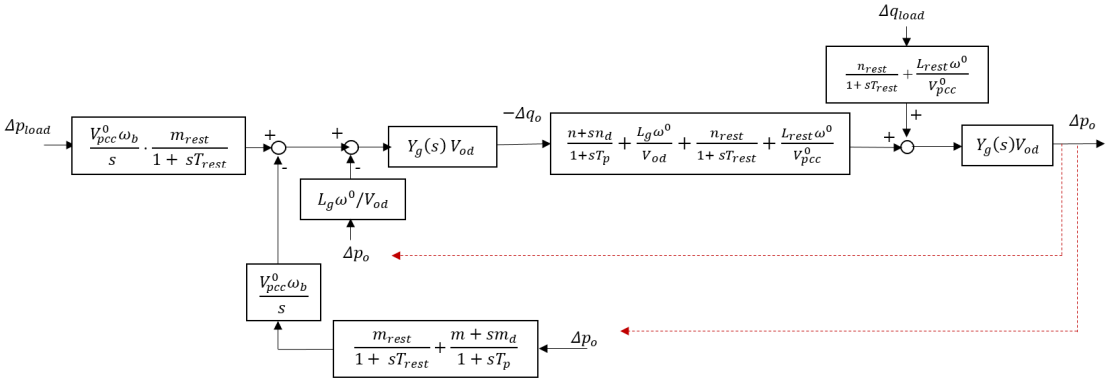

(a) Step 4

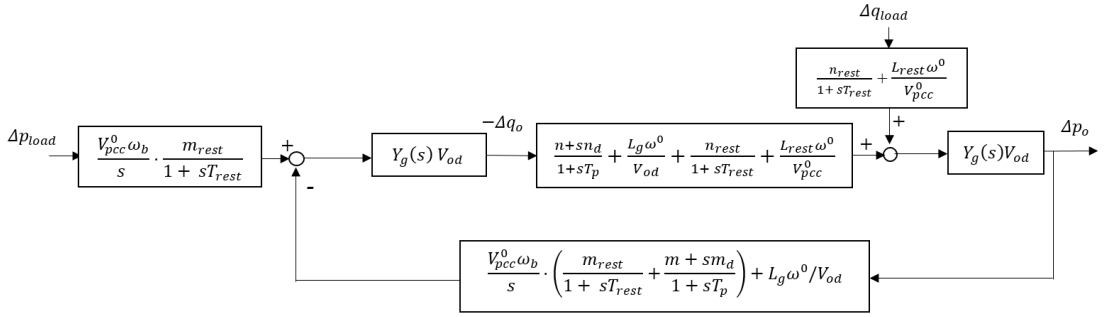

(b) Step 5

FIGURE 2.31: Model of the converter in grid-connected mode. Steps 4-5

Active load variation

$$\Delta p_o(\infty) = \frac{m_{rest}}{m + m_{rest}} \cdot \Delta p_{load} = \frac{\frac{1}{m}}{\frac{1}{m} + \frac{1}{m_{rest}}} \cdot \Delta p_{load} \tag{2.120}$$

$$\Delta q_o(\infty) = -\frac{R_g}{V_{od}} \cdot \frac{1}{n + n_{rest} + \omega^0 L_g/V_{od} + \omega^0 L_{rest}/V_{pcc}} \cdot \frac{m_{rest}}{m + m_{rest}} \cdot \Delta p_{load} \tag{2.121}$$

Reactive load variation

$$\Delta p_o(\infty) = 0 \cdot \Delta q_{load} \tag{2.122}$$

$$\Delta q_o(\infty) = -\frac{n_{rest} + \omega^0 L_{rest}/V_{pcc}}{n_{rest} + \omega^0 L_{rest}/V_{pcc} + n + \omega^0 L_g/V_{od}} \cdot \Delta q_{load} \tag{2.123}$$

The following behaviour already identified in grid-connected conditions is confirmed in island mode:

- as regards active power, the droop regulation is able to share the contribution between the converters proportionally to their rated power;
- reactive injection is contemporaneously affected by the proportional voltage droop coefficient n and by the output impedance of the converter, as well as by the changes in the active absorption of the loads.

2.11 Conclusion

In this chapter, the model of the converter under droop regulation is analysed. The developed model allows to reconstruct the behaviour of the converter both in grid-connected and island mode, predicting injected active and reactive powers after changes of the droop intersections as well as the contribution to the system regulation under variations of the local load. The design of the internal controller has been carried out considering the non-ideal compensation of the current feedback, as well as the effect of the coupling coefficients.

Even though the procedure is based on standard control theory, the analytical evaluation of the effects associated to the non-ideal current compensation in the voltage control loop is generally not analysed in literature. Most of the available papers just propose the introduction of reduced-compensation coefficients without analysing the impact on the equivalent control pass-band: the application of the complex-coefficient functions theory, in this perspective, provides a powerful tool to take into account the exact system dynamics in a straightforward way.

Furthermore, the chapter proposes a new design method for derivative droop coefficients based on the non-linear droop coupling effects identification. The proposed representation enables to highlight the dynamical interactions of the physical and control parameters and can be studied both analytically and numerically.

Chapter 3

Virtual impedance model

3.1 Chapter introduction

In this chapter the virtual impedance control will be introduced. This algorithm allows to improve the performances of traditional droop equations even under the case of an equivalent resistive network; even though this technique has already been proposed in literature, it is difficult to find a straightforward design procedure for the definition of its internal parameters. Thus, in this chapter, it will be proposed a novel design procedure based on the analysis of axes coupling, which allows to determine a stability region for virtual impedance parameters as a function of the external grid characteristics. Additionally it will be highlighted the effect of this additional feedback on the regulation performances of droop-controlled converters operated in grid-connected or island mode.

3.2 State of the art for virtual impedance control

As already pointed out in the previous chapter, the traditional droop scheme shows a significant reduction of its regulation performances when the output impedance of the converter shows a predominant resistive nature. Even though an inverse-droop definition can be applied in case of highly resistive conditions, still this alternative may under-perform in the inductive case. In this perspective, the best available technique to modify the equivalent nature of the system as seen by the converter is represented by the virtual impedance, which has been initially proposed for a single-phase case in [33]. This additional control loop emulates the presence of a generic fictitious element in series (or in parallel) to the physical one; even though different alternative configurations have been presented in literature [34]-[35], here we will refer to the case in which an ohmic-inductive element is mimicked.

This concept is not new and, actually, a vast literature is available as concern the topic; virtual impedance concept has proved to be an effective solution for several problems related to the operations of power converters in island conditions:

- it allows to improve the accuracy of the reactive power sharing between droop converters interfaced to a microgrid system, particularly when each converter shows a different output impedance. This aspect is analysed in [36] and [37], even though in both approaches it is assumed that each converter remains stable independently of the imposed value of the virtual impedance, which is a very strong assumption.
- In [38] and [39], the structure of the virtual impedance is modified to damp selected harmonics into the system, even though the proposed modifications practically prevent from a direct analytical calculation of the stability limits for the converters.

- An interesting work in [40] analyses the stability boundaries for the virtual impedance loop under several interface conditions; the goal is to calculate stability regions for the converter as a function of the actual configuration of the system. Nevertheless the proposed approach is based on the numeric calculation of a high-order eigenvalue model and thus it is characterized by a significant computational cost when extended to multi-converters systems.
- In [41] and [42] it is proposed to exploit a similar concept for secondary regulation inside the microgrid; a single control coefficient is taken into account, even though it is not analysed in deep the effect of axes coupling inside the converter after virtual impedance insertion.

Thus in this chapter, starting from the draft idea proposed in [43], it is presented a new design model of the virtual impedance that aims at identifying the stability regions for the virtual impedance parameters as a function of the interactions with the external system. The approach followed is mainly analytical: it has the objective of identifying simplified transfer functions that allow to predict the main stability properties of the converter under virtual impedance control.

3.3 Virtual impedance design approach

3.3.1 Structure of the control

Consider the introduction of the virtual impedance loop in the control scheme of the converter (Fig. 3.1), as an additional linear controller which changes the voltage reference as a function of the output current $\overline{i}_o$. Three different terms are taken into account: a real coefficient R_V (virtual resistance), a coupling element L_{VS} (which defines the static virtual reactance) and an approximate derivative, with per-unit time constant τ_d, proportional to the coefficient L_{VD}. This last term identifies the dynamic virtual reactance.

$$\overline{Z}_V = R_V + j\omega L_{VS} + \frac{s/\omega_b}{1 + \tau_d \cdot s/\omega_b} L_{VD} \tag{3.1}$$

This formulation has been chosen as it is similar to the expression of an inductor as seen by a rotating reference frame.

3.3.2 Assumptions

In the derivation of the virtual impedance design model, the following assumptions are considered:

1. the converter under study is supplied by a DC constant voltage source, e.g. an electrochemical storage unit;
2. The space-vector that represents the external grid $\overline{v}_g$ is assumed constant and equal to its nominal value; the time constant $T_g = \frac{L_g}{R_g \omega_b}$ takes into account the equivalent output impedance of the converter; resonance effects with possible parasitic capacitances are not contemplated into the model.
3. The internal voltage loop is modelled as a first-order unitary gain low-pass filter, with the cut-off angular frequency ω_{cV} defined according to the procedure reported in the previous chapter.

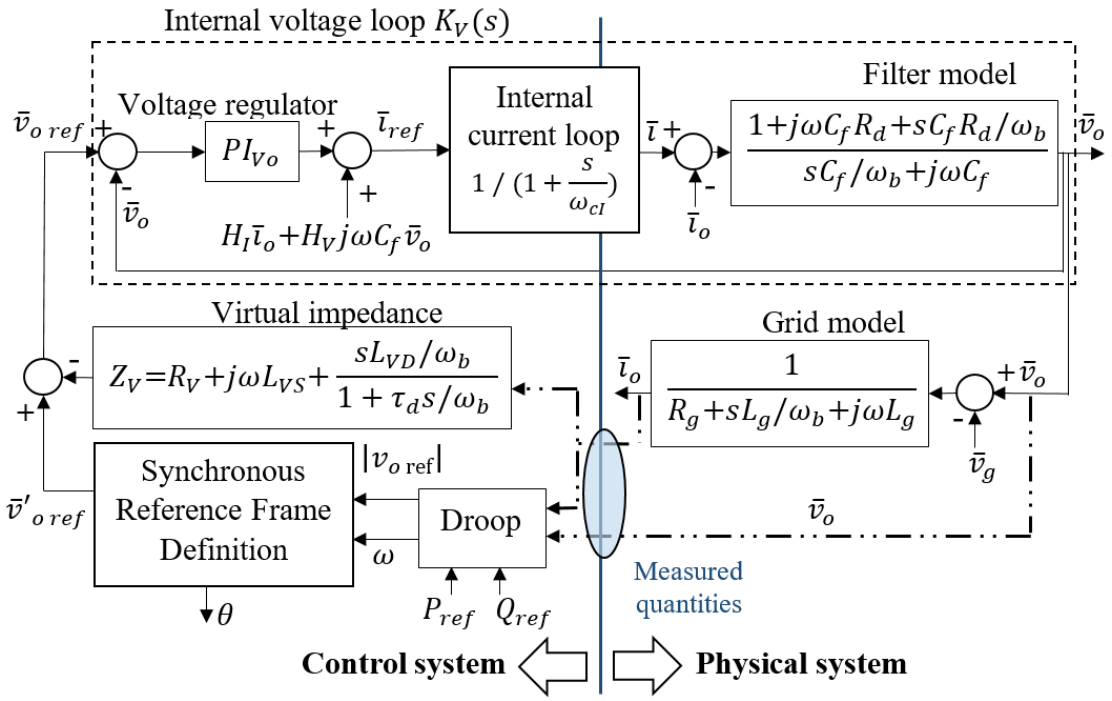

FIGURE 3.1: Equivalent model of the control system with virtual impedance.

4. The effect of the external droop is not included in the simplified design model of the virtual-impedance: it behaves as a slow-varying reference with a dynamic determined by the time constant T_p (see Table 2.2). As T_p^{-1} is significantly lower than the voltage loop cut-off angular frequency ω_{cV}, the external dynamic is neglected.

3.3.3 Design procedure

The proposed design approach is based on the identification of simplified transfer functions able to reconstruct the stability properties of the converter under virtual impedance design. The starting point of the analysis is the control model in Fig. 3.1; introducing the hypotheses of section (3.3.2) and identifying separate block diagrams for the direct and quadrature components allows to build the models reported in Fig.3.2.

The combination of the sub-diagrams of Fig. 3.2 into a unique dynamic model (Fig. 3.3) can be performed highlighting the axes coupling produced by the physical L_g and virtual inductance L_{VS}. This allows to identify stability criteria for the loop functions and, subsequently, design constraints for the regulation parameters.

- The first step in the analysis regards the stability of the loop $L_1(s)$ as reported in Fig. 3.3: the parameters that play a role in the stability of this loop are R_V and L_{VD}. The closed loop function $Y'_{eq\,dd}(s)$ is also calculated.
- The second step of the algorithm will derive some design conditions for L_{VS} based on the stability of the second loop $L_2(s)$, which includes $Y'_{eq\,dd}(s)$ as a sub-block. The external loop $L_2(s)$ is shown in Fig. 3.4.

Even though the general design approach holds in all the possible virtual impedance configurations, some small differences occur in the approximated function definitions depending on the value of L_{VD}. Thus the above presented design procedure will be developed separately for the *static* ($R_V \neq 0$, $L_{VS} \neq 0$, $L_{VD} = 0$) case and the *dynamic* ($R_V \neq 0$, $L_{VS} \neq 0$, $L_{VD} \neq 0$) one, to provide a better understanding of the proposed approach in all possible cases of interest.

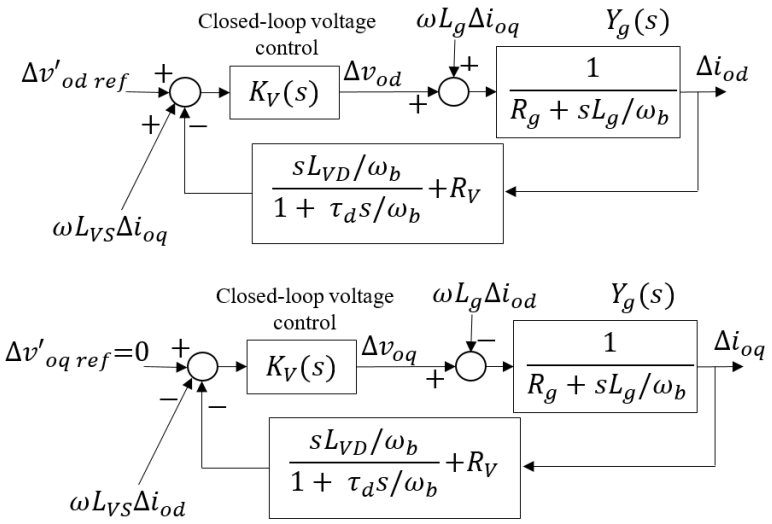

FIGURE 3.2: Direct and quadrature projections of the linearised system used for virtual impedance design. Droop dynamics, which are slower than the voltage controller frequencies, have been neglected.

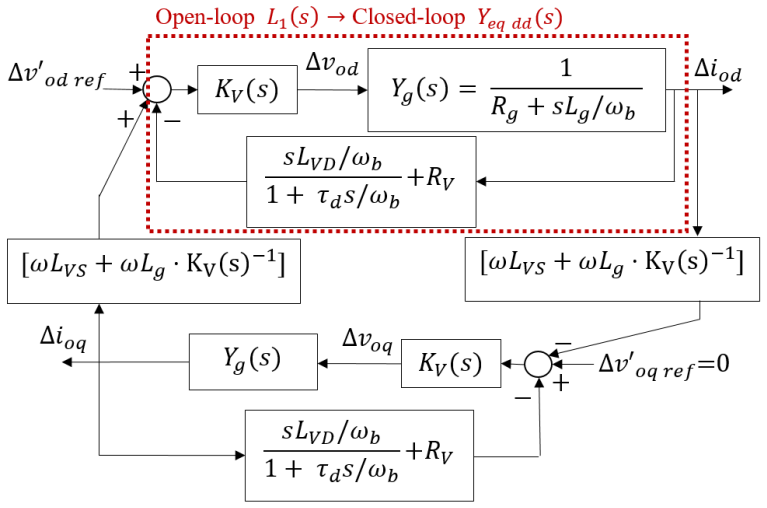

FIGURE 3.3: Complete linearized model, which takes into account both the effects of the virtual impedance and the coupling between direct and quadrature axis

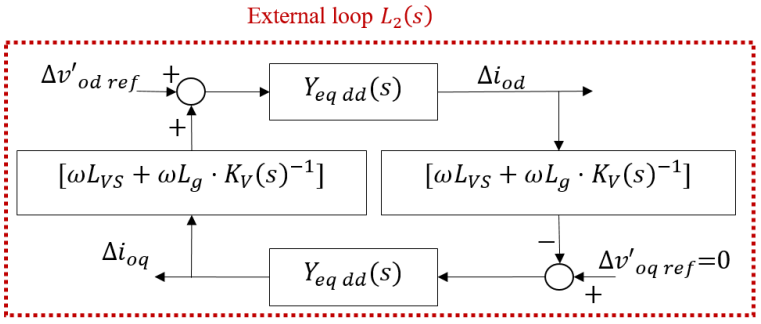

FIGURE 3.4: External loop for the calculation of the phase margin associated to the static virtual inductance L_{VS}.

3.4 Derivation of the stability model

3.4.1 Static virtual impedance ($R_V \neq 0, \quad L_{VS} \neq 0, \quad L_{VD} = 0$)

Consider the model reported in Fig. 3.3: the open-loop function $L_1(s)$ is given by (3.2) and the representation of the associated asymptotic Bode diagram is reported in Fig. 3.5. Looking at the phase profile, it is possible to see that a negative value $R_V < 0$ is chosen in the loop: this is reasonable according to what was stated in the previous chapter, as the objective of the virtual impedance is to amplify the inductive nature of the equivalent output impedance with respect to the resistive one.

$$L_1(s) = K_V(s) \cdot Y_g(s) \cdot R_V = \frac{R_V}{R_g} \cdot \frac{1}{1 + \frac{s}{\omega_{cV}}} \cdot \frac{1}{1 + s\,T_g} \tag{3.2}$$

Equation (3.2) shows a pole associated to the internal voltage control in ω_{cV} and one associated to the external grid in $T_g^{-1} = \omega_b \cdot R_g/L_g$; nevertheless their relative position is not defined a priori, as T_g^{-1} may be higher or lower with respect to ω_{cV}. The following notation will be adopted in order to identify the slower and the faster pole inside the control:

$$\omega_1 = \max\left(T_g^{-1}; \omega_{cV}\right) \qquad \omega_2 = \min\left(T_g^{-1}; \omega_{cV}\right) \tag{3.3}$$

The introduction of a negative virtual resistance R_V has an effect on the stability of the loop $L_1(s)$: in order to maintain stable operations for the converter it is necessary to keep a gain margin $\mu_g > 1$. In this way the system does not show positive-real-part poles and its Nyquist diagram is always contained in the unitary circle (Fig. 3.6): the condition is verified if $|R_V| < R_g$.

$$\mu_g = R_g/|R_V| > 1 \quad \rightarrow |R_V| < R_g \tag{3.4}$$

Once identified the stability condition (3.4) for the virtual resistance R_V, it is necessary to determine its effect on the internal dynamics associated to the equivalent admittance $Y'_{eq\ dd}$, which takes into account the nature of the external system as seen

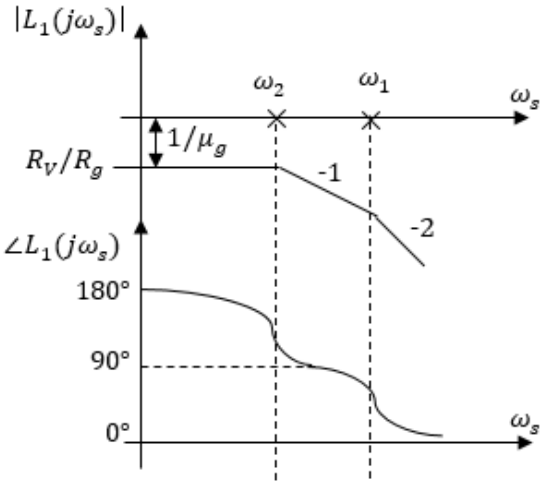

FIGURE 3.5: Asymptotic diagram of the open-loop transfer function $L_1(s)$. A gain margin μ_g higher than one must be chosen, so $|R_V| < R_g$.

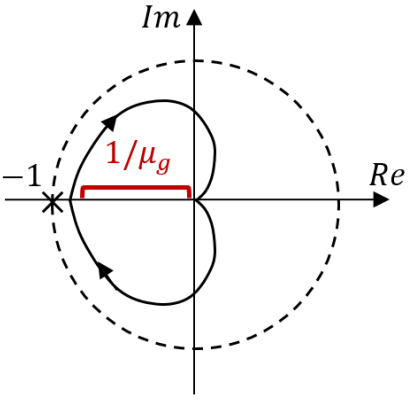

FIGURE 3.6: Nyquist diagram of the open-loop transfer function $L_1(s)$.

by the voltage reference imposed by the droop. In absence of the virtual impedance ($R_V = 0$), the admittance of the network as seen by the control is given by (3.5).

$$Y_{eq\ dd}(s) = \frac{\Delta i_{od}}{\Delta v_{od\ \mathrm{ref}}} = K_V(s) \cdot Y_g(s) = \frac{1/R_g}{\left(1 + \frac{s}{\omega_1}\right) \cdot \left(1 + \frac{s}{\omega_2}\right)} \tag{3.5}$$

The introduction of the parameter $R_V \neq 0$ changes (3.5) into (3.6):

$$\begin{aligned} Y'_{eq\ dd}(s) &= \frac{\Delta i_{od}}{\Delta v'_{od\ \mathrm{ref}}} = K_V(s) \cdot Y_g(s) \cdot (1 + L_1(s))^{-1} = \\ &= \frac{1/R_g}{\left(1 + \frac{s}{\omega_1}\right) \cdot \left(1 + \frac{s}{\omega_2}\right) + R_V/R_g} = \frac{1}{R_g + R_V} \cdot \frac{1}{1 + \frac{s}{\omega'_1}} \cdot \frac{1}{1 + \frac{s}{\omega'_2}} \end{aligned} \tag{3.6}$$

Figure 3.7 represents the equivalent admittance between voltage reference $\Delta v'_{od\,ref}$ and output current Δi_{od}, with and without the virtual resistance R_V. The function $Y'_{eq\,dd}$ shows two poles, respectively associated to the angular frequencies ω'_1 and ω'_2. Exact expressions are given in (3.7), normalized with respect to ω_1; written in this way, the position of the modified dynamics becomes exclusively function of the ratio ω_1/ω_2 and of the virtual resistance R_V/R_g.

$$\frac{\omega'_{1,2}}{\omega_1} = 0.5 \cdot \left(1 + \frac{\omega_2}{\omega_1}\right) \cdot \left[1 \pm \sqrt{1 - \left(1 + \frac{R_V}{R_g}\right)\varepsilon}\right] \quad \text{where } \varepsilon = \frac{4 \cdot \omega_1/\omega_2}{\left(1 + \frac{\omega_1}{\omega_2}\right)^2} \tag{3.7}$$

The introduction of a negative virtual resistance R_V in the range $R_V \in (-R_g, 0)$ maintains both the dynamics of $Y'_{eq\,dd}$ stable (Fig. 3.8): increasingly negative values of R_V move the pole ω'_2 to a slower frequency range, while tend to accelerate the fast one ω'_1.

Obviously the position of ω'_1 and ω'_2 can be derived from (3.7), even though these expressions in general need to be evaluated numerically; moreover the presence of the square root complicates the analytical writing of the functions associated to the external loop $L_s(s)$ stability, which includes $Y_{eq\ dd}(s)$ as a sub-block. In this perspective, it may be useful to derive asymptotic simplified expressions able to model the general dependency of ω'_1 and ω'_2 with respect to ω_1, ω_2 and R_V; asymptotic formulations also

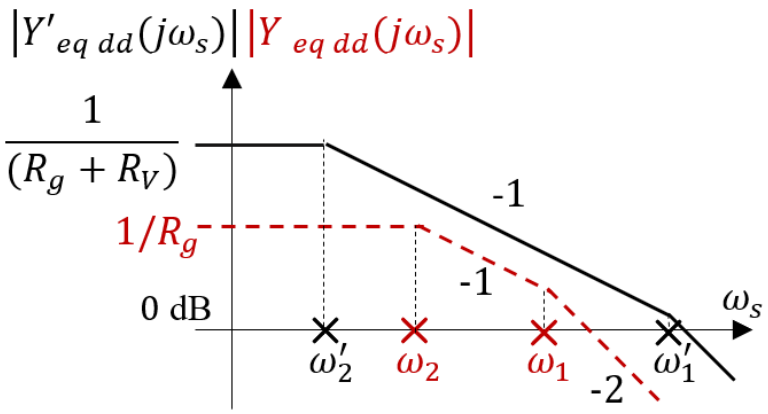

FIGURE 3.7: In solid line, the asymptotic Bode diagram of the function $Y'_{eq\ dd}(s)$ with negative virtual resistance R_V (3.6). In dashed-line, as a comparison, it is reported the diagram of $Y_{eq\ dd}(s)$ without virtual resistance R_V (3.5).

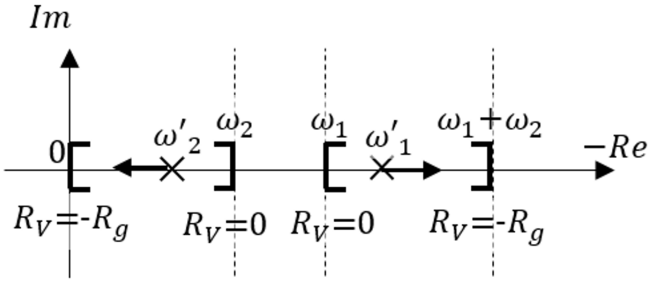

FIGURE 3.8: Exact poles of (3.6) as function of the virtual resistance $R_V \in (-R_g; 0]$

allow an easier understanding of the transfer function representation provided in Fig. 3.7.

Depending on the ratio ω_1/ω_2, two different asymptotic trends can be identified for the modified dynamics ω'_1 / ω'_2.

If $\varepsilon \to 1$, the asymptotic expression of the poles angular frequencies are given by (3.8).

$$\omega'_{1,\ 2} = \frac{\omega_1 + \omega_2}{2} \cdot \left[1 \pm \sqrt{-\frac{R_V}{R_g}}\right] \tag{3.8}$$

On the other hand, when $\varepsilon \to 0$ the dependency of the pole position with respect to the virtual resistance becomes linear:

$$\omega'_1 \cong\ \omega_1 - \omega_2 \cdot (R_V/R_g) \tag{3.9}$$

$$\omega'_2 \cong\ \omega_2 \cdot (1 + R_V/R_g) \tag{3.10}$$

Figures 3.9(a) and 3.9(b) show the exact expressions of the angular frequencies ω'_1 and ω'_2 respectively, under different values of the ratio ω_1/ω_2. As a comparison, the approximated expressions obtained under the hypothesis $\varepsilon = 1$ (associated to equation (3.8)) or $\varepsilon = 0$ (equations (3.9)-(3.10)) are reported.

The representation provided in Fig. 3.9(a) and 3.9(b) highlights the different behaviour of the two approximations at the extremes of the interval. Obviously each asymptotic representation shows a higher consistency when the underlying hypothesis is

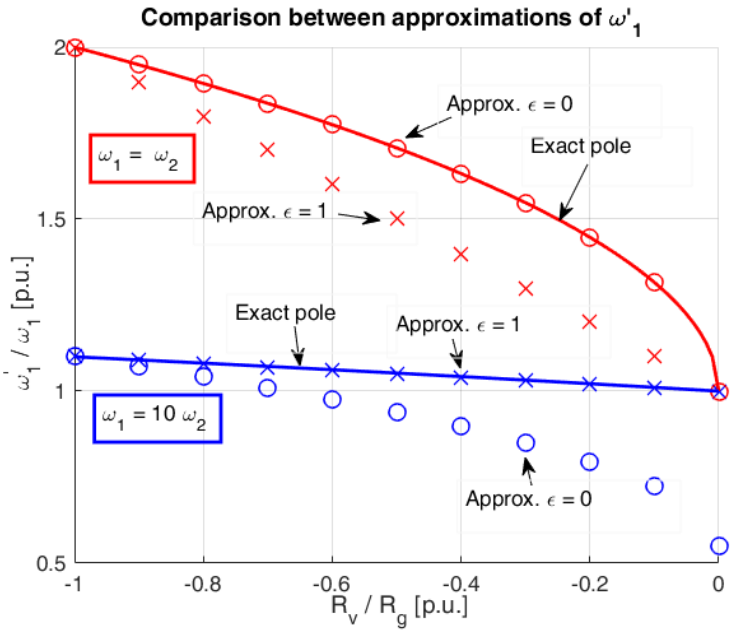

(a) $\omega_1^{'}/\omega_1$

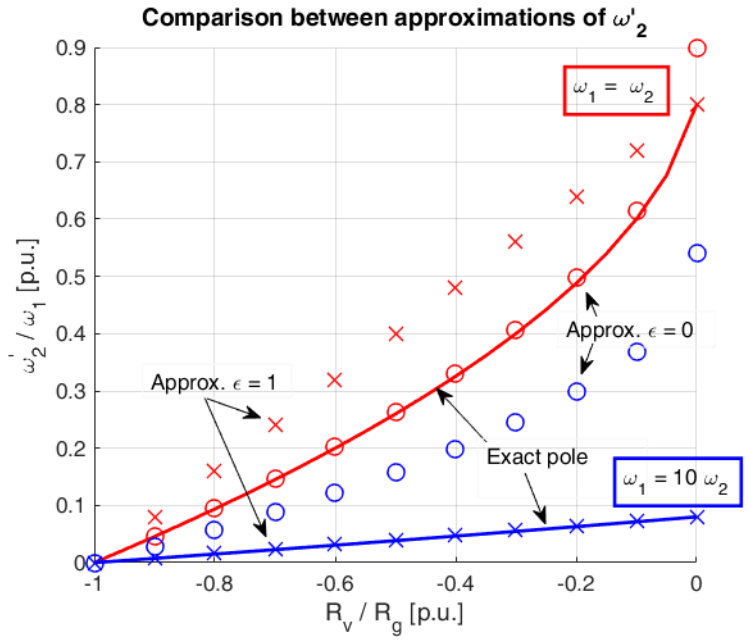

(b) $\omega_2^{'}/\omega_1$

FIGURE 3.9: Comparison between exact (3.7) and approximated (3.8) - (3.10) expressions of the poles ω'_1 and ω'_2 as a function of $R_V \in (-R_g, 0]$, under different ratios ω_1/ω_2. In (a) the trend associated to ω'_1 is reported, in (b) the one of ω'_2.

verified, thus (3.8) provides lower estimation error when $\omega_1 \cong \omega_2$, as well as (3.9)-(3.10) do when $\omega_1 >> \omega_2$.

Nevertheless, differently from (3.8), expressions (3.9)-(3.10) always match the exact values of the angular frequencies ω_1'-ω_2' at the extremes of the virtual resistance variation range $R_V \in (-R_g, 0]$. Thus they are able to predict the general evolution of the poles in all the cases of practical interest: in the following, expressions (3.9)-(3.10) will be used inside (3.6) to express the positions of ω_1' and ω_2'.

Once identified $Y'_{eq\ dd}$ as the closed-loop transfer function associated to $L_1(s)$ and the expressions (3.9)-(3.10) as asymptotic approximations of the singularities, the stability function $L_2(s)$ associated to the external coupling loop can be calculated (3.11): the dynamical properties associated to axes coupling as expressed by $L_2(s)$ can be used to obtain the maximum stable value for static virtual inductance parameter L_{VS}.

$$L_2(s) = Y'^2_{eq\ dd} \cdot \left(\omega L_{VS} + \omega L_g \cdot K_V(s)^{-1}\right)^2 = \tag{3.11}$$

$$= k^2 \cdot \frac{\left(1 + \frac{sL_g}{\omega_{cV}(L_g + L_{VS})}\right)^2}{\left(1 + \frac{s}{\omega_1'}\right)^2 \cdot \left(1 + \frac{s}{\omega_2'}\right)^2} = k^2 \cdot \frac{\left(1 + \frac{s}{\omega_z}\right)^2}{\left(1 + \frac{s}{\omega_1'}\right)^2 \cdot \left(1 + \frac{s}{\omega_2'}\right)^2} \tag{3.12}$$

where $k = \frac{\omega L_g + \omega L_{VS}}{R_g + R_V}$.

The parameter k in $L_2(s)$ has a strong impact on the performances of the control, as it represents the equivalent per-unit X/R ratio of the output impedance as seen by the control system of the converter. The choice of the factor k needs to take into account several aspects:

- a low value guarantees good stability for the loop $L_2(s)$, even though it is not the best solution from droop perspective as it indicates a high resistive nature for the interface impedance;
- a high value of k amplifies the inductive nature of the interface impedance, but it needs to be properly designed to avoid stability issues associated to the loop function $L_2(s)$. Values of k around $k \approx 3-4$ guarantee good performances for the droop, as they correspond to an equivalent characteristic angle of the "modified" interface impedance around $\theta = \arctan(k) \cong 75\,\text{deg}$.

The stability properties of the function $L_2(s)$ can be studied numerically by means of the corresponding Bode diagram reported in Fig. 3.10; moreover in most typical cases it is possible to derive a simple analytical expression of the cut-off angular frequency $\tilde{\omega}_{L2}$ to be used for the analytical evaluation of the loop phase margin. In particular:

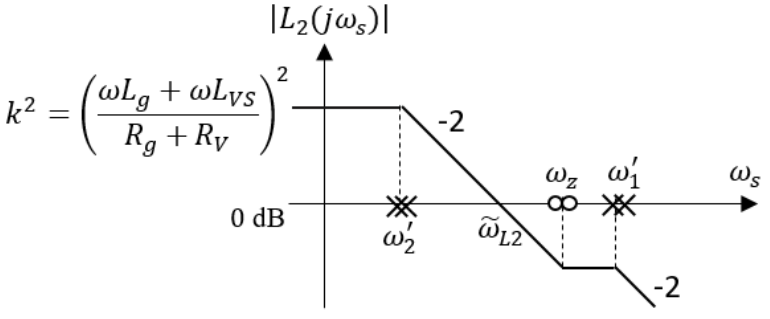

FIGURE 3.10: Asymptotic Bode diagram of the external loop function $L_2(s)$

- even for $k \approx 3-4$, the system shows a predominant inductive behaviour and thus there is no need to choose higher values; thus the static gain of the function $L_2(s)$ is generally limited.
- As far as a negative resistance R_V is introduced, the couple of poles in ω_2' moves towards smaller frequency and thus exhibits a significant influence in the determination of the angular cut-off frequency; this behaviour is particularly amplified by the presence of a double pole in ω_2' which introduces a slope of $-40\,dB$ in the asymptotic Bode diagram.

Given these considerations, the intersection of the loop function $L_2(s)$ with the $0\,dB$ axis is practically determined by the following simplified expression:

$$\widetilde{\omega}_{L2} \cong \omega_2^{'} \cdot \sqrt{k^2-1} \tag{3.13}$$

Substituting (3.13) in (3.11) allows to express the phase margin of the global system in an analytical way (3.14). Even though the effect of ω_Z and ω_1' were neglected in the evaluation of the approximated cut-off angular frequency $\tilde{\omega}_{L2}$, they can be easily included in (3.14) to provide a higher consistency for the result.

$$\begin{aligned}\phi_{m2} = \pi + \measuredangle L_2(j\widetilde{\omega}_{L2}) = \pi - 2{\cdot}\tan^{-1}\left(\sqrt{k^2-1}\right) + \\ - 2\cdot\tan^{-1}\left(\omega_2\cdot\frac{R_g+R_V}{(R_g\omega_1 - R_V\omega_2)}\cdot\sqrt{k^2-1}\right) + \\ + 2\cdot\tan^{-1}\left(\omega_2 L_g\cdot\frac{R_g+R_V}{\omega_{cV}\cdot R_g\cdot(L_g+L_{VS})}\cdot\sqrt{k^2-1}\right)\end{aligned} \tag{3.14}$$

The application of this stability characteristic to the operation of the converters, as well as the validation of the proposed model in a simulated and experimental set-up, will be reported in the next section of the chapter. Before doing this, it is necessary to analyse the case of the dynamic virtual reactance.

3.4.2 Dynamic virtual impedance ($R_V \neq 0, \quad L_{VS} \neq 0,\ L_{VD} \neq 0$)

Consider the modification introduced by L_{VD} into the dynamical model of the converter. A procedure similar to the one of the static case will be carried out, even though some approximations need to be managed properly. As it was previously done, the first step of the analysis takes into account the loop function $L_1(s)$ (Fig. 3.3).

$$L_1(s) = K_V(s)\cdot Y_g(s)\cdot\left(R_V + \frac{sL_{VD}/\omega_b}{1 + s\tau_d/\omega_b}\right) =$$

$$= \frac{R_V}{R_g}\cdot\frac{1}{\left(1+\frac{s}{\omega_1}\right)\left(1+\frac{s}{\omega_2}\right)}\cdot\left(\frac{1 + s\tau'_d/\omega_b}{1 + s\tau_d/\omega_b}\right) \tag{3.15}$$

where $\tau'_d = \left(\frac{L_{VD}}{R_V} + \tau_d\right)$.

As concerns τ_d, it must be chosen so that the introduced pole (ω_b/τ_d) does not alter the stability properties of the internal current loop $L_1(s)$. In practice, ω_b/τ_d determines the frequency range in which the derivative controller is attenuated, avoiding the amplification of high-frequency components in the derivation process. In this case it was chosen to limit virtual impedance effect to $\omega_b/\tau_d \cong 2\pi\cdot 1000$ rad/s. The position of the

pole should be chosen to higher than the ω_1 and lower than the switching dynamics: this condition allows to have a fast impedance emulation but avoids any possible interference with the converter modulation.

On the other hand, the sign of the equivalent per-unit time constant τ'_d is influenced by the relative magnitude of the coefficients R_V, L_{VS} and τ_d involved in its definition. Keeping in mind the negative sign of R_V according to the description provided in the previous subsection, it is possible to identify three different conditions:

1. $L_{VD} < 0$: highly negative values of the parameter L_{VD} bring the system towards instability as shown by the Bode and Nyquist diagrams reported in Fig. 3.11; the time constant τ'_d is positive.
2. $0 < L_{VD} < 2\tau_\mathrm{d}\,|R_V|$: independently of the sign of τ'_d, it holds $|\tau'_d| < \tau_d$. The zero in (ω_b/τ'_d) associated to the dynamic virtual reactance is located after the pole in (ω_b/τ_d); the derivative term practically does not affect the stability of the converter. Bode and Nyquist diagrams for this case are reported in Fig. 3.12.
3. $L_{VD} > 2\tau_\mathrm{d}\,|R_V|$: time constant τ'_d is negative and in magnitude it holds $\left|\tau'_d\right| > \tau_d$ (as $R_V < 0$). This case is the most interesting from the system perspective, as the positive derivative coefficient L_{VD} introduces a leading effect into the loop $L_1(s)$: this enhances the responsiveness of the control system and, in particular, its transitory P/Q decoupling. The asymptotic Bode and Nyquist diagrams for this case are reported in Fig. 3.13.

If we refer to the condition identified in the third case ($L_{VD} > 2\tau_\mathrm{d}\,|R_V|$), the expression associated to the loop function at low frequency can be approximated as in (3.16).

$$L_1(s) \cong \frac{R_V}{R_g} \cdot \frac{(1 + s\tau'_d/\omega_b)}{\left(1+\frac{s}{\omega_1}\right)\left(1+\frac{s}{\omega_2}\right)} \quad \text{for} \quad s{=}j\omega_s \leq \frac{j\omega_b}{\tau_d} \tag{3.16}$$

The condition $L_{VD} > 2\tau_\mathrm{d}\,|R_V|$ defines a minimum suggested value to improve the stability of the control system; nevertheless it is also necessary to identify a superior threshold. The maximum acceptable value for L_{VD} that guarantees sufficient phase margin at the second intersection with the $0\,dB$ axis can be identified according to the sufficient stability condition expressed by the Bode theorem.

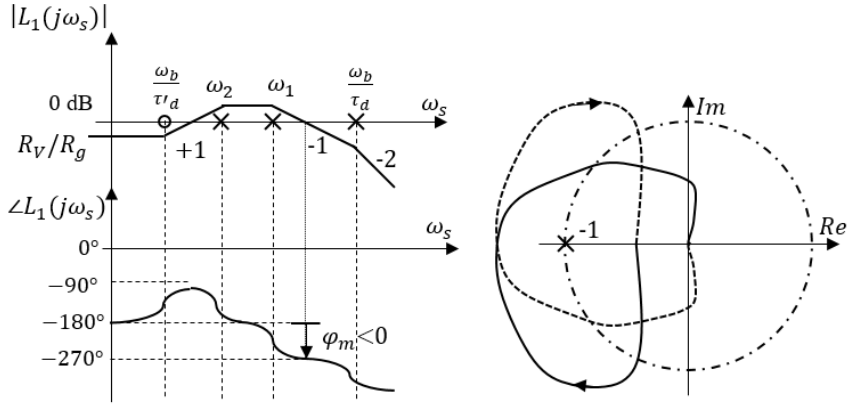

FIGURE 3.11: Bode and Nyquist diagrams of the transfer function $L_1(s)$ when $L_{VD} < 0$. The system is unstable.

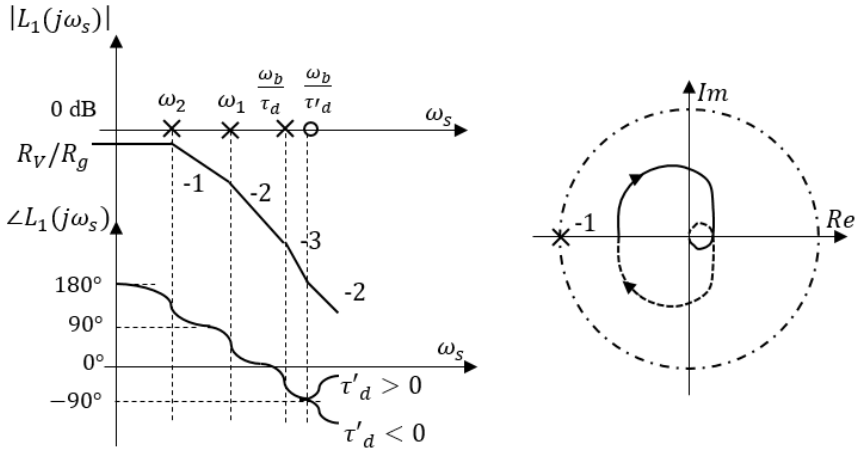

FIGURE 3.12: Bode and Nyquist diagrams of the transfer function $L_1(s)$ when $0 < L_{VD} < 2\tau_d |R_V|$. The system is stable.

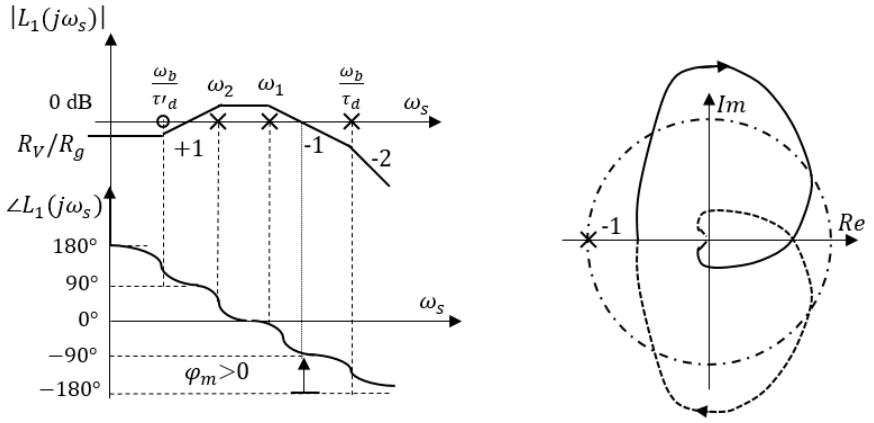

FIGURE 3.13: Bode and Nyquist diagrams of the transfer function $L_1(s)$ when $L_{VD} > 2\tau_d |R_V|$. The system is stable.

In particular, the maximum value of L_{VD} able to produce an intersection with -20 dB slope can be obtained from the asymptotic approximation of the transfer function (3.16) close to the second intersection.

$$L_2(s) \sim \frac{R_V}{R_g} \cdot \frac{\tau'_d}{\omega_b} \cdot \frac{\omega_1 \omega_2}{s} \quad \text{for } \omega_1 < \omega_s < \omega_b/\tau_d \tag{3.17}$$

Imposing the intersection at $\frac{\omega_b}{\tau_d}$ leads to (3.18);

$$\left|\tau'_{d\ max}\right| < \left|\frac{R_g}{R_V}\ \omega_1\ \omega_2\ \tau_d\right| \tag{3.18}$$

Thus referring to the definition in τ'_d (3.15), it is possible to reconstruct the maximum value for L_{VD}.

$$L_{VD} < \ (\frac{\omega_b^2}{\omega_1 \omega_2 \tau_d} R_g + \tau_d |R_V|) \tag{3.19}$$

Following the same approach developed for the static case, it is necessary to calculate the analytical expression of the transfer function $Y'_{eq\ dd}(s)$, according to the scheme reported in Fig. 3.4. In this case the calculation leads to expression (3.20).

$$Y'_{eq\ dd}(s) = \frac{1/R_g}{\left(1+\frac{s}{\omega_1}\right)\left(1+\frac{s}{\omega_2}\right) + R_V/R_g \cdot (1+\ s\tau'_d/\omega_b)} \tag{3.20}$$

The poles[1] of the function (3.20) are contained in the interval reported in Fig. 3.14 for R_V ranging in $R_V \in (-R_g; 0)$, even though in this case one of the extremes of the interval is function of the zero time constant τ'_d. A high value of L_{VD}, within the stability limit imposed by (3.19), produces $\tau'_d < 0$ and moves the high pole ω'_1 to even higher frequencies, contributing to the stabilization of the global coupling loop L_2 which includes $Y'_{eq\ dd}$ as a sub-block.

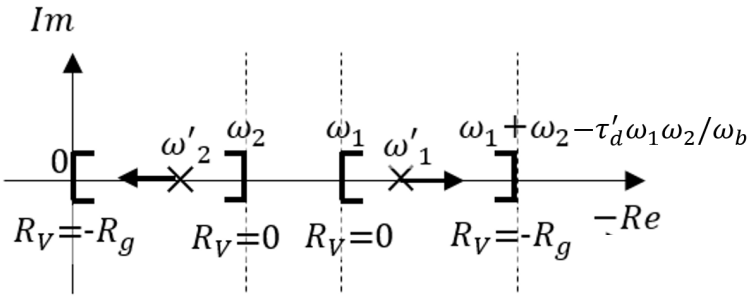

FIGURE 3.14: Exact poles position as a function of the virtual resistance $R_V \in [-R_g; 0]$ in the dynamic case.

Even though in the dynamic case the behaviour of the transfer function $Y'_{eq\ dd}$ is similar to the one associated to the static case (Fig. 3.7), still it has to be taken into account that the simplification of the high-frequency pole in ω_b/τ_d (3.16) introduces a higher degree of uncertainty into the model.

Approximated positions of the poles ω'_1-ω'_2 are obtained assuming a linear behaviour with respect to R_V in the intervals reported in Fig. 3.14, even though in this case the expressions are given by (3.21)-(3.22) instead of (3.9) - (3.10).

$$\omega'_1 = \ \omega_1 - (\omega_2 - \ \tau'_d\omega_1\omega_2/\omega_b) \cdot (R_V/R_g) \tag{3.21}$$

$$\omega'_2 = \ \omega_2 \cdot (1 + R_V/R_g) \tag{3.22}$$

The loop function $L_2(s)$ associated to the axes coupling is derived from Fig. 3.4, as in the static case, even though here the expression associated to $Y'_{eq\ dd}$ is different.

$$L_2(s) \cong \ Y'^2_{eq\ dd}(s) \cdot \left(\omega L_{VS} + \omega L_g \cdot K_V(s)^{-1}\right)^2 \tag{3.23}$$

The equivalent phase margin of the loop $L_2(s)$ is given by the (3.14), provided that the corresponding approximated expressions of the poles (3.21) - (3.22) of the dynamic case are used instead of (3.9) - (3.10). Keeping the same parameters for the external grid and control terms R_V and L_{VS}, the system $L_2(s)$ shows a higher phase margin in the dynamic case ($L_{VD} \neq 0$) with respect to the static one ($L_{VD} = 0$) as the pole in ω'_1 moves to higher frequencies.

[1]Expression: $\omega'_{1,2} = 0.5 \cdot \left[-\left(\omega_1+\omega_2+\frac{R_V}{R_g}\frac{\tau'_d}{\omega_b}\omega_1\omega_2\right) \pm \sqrt{\left(\omega_1+\omega_2+\frac{R_V}{R_g}\frac{\tau'_d}{\omega_b}\omega_1\omega_2\right)^2 - 4\omega_1\omega_2\left(1+\frac{R_V}{R_g}\right)}\right]$

3.4.3 Guidelines for virtual impedance design

The analytical study of the virtual impedance stability conditions allows to identify reasonable design criteria for its control parameters: thus the list in the following configures as a simple procedure to size the virtual impedance parameters, both a priori or in real-time.

1. The pole associated to the voltage control ω_{cV} as well as the one related to the grid $T_g^{-1} = \frac{R_g \omega_b}{L_g}$ are labelled as ω_1 and ω_2 according to (3.3). As regards the pole associated to the voltage control ω_{cV}, it is generally known from the desired specification of the converter control. The one associated to the external grid T_g^{-1} can be reconstructed from on-line impedance estimation techniques that will be covered in the next chapter: at this moment, it is assumed as a constant.
2. The gain margin of the open-loop transfer function $L_1(s)$ associated to direct axis components equals $R_g/|R_V|$. In order to amplify the inductive characteristics of the external output impedance it is necessary to choose $R_V<0$; moreover the stability condition (3.4) imposes $|R_V| < R_g$.
3. The per-unit time constant τ_d associated to the approximate derivative in the dynamic case is chosen to limit the virtual impedance effect at high frequency. In this case it is chosen $\omega_b/\tau_d \cong 2\pi \cdot 1000$ rad/s according to the comment to (3.15).
4. The dynamic virtual reactance term L_{VD} (if present) can be designed referring to the stability condition (3.19). This leads to the following allowed interval for the parameters L_{VD}.

$$0 < L_{VD} < \frac{\omega_b^2}{\omega_1 \omega_2 \tau_d} R_g + \tau_d |R_V| \tag{3.24}$$

   Moreover, it is often convenient to make its design independent of the virtual resistance R_V; this can be easily done considering that τ_d is small, thus in the right side of the inequality the second term is negligible.

$$0 < L_{VD} < \frac{\omega_b^2}{\omega_1 \omega_2 \tau_d} R_g \tag{3.25}$$

5. The approximated expressions of the poles in $Y'_{eq\ dd}(s)$ are given by (3.9) - (3.10) for the static case, or by (3.21) - (3.22) in the dynamic one. It was shown in the derivation of the mathematical model that this operation allows to express $Y'_{eq\ dd}(s)$ in an analytical form and, thus, to derive compact expressions for the phase margin in the coupling loop $L_2(s)$.
6. Depending on the imposed value of virtual resistance R_V and on the actual grid characteristics from the real-time impedance estimation algorithm reported in the next chapter, the converter can be operated maintaining a constant decoupling coefficient $k \approx 3 - 4$ as defined before:

$$k = \frac{L_{VS} + L_g}{R_V + R_g} \tag{3.26}$$

   Nevertheless, it is necessary to verify that the desired configuration of the parameters is compatible with the derived stability model; thus, the maximum value of the virtual inductance L_{VS} has to be limited according to (3.13) - (3.14) for the static case or to (3.23) for the dynamic one.

Some simulated and experimental tests will be carried out in order to verify the correctness of the obtained dynamical model. As the main goal of this part is to verify

the model consistency, it will be assumed that the values of the external parameters R_g and L_g are known and that, at each instant, the converter operates keeping constant virtual impedance parameters R_V, L_{VD}, L_{VS} and τ_d.

3.5 Effect of the virtual impedance on power decoupling at steady state

The virtual impedance influence on the steady-state power decoupling can be verified extending the droop model developed in the previous chapter. Figure 3.15 depicts the evolution of Fig. 2.20 when virtual impedance is also taken into account.

Performing the same operations already introduced in section 2.9, the model in Fig. 3.16(a) can be obtained. Moreover, as in this phase we are interested in the steady state conditions, Fig. 3.16(b) can be derived introducing the asymptotic behaviour for $s \to 0$. The transfer function $Y'_{eq\ dd}(s)$ reported in Fig. 3.16(b) practically coincides with the one introduced in (3.20); its behaviour at steady state is thus given by:

$$Y'_{eq\ dd}(0) = \frac{1}{R_g + R_V} \tag{3.27}$$

Thus the asymptotic active / reactive power changes after a step variation of the frequency and voltage droop intersections ($\Delta\omega^*$, ΔV^*) can be calculated by the following expressions, obtainable from Fig. 3.16(b):

$$\Delta p_o(\infty)\Big|_{\Delta\omega^*} = \lim_{s\to 0} \frac{V^0_{pcc}\,\omega_b}{s} \cdot \frac{{Y'_{eq\,dd}}^2(0)\ V^2_{o\,d}\ N^*(0)}{1 + {Y'_{eq\,dd}}^2(0)\ V^2_{o\,d}\ N^*(0)\ M^*(0)} \cdot \Delta\omega^* = \frac{\Delta\omega^*}{m} \tag{3.28}$$

$$\Delta p_o(\infty)\Big|_{\Delta V^*} = \frac{Y'_{eq\,dd}(0)\ V_{o\,d}}{1 + {Y'_{eq\,dd}}^2(0)\ V^2_{o\,d}\ N^*(0)\ M^*(0)} \cdot \Delta V^* = 0 \tag{3.29}$$

$$\begin{aligned}\Delta q_o(\infty)\Big|_{\Delta\omega^*} &= \lim_{s\to 0} -\frac{V^0_{pcc}\,\omega_b}{s} \cdot \frac{Y'_{eq\,dd}(0)\ V_{o\,d}}{1 + {Y'_{eq\,dd}}^2(0)\ V^2_{o\,d}\ N^*(0)\ M^*(0)}\Delta\omega^* = \\ &= -\frac{R_g + R_V}{V_{od} n + (L_g + L_{VS})\,\omega} \cdot \frac{\Delta\omega^*}{m} = -\frac{1}{\frac{V_{od} n}{R_g + R_V} + k^2} \cdot \frac{\Delta\omega^*}{m}\end{aligned} \tag{3.30}$$

$$\begin{aligned}\Delta q_o(\infty)\Big|_{\Delta V^*} &= \frac{{Y'_{eq\,dd}}^2(0)\ V^2_{o\,d}\ M^*(0)}{1 + {Y'_{eq\,dd}}^2(0)\ V^2_{o\,d}\ N^*(0)\ M^*(0)} \cdot \Delta V^* = \\ &= \frac{\Delta V^*}{n + (L_g + L_{VS})\,\omega / V_{od}}\end{aligned} \tag{3.31}$$

Equations (3.28)-(3.31) show the following properties associated to the virtual impedance:

- a change in the frequency droop produces an undesired variation of the reactive injection, even though this effect is significantly reduced by the combination of a negative virtual resistance $R_V < 0$ and the static virtual reactance (with $L_{VS} > 0$), as both contribute to the increase of the decoupling coefficient k.
- active power is not influenced by the variation of the voltage droop intersection.

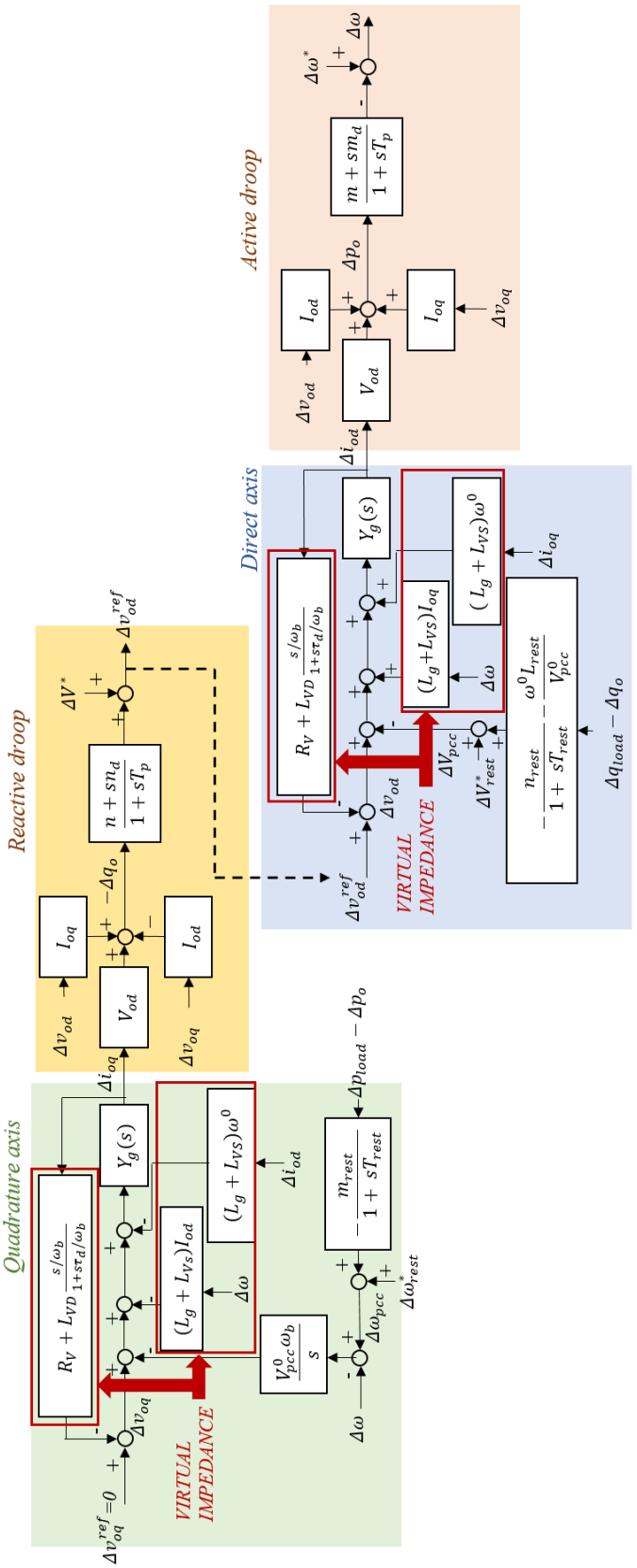

FIGURE 3.15: Complete representation of the linearised droop system with virtual impedance. The block diagram reported here represents the extension of Fig. 2.20 for the virtual impedance case; modifications with respect to the traditional droop scheme of Fig. 2.20 are highlighted with a red frame.

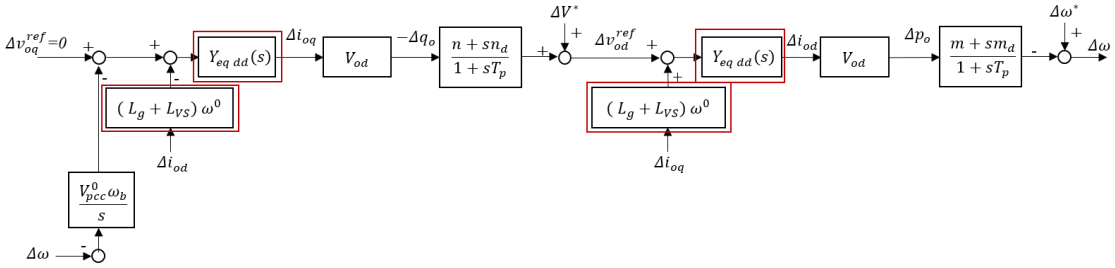

(a) Equivalent model in grid-connected mode with virtual impedance

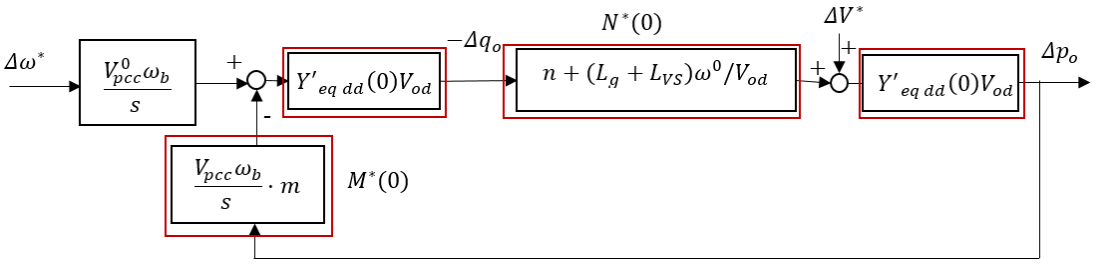

(b) Steady state model

FIGURE 3.16: Effect of the virtual impedance on power decoupling in grid-connected mode. Modifications with respect to the traditional droop scheme of Fig. 2.20 are highlighted with a red frame.

3.6 Model verification

The goal of this section is to verify the mathematical correctness of the derived dynamical model. Two different values of the interface impedance conditions are taken into account, in order to test the system in different conditions; the converter under test is connected to the public grid of the laboratory, according to the scheme in Fig. 2.2(a) (here reported again for an easier understanding), by means of the impedances reported in Table 3.1. The physical explanation of the experimental set-up in grid-connected mode is reported in Appendix D.

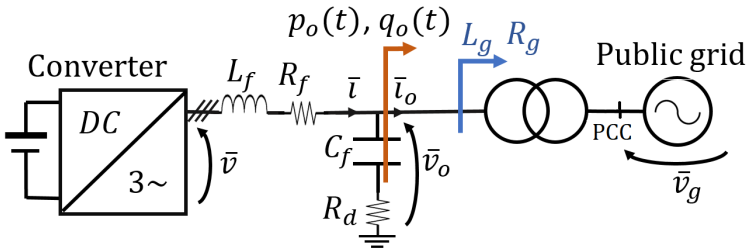

Recall from Fig. 2.2(a): operations of the converter in grid-connected mode.

3.6.1 Strong grid - Case study 1

Figure 3.18 shows the simulated and experimental stability limits, compared to the ones that can be obtained from the analytical calculation of the dynamical model previously derived. In each graph a stability map is represented, which allows to obtain

TABLE 3.1: Test conditions for the verification of the proposed dynamical model in grid-connected mode.

Case	*Condition*	*Physical parameters* [p.u.]
1	Strong grid	$Z_g = 0.019$; $\varphi_g = 20$ deg.
2	Weak grid	$Z_g = 0.284$; $\varphi_g = 34$ deg.

the phase margin of the coupling loop as a function of the physical and control parameters (see (3.14) for the static case and (3.23) for the dynamic one); as a comparison, the stability limits obtained experimentally and the simulated ones from the Simulink environment are included.

All three sources (experimental, simulated and approximated analytical) show the same general tendency as regards the prediction of the stability limit, even though some differences exist because of the nature of each model.

Comparing the simulated and simplified analytical systems, it is possible to see that the proposed approach tends to predict higher phase margin with respect to the simulated ones; this is reasonable considering the introduced simplifications, that may partially affect the numeric consistency of the results. Nevertheless it is possible to see that, in terms of phase margin, the difference is negligible (around 20 deg.), especially keeping in mind that typically it is suggested to operate the system with at least 50 deg. of margin [44].

On the other side, experimental tests generally show a higher stability with respect to the theoretical ones; this is mainly due to the presence of parasitic losses into the real system, which are hardly measurable during the operation of the converter. Another significant source of uncertainty is associated to the public network conditions, which are time-varying and typically unknown: even though its typical characteristic impedance is lower than the transformer one, still it contributes to the mismatch between the experimental and analytical cases.

Furthermore it is possible to observe that, keeping the same values for the parameters R_V-L_{VS}, the stability margins associated to the dynamic case (Fig. 3.18(b)) are higher than the corresponding static ones (Fig. 3.18(a)) thanks to the positive effect introduced by the derivative term L_{VD} in the control. The leading effect provided by the derivative enhances the phase margin of the coupling feedback, allowing a wider admissible operating range for the virtual impedance itself. As a drawback, the higher number of hypotheses invoked in the derivation of (3.23) causes a stronger discrepancy of the experimental dynamic case (Fig. 3.18(b)) with respect to the static one (Fig. 3.18(a)): the equivalent cut-off frequencies of the loops involved in the stability definition grow and the internal dynamics would require a more detailed modelling.

In reality, the discrepancy between theoretical and experimental model does not jeopardize the usefulness of the analytical approach: the proposed stability model configures as a real-time check for the consistency of the virtual impedance settings during time-varying conditions of the system and the possible mismatch between the physical and theoretical dynamics is often taken into account assuming a safety phase margin generally much higher than the limited mismatch experienced.

3.6.2 Weak grid - Case study 2

In Fig.3.19 the same comparison between simulated and analytical stability limits for a weak grid is reported. The first consideration regards the lower value for the maximum acceptable virtual impedance, with respect to the strong grid case: as the

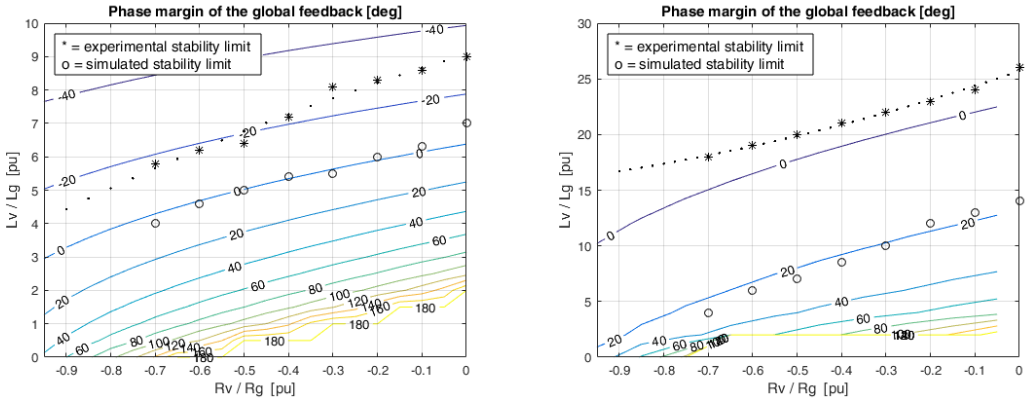

(a) Static case ($L_{VD} = 0$) (b) Dyanamic case ($L_{VD} = 6\ L_{VS},\ \tau_d = 0.1$ p.u.)

FIGURE 3.18: Analytical phase margin curves compared to simulated and experimental ones. CASE STUDY 1 - (strong grid). The theoretical stability values coincide with the experimental and simulated ones.

equivalent interface impedance increases, the system tends to evolve toward instability and the admissible values [R_V, L_{VS}, L_{VD}] reduce. Nevertheless, the results associated to the analytical model show a good consistency with the simulated ones both for the static and dynamic case: this validates the correctness of the proposed mathematical model.

A further consideration needs to be done on the mutual effects between the reactive droop coefficients and the virtual impedance control. Both experimentally and in simulations, it has been experienced a general reduction of the analytical model consistency after the introduction of high reactive droop slopes n or reducing the time constants T_p: as soon as the external droop increases its bandwidth, it behaves as an additional parallel coupling feedback between the direct and quadrature axes and the stability expressions associated to the virtual impedance (3.14)-(3.23) should include the dependency with respect to the droop coefficients. Even though for the considered pass-bands (Appendix D) the dynamical decoupling is guaranteed, the application of different design simplifications could lead to dissimilar dynamical properties [6]. Still the analytical approach can help: the extension of the system complete model as reported in Fig. 3.15 already includes the mutual interaction of the reactive droop and the virtual impedance without any further simplification, also for the cases in which the loops show similar speeds. Despite the model still has to be analytically solved in all the practical cases of interest, still its complete definition includes the dynamical properties of the system in a general way.

3.7 Functional behaviour of the virtual impedance in grid-connected mode

Beside the verification of the stability limits, it is also important to verify the effects associated to the insertion of the virtual impedance in the control of the converter. The goal is to verify the stability improvements during grid-connected operations (in this section) or in island mode (next section).

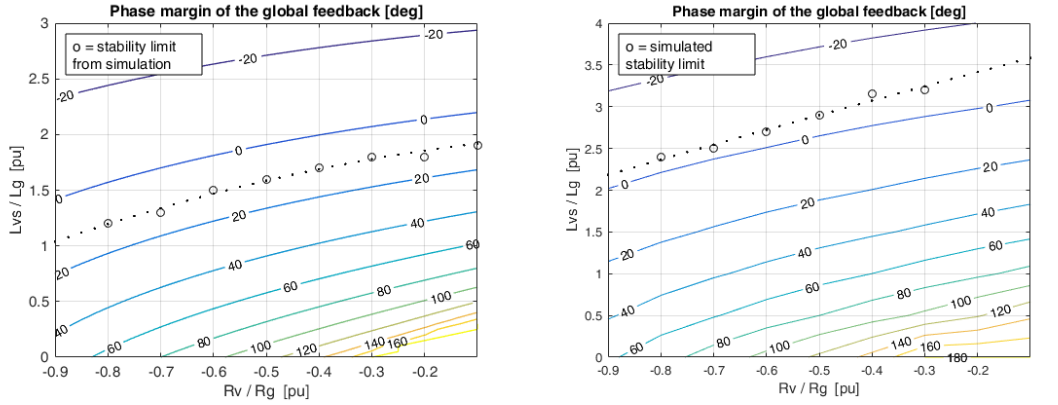

(a) Static case ($L_{VD} = 0$) (b) Dyanamic case ($L_{VD} = 0.7\ L_{VS},\ \tau_d = 0.1$

FIGURE 3.19: Analytical phase margin curves compared to simulated ones. CASE STUDY 2 - (weak grid). The theoretical stability values coincide with the simulated ones.

3.7.1 Strong grid - Case study 1

Figure 3.20 shows the transient associated to the converter operated in grid-connected mode in case 1 of Table 3.1, under different values of the virtual resistance R_V. While the converter is operated in parallel to the grid, the active droop intersection is changed by $\Delta\omega^* = 0.01$ p.u.: this corresponds to a change of the reference power equal to $\Delta P_{ref} = \Delta\omega^*/m = 0.1$ p.u. from the converter to the grid. In the initial configuration of the system (Fig. (3.20(a))), the equivalent decoupling coefficient k is very small: even though the converter is able to properly modulate its active injection as a consequence of change in the droop reference, still this modification produces an undesired variation of the reactive power. The introduction of a negative value for the virtual resistance R_V (compatible with the allowed stability region in Fig. 3.18(a)) allows to foster an independent contribution of the active and reactive injections for the converter.

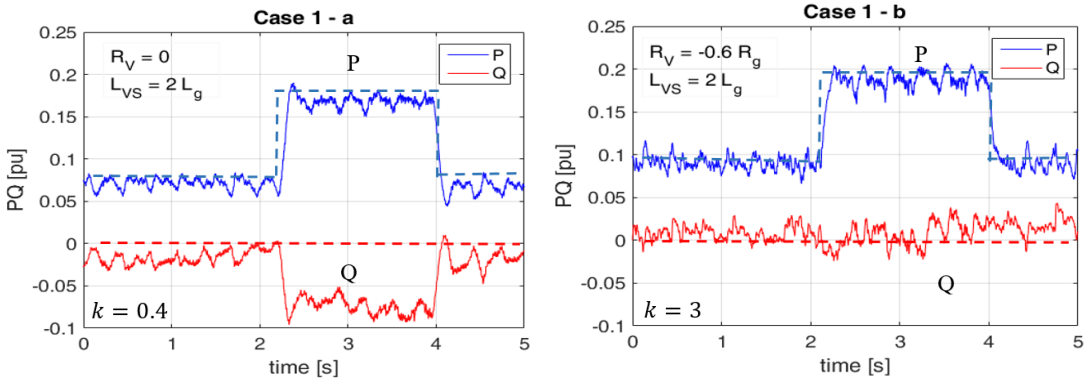

(a) $R_V = 0$ (b) $R_V \neq 0$

FIGURE 3.20: Experimental power decoupling improvements by increasing negative values of the virtual resistance R_V. Frequency droop step changes $\Delta\omega^* = 0.01$ p.u. are introduced. The static virtual impedance introduction improves the power decoupling.

3.7.2 Weak grid - Case study 2

In Figure 3.21 the effect of the introduction of the dynamic virtual reactance L_{VD} in the control system of the converter is analysed (case study 2, Tab. 3.1). Figure 3.21 shows the step variation of the active and reactive power injections (obtained respectively shifting the frequency and voltage droop characteristics) in grid-connected mode.

Small values of the static virtual impedance are inserted in the control, even though the decoupling index k results lower than the ideal one. Under variation of the active power (Fig. 3.21(a)), the reactive injection undergoes an initial transient and a subsequent variation of its steady state condition; as regard the change in the reactive power (Fig. 3.21(b)), it does not affect the steady state behaviour in the active injection.

The dynamic term L_{VD} introduction does not affect the decoupling at steady state, even though it produces a significant improvement of the transients. According to the mathematical model reported in the previous sections, this term increases the phase margin of the loop $L_2(s)$: experimentally, this can be seen from the reduction of the over-shoot transients in Fig. 3.21(c) and 3.21(d) compared to Fig. 3.21(a) and 3.21(b), which denote a higher equivalent damping for the system.

3.7.3 Power decoupling at steady state: experimental validation

Consider the complete dynamical model of the system (Fig. 3.15), from which the steady state equations for the active and reactive injection subsequent to a variation

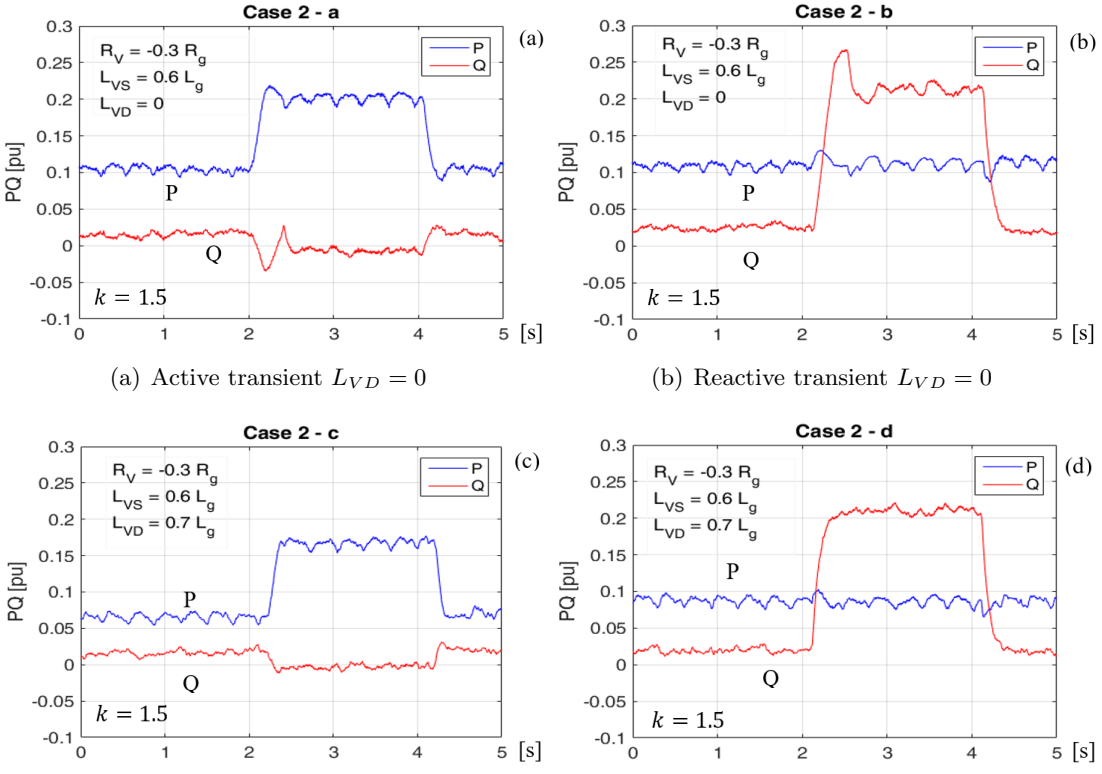

(a) Active transient $L_{VD} = 0$

(b) Reactive transient $L_{VD} = 0$

(c) Active transient $L_{VD} \neq 0$

(d) Reactive transient $L_{VD} \neq 0$

FIGURE 3.21: Experimental transients improvement by L_{VD}. In (a) and (c) step changes of the frequency droop equal to $\Delta\omega^* = 0.01$ p.u. are considered, while in (b) and (d) voltage droop variations $\Delta V^* = 0.04$ p.u.: the introduction of the dynamic virtual impedance L_{VD} improves the transitory converter behaviour.

of the droop intersections have been obtained (3.28)-(3.31): in this section, the correspondence of the model with the obtained experimental transients is considered and analysed (Table 3.2). Both the cases of the strong and weak grids are taken into account, respectively referring to Fig.3.20(a)-3.20(b) and Fig.3.21(a)-3.21(b); both frequency and voltage droop intersections changes are considered in order to include all possible cases.

Comparing the results reported in Table 3.2, it is possible to derive the following considerations:

- as regards the active power changes, the natural integral effect already highlighted in Fig.3.15 guarantees the total correspondence between the theoretical model and the experimental results under step changes of both the frequency and voltage droop intersections.
- As analysed in Fig.3.15 and (3.30)-(3.31), the equivalent feedbacks involving the reactive power do not include natural integral effects and thus the uncertainty with respect to the non-ideal evaluation of the interface and grid impedances produces higher discrepancies between the theoretical and experimental values. Still the sign of the variation and its order of magnitude confirm the applicability of the proposed dynamical model.

3.8 Functional behaviour in island mode

In this section the behaviour of a couple of converters operated in island is analysed, according to the scheme in Fig. 2.2(b) (here recalled for the sake of clarity). Interface impedances of each converter are reported in Table 3.3. The physical explanation of the experimental set-up in island mode is reported in Appendix D. In order to emulate the presence of an ideal voltage source on the DC side of the converters, a rectified voltage from the the public network is exploited.

3.8.1 Power balance between parallel connected converters

Figure 3.23 shows the effect of the virtual impedance on the power balance between different units connected in parallel in the supply of a local load during island operations. Possible differences in the offset of the acquisition system [45], as well as the mismatch of the interface impedances, produce unequal load sharing between parallel units. In

Table 3.2: Power decoupling - Experimental and theoretical values

Case *Figure*	*Variation*	Δp_o (theoret.)	Δp_o (experim.)	Δq_o (theoret.)	Δq_o (experim.)
1 - Fig.3.20(a)	$\Delta\omega^* = 0.01$ p.u.	0.1 p.u.	0.1 p.u.	-0.09 p.u.	-0.08 p.u.
1 - Fig.3.20(b)	$\Delta\omega^* = 0.01$ p.u.	0.1 p.u.	0.1 p.u.	$\cong 0$ p.u.	$\cong 0$ p.u.
2 - Fig.3.21(a)	$\Delta\omega* = 0.01$ p.u.	0.1 p.u.	0.1 p.u.	-0.03 p.u.	-0.02 p.u.
2 - Fig.3.21(b)	$\Delta V* = 0.01$ p.u.	0 p.u.	0 p.u.	0.16 p.u.	0.19 p.u.

Table 3.3: Test conditions for the converters operated in island.

Converter	*Control type*	*Interface impedance* [p.u.]
1	Droop	$Z_{g1} = 0.030$ $\varphi_{g1} = 53$ deg.
2	Droop	$Z_{g2} = 0.019$ $\varphi_{g2} = 20$ deg.

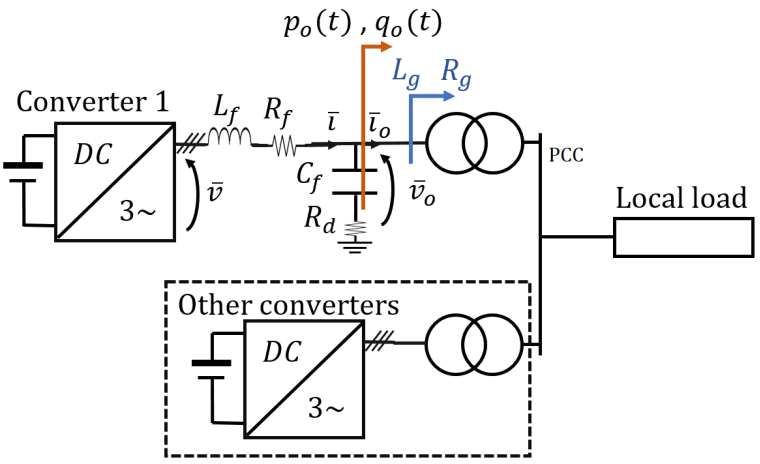

Recall: operations of the converter in island mode.

this, case an inductive-resistive load $P_{load} \cong 0.3$ p.u - $Q_{load} \cong 0.2$ p.u. is taken into account; as the two converters are characterized by the same nominal power, the ideal condition would imply a perfect load balance between the units, both for the active and reactive power. Figures 3.23(a)-3.23(d) depict the experimental load sharing experienced by the two converters under different values of the virtual impedance: the corresponding measurements are reported in Tab.3.4.

As concerns the active power, all four cases result equivalent: independently of the applied virtual impedance, the active load results perfectly balanced between the two units. On the other hand, reactive distribution shows a highly uneven behaviour. Referring to Fig.3.23(a), it is even possible to highlight the presence of a circulating reactive component: the first unit not only supplies the entire reactive load, but even induces a negative reactive flow through the second converter, which behaves as a physical inductor (according to the chosen generators convention, a positive injected reactive power is experienced when the converter behaves as a physical capacitor). In case a higher load were be applied, this condition would worsen as the first unit would easily reach its maximum capability. In this perspective, the virtual impedance introduction guarantees a more balanced distribution of the reactive injection, as it is possible to see from Fig.(3.23(d)).

3.8.2 Transients improvement

Figure 3.24 shows the transients improvement under different settings of the virtual impedance. In this test, the variations of the active local load ($\Delta P_l = 0.1$ p.u.) is considered. In the ideal case, the two units equally share both the active and reactive power; nevertheless, the different interface impedances and the mathematical nature of

Table 3.4: Load sharing in island condition

Case	*Active share (Conv.1-2)*	*Reactive share (Conv.1-2)*
1	50% / 50%	110% / -10%
2	50% / 50%	96% / 4%
3	50% / 50%	74% / 26%
4	50% / 50%	55% / 45%

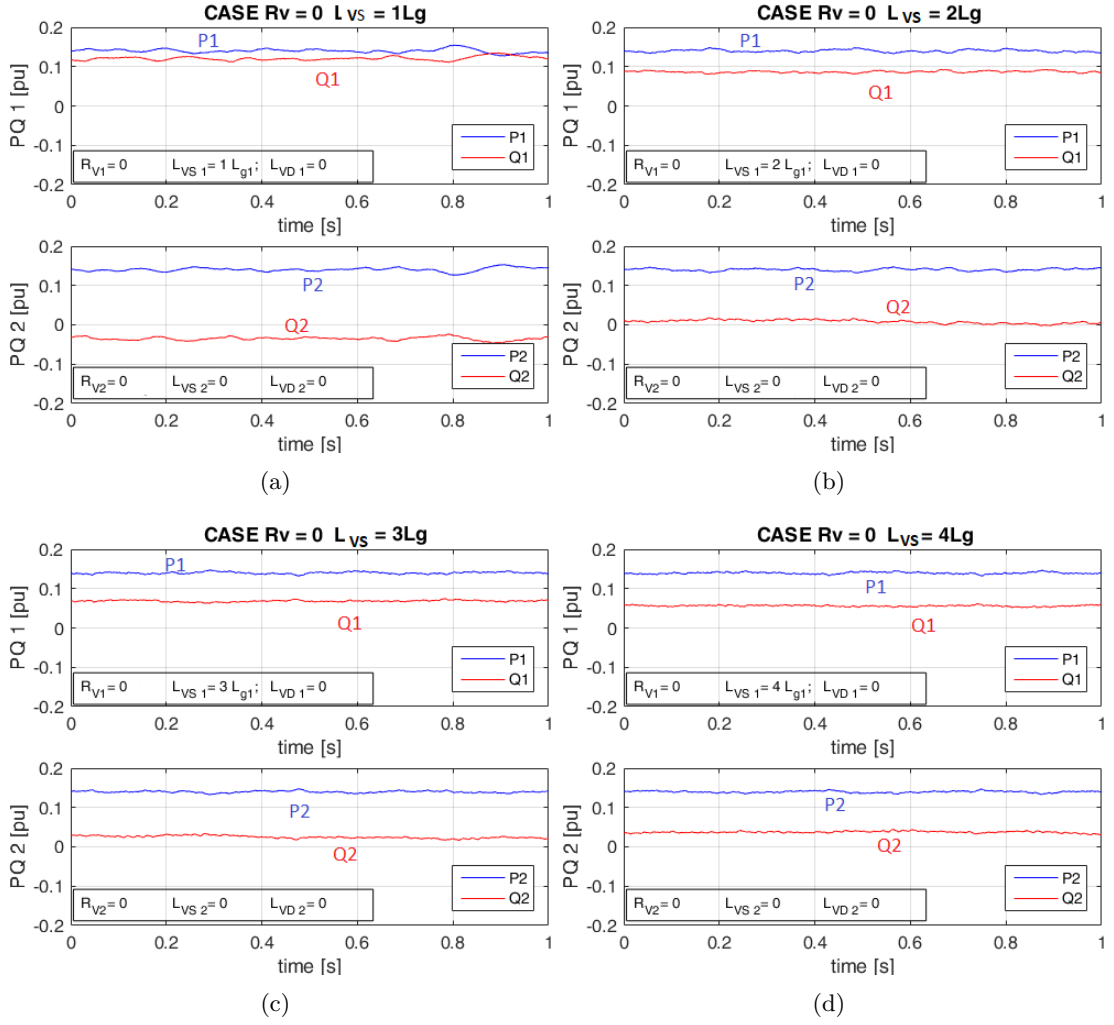

FIGURE 3.23: Experimental power balance in island conditions by means of the virtual impedance. Virtual impedance control has been applied exclusively to the first converter. An increase of the static inductance L_{VS} implies a more regular reactive sharing between parallel connected units.

the reactive droop produce an unequal reactive load sharing between the converters. As already highlighted in Sect.3.8.1, the introduction of the static virtual inductance L_{VS} enhances the steady-state balance, even though the transient of the reactive power in the second converter shows a significant overshoot; this stands for a low phase margin for the system. The dynamic term L_{VD} improves the stability of the system, as it can be seen in Fig. 3.24(c).

3.8.3 Direct converter connection to the external grid

This subsection analyses the possibility to directly interface a converter to an external network by means of the so called soft-start connection.

In [5], the introduction of a time-varying virtual impedance loop is proposed, to allow a direct connection of the converter to the system; in the following, instead of the time-varying term, the dynamic virtual inductance is exploited. Consider a single unit (converter 1) initially supplying an ohmic-resistive passive load in island. The load is characterized by nominal active and reactive powers equal to $P_{load} = 0.1$ p.u. and

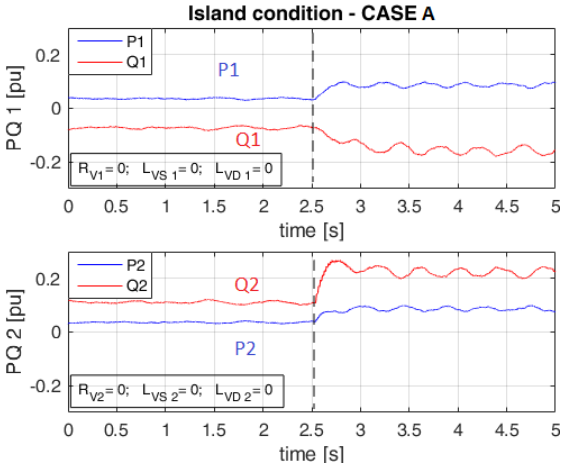

(a)

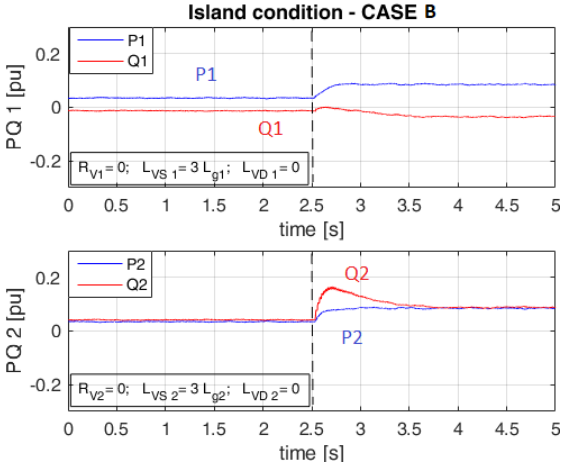

(b)

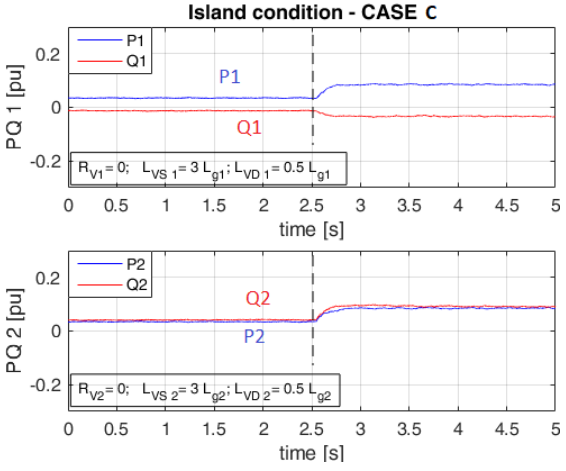

(c)

FIGURE 3.24: Experimental transients improvement in island conditions by means of the virtual impedance. In (a) no virtual impedance is introduce. In (b) static virtual impedance terms are considered: this improves the reactive power sharing at steady-state. In (c), the dynamic virtual reactance $L_{VD} \neq 0$ enhances transitory performances.

$Q_{load} = 0.05$ p.u.; the modulation algorithm of the second converter is not active. After a certain instant ($t = 3$ s in the first case and $t = 5$ in the second one), the second converter is activated, without (Fig. 3.25(a)) or with (Fig. 3.25(b)) the virtual impedance: it is possible to see a significant reduction of the oscillations associated to the introduction of the second unit and, as a consequence, a higher damping of the unidirectional circulating power components between the converters.

3.9 Conclusion

In this chapter the mathematical model associated to the virtual impedance introduction in the converter control has been analysed. This additional loop behaves as a

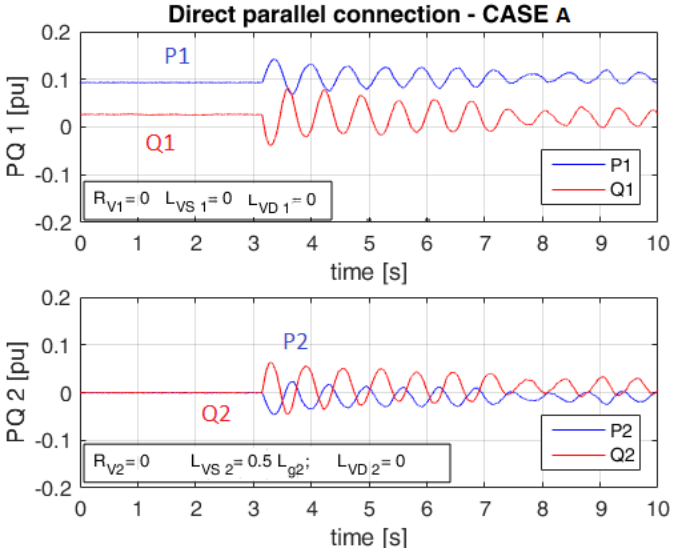

(a) Direct connection without virtual impedance

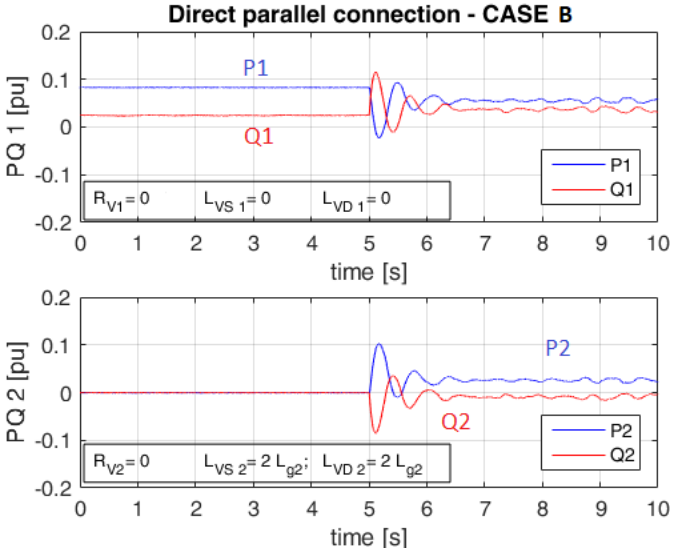

(b) Direct connection with virtual impedance

FIGURE 3.25: Experimental direct insertion of the converter by means of the virtual impedance control. Virtual impedance introduction allows a more regular insertion of the converter, as it is possible to observe comparing (a) and (b).

fictitious element in series with the physical converter interface. Even though several examples related to the introduction of this control have been identified in literature, it is difficult to find a comprehensive model able to predict the stability conditions related to the introduction of this control algorithm.

In this perspective, a rigorous dynamical model of the system equipped with virtual impedance has been derived, highlighting its interaction with the physical circuit elements for the determination of the system global phase margin. The model has been derived analytically: this has enabled the identification of a simplified design procedure for virtual impedance parameters which includes the information related to the existing dynamics.

The adopted design model represents a novelty as it proposes to highlight the internal axes-coupling as a measure of the system stability: the advantage lies in the identification of easy formulations for the global system phase margin, which require a limited computational capability and can be easily implemented on any real-time microcontroller. Still it is necessary to highlight the higher sensitivity of the technique in case some of the introduced assumptions are not fully verified.

The general correctness of the proposed approach has been verified both experimentally and with simulations. Additionally the system has been tested under various operational conditions of the converter, so as to highlight the improvements derived from its introduction, both in grid-connected and island mode.

From the reported analysis, it becomes evident the need to estimate in real time the equivalent output impedance of the converter and consequently to have the possibility to automatically tune the virtual impedance parameters, according to the developed dynamical model, as a function of the external network conditions. This important aspect will be developed in the next chapter.

Chapter 4

On-line impedance estimation

4.1 Chapter introduction

In this chapter a technique for the reconstruction of the equivalent interface impedance of the converter with the external network will be developed. As previously highlighted, this feature is particularly important as the converter control shows a great sensitivity with respect to interface impedance; moreover, this parameter is time-varying by definition, as it depends on the conditions of the external network: in this perspective, on-line estimation represents a possible way to adaptively changing the set-up of the internal controller under variations of the external system conditions.

4.2 State of the art of real-time impedance estimation techniques

4.2.1 Proposed approaches

On-line impedance estimation is becoming a common feature of grid connected converters, in the perspective of real-time identification of the dynamic characteristic of the external network as seen by the converter. Since the state of the external system changes as a function of topology as wells as of the number and type of units connected to the system, it is necessary that the reconstruction technique is carried out in real time to keep track of the time-changing characteristics of the grid.

From the mathematical point of view, the input impedance reconstruction requires the identification of the frequency response of the transfer function $\bar{Z}(\omega_s)$ in the desired part of the spectrum, thus the computational effort of the reconstruction is directly proportional to the desired frequency resolution and to the bandwidth of the reconstruction.

Before entering into the details of the proposed technique, the state of the art associated to this topic is analysed. All the proposed on-line grid impedance reconstruction techniques are based on the following concept: a known excitation is applied and it is analysed the dynamic response of the system after the introduction of the disturbance, in order to determine the response of the network in each part of the considered frequency range [46]. Even though all the methods require the introduction of a transitory behaviour to excite the dynamics of the system, each technique is characterized by a different impact on the rest of the network, as well as by different reconstruction performances and computational efforts.

Here a short list of the proposed approaches is shown; the objective of the analysis is to point out the similarities and differences between the existing literature and the

proposed technique that will be developed in the following, as well as the positive and negative features of each approach.

A traditional technique reported in [47] consists in the analysis of the voltage variation at the fundamental frequency caused by the introduction of a physical linear element with known impedance; the modification of the phasors associated to the absorbed current and local voltage before and after the topological change allows to reconstruct the parameters of the grid (modelled as a resistive-inductive series impedance) at the fundamental frequency. Every linear constant-impedance element can be used as disturbing element, provided that its electrical characteristic is known; typically, a local constant-impedance load or a capacitor bank can be used. More recent researches on the topic have proposed a similar approach: in [48] and [49] periodic step variations of the injected active and reactive powers from an electronic converter allow to identify two different equilibrium states for the system. Impedance identification is carried out comparing the steady state values in the two operating conditions. Even though these techniques are characterized by a low computational effort, they require significant changes in the waveforms.

Other approaches proposed in literature are based on the analysis of transitory behaviour associated to the set-point variations; even though the excitation of the system occurs as a change in the current reference at the fundamental harmonic, the reconstruction is carried out analysing the transitory behaviour instead of the steady state one. Different reconstruction methods have been proposed based on this approach, but with different algorithms: in [50]-[51] and [52]-[53] similar identification models are proposed, based on Extended Kalman filter or least square analysis, while in [54] Time Series theory is taken into account.

Another approach often proposed in literature consists in the introduction of a wide bandwidth disturbance (often a voltage pulse) to excite a consistent part of the frequency spectrum, reconstructing the equivalent impedance of the network by performing frequency analysis on the response. Typical applications of this technique require the on-line calculation of the Discrete Fourier Transform associated to the input and output signals [55]-[56], while others exploit Wavelet Transform [57]-[58]. Even though these techniques allow a wideband reconstruction of the desired frequency profile, their implementation on low computational power micro-controllers is not always easy and requires a significant memory on the device. Moreover, the accuracy of these techniques is generally low close to the frequencies at which the system shows a harmonic voltage component.

A last approach regards the exploitation of single harmonics, whose values can be modulated in order to assess the dynamical response of the system at that specific frequencies. Even though this method does not allow to reconstruct the frequency profile in a large bandwidth, still from the computational point of view is very convenient as it allows to reduce the order of the inversion model and can be implemented on every hardware setup. Nevertheless, the most critical point of this technique regards the choice of the harmonics to be controlled for the estimation. In [59] and [60] it is proposed to use inter-harmonics close to the fundamental one in order to easily interpolate the equivalent impedance seen at 50 Hz. In [61] high order harmonics are proposed, even though open-circuit voltages naturally present in the network at that specific frequencies are not taken into account.

4.2.2 Comparison between the proposed method and the existing literature

In the next section, a technique based on the control of natural system harmonics will be proposed, which allows to take into account the natural presence of open-circuit voltage at the specific used frequencies. Before entering into the details of the mathematical model, some advantages are identified:

- the decision to exploit the natural harmonics of the system reduces its impact on the rest of the network, as it avoids the introduction of spurious components; nevertheless, this decision impacts on the control system design, as it must operate in a differential way to reduce its sensitivity with respect to external network open-circuit voltages at the frequencies of interest.
- The low value of the harmonic disturbance makes the converter compatible with the interconnection standards defined in terms of harmonic content.
- The realization cost of the technique, both in terms of memory and of computational effort, is low if compared to wide bandwidth identification methods and still allows to reconstruct the equivalent impedance at the fundamental harmonic in a consistent way, which is the goal of the algorithm.

On the other hand, some disadvantages can be identified:

- the reconstruction technique is founded on a model-based approach, as it assumes an inductive-resistive (or capacitive-resistive) behaviour; thus, it may provide inconsistent results as the physical system shows resonant behaviour close to the exploited frequencies;
- the result of the estimation is clearly affected by other converters control in case the percentage of electronic units connected to the microgrid is consistent; even though this aspect has a high impact on the stability of the system, still it represents an open issue in literature and, at the current stage, all the proposed techniques are affected by this sensitivity.

4.3 Impedance Measurement Model

Consider a power converter interfaced to an external three-phase low-voltage grid as already introduced in the previous chapters (Fig. 4.1). The fundamental component can be controlled by means of a droop-scheme; nevertheless, as the impedance estimation technique acts solely on the internal voltage and current loops, it results independent of the droop characteristics.

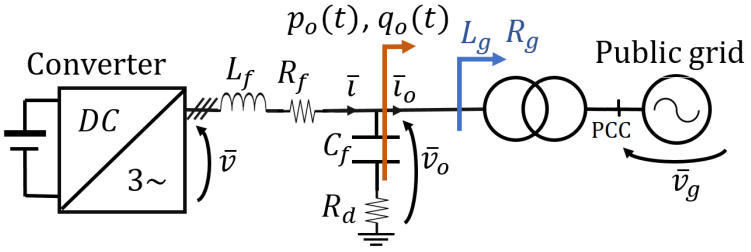

FIGURE 4.1: Considered converter scheme for grid impedance parameters identification.

The objective of the estimation technique is to identify the equivalent parameters R_g and L_g as seen by the converter at the external network interface in order to be able to control its regulation parameters in an effective way, according to (2.55) - (2.56).

Two constraints have to be identified in the design of the technique:

- reduce the impact of the estimation on the rest of the network;
- keep the lowest possible computational effort for the system.

Thus the idea consists in the modulation of current $\bar{i}_{oh}$ or voltage $\bar{v}_{oh}$ harmonics naturally present into the system and lately reconstruct the impedance profile according to the typical least square inversion method. From the control system perspective, the objective is to guarantee a robust control of either the harmonic current $\bar{i}_{oh}$ or voltage $\bar{v}_{oh}$ and be able to measure the other physical quantity.

Thus it is natural to take into account two alternatives:

- *Voltage-controlled mode*: harmonic voltage $\bar{v}_{oh}$ is regulated and the corresponding current $\bar{i}_{oh}$ is measured;
- *Current-controlled mode*: harmonic current $\bar{i}_{oh}$ is regulated and the corresponding voltage $\bar{v}_{oh}$ is measured.

The components exploited for the reconstruction are 5^{th} and 7^{th} harmonics; the choice has been done considering some key aspects:

- harmonic limits for odd harmonics are typically less stringent with respect to even harmonic ones;
- resonance phenomena in this frequency range are uncommon, at least for medium and low voltage microgrids;
- the control systems of several converters are already equipped with controllers designed for the regulation of these components.

Three independent rotating reference frames can thus be identified: beside the one synchronous with the fundamental harmonic dq, it is possible to define the ones associated with the considered harmonics ($dq5$ and $dq7$). According to the typical construction of three-phase systems, the 7^{th} order harmonic is a positive-sequence component, while the 5^{th} is a negative-sequence one; this condition is taken into account in the angular rotation definition of the $dq5$ and $dq7$ frames (Fig. 4.2).

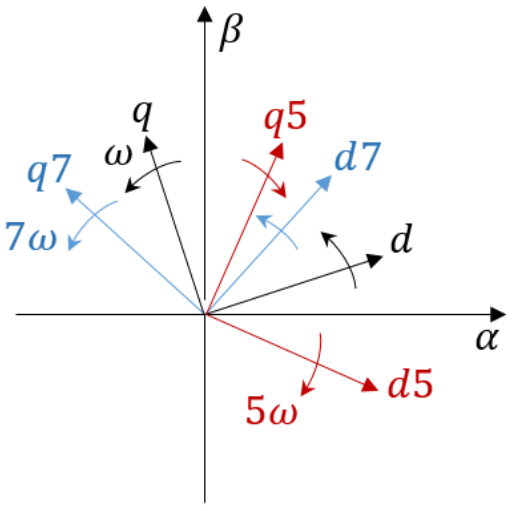

FIGURE 4.2: Axes system inside the control, for on-line impedance estimation.

From the conceptual point of view, two different sub-functions are associated to the equivalent output impedance reconstruction algorithm:

- *Harmonic control*: it imposes the desired values for the current / voltage harmonic amplitudes.
- *Acquisition and inversion model*: elaboration of the acquired state variables and impedance estimation.

4.4 Harmonic control

4.4.1 Voltage-controlled mode

Consider the equivalent algorithm reported in Fig. 4.3(a), which shows the conceptual operations of the converter while performing harmonic management for the impedance identification. The algorithm consists in the alternation of two different phases associated to the temporal periods T_1 and T_2. During each part of the algorithm, a different harmonic reference is chosen for the 5^{th} and 7^{th} order harmonics.

$$\begin{cases} 0 \leq t < T_1 \quad V_5 = V_7 = 0 \\ T_1 \leq t < T_1 + T_2 \quad V_5 = V_7 \neq 0 \end{cases} \tag{4.1}$$

Figure 4.3(b) shows the required changes in the regulation system to properly impose the desired value of harmonic voltage. As the converter control architecture is designed on synchronous dq axes, the additional input associated to the 5^{th} and 7^{th} order harmonics is seen from the synchronous frame as an equivalent 6^{th}-order harmonic. This allows to simplify the control scheme of the converter, since a single additional resonant controller, placed in parallel to the PI already designed for the fundamental, enables the control of both additional voltage references. The reference voltage associated to the fundamental component $v_{o\,dq}^{ref}$ comes from the droop, according to the traditional scheme reported in the previous chapters (Fig. 4.3(b)).

The resonant controller (4.2) has been designed according to [26] and discretized following [62]. Its resonance peak is placed in correspondence to the 6^{th} order harmonic: the analytical calculation of the discrete form allows to adapt the position of the resonance peak even under the drift of the fundamental component and keep the resonance peak placed in correspondence to the desired harmonic. The characteristics of the resonant function are reported in Appendix C.1.

$$R_6(s) = \frac{\frac{s}{\omega_6}}{(\frac{s}{\omega_6})^2 + 2\xi\frac{s}{\omega_6} + 1} \tag{4.2}$$

4.4.2 Current-controlled mode

The second scheme controls the harmonic current $\bar{i}_o$ instead of the voltage $\bar{v}_o$. In this case, the algorithm evolves as in Fig. 4.4(a): similarly to the voltage-controlled scheme, two alternating conditions are imposed acting on the harmonic reference.

$$\begin{cases} 0 \leq t < T_1 \quad I_5 = I_7 = 0 \\ T_1 \leq t < T_1 + T_2 \quad I_5 = I_7 \neq 0 \end{cases} \tag{4.3}$$

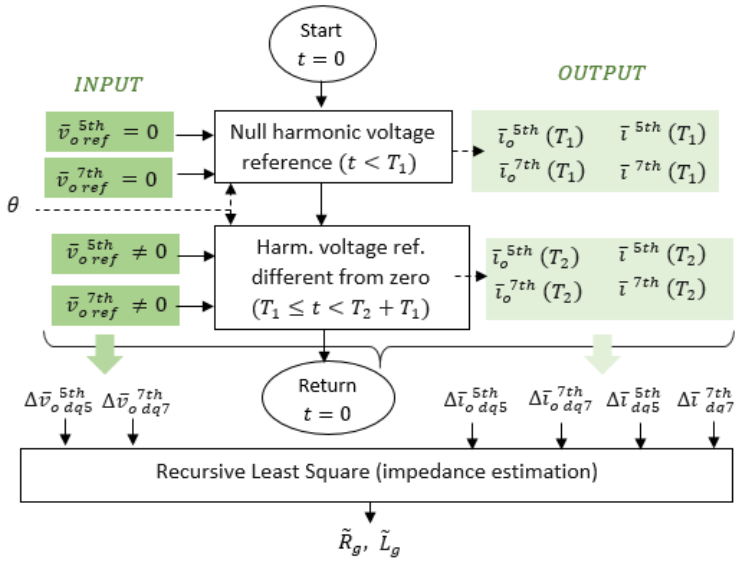

(a) Algorithm for voltage-controlled estimation

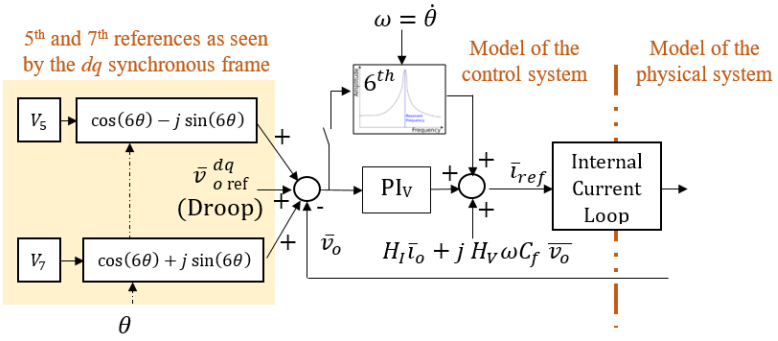

(b) Modified voltage $\bar{v}_o$ regulation

FIGURE 4.3: Algorithm (a) and control scheme (b) used for impedance estimation with harmonic voltage control. The procedure develops in two iterative phases: the alternation of the harmonic reference voltage allows to define the differential model used for impedance reconstruction.

In order to properly control the harmonic current value, the regulation scheme should be modified as in Fig. 4.4(b). The presence of two parallel resonant controllers allows a full controllability of the injected 5^{th} and 7^{th} order harmonics currents.

Figure 4.4(a) highlights that, in the current-controlled mode, the values of the estimated grid parameters $\tilde{R}_g$ and $\tilde{L}_g$ are sent back to the harmonic regulation algorithm. This is due to the inherent sensitivity of the regulator with respect to the external grid admittance $Y_g(s)$, that is actually the desired estimated quantity: this condition introduces some issues in the regulator definition, as their dynamical properties are dependant on the quantity the system itself is asked to estimate.

The decision to regulate the harmonic current $\bar{\imath}_o^h$ instead of the voltage $\bar{v}_o^h$ introduces a significant complexity in the control scheme:

- at the fundamental frequency, the converter has to behave as a sinusoidal voltage source, whose amplitude and angular frequency are determined by the droop control;

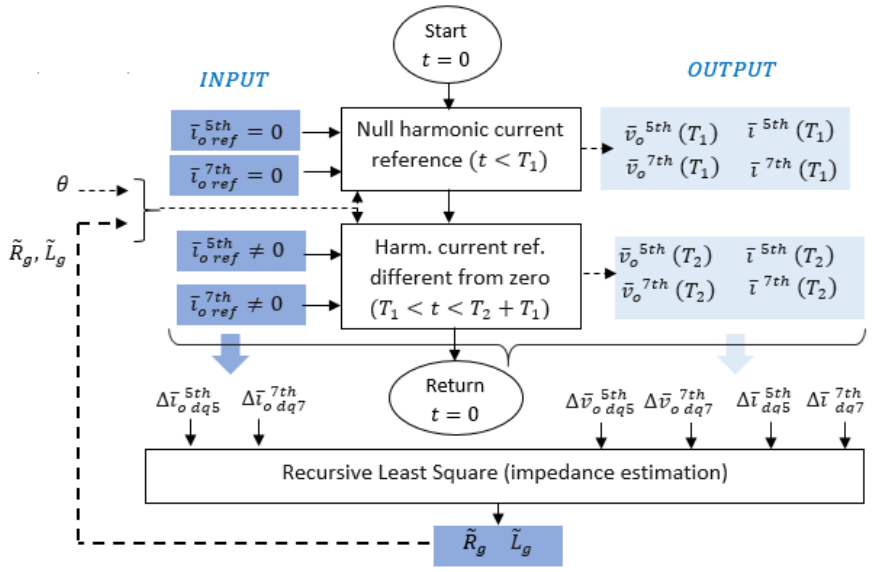

(a) Algorithm for current-controlled estimation

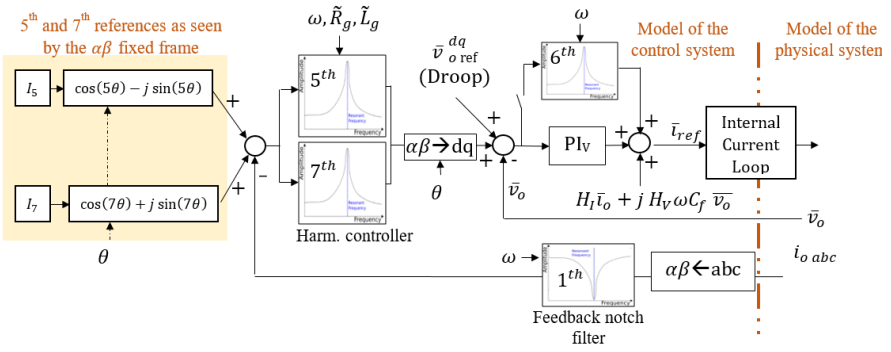

(b) Control structure

FIGURE 4.4: Algorithm (a) and control scheme (b) used for impedance estimation with harmonic current control. The regulation iteratively imposes two different harmonic current levels and defines the differential model used for impedance reconstruction. Estimated parameters $\tilde{R}_g$ and $\tilde{L}_g$ are sent back to the controllers, to compensate the output admittance $Y_g(s)$ delay.

- in correspondence to the 5^{th} and 7^{th} harmonics, the converter is controlled as an harmonic current source.

In order to meet these two constraints, the control architecture becomes more articulated. In Fig. 4.4(b), as an example, it is possible to see the introduction of a strong notch filter on the current $\bar{\imath}_o$ feedback associated to the harmonic control: this regulator, tuned at the fundamental frequency, is introduced in order to avoid a possible interference of the harmonic control with the droop.

The structure of the harmonic controllers $R_5(s)$ and $R_7(s)$ is modified with respect to the typical one analysed in Appendix C.1 to compensate the phase delay associated grid admittance $Y_g(s)$. The introduced modification consists in a leading network whose parameters are obtained from the impedance estimation process itself; T_a determines a

high-frequency pole used to make the system realizable ($T_a^{-1} = 1 \cdot 10^4$ rad/s).

$$R_{5-7}(s) = \frac{\frac{s}{\omega_{5-7}}}{(\frac{s}{\omega_{5-7}})^2 + 2\xi\frac{s}{\omega_{5-7}} + 1} \cdot \frac{\tilde{R}_g + s\tilde{L}_g/\omega_b}{1 + sT_a} \tag{4.4}$$

Furthermore, the harmonic control is carried on in the $\alpha\beta$ frame to avoid the presence of motional terms associated to the equivalent output grid inductance L_g. The combination of all these aspects leads to the control structure illustrated in Fig. 4.4(b).

4.5 Inversion model for impedance identification (R_g - L_g).

The inversion model represents the portion of the algorithm that performs the reconstruction of the impedance parameters. The simplest form of the algorithm models the equivalent grid as an inductive-resistive impedance, characterized by the terms R_g and L_g; this approach goes under the name of finite parametric reconstruction problem, as it allows to identify the values of the parameters that best fit the state equations of a pre-determined model, which in this case is the Kirchhoff's voltage law associated to the interface impedance.

Consider the Kirchhoff's voltage and current equations associated to the interface impedance and to the filter capacitor respectively. These equations obviously hold for the generic harmonic ω_h (in per-unit with respect to ω_b, $h = 5 - 7$); as for the notation of the state variables, the superscript stands for the harmonic order and the subscript for the reference system to which it is referred. Each component shows a constant amplitude during each of the harmonic control algorithm phases (Fig. 4.3(a) and Fig. 4.4(a)) provided that it is referred to its synchronous frame, $dq5$ for the 5^{th} harmonic, $dq7$ for the 7^{th} one.

$$\bar{v}^h_{o\,dq\,h} = R_g\bar{i}^h_{o\,dq\,h} + j\omega_h L_g\bar{i}^h_{o\,dq\,h} + L_g\frac{s}{\omega_b}\bar{i}^h_{o\,dq\,h} + \bar{v}^h_{g\,dq\,h} \tag{4.5}$$

$$C_f\left(\frac{s}{\omega_b} + j\omega_h\right)\bar{v}^h_{o\,dq\,h} = \left(1 + j\omega_h R_d C_f + R_d C_f\frac{s}{\omega_b}\right)\cdot\left(\bar{i}^h_{dq\,h} - \bar{i}^h_{o\,dq\,h}\right) \tag{4.6}$$

Now it is necessary to provide a formal definition of the differential parameters as reported in Fig. 4.3(a) and Fig. 4.4(a): in both cases the control system imposes two different reference conditions (identified by T_1 and T_2 according to (4.1)-(4.3)) where the system reaches alternated steady state conditions. Thus for each state variable it is possible to define a differential quantity (indicated by the symbol Δ) that corresponds to the difference of the two steady state levels. As each harmonic is referred to its own rotating reference system (Fig. 4.2), state differences are theoretically constant under the square-wave harmonic references.

$$\Delta\bar{v}^h_{o\,dq\,h} = \bar{v}^h_{o\,dq\,h}(t = T_2 + T_1) - \bar{v}^h_{o\,dq\,h}(t = T_1) \tag{4.7}$$

$$\Delta\bar{i}^h_{o\,dq\,h} = \bar{i}^h_{o\,dq\,h}(t = T_2 + T_1) - \bar{i}^h_{o\,dq\,h}(t = T_1) \tag{4.8}$$

$$\Delta\bar{i}^h_{dq\,h} = \bar{i}^h_{dq\,h}(t = T_2 + T_1) - \bar{i}^h_{dq\,h}(t = T_1) \tag{4.9}$$

In reality, each left-side term of the difference in (4.7)-(4.9) is obtained as an average of the last samples in order to filter out high-order harmonics; nevertheless, from the

conceptual point of view it is possible to assume (4.7)-(4.9) as the difference of single-instant terms at the specific time steps $t = T_1$ and $t = T_1 + T_2$. Obviously as the algorithm is iteratively repeated, the terms in the difference are alternatively updated at each sub-iteration of the algorithm.

If we consider steady state conditions in (4.5) and (4.6) ($s \to 0$), it is possible to substitute (4.5) in (4.6) and express the result as a function of the differential terms in (4.7)-(4.9). Assuming that the harmonic voltage components $\bar{v}_{g\,h}$ do not significantly change between the two phases of the algorithm, the differential model in (4.10)-(4.11) can be derived.

$$\Delta\bar{v}^{h}_{o\,dq\,h} = R_g\Delta\bar{i}^{h}_{o\,dq\,h} + j\omega_h L_g\Delta\bar{i}^{h}_{o\,dq\,h} \tag{4.10}$$

$$\Delta\bar{i}^{h}_{o\,dq\,h}\cdot\left(1-\omega_h^2 L_g C_f\right) + j\omega_h C_f\cdot(R_d+R_g)\cdot\Delta\bar{i}^{h}_{o\,dq\,h} = \Delta\bar{i}^{h}_{dq\,h} + j\omega_h C_f R_d\Delta\bar{i}^{h}_{o\,dq\,h} \tag{4.11}$$

Relations (4.10) and (4.11) are two independent complex equations in the unknowns R_g and L_g, as all other terms are known from the acquisition system. The differential nature of the algorithm makes it independent of the open-circuit harmonic voltage $\bar{v}_{g\,h}$, provided that these components do not evolve in a significantly fast way. This allows to perform harmonic impedance reconstruction at the natural network components and thus avoids the introduction of spurious frequencies into the system.

Theoretically, a single harmonic component would be enough for impedance estimation. Moreover, this would lead to a strong sensitivity with respect to acquisition errors and measurement uncertainties. In this perspective, the exploitation of two harmonics (5^{th} and 7^{th}) and two formally independent equations (4.10)-(4.11) allows to increase the order of the system and exploit the filtering properties of the Least Square approach. The model can be written in the linear form $A\cdot x = b$, where:

$$x = [R_g\ L_g]^{-1} \quad A = \begin{bmatrix} \Delta i^{5th}_{o\,d5} & -\omega_5\Delta i^{5th}_{o\,q5} \\ \Delta i^{5th}_{o\,q5} & +\omega_5\Delta i^{5th}_{o\,d5} \\ \Delta i^{7th}_{o\,d7} & -\omega_7\Delta i^{7th}_{o\,q7} \\ \Delta i^{7th}_{o\,q7} & +\omega_7\Delta i^{7th}_{o\,d7} \\ +\omega_5 C_f\Delta i^{5th}_{o\,q5} & \omega_5^2 C_f\Delta i^{5th}_{o\,d5} \\ -\omega_5 C_f\Delta i^{5th}_{o\,q5} & \omega_5^2 C_f\Delta i^{5th}_{o\,q5} \\ +\omega_7 C_f\Delta i^{7th}_{o\,q7} & \omega_7^2 C_f\Delta i^{7th}_{o\,d7} \\ -\omega_7 C_f\Delta i^{7th}_{o\,q7} & \omega_7^2 C_f\Delta i^{7th}_{o\,q7} \end{bmatrix} \tag{4.12}$$

$$b = \begin{bmatrix} \Delta v^{5th}_{o\,d5} \\ \Delta v^{5th}_{o\,q5} \\ \Delta v^{7th}_{o\,d7} \\ \Delta v^{7th}_{o\,q7} \\ (\Delta i^{5th}_{o\,d5} - \Delta i^{5th}_{d5}) - \omega_5 C_f R_d\cdot(\Delta i^{5th}_{o\,q5} - \Delta i^{5th}_{q5}) \\ (\Delta i^{5th}_{o\,q5} - \Delta i^{5th}_{q5}) + \omega_5 C_f R_d\cdot(\Delta i^{5th}_{o\,d5} - \Delta i^{5th}_{d5}) \\ (\Delta i^{7th}_{o\,d7} - \Delta i^{7th}_{d7}) - \omega_7 C_f R_d\cdot(\Delta i^{7th}_{o\,q7} - \Delta i^{7th}_{q7}) \\ (\Delta i^{7th}_{o\,q7} - \Delta i^{7th}_{q7}) + \omega_7 C_f R_d\cdot(\Delta i^{7th}_{o\,d7} - \Delta i^{7th}_{d7}) \end{bmatrix} \tag{4.13}$$

In (4.12) and (4.13), $\omega_7 = 7\cdot\omega$ as the 7^{th}-order harmonic is a direct sequence component, $\omega_5 = 5\cdot\omega$ as the 5^{th} is a negative sequence one.

The solution to the Least Square problem can be calculated as in (4.14). In the following, the same uncertainty level has been assumed for all the measured quantities and absence of correlation between measurement uncertainties; thus:

$$x = (A^T A)^{-1} \cdot A^T \cdot b \tag{4.14}$$

The processing of the data to be used for the impedance evaluation is carried out according to the scheme reported in Fig.4.5. The acquired quantities are filtered by means of a strong notch filter to remove the fundamental harmonic component and later by resonant filters to extract the single harmonics (5^{th} and 7^{th}). All the coefficients of the digital filters are adaptively updated according to the actual frequency of the system ω, that in island operations may be different from the nominal one $\omega_n = 1$ p.u. .

It is possible to see that both the output current $\bar{i}_o$ and the filter one $\bar{i}$ are acquired and pre-processed; even though from the mathematical point of view there is no need to add this redundancy in the acquisition inversion process, still this introduction allows to compensate random and biased error that may be present in the inversion model.

4.6 Experimental tests

4.6.1 Current-controlled mode

Consider the experimental waveform of the 5^{th} harmonic current as seen by the $dq5$ frame in Fig. 4.6 and the corresponding voltages in Fig. 4.7. The profiles allow to have a visual understanding of the harmonic control performed on the system: the regulator imposes an alternation between two different states, each associated to a pre-determined harmonic amplitude. The duration of each state is identified by the time-ranges T_1 and T_2, where $T_1 = T_2 = 500$ ms:

- during T_1, a null harmonic current reference is imposed ($I_5 = 0$);
- during T_2, the harmonic current amplitude is set equal to 0.02 p.u.

The same condition is applied for the 7^{th} order component. The measured current and voltage harmonic amplitudes during time ranges T_1 and T_2 are the base for the differential inversion introduced in Sect.4.5. Furthermore, from the experimental behaviours

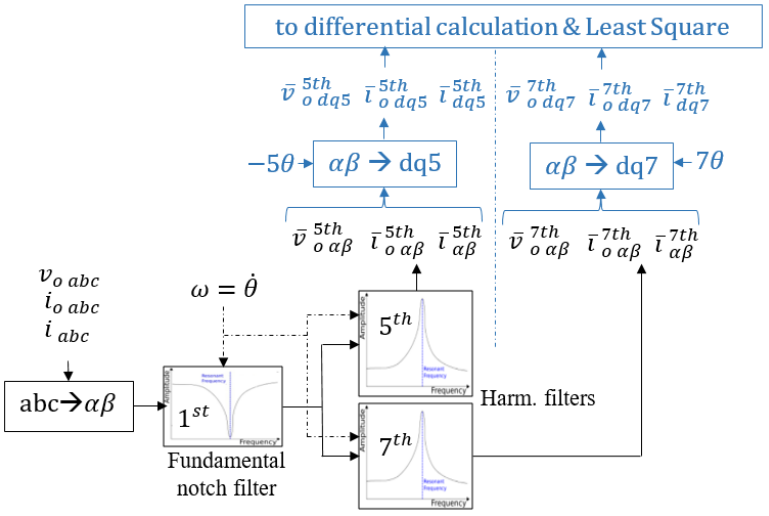

FIGURE 4.5: Pre-processing of the data to be used for the impedance reconstruction.

reported in Fig.4.6 and Fig.4.7 it is possible to highlight some important considerations associated to the actual behaviour of the system:

- the resonant controllers enable an almost perfect match of the actual harmonic amplitude with the desired one;
- the digital acquisition filters represented in Fig.4.5 guarantee a low disturbance in the reconstructed harmonic quantities, which result to be fairly constant and lowly distorted during both the conditions imposed by the control.
- From the graphs, it is also possible to highlight the introduction of a transition ramp between the two states; this allows to reduce the harmonic transients and prevents from the occurrence of lowly-damped overshoots associated to the resonant controllers dynamical response.

All these aspects allow to keep a limited intentional disturbance caused by the estimation algorithm (and thus a low impact on the rest of the network), while guaranteeing

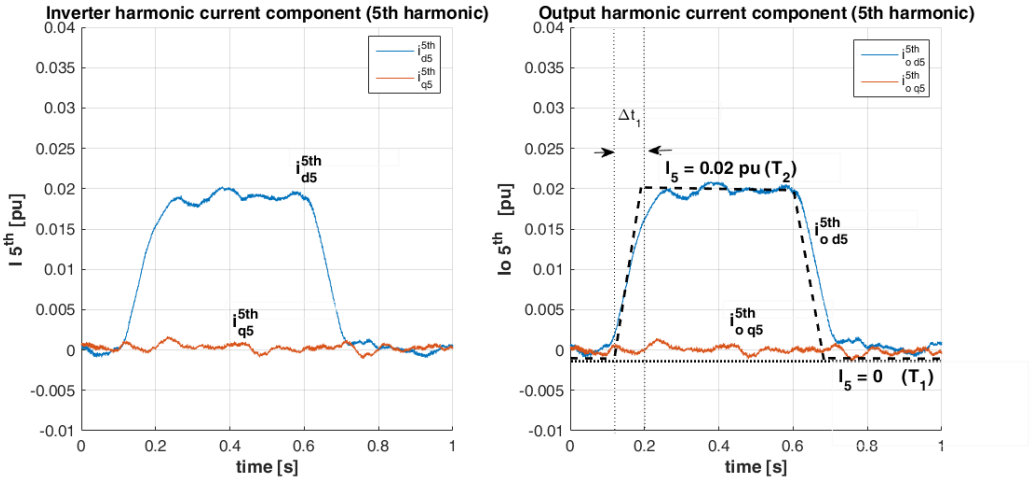

FIGURE 4.6: Detail of the 5^{th} order harmonic current as seen by the $dq5$ frame. The algorithm imposes two steady state conditions. The ramp between the two steady states has been introduced to avoid the insurgence of transients on the reconstruction. In (a) the filter current $\bar{i}^{5th}_{dq5}$ is represented while in (b) the output current $\bar{i}^{5th}_{o\,dq5}$.

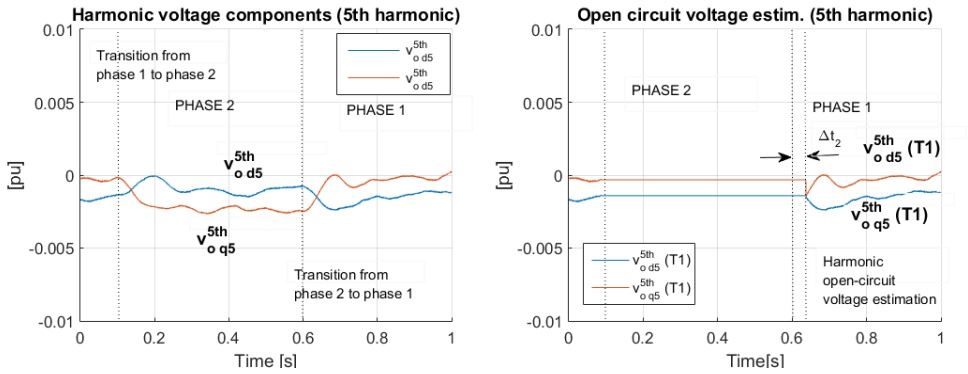

FIGURE 4.7: Detail of the 5^{th} order harmonic voltages as seen by the $dq5$ frame. In (a) the profile associated to the instantaneous harmonic voltage $\bar{v}^{5th}_{o\,dq5}$ is reported, while in (b) the open-circuit harmonic voltage estimation used in the reconstruction process is reproduced: the estimated open-circuit harmonic component matches with the instantaneous one only during phase T_1, where the harmonic current is zero.

an acceptable resolution of the reconstructed quantities. In order to validate this affirmation, consider the time profiles associated to the phase current and voltages (Fig. 4.9) in correspondence to the same transition reported in 4.6 between the time-ranges T_1 and T_2: from a macroscopic perspective, the system operates sinusoidally independently of the estimation algorithm. A more numerically-consistent analysis can be done referring to the spectral profiles of the quantities in three different conditions:

- when the converter is operated with a simple droop control, with no impedance estimation enabled;
- during the algorithm operations, in the time-ranges T_1 and T_2 respectively.

The comparison between the harmonic amplitudes in the three conditions is reported in Fig.4.8, where the normalized widths of each component are referred in per-unit: looking at the numerical values, it is possible to see the substantial correspondence of the order of magnitudes during the alternation of the algorithm phases, both as regards the harmonic voltage and the corresponding currents. The complete spectra associated to these conditions are reported in Fig.4.10 for verification: the profiles verify the regulation capability of the system in imposing the desired harmonic profile and, furthermore, highlight the practical absence of spurious components which would negatively significantly impact on the network power quality.

Figure 4.11 and Figure 4.12 show respectively the spectra of the estimated parameters R_g - L_g obtained from the Least Square model and the time profile of the estimation itself: in both graphs, the reconstructed quantities are compared with the ones calculated from off-line measurement, which are assumed as benchmark for the on-line algorithm assessment. Analysing the frequency profile of the reconstruction (Fig.4.11), it is possible to observe the presence of low-order components, especially in the resistance estimation; in the time profile, this corresponds to higher transitory phenomena between one phase and the subsequent one. These terms are practically absent in the equivalent inductance reconstruction, which exhibits a more regular profile both in the time and in the frequency domain. The reason of these transitory phenomena lies in the non-ideal dynamical decoupling between the internal controllers of the system.

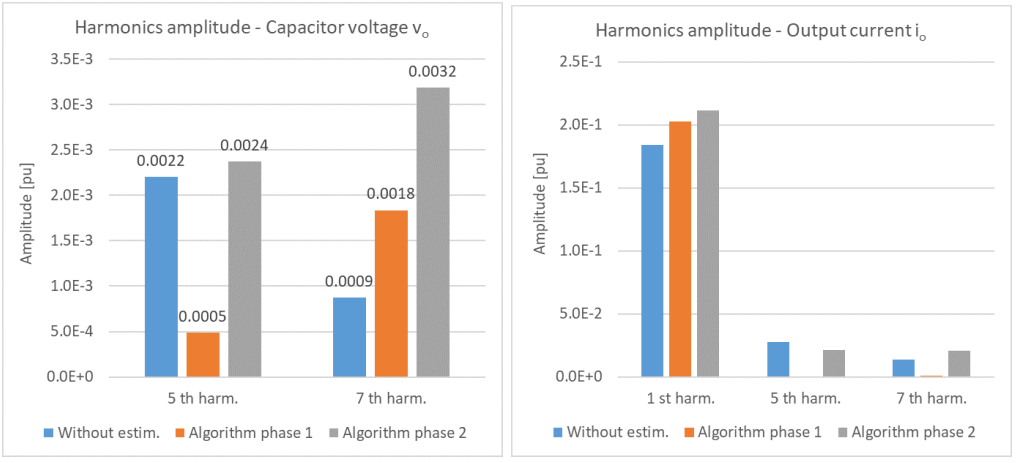

(a) Harmonic voltage comparison

(b) Harmonic current comparison

FIGURE 4.8: Harmonic comparison with the ones obtainable when the impedance estimation is not active. The considered values are similar to the ones typically obtained when the estimation algorithm is not applied: this is an index of the limited impact of the technique on the network behaviour.

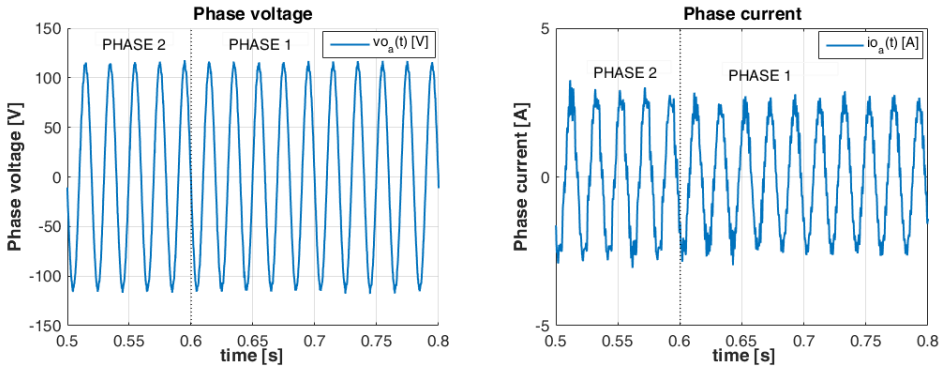

FIGURE 4.9: Phase profiles of the voltage and current during impedance estimation: the system continuously operates in sinusoidal conditions independently of the estimation algorithm.

This aspect can be also seen introducing a controlled step-change in the equivalent output impedance of the system (Fig.4.13), obtained from the commutation of converter output terminals from a circuit with know additional inductance to a low-impedance path. While the estimation $\tilde{L}_g$ shows a regular profile and it smoothly evolves from one value to the subsequent one matching the expected values with an acceptable consistency, the resistance reconstruction $\tilde{R}_g$ exhibits a more distorted profile, even though its average value matches with the expected one.

Figure 4.13 also highlights that the harmonic current amplitude continues to differentially operate between the desired levels, beside the changes in the actual converter interface: this clearly represents the major advantage of the technique, as the identification of suitable thresholds for the harmonic current in the two states (T_1-T_2) automatically guarantees the compliance with those grid standards that impose limitations on the amplitude of the absorbed current components from active loads.

Moreover it poses significant disadvantages and complexities in the control:

- even though in principle the compensation of the grid pole (4.4) guarantees consistency to the method, in reality the adaptation procedure is critical and tends to amplify the uncertainty of the estimation;
- the implementation of the technique on more converters in the same microgrid produces wrong results; the reason is that the units have a different control strategy at the 5^{th} and 7^{th} harmonics (harmonic current source) with respect to the one carried out for the fundamental component (droop-controlled voltage source).

4.6.2 Voltage control mode

Figure 4.14 reports the results associated to the impedance estimation performed by means of the harmonic voltage control mode, both in grid connected (condition 5) or when the converter is supplying a single local passive load operated in island (conditions 1-4); the results from the real-time estimation are compared to the ones from off-line measurement, assumed as benchmarks for the evaluation. The time profiles of the estimations evaluated in Fig.4.14 are reported in Fig.4.15 for verification.

In order to evaluate the performances of the voltage-controlled approach against the current-controlled one previously reported, some performance indexes are evaluated:

- the normalized estimation error, for the reconstructed resistance and inductance respectively; this quantity takes into account the algorithm mismatch. The variables $\tilde{R}_{g\,0}$ and $\tilde{L}_{g\,0}$ indicate the average values of the estimations, which are physically located in correspondence to the DC components of the corresponding spectral

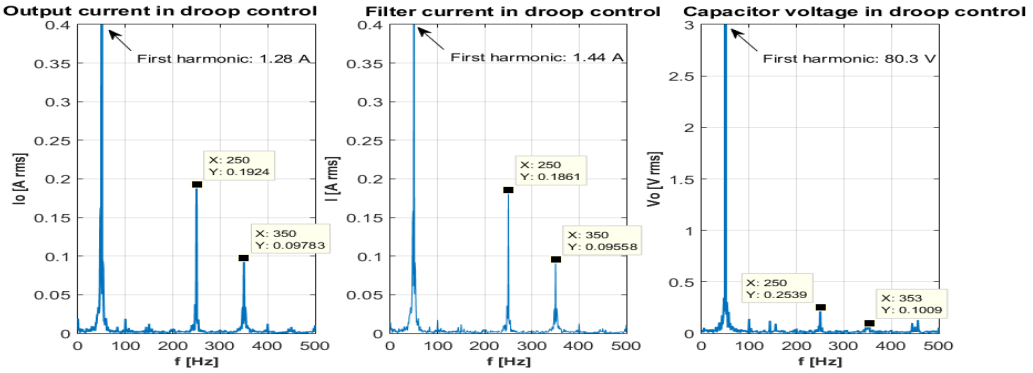

(a) Droop control with no impedance estimation algorithm

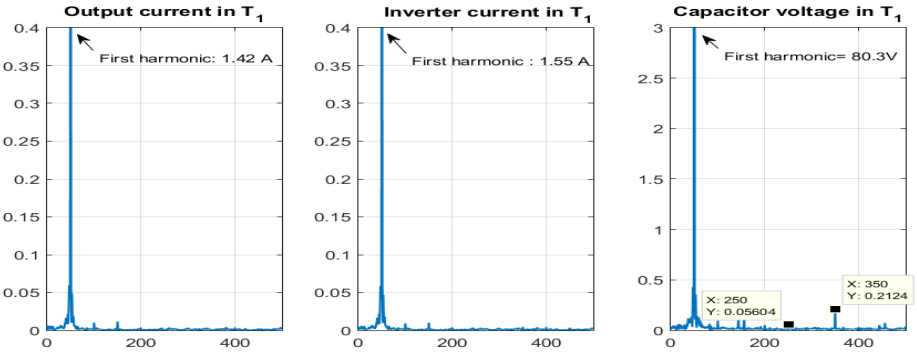

(b) Null harmonic current reference $I_5 = I_7 = 0$ (that it the time frame identified by T_1)

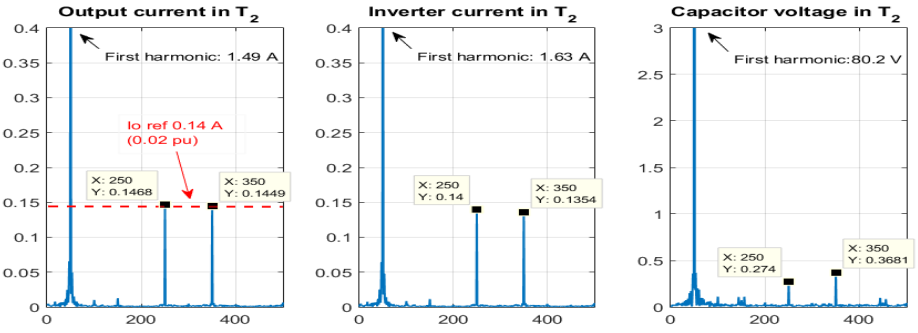

(c) Harmonic current reference $I_5 = I_7 = 0.02$ p.u. (that it the time frame identified by T_2)

FIGURE 4.10: Spectra of the state variables during the three different conditions of the system: (a) simple droop control, with no impedance estimation, (b) null harmonic reference current condition and (c) non-null harmonic reference. The graphs show the regulation capability of the control system, which is able to impose the desired values of harmonic current in both phases (T_1 and T_2) of the algorithm and the absence of spurious components.

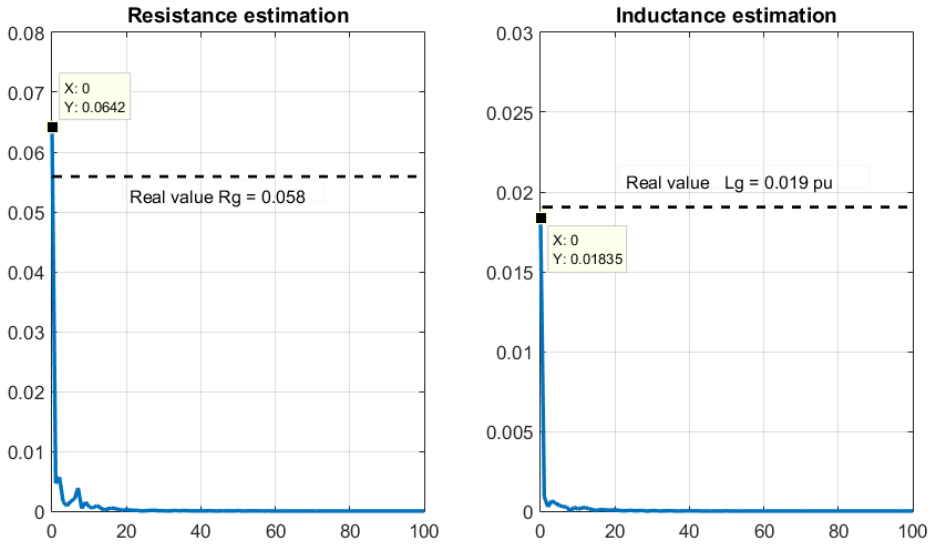

FIGURE 4.11: Spectra associated to the estimated parameters during constant operating conditions. The analysis reveals the presence of a higher disturbance on the reconstructed resistance $\tilde{R}_g$ at low frequencies with respect to the inductance $\tilde{L}_g$.

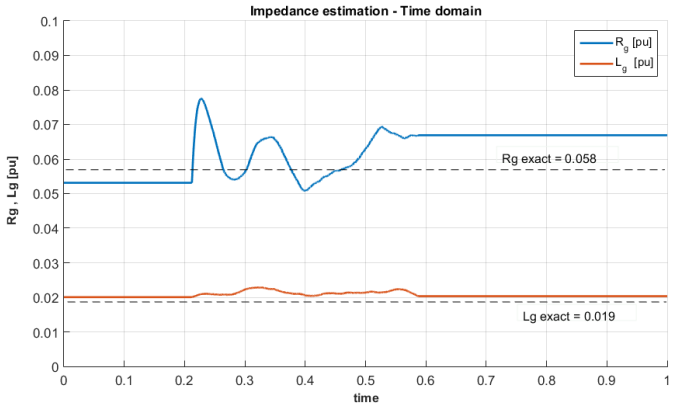

FIGURE 4.12: Profile of the reconstructed quantities in time domain, under current-controlled algorithm.

representations.

$$\epsilon\, R_g = \frac{\left|\tilde{R}_{g\,0} - R_{g\,real}\right|}{R_{g\,real}} \quad \epsilon\, L_g = \frac{\left|\tilde{L}_{g\,0} - L_{g\,real}\right|}{L_{g\,real}} \tag{4.15}$$

- The cumulative sum of the spectral components up to 100 Hz (with the exclusion of the average term), normalized with respect to the real value; this quantity measures the time-variability under constant operating conditions: the higher the index, the highly-disturbed is the reconstruction.

$$CS\, R_g = \sum_{h\neq 0}^{100\,Hz} \frac{\left|\tilde{R}_{g\,h}\right|}{R_{g\,real}} \quad CS\, L_g = \sum_{h\neq 0}^{100\,Hz} \frac{\left|\tilde{L}_{g\,h}\right|}{L_{g\,real}} \tag{4.16}$$

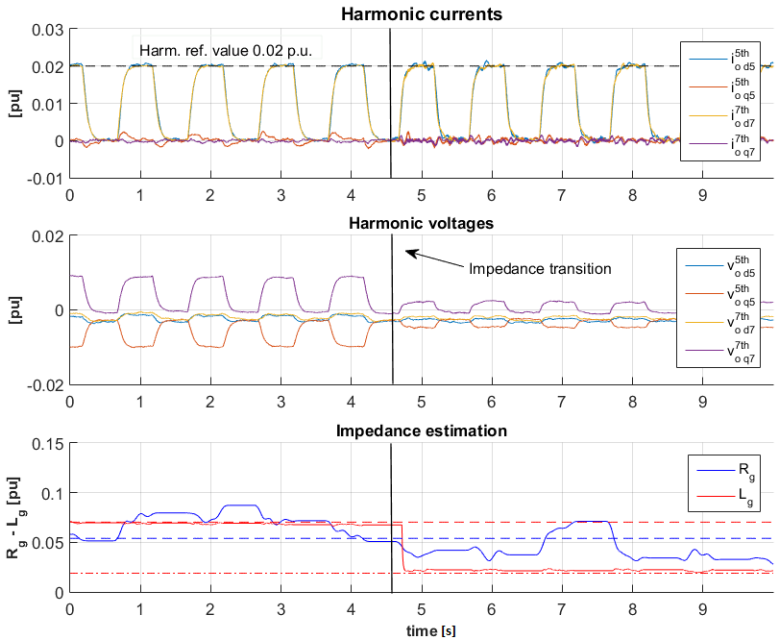

FIGURE 4.13: Time profile of the reconstructed values under step changes of the interface inductance. It is possible to see that the reconstruction of the resistance is heavily affected by slow oscillating components that compromise the effectiveness of the reconstruction.

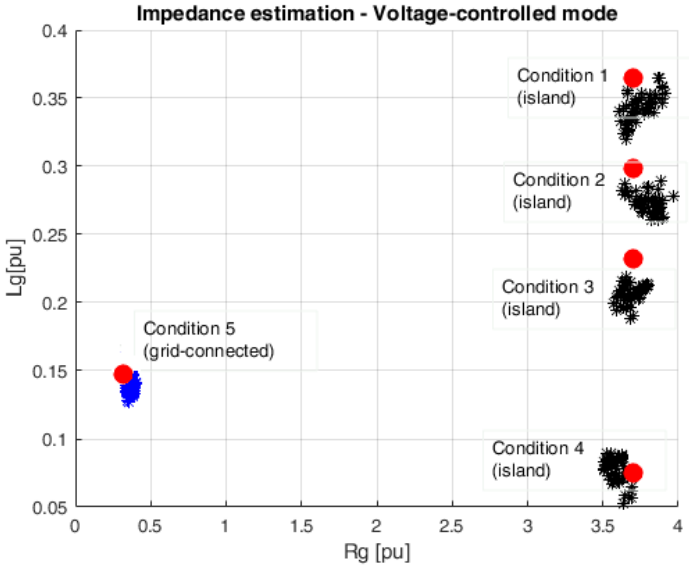

FIGURE 4.14: Equivalent system impedance estimation in island (conditions 1-4) or with a single converter operated in grid-connected mode (condition 5). On-line estimated values (asterisks) are compared to the ones obtained from off-line characterization of the system (dots).

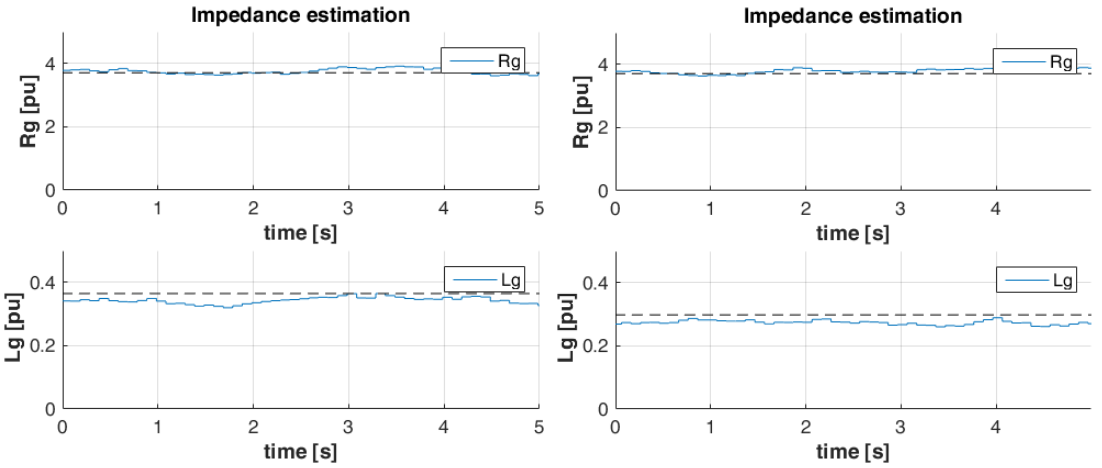

(a) Condition 1 (Island mode)

(b) Condition 2 (Island mode)

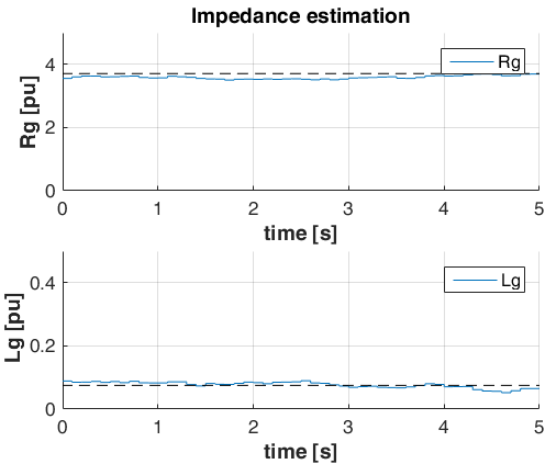

(c) Condition 4 (Island mode)

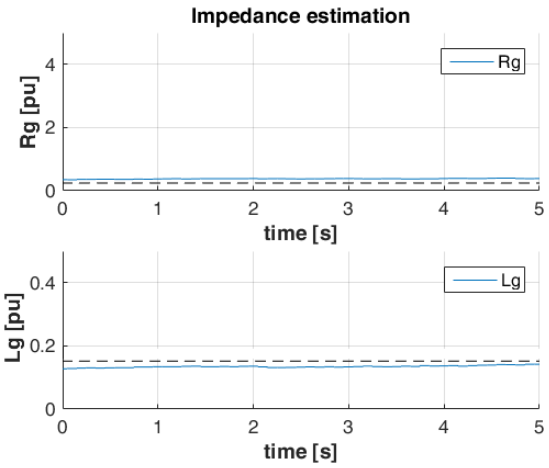

(d) Condition 5 (Grid-connected mode)

FIGURE 4.15: Time profile of the impedance estimation with voltage controlled mode. A low harmonic disturbance can be noticed on the estimation.

The spectral profile in Fig.4.11 is taken into account for what concerns the current-controlled approach, while the spectral profile in Fig.4.16 (associated to the time-behaviour in Fig.4.15-(d)) is used as a benchmark for the voltage-oriented architecture; the numerical comparison is carried out in Table 4.1. According to the definition of the performance indexes, lower values stand for more precise and robust estimations. As a general consideration, the voltage estimator shows better global performances both as regards the absolute error and the cumulative sum of the transitory spectral components: the simpler control scheme that characterizes this architecture enables a better coordination of the internal controllers pass-bands and a higher dynamical decoupling between the different control sub-functions. The limited number of loops for the voltage-oriented scheme (Fig.4.3(b)), compared to the current-oriented one (Fig.4.4(b)), significantly simplifies the algorithm design and enhances its dynamical performances.

The major negative aspect of the voltage-oriented architecture regards the impossibility to guarantee, a priori, the control of the maximum value of the harmonic current injection. At the current state, the technical standards typically used for the definition of the maximum allowed disturbance from power converters present different approaches and thus it is difficult to assess the predominance of one method over the other: the

TABLE 4.1: Comparison of the impedance estimation techniques

Performance index	Voltage-controlled est.	Current-controlled est.
$\epsilon\, R_g$	4.3%	22%
$\epsilon\, L_g$	5.2%	2.6%
$CS\, R_g$	1.3	1.8
$CS\, L_g$	1.1	1.3

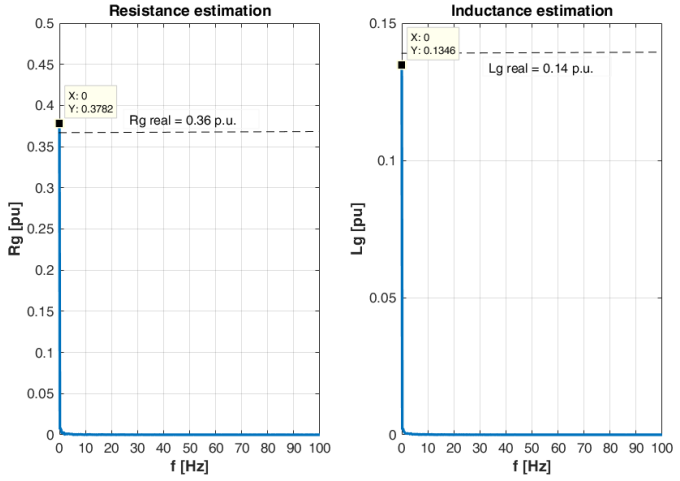

FIGURE 4.16: Spectral evaluation of voltage-controlled impedance estimation; values refer to the time profile reported in Fig.4.15-(d).

updated version of the IEEE-519 [63] defines maximum harmonic values for the injected currents (thus pushing towards techniques in which the disturbance acceptability is evaluated in terms of current harmonics), while most of the European norms and grid standards (e.g. [64]) express the admissible limits in terms of maximum harmonic voltages at the interface. In this sense, the normative harmonization process will determine the technical evolution of these techniques.

4.7 Conclusion

In this section of the thesis the problem of impedance estimation has been tackled; two simple methods have been developed and tested, while their characteristic features have been compared to the existing literature on the topic. Both proposed algorithms do not require spectrum calculation and they are useful for the impedance reconstruction in a limited frequency range. Even though these procedures do not configure as a substitute to wide-bandwidth impedance characterizations, still they can represent good alternatives to provide synthetic input values to adaptive schemes in grid-connected converters. Moreover, the possibility to exploit natural harmonics of the grid allows to reduce the disturbance produced by the method on the rest of the network.

Clearly the exploitation of a modulating disturbance to reconstruct the system behaviour is at the base of any identification technique and it is not a novelty: still it is important to design both the control and the reconstruction algorithm to guarantee sufficient precision in the estimation and limited impact on the rest of the system. The proposed algorithms have been designed under these constraints: the exploitation of

natural system harmonics and the small disturbance value guarantee a limited impact for the rest of the system, while the differential structure and the inversion algorithm coordination with the converter control allow a sufficient precision in the reconstruction.

References - part I

[1] J. W. Simpson-Porco, F. Dörfler, and F. Bullo, "Voltage stabilization in microgrids via quadratic droop control," *IEEE Transactions on Automatic Control*, vol. 62, pp. 1239–1253, March 2017.

[2] B. Gentile, J. W. Simpson-Porco, F. Dörfler, S. Zampieri, and F. Bullo, "On reactive power flow and voltage stability in microgrids," in *2014 American Control Conference*, pp. 759–764, June 2014.

[3] J. W. Simpson-Porco, F. Dörfler, F. Bullo, Q. Shafiee, and J. M. Guerrero, "Stability, power sharing, and distributed secondary control in droop-controlled microgrids," in *2013 IEEE International Conference on Smart Grid Communications (SmartGridComm)*, pp. 672–677, Oct 2013.

[4] G. Lou, W. Gu, L. Wang, B. Xu, M. Wu, and W. Sheng, "Decentralised secondary voltage and frequency control scheme for islanded microgrid based on adaptive state estimator," *IET Generation, Transmission Distribution*, vol. 11, no. 15, pp. 3683–3693, 2017.

[5] J. M. Guerrero, J. C. Vasquez, J. Matas, L. G. de Vicuna, and M. Castilla, "Hierarchical control of droop-controlled ac and dc microgrids—a general approach toward standardization," *IEEE Transactions on Industrial Electronics*, vol. 58, pp. 158–172, Jan 2011.

[6] Y. Sun, X. Hou, J. Yang, H. Han, M. Su, and J. M. Guerrero, "New perspectives on droop control in ac microgrid," *IEEE Transactions on Industrial Electronics*, vol. 64, pp. 5741–5745, July 2017.

[7] J. Rocabert, A. Luna, F. Blaabjerg, and P. Rodríguez, "Control of power converters in ac microgrids," *IEEE Transactions on Power Electronics*, vol. 27, pp. 4734–4749, Nov 2012.

[8] J. M. Guerrero, J. C. Vasquez, J. Matas, M. Castilla, and L. G. de Vicuna, "Control strategy for flexible microgrid based on parallel line-interactive ups systems," *IEEE Transactions on Industrial Electronics*, vol. 56, pp. 726–736, March 2009.

[9] Terna, *"Allegato A15 - Partecipazione alla Regolazione di Frequenza e Frequenza-Potenza" (Italian grid code).* Available at: www.terna.it, 2008. Attachment to the Italian grid code.

[10] ENTSO-E, *"Establishing a network code on requirements for grid connection of generators".* Official Journal of the European Union, 2016. approved by European Commission, decree 2016 / 361.

[11] M. Liserre, F. Blaabjerg, and S. Hansen, "Design and control of an lcl-filter-based three-phase active rectifier," *IEEE Transactions on Industry Applications*, vol. 41, pp. 1281–1291, Sept 2005.

[12] Y. A. I. Mohamed and E. F. El-Saadany, "Adaptive decentralized droop controller to preserve power sharing stability of paralleled inverters in distributed generation microgrids," *IEEE Transactions on Power Electronics*, vol. 23, pp. 2806–2816, Nov 2008.

[13] J. M. Guerrero, J. Matas, L. G. D. V. D. Vicuna, M. Castilla, and J. Miret, "Wireless-control strategy for parallel operation of distributed-generation inverters," *IEEE Transactions on Industrial Electronics*, vol. 53, pp. 1461–1470, Oct 2006.

[14] F. Iliceto, *Impianti elettrici.* Patron Editore, 1981.

[15] N. Faletti and P. Chizzolini, *Trasmissione e distribuzione dell'energia elettrica (parte I e part II).* Patron Editore, 1987.

[16] G. Foglia, L. Frosio, M. Iacchetti, and R. Perini, ""Control loops design in a grid-supporting mode inverter connected to a Microgrid"," in *17th European Conf. on Power Electronics and Applications (EPE 2015), issue 540*, (Geneve (Switzerland)), Sept. 2015.

[17] J. Sun, "Small-signal methods for ac distributed power systems–a review," *IEEE Transactions on Power Electronics*, vol. 24, pp. 2545–2554, Nov 2009.

[18] L. Harnefors, "Modeling of three-phase dynamic systems using complex transfer functions and transfer matrices," *IEEE Transactions on Industrial Electronics*, vol. 54, pp. 2239–2248, Aug 2007.

[19] S. Gataric and N. R. Garrigan, "Modeling and design of three-phase systems using complex transfer functions," in *30th Annual IEEE Power Electronics Specialists Conference. Record. (Cat. No.99CH36321)*, vol. 2, pp. 691–697 vol.2, July 1999.

[20] M. Cespedes and J. Sun, "Impedance modeling and analysis of grid-connected voltage-source converters," *IEEE Transactions on Power Electronics*, vol. 29, pp. 1254–1261, March 2014.

[21] M. Cespedes and J. Sun, "Renewable energy systems instability involving grid-parallel inverters," in *2009 Twenty-Fourth Annual IEEE Applied Power Electronics Conference and Exposition*, pp. 1971–1977, Feb 2009.

[22] X. Wang, L. Harnefors, and F. Blaabjerg, "Unified impedance model of grid-connected voltage-source converters," *IEEE Transactions on Power Electronics*, vol. 33, pp. 1775–1787, Feb 2018.

[23] M. K. Bakhshizadeh, X. Wang, F. Blaabjerg, J. Hjerrild, . Kocewiak, C. L. Bak, and B. Hesselbæk, "Couplings in phase domain impedance modeling of grid-connected converters," *IEEE Transactions on Power Electronics*, vol. 31, pp. 6792–6796, Oct 2016.

[24] M. Belkhayat *Ph.D. thesis, Purdue University.*

[25] K. W. Martin, "Complex signal processing is not complex," *IEEE Transactions on Circuits and Systems I: Regular Papers*, vol. 51, pp. 1823–1836, Sept 2004.

[26] R. Teodorescu, F. Blaabjerg, M. Liserre, and P. C. Loh, "Proportional-resonant controllers and filters for grid-connected voltage-source converters," *IEE Proceedings - Electric Power Applications*, vol. 153, pp. 750–762, September 2006.

[27] D. N. Zmood, D. G. Holmes, and G. H. Bode, "Frequency-domain analysis of three-phase linear current regulators," *IEEE Transactions on Industry Applications*, vol. 37, pp. 601–610, March 2001.

[28] X. Wang, F. Blaabjerg, and M. Liserre, "An active damper to suppress multiple resonances with unknown frequencies," in *2014 IEEE Applied Power Electronics Conference and Exposition - APEC 2014*, pp. 2184–2191, March 2014.

[29] A. Bolzoni, G. M. Foglia, L. Frosio, M. F. Iacchetti, and R. Perini, "Impact of line and control parameters on droop stability in inverters for distributed generation," *IEEE Transactions on Smart Grid*, pp. 1–1, 2018.

[30] P. Kundur, *"Power system stability and control".* Mc. Graw Hill, 1993.

[31] E. A. A. Coelho, P. C. Cortizo, and P. F. D. Garcia, "Small-signal stability for parallel-connected inverters in stand-alone ac supply systems," *IEEE Transactions*

on Industry Applications, vol. 38, pp. 533–542, March 2002.

[32] R. Majumder, G. Ledwich, A. Ghosh, S. Chakrabarti, and F. Zare, "Droop control of converter-interfaced microsources in rural distributed generation," *IEEE Transactions on Power Delivery*, vol. 25, pp. 2768–2778, Oct 2010.

[33] J. M. Guerrero, L. G. de Vicuna, J. Matas, M. Castilla, and J. Miret, "Output impedance design of parallel-connected ups inverters with wireless load-sharing control," *IEEE Transactions on Industrial Electronics*, vol. 52, pp. 1126–1135, Aug 2005.

[34] A. Micallef, M. Apap, C. Spiteri-Staines, and J. M. Guerrero, "Performance comparison for virtual impedance techniques used in droop controlled islanded microgrids," in *2016 International Symposium on Power Electronics, Electrical Drives, Automation and Motion (SPEEDAM)*, pp. 695–700, June 2016.

[35] X. Wang, Y. W. Li, F. Blaabjerg, and P. C. Loh, "Virtual-impedance-based control for voltage-source and current-source converters," *IEEE Transactions on Power Electronics*, vol. 30, pp. 7019–7037, Dec 2015.

[36] M. Gao, M. Chen, C. Wang, and Z. Qian, "An accurate power-sharing control method based on circulating-current power phasor model in voltage-source inverter parallel-operation system," *IEEE Transactions on Power Electronics*, vol. 33, pp. 4458–4476, May 2018.

[37] Y. Karimi, H. Oraee, and J. M. Guerrero, "Decentralized method for load sharing and power management in a hybrid single/three-phase-islanded microgrid consisting of hybrid source pv/battery units," *IEEE Transactions on Power Electronics*, vol. 32, pp. 6135–6144, Aug 2017.

[38] C. Blanco, D. Reigosa, J. C. Vasquez, J. M. Guerrero, and F. Briz, "Virtual admittance loop for voltage harmonic compensation in microgrids," *IEEE Transactions on Industry Applications*, vol. 52, pp. 3348–3356, July 2016.

[39] A. Micallef, M. Apap, C. Spiteri-Staines, J. M. Guerrero, and J. C. Vasquez, "Reactive power sharing and voltage harmonic distortion compensation of droop controlled single phase islanded microgrids," *IEEE Transactions on Smart Grid*, vol. 5, pp. 1149–1158, May 2014.

[40] J. He and Y. W. Li, "Analysis, design, and implementation of virtual impedance for power electronics interfaced distributed generation," *IEEE Transactions on Industry Applications*, vol. 47, pp. 2525–2538, Nov 2011.

[41] H. Mahmood, D. Michaelson, and J. Jiang, "Accurate reactive power sharing in an islanded microgrid using adaptive virtual impedances," *IEEE Transactions on Power Electronics*, vol. 30, pp. 1605–1617, March 2015.

[42] T. V. Hoang and H. Lee, "An adaptive virtual impedance control scheme to eliminate the reactive-power-sharing errors in an islanding meshed microgrid," *IEEE Journal of Emerging and Selected Topics in Power Electronics*, vol. 6, pp. 966–976, June 2018.

[43] A. Bolzoni, R. Perini, and L. Frosio, "A stability-oriented design method for virtual impedance loop in droop-controlled converters," in *2017 IEEE International Conference on Environment and Electrical Engineering and 2017 IEEE Industrial and Commercial Power Systems Europe (EEEIC / I CPS Europe)*, pp. 1–6, June 2017.

[44] P. Bolzern, R. Scattolini, and N. Schiavoni, *"Fondamenti di controlli automatici"*. McGraw-Hill, 2008.

[45] S. V. Iyer, M. N. Belur, and M. C. Chandorkar, "Analysis and mitigation of voltage offsets in multi-inverter microgrids," *IEEE Transactions on Energy Conversion*, vol. 26, pp. 354–363, March 2011.

[46] A. Robert, T. Deflandre, E. Gunther, R. Bergeron, A. Emanuel, A. Ferrante, G. S. Finlay, R. Gretsch, A. Guarini, J. L. G. Iglesias, D. Hartmann, M. Lahtinen, R. Marshall, K. Oonishi, C. Pincella, S. Poulsen, P. Ribeiro, M. Samotyj, K. Sand, J. Smid, P. Wright, and Y. S. Zhelesko, "Guide for assessing the network harmonic impedance," in *14th International Conference and Exhibition on Electricity Distribution. Part 1. Contributions (IEE Conf. Publ. No. 438)*, vol. 2, pp. 3/1–310 vol.2, June 1997.

[47] L. S. Czarnecki and Z. Staroszczyk, "On-line measurement of equivalent parameters of distribution system and its load for harmonic frequencies," in *Proceedings of 1995 IEEE Instrumentation and Measurement Technology Conference - IMTC '95*, pp. 692–, April 1995.

[48] A. V. Timbus, R. Teodorescu, and P. Rodriguez, "Grid impedance identification based on active power variations and grid voltage control," in *2007 IEEE Industry Applications Annual Meeting*, pp. 949–954, Sept 2007.

[49] M. Ciobotaru, V. Agelidis, and R. Teodorescu, "Line impedance estimation using model based identification technique," in *Proceedings of the 2011 14th European Conference on Power Electronics and Applications*, pp. 1–9, Aug 2011.

[50] N. Hoffmann and F. W. Fuchs, "Minimal invasive equivalent grid impedance estimation in inductive–resistive power networks using extended kalman filter," *IEEE Transactions on Power Electronics*, vol. 29, pp. 631–641, Feb 2014.

[51] A. Bagheri, M. Mardaneh, A. Rajaei, and A. Rahideh, "Detection of grid voltage fundamental and harmonic components using kalman filter and generalized averaging method," *IEEE Transactions on Power Electronics*, vol. 31, pp. 1064–1073, Feb 2016.

[52] S. Sanchez and M. Molinas, "Large signal stability analysis at the common coupling point of a dc microgrid: A grid impedance estimation approach based on a recursive method," *IEEE Transactions on Energy Conversion*, vol. 30, pp. 122–131, March 2015.

[53] P. García, J. M. Guerrero, J. García, . Navarro-Rodríguez, and M. Sumner, "Low frequency signal injection for grid impedance estimation in three phase systems," in *2014 IEEE Energy Conversion Congress and Exposition (ECCE)*, pp. 1542–1549, Sept 2014.

[54] M. A. Azzouz and E. F. El-Saadany, "Multivariable grid admittance identification for impedance stabilization of active distribution networks," *IEEE Transactions on Smart Grid*, vol. 8, pp. 1116–1128, May 2017.

[55] M. Céspedes and J. Sun, "Online grid impedance identification for adaptive control of grid-connected inverters," in *2012 IEEE Energy Conversion Congress and Exposition (ECCE)*, pp. 914–921, Sept 2012.

[56] M. Cespedes and J. Sun, "Adaptive control of grid-connected inverters based on online grid impedance measurements," *IEEE Transactions on Sustainable Energy*, vol. 5, pp. 516–523, April 2014.

[57] M. Sumner, B. Palethorpe, and D. W. P. Thomas, "Impedance measurement for improved power quality-part 1: the measurement technique," *IEEE Transactions on Power Delivery*, vol. 19, pp. 1442–1448, July 2004.

[58] M. Sumner, B. Palethorpe, and D. W. P. Thomas, "Impedance measurement for improved power quality-part 2: a new technique for stand-alone active shunt filter control," *IEEE Transactions on Power Delivery*, vol. 19, pp. 1457–1463, July 2004.

[59] M. Ciobotaru, R. Teodorescu, and F. Blaabjerg, "On-line grid impedance estimation based on harmonic injection for grid-connected pv inverter," in *2007 IEEE International Symposium on Industrial Electronics*, pp. 2437–2442, June 2007.

[60] L. Asiminoaei, R. Teodorescu, F. Blaabjerg, and U. Borup, "A digital controlled pv-inverter with grid impedance estimation for ens detection," *IEEE Transactions on Power Electronics*, vol. 20, pp. 1480–1490, Nov 2005.

[61] J. Xia, Y. Guo, and X. Zhang, "Online grid inductance estimation for electric traction pwm rectifier based on dual-frequency harmonic current injection," in *IECON 2017 - 43rd Annual Conference of the IEEE Industrial Electronics Society*, pp. 1347–1352, Oct 2017.

[62] A. G. Yepes, F. D. Freijedo, J. Doval-Gandoy, . López, J. Malvar, and P. Fernandez-Comesaña, "Effects of discretization methods on the performance of resonant controllers," *IEEE Transactions on Power Electronics*, vol. 25, pp. 1692–1712, July 2010.

[63] "Ieee recommended practice and requirements for harmonic control in electric power systems," *IEEE Std 519-2014 (Revision of IEEE Std 519-1992)*, pp. 1–29, June 2014.

[64] Comitato Elettrotecnico Italiano CEI, *"Reference technical rules for the connection of active and passive consumers to the HV and MV electrical networks of distribution company", CEI 0-16*, 2016. Attachment to the Italian grid code.

Part II

Frequency transients improvement by means of non-dispatchable units: inertia emulation.

Introduction to part II

In this part of the thesis, the problem of frequency transients in a microgrid is analysed . Even though for traditional power systems the balance between generated and absorbed power is guaranteed by the high regulation energy availability, in microgrids generally the margins are significantly reduced and it is necessary to understand if a transitory power unbalance can be withstood or, on the contrary, may lead to unacceptable operating conditions. The mathematical and experimental analysis will show that the typical case may be the last one: even though the theoretical steady-state power balance may be easily guaranteed by the primary regulation performed on the system, still the amplitude of frequency transients can lead to the intervention of protections and, thus, to the microgrid shut-down.

In order to avoid this undesired situation, it is considered the possibility to heal frequency transients by means of a smarter management of the un-dispatchable units connected to the system: this approach goes under the name of *synthetic inertia*. Synthetic inertia [1] consists in a derivative active power support from non-dispatchable PQ units connected to small microgrids networks with weak regulation availability. The proposed schemes allow to reduces frequency transients excursion during the initial instants after the event, enabling the emulation of inertial physical behaviour by means of the interface converters.

In the next chapters it will be shown the conceptual development of the control technique and the aspects related to experimental implementation: starting from the definition of typical case studies, it will be derived a mathematical model able to describe the physical behaviour of the system and it will be shown how the introduction of inertia control can significantly improve the system performances during transitory unbalances between load and production. Different inertia emulation schemes will be taken into account and compared. Moreover, it will be also taken into account the issue of angular quantities estimation under disturbed network conditions.

Chapter 5

System definition and case studies for synthetic inertia

5.1 Introduction

This chapter will introduce the case studies and the foundational theoretical principles associated to the provision of inertia support in weak grids. Starting from the typical control structure of a grid-following converter, two different inertia schemes will be introduced and lately analysed in the next chapters. A common design frame able to keep into account both the case of a network with fast primary regulation, obtained by static converters equipped with droop control, and the one with traditional generators will be taken into considered.

5.2 Nomenclature

- T_a: external grid starting time [s];
- K_{reg}: regulating energy of the external grid primary frequency regulation [pu];
- τ: external grid internal regulation delay [s];
- θ, ω: angle and per-unit angular frequency of the voltage $\bar{v}_o$ at the coupling point;
- $\tilde{\theta}$, $\tilde{\omega}$: angle and per-unit angular frequency as estimated by the phase-locked loop (PLL);
- ω_{FLL}: per unit angular frequency as estimated by the frequency-locked loop (FLL) [pu];
- α_{FLL}: per unit angular frequency derivative as estimated by the frequency-locked loop (FLL) [pu/s];
- τ_{FLL}: time constant associated to the FLL estimation [s];

5.3 State of the art for synthetic inertia control

The concept of the synthetic inertia is a trending topic in power engineering and power electronics research. From a normative perspective, ENTSO-E [1] identifies the need of new regulation paradigms for modern power systems with a significant penetration of electronically-interfaced units. The goal of this analysis is to identify some control schemes able to increase the system robustness by providing regulation support to the network during the natural variability of the generation and load.

A preliminary analysis has identified the droop control as the best available technique to provide transitory and steady-state regulation to power systems and microgrids. The positive impact of droop regulation on network transients is well documented in literature [2]; nonetheless, this regulation scheme requires a constant DC voltage source and thus it is not always applicable to distributed resources.

Several researchers have analysed the possibility to provide regulation services from non-dispatchable units acting on the operating point of the distributed resource, even though energetic constrains have to be taken into account. Some authors proposed to keep a regulation margin with respect to the maximum production [3]-[4]: this approach requires an on-line estimation of the theoretical available power, which may be somehow critical [5]. A second approach, also implemented in most of the grid standards [6], proposes a non-symmetrical regulation for increasing and decreasing angular frequency transients [7]-[8]: the drawback of these architectures is the inherent sensitivity of the regulation characteristics with respect to the disturbance sign.

In this perspective, synthetic inertia seems to be a good regulation scheme to provide additional damping to frequency transients [9]. The technique consists in the emulation of the dynamical characteristic of a rotating mass in the converter control and requires an energy buffer to be used during transitory regulation: nonetheless, its derivative nature allows the complete recovery of the energy buffer at the end of the transient.

The first example of synthetic inertia application has been introduced in [10] for wind power systems, where it is possible to exploit both the natural kinetic energy of the turbine or a local energetic buffer realised by means of a supercapacitors. A similar approach is proposed in [11], even thought in this case the inertia regulation is a consequence of the design of the converter synchronization system.

In [12]-[13] and [14], the inertia provision by means of HVDC systems is analysed, while in [15] large-scale capacitors are considered. Nevertheless, in all these cases, a complete and comprehensive state-space model of the converter under inertia support is not developed and the identification of stability conditions is performed on a simulated numerical base.

First experimental tests of the inertia control have been developed only recently [16]-[17], even though the dynamical model that determines the stability properties of the service provision is not identified and the characterization of the angular quantities estimation under disturbed network conditions is not taken into account.

In the next chapters, the dynamical model of a power converter under inertia regulation is developed and validated: this will be used to identify stability conditions for the synthetic inertia parameters depending on the characteristics of the external network. Furthermore, the proposed control strategies will be experimentally tested, with a focus on angular quantities reconstruction under disturbed network conditions.

5.4 Case study definition

Consider two layouts reported in Fig.5.1. These architectures comprise:

- some non-dispatchable production units (e.g. photovoltaic generators) or loads, whose power injection/absorption is typically independent of the external condition of the microgrid;
- a certain number of dispatchable units, able to provide regulation services to the grid during island operations by means of primary regulation.

In this chapter, the focus is on the control scheme of the non-dispatchable unit (PQ architecture), when equipped with inertia provision schemes. Nevertheless, the dynamical characterization of the grid-following system is influenced by the dispatchable unit

that is actually performing primary frequency regulation on the network, thus the first step is to identify the analysis case studies from the identification of dispatchable unit configuration.

Depending on their nature, dispatchable units may be interfaced to the system by means of power electronic converters (e.g storage) or traditional machines (e.g. diesel generators or micro-turbines). Extreme cases reported in Fig. 5.1(a) and 5.1(b), in which the regulation service is provided by a single typology of unit, are identified. The goal associated to case studies definition is the following: determine a common and rigorous mathematical model of the system able to predict frequency transients characteristics under a certain power imbalance caused by the connection/disconnection of a local load or by the transition from grid-connected to island mode. To do so, characteristic values associated to the primary frequency regulation for the schemes in Fig.5.1(a) and 5.1(b) are reported in Table 5.1 and 5.2 respectively. The same PQ unit has been considered in the two case studies, whose values are reported in Table 5.3.

Values in Table 5.1-5.2-5.3 have been determined from physical and mathematical considerations on the problem.

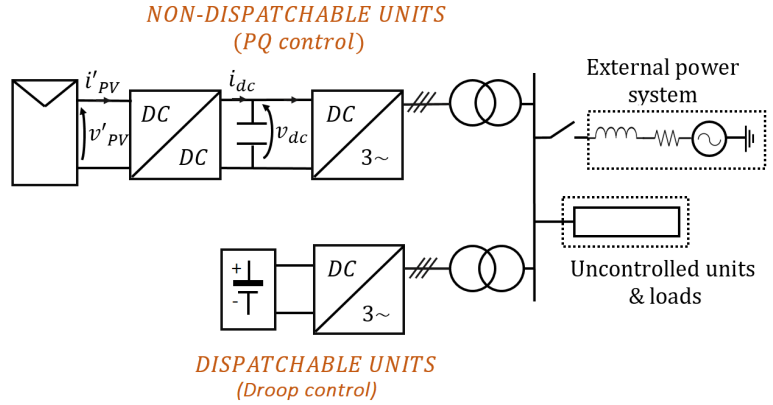

(a)

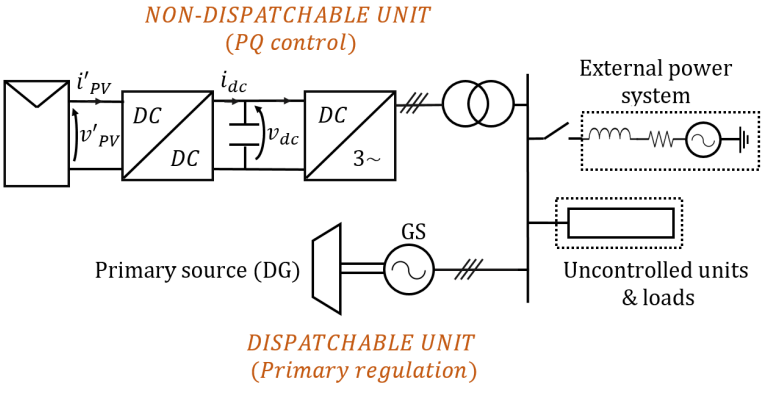

(b)

FIGURE 5.1: Typical layouts used for the analysis of frequency transients in low-inertia systems. Case (a) corresponds to a microgrid in which all the production is interfaced by means of electronic converters, while in case (b) it is considered the presence of regulation units interfaced to the system by means of physical inertias (e.g. synchronous generators).

TABLE 5.1: Parameters for CASE STUDY 1 of the synthetic inertia analysis

Droop-controlled converter		
Parameter	*Symbol*	*Numeric value*
Nominal power	A_1	2.4 kVA
Active droop coefficient	m	0.020 per-unit
Droop time constant	T_p	0.20 s
Internal voltage regulation time constant	$\tau_{\text{droop}} = \omega_{cV}^{-1}$	3.2 ms

TABLE 5.2: Parameters for CASE STUDY 2 of the synthetic inertia analysis

Traditional regulation unit		
Parameter	*Symbol*	*Numeric value*
Nominal power	A_1	2.4 kVA
Starting time	T_a	10 s
Regulating energy	K_{reg}	50 p.u.
Time constant of the internal regulation delay	τ	500 ms

TABLE 5.3: Parameters for PQ converter, common to CASE STUDY 1 and CASE STUDY 2

PQ unit		
Parameter	*Symbol*	*Numeric value*
Base system (voltage, ang. frequency, power)	V_b, ω_b, A_b	200 V, $2\pi \cdot 50$ rad/s , 2.4 kVA
Nominal power	A_1	2.4 kVA
Current and DC voltage loops cut-off ang. frequencies	ω_{cI}, $\omega_{c\,dc}$	$2\pi \cdot 350$ rad/s, $2\pi \cdot 2.5$ rad/s
FLL time constant	τ_{FLL}	80^{-1} s

- Base voltage and design power for the PQ unit have been determined from the available experimental microgrid setup.
- Droop parameters m and T_p in Table 5.1 have been chosen such as to provide a tinier regulation on the grid with respect to the ones presented in Part I ($m = 0.01$ p.u. and $T_p = 0.1$ s), to better highlight the effect of frequency support from the PQ unit under synthetic inertia control.
- The time constant of the internal droop delay τ_{droop} in Table 5.1 is the inverse of the AC voltage cut-off frequency regulation loop ω_{cV}, according to the Table 2.1 in Part I.
- Regulating energy K_{reg} in Table 5.2 is the one required by code standards for dispatchable units [18].
- Starting time T_a is independent of the physical nature of the primary source: referring to [19] - [20] - [21], it ranges between $T_a \cong 6 \div 12$ s; in the case study, it was chosen $T_a = 10$ s.
- The equivalent time constant of the primary regulation delay τ derives from the internal dynamics related to the insensitivity of the frequency controller. It is considered the maximum delay associated to the intervention of primary regulation, around 500 ms, even though this value may be subject to a significant variability

depending on the nature of the installed measurement apparatus.

The adopted methodology has followed the conceptual steps reported in the list below.

1. A common analytical model able to contemporaneously take into account the primary regulation performed by the static units (as in Fig. 5.1(b)) and the traditional ones (Fig. 5.1(a)) will be developed.
2. A detailed characterization for the PQ converter is introduced, which allows a rigorous design of its control parameters.
3. Combining the models associated to regulation unit and the PQ one, a design frame for synthetic inertia is carried out: two applicable schemes will be considered, respectively acting of different loops inside the converter control.

The circuit in Fig. 5.2 is a common representation of the physical systems in Fig.5.1(b) and 5.1(a). Neglecting the parasitic losses, the network instantaneous power balance gives:

$$p_g + p_{out} + p_{conv} = 0 \tag{5.1}$$

where

- p_g represents the independent accelerating power of the system;
- p_{out} is the instantaneous contribution from the regulation units and physical inertias of the system;
- p_{conv} is the power injected by grid-following converters, which is typically independent of the external state of the system, except when synthetic inertia is added.

If we refer to the differential model, (5.1) evolves in (5.2), where:

- Δp_g is the variation of load absorption ($\Delta p_g < 0$ active load increase, $\Delta p_g > 0$ active load decrease);
- Δp_{out} is the contribution from physical inertias in the system and from primary regulation;
- Δp_{conv} is the contribution from non-dispatchable units. If the converter is controlled in grid-following mode $\Delta p_{conv} = 0$; if synthetic inertia is added, it becomes $\Delta p_{conv} \neq 0$.

$$\Delta p_g + \Delta p_{out} + \Delta p_{conv} = 0 \tag{5.2}$$

In this chapter, the base case without synthetic inertia is taken into account ($\Delta p_{conv} = 0$). The first aspect regards the contribution of regulating units under load changes.

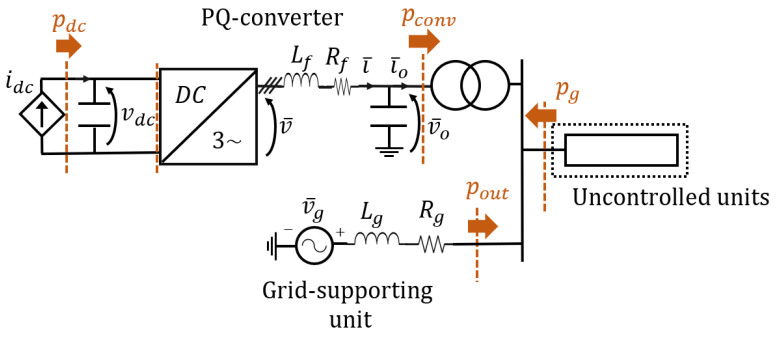

FIGURE 5.2: Equivalent circuit used for frequency transients analysis.

5.5 Regulating units contribution

In this section, a common model of the grid-supporting unit able to keep into account both the case of traditional generation and static converter is developed. The aim is to derive a formal equivalence between droop control and primary frequency regulation and analyse the different configurations by means of the same mathematical scheme. Even though it is intuitive to underline a common behaviour of the two structures, still it is interesting to derive an analytical parallelism between the two cases.

5.5.1 System regulation performed by traditional units

Consider the physical conditions reported in Fig. 5.1(b) and the circuit in Fig.5.2. No synthetic inertia is provided from the PQ unit ($\Delta p_{conv} = 0$).

Under a change of the local load $\Delta p_g \neq 0$, the system angular frequency undergoes a transient and the grid-supporting unit changes its output Δp_{out} according to two effects:

- the kinetic energy variation from physical inertias in the system;
- the stabilizing effect provided by the primary frequency regulation.

$$\Delta p_{out} = \Delta p_{inertia} + \Delta p_{reg} \tag{5.3}$$

The inertias effect can be considered referring to the swing equation [22], which models the linearised behaviour associated to the kinetic energy derivative: an angular frequency change $\Delta\omega$ [p.u.] on the external system produces a variation of the injected power $\Delta p_{inertia}$ [p.u.] according to:

$$\Delta p_{inertia} \cdot A_b = \Delta p \left[\frac{1}{2} J \cdot \left(\frac{\omega_g \omega_b}{n} \right)^2 \right] = -\frac{J \omega_b^2}{n^2} \omega^0 p \Delta\omega \tag{5.4}$$

where:

- J is the total moment of inertia associated to the system in [kg m^2];
- ω is the per-unit angular frequency in electrical degrees;
- n is the number of pole-pairs of the equivalent machine.

Assuming that the system was operating in nominal conditions before the transient occurrence ($\omega^0 \simeq 1$) and defining the equivalent starting time of the system as $T_a = \frac{J\,\omega_b^2}{n^2\,A_b}$, equation (5.4) becomes (5.5). As the dynamic is linear, Laplace variable s is considered.

$$\Delta p_{inertia} = -T_a \cdot s\,\Delta\omega \quad \text{where} \quad T_a = \frac{J\,\omega_b^2}{n^2\,A_b} \tag{5.5}$$

The inertia contribution $\Delta p_{inertia}$ is positive when $\Delta\omega$ is negative, that is the machine injects power into the grid when the angular frequency reduces, as the kinetic energy of the rotating mass decreases.

As regards primary regulation, it tends to compensate angular frequency dynamics on the system injecting a differential power Δp_{reg} according to a negative proportional law, whose input corresponds to the angular frequency variation $\Delta\omega$; moreover the physical modulation of the injected power from primary source happens only after a delay associated to the internal plant dynamics. This effect can be taken into account with the equivalent time constant τ. Thus the primary regulation effect can be expressed

by (5.6) and (5.7) for time and Laplace domains respectively.

$$\Delta p_{reg} = -K_{reg} \cdot \Delta\omega(t-\tau) \tag{5.6}$$
$$\Delta p_{reg} = -K_{reg} \cdot \Delta\omega \cdot e^{-s\tau} \tag{5.7}$$

The first-order asymptotic expression of the delay according to Padè approximations [23] leads to the equivalent transfer function in (5.8).

$$\Delta p_{reg} = -K_{reg} \frac{1}{1+s\tau} \cdot \Delta\omega \tag{5.8}$$

Now it is possible to combine (5.5) and (5.8) in (5.9); substituting the result in (5.2) (always under the condition $\Delta p_{conv} = 0$) leads to the dynamical model reported in Fig. 5.3 and expressed by equation (5.10). The direct branch of the loop takes into account the inertia properties of the network, while the feedback models the primary frequency regulation and its internal delay.

$$\Delta p_{out} = \Delta p_{inertia} + \Delta p_{reg} = \left(-s\,T_a - K_{reg} \cdot \frac{1}{1+s\tau}\right) \cdot \Delta\omega \tag{5.9}$$

as $\Delta p_{out} + \Delta p_g + \Delta p_{conv} = 0$ and $\Delta p_{conv} = 0$:

$$\Delta\omega = -\frac{1+s\,\tau}{s^2\,T_a\,\tau + s\,T_a + K_{reg}} \cdot \Delta p_{out} = \frac{1+s\,\tau}{s^2\,T_a\,\tau + s\,T_a + K_{reg}} \cdot \Delta p_g \tag{5.10}$$

In case the nominal power is different with respect to the base ones, modified grid parameters T'_a and K'_{reg} should be introduced rather than the original; the following typical equivalences hold: $T'_a = T_a \cdot \frac{A_{n1}}{A_b}$ and $K'_{reg} = K_{reg} \cdot \frac{A_{n1}}{A_b}$. This allows to model, from the perspective of the PQ converter, to equivalent dynamics of a generic grid under traditional primary frequency regulation (5.10).

5.5.2 Equivalence of traditional regulation with droop control

Comparing (5.10) with the dynamical behaviour associated to the droop control as reported in Part I, it is possible to determine a formal equivalence between the physical and control parameters included in the two formulations. As recalled in (5.11) for clarity, droop control imposes an angular frequency ω for the three-phase reference voltages proportional to the instantaneous active power p_{out}; droop derivative coefficient

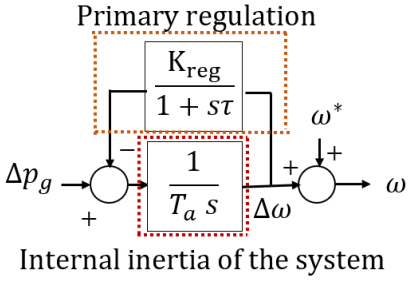

FIGURE 5.3: Dynamical model used for frequency transients in traditional grids. It includes the effect of the system inertia and the primary regulation performed by dispatchable units.

m_d is not considered in this analysis:

$$\omega = \omega^* - \frac{m}{1 + p\,T_p} \cdot p_{out} \tag{5.11}$$

where $m^{-1} = \left(\sum_{i=1}^{N} \frac{1}{m_i}\right)$ and N is the number of units which are performing the regulation. Considering the variations,

$$\Delta\omega = -\frac{m}{1 + p\,T_p} \cdot \Delta p_{out} \tag{5.12}$$

In (5.12) it is also necessary to include the effect associated to the internal delay of the voltage loop inside the converter, which can be roughly approximated as a unitary gain single-pole function with a time constant τ_{droop} equal to the inverse of the voltage control loop cut-off frequency $\tau_{droop} = \omega_{cV}^{-1}$ as designed in Part I. The numerical value is reported in Table 5.1. Thus moving to the Laplace domain, (5.12) becomes (5.14). As in this case we are assuming that the PQ converter is not providing any synthetic inertia contribution ($\Delta p_{conv} = 0$), the introduction of (5.2) in (5.14) leads to (5.15)

$$\Delta\omega = -\frac{1}{1 + s\tau_{\text{droop}}} \cdot \left(\frac{m}{1 + s\,T_p}\right) \cdot \Delta p_{out} \tag{5.13}$$

$$= -\frac{1}{s^2 \frac{T_P\,\tau_{\text{droop}}}{m} + s\frac{\tau_{\text{droop}} + T_p}{m} + \frac{1}{m}} \cdot \Delta p_{out} \tag{5.14}$$

$$\text{as} \quad \Delta p_{out} + \Delta p_g + \Delta p_{conv} = 0 \quad \text{and } \Delta p_{conv} = 0:$$

$$\Delta\omega = \frac{1}{s^2 \frac{T_P\,\tau_{\text{droop}}}{m} + s\frac{\tau_{\text{droop}} + T_p}{m} + \frac{1}{m}} \cdot \Delta p_g \tag{5.15}$$

Pole comparison among (5.10) and (5.15) leads to the following formal equivalence.

$$\begin{cases} \tau = \frac{T_p\,\tau_{\text{droop}}}{T_p + \tau_{\text{droop}}} \\ T_a = \frac{T_p}{m} + \frac{\tau_{\text{droop}}}{m} \\ K_{reg} = \frac{1}{m} \end{cases} \tag{5.16}$$

As the internal delay τ_{droop} is typically significantly smaller than the time constant value T_p, the numerical correspondence of the droop parameters with the traditional regulation model is given by:

$$\begin{cases} \tau = \tau_{\text{droop}} \\ T_a = \frac{T_p}{m} \\ K_{reg} = \frac{1}{m} \end{cases} \tag{5.17}$$

This procedure allows to interpret the droop control as a traditional primary frequency regulation expressed by (5.10), provided that correct numerical values are used. This enables the definition of a uniform design procedure for the synthetic inertia, in which the system is always modelled as in (5.10). Applying (5.17) to the droop parameters reported in Table 5.1, the corresponding grid equivalents can be obtained:

Case study 1

$$\begin{cases} \tau = \tau_{\text{droop}} = 3.2\,ms \\ T_a = \frac{T_p}{m} = 10\,s \\ K_{reg} = \frac{1}{m} = 50\,\text{per-unit} \end{cases} \tag{5.18}$$

5.6 Real control architecture for a photovoltaic scheme

Consider the general regulation schemes for a double-stage conversion photovoltaic unit as reported in Figure 5.4.

In this introductory paragraph, a short description of each part of the control is reported, to provide a general understanding of the analysed structure [24]. Later in the chapter, all the design models used for the sizing of the regulators will be reported in details.

- An external Phase Locked Loop (PLL) acquires a set of uncontrolled three-phase voltages in correspondence to the Point of Common Connection (PCC) with the external grid. The PLL defines the angle θ used for rotating-reference Park transform and allows to maintain the converter-control synchronous with the external grid.
- Linear controllers are used for the regulation of the DC voltage and of the injected active and reactive powers. The DC bus controller generates a reference for the current control, which is able to regulate the active power injection. As concerns the reactive power, the reference signal may be considered an independent input or can be generated from an external reactive-support algorithm (not included in Figure 5.4).
- The system in Figure 5.4 also includes the Maximum Power Point tracking (MPPT) algorithm [25]-[5]. In the double-stage conversion architecture, the MPPT acts on the duty cycle of the intermediate DC-DC unit: this allows the introduction of an additional degree of freedom for the system, as the DC bus voltage reference is not defined by other sub-controls and can be exploited for inertia regulation.

5.7 Non-linear dynamical model of the converter

The goal of this section is to identify the dynamical system associated to the converter when it is interfaced with the external grid by means of the PQ scheme reported in Figure 5.5. The equivalent control structure in Figure 5.5 is independent of the primary

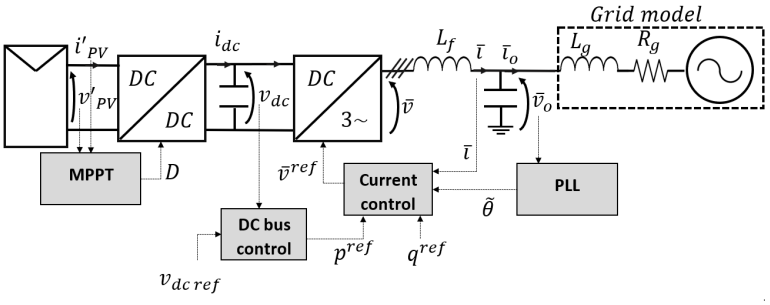

FIGURE 5.4: Functional structure of the control system for double-stage photovoltaic unit. The introduction of an additional degree of freedom decouples the DC bus reference from the MPPT algorithm.

source nature: the definition of the dynamical model allows to determine the correct regulation parameters and identify the characteristic dynamics of the converter. The non-linear reported in Fig. 5.5 can be obtained from the equations associated to the control and to the physical system; it can be subsequently studied resorting to numerical or analytical methods.

Consider the physical layout of the system as reported in Figure 5.6. On the AC side, a typical LCL circuit is introduced to damp switching components introduced by the modulation, similarly to what was already done for the droop control. The DC side is modelled as a controlled current source in parallel to the physical DC bus of the converter: the functional relation between the current source and the actual voltage on the DC bus depends on the nature of the primary source.

Physical equations associated to the structure in Figure 5.6 can be easily obtained from Kirchhoff current and voltage laws, and from the power balance performed on the DC sections. As a notation, all the quantities on the AC side are expressed in the Park domain; all the parameters and state variables are referred in per-unit, except for the time derivative operator p in $[\mathrm{s}^{-1}]$.

The dynamic associated to the DC bus capacitor can be obtained from the power balance in Figure 5.6, assuming absence of losses for the converter:

$$(p_{dc} - Re\left[\bar{v}_{dq} \cdot \bar{i}^{*}_{dq}\right]) \cdot A_b = p\left(\frac{1}{2} C_{dc} \cdot (v_{dc} \cdot V_{b\,dc})^2\right) \tag{5.19}$$

where C_{dc} stands for the physical capacitance on the DC side expressed in [F], v_{dc} is the capacitor voltage in per-unit and $V_{b\,dc}$ is the base voltage for the DC side in

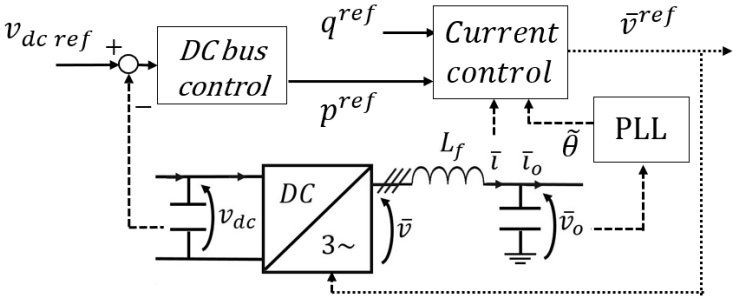

FIGURE 5.5: Simplified block structure of the PQ control, obtained considering the common architecture of the schemes in section 5.6. The regulation is realized with an external DC-bus voltage control and an internal current control; an independent phase-locked loop (PLL) determines the control frame, synchronous with the external grid.

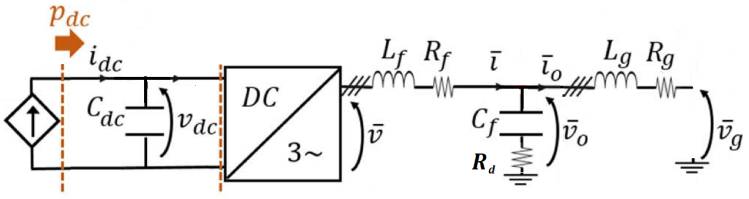

FIGURE 5.6: Equivalent control system associated to the converter, when it is operated in PQ mode. As the DC-bus and the equivalent primary source $i_{dc} = f(v_{dc})$ play a role in the definition of converter dynamics, they have been included in the circuit differently from the case of the droop-controlled unit.

[V]. Additionally, p_{dc} expresses the per-unit power produced by the primary source, referred to the common base power A_b, which determines the charging/discharging of the capacitor. Defining the time constant $\tau_{dc} = C_{dc} \cdot V_{b\,dc}^2 / A_b$, it is possible to derive the non-linear model associated to the DC bus.

$$p_{dc} - Re\left[\bar{v}_{dq} \cdot \bar{i}_{dq}^{*}\right] = \tau_{dc} v_{dc} \cdot p v_{dc} \quad \text{where } \tau_{dc} = C_{dc} \cdot V_{b\,dc}^2 / A_b \tag{5.20}$$

$$p v_{dc} = \frac{1}{\tau_{dc} v_{dc}} \cdot (I_{dc} v_{dc} - (v_d i_d + v_q i_q)) \tag{5.21}$$

The equations associated to the physical AC side circuit can be written referred to a synchronous reference dq, rotating with the angular frequency ω of the external grid, and are formally equivalent to the ones derived for the droop case:

$$\bar{v}_{dq} = R_f \bar{i}_{dq} + \frac{p}{\omega_b} L_f \bar{i}_{dq} + j\omega L_f \bar{i}_{dq} + \bar{v}_{o\,dq} \tag{5.22}$$

$$\bar{v}_{o\,dq} = R_d \cdot (\bar{i}_{dq} - \bar{i}_{o\,dq}) + \frac{\bar{i}_{dq} - \bar{i}_{o\,dq}}{\frac{p}{\omega_b} C_f + j\omega C_f} \tag{5.23}$$

$$\bar{v}_{o\,dq} = R_g \bar{i}_{o\,dq} + \frac{p}{\omega_b} L_g \bar{i}_{o\,dq} + j\omega L_g \bar{i}_{o\,dq} + \bar{v}_{g\,dq} \tag{5.24}$$

Thus:

$$p\bar{i} = \frac{\omega_b}{L_f} \cdot (\bar{v} - \bar{v}_o - j\omega L_f \bar{i} - R_f \bar{i}) \tag{5.25}$$

$$p\bar{i}_o = \frac{\omega_b}{L_g} \cdot (\bar{v}_o - \bar{v}_g - j\omega L_g \bar{i}_o - R_g \bar{i}_o) \tag{5.26}$$

$$p\bar{v}_o = \frac{\omega_b}{C_f} \cdot (-j\omega C_f \bar{v}_o + (1 + j\omega C_f R_d) \cdot (\bar{i} - \bar{i}_o)) + R_d \cdot (p\bar{i} - p\bar{i}_o) \tag{5.27}$$

The control system accepts in input the reference DC bus voltage $v_{dc\,\mathrm{ref}}$ and the injected reactive power reference q^{ref}. Two loops are respectively associated to the control of the constant DC voltage and of the AC side current components. As regards the design of current regulator, it is carried out following the same procedure (Appendix B) adopted for the droop scheme. On the other hand, the characteristics of the DC-voltage controllers will be analysed in Section 5.9, after having identified the linearised characteristics of the dominant system dynamics.

The DC-bus control determines the active power reference p_{dc}^{ref} according to a proportional-integral (or simply proportion) linear regulator, expressed as in (5.28)-(5.29); E_{dc} in (5.28) represents the integral error associated to the PI regulator included in the voltage loop, provided that $k_{i\,dc} \neq 0$.

$$p E_{dc} = (v_{dc\,ref} - v_{dc}) \tag{5.28}$$

$$p_{dc}^{ref} = [k_{p\,dc} \cdot (v_{dc\,ref} - v_{dc}) + k_{i\,dc} \cdot E_{dc}] \tag{5.29}$$

In case no synthetic inertia is included into the system, equation (5.29) defines the active reference power for the internal current control ($p^{ref} = p_{dc}^{ref}$), while the reactive q^{ref} is assumed as an independent input. From the active and reactive desired injections, it is possible to obtain direct and quadrature current references simply dividing by the voltage magnitude $\bar{v}_o$, which in normally close to one.

$$\Delta i_{o\,d}^{ref} = \frac{\Delta p^{ref}}{|\bar{v}_o|} \tag{5.30}$$

$$\Delta i_{o\,q}^{ref} = -\frac{\Delta q^{ref}}{|\bar{v}_o|} \tag{5.31}$$

A feed-forward compensation proportional to the coefficient H_V is introduced in order to compensate the effects associated to the filter capacitor. As it was done for the derivation of the simplified linearised model of the droop control, also here it is possible to neglect the effects of the damping resistor in the design of the feed-forward compensation. Provided that the coefficient H_V is close to one and the filter capacitance C_f is known with a good accuracy, it is possible to control both active and reactive injections into the grid with a reduced number of sensors and with no need to measure the output current $\bar{i}_o$.

In Figure 5.7, it is provided a compact representation of the non-linear system associated to the current and DC-voltage controls.

An interesting point is related to the definition of the reference frame of the control $\tilde{d}\tilde{q}$ and its relationship with the real synchronous frame dq. To formalize the problem mathematically, the dynamic properties of the PLL (which aligns the control frame $\tilde{d}\tilde{q}$ to the synchronous one dq, as shown in Figure 5.8) have to be identified. The first frame, defined by the angle θ, corresponds to the one synchronous with the external grid and aligned to the actual voltage $\bar{v}_o$; the second one corresponds to the control frame created by the PLL algorithm, and it is defined by the angle $\tilde{\theta}$.

The PLL design is reported in Appendix B; still it is possible to evaluate the effect of the double reference frames (dq and $\tilde{d}\tilde{q}$). Consider a the voltage space vector $\bar{v}_{o\,\alpha\beta}$ referred to absolute fixed coordinate system $\alpha\beta$; from the control frame $\tilde{d}\tilde{q}$ perspective, the space vector can be expressed as:

$$\bar{v}_{o\,\tilde{d}\tilde{q}} = \bar{v}_{o\,\alpha\beta} e^{-j\tilde{\theta}} \tag{5.32}$$

while the one associated to the synchronous system dq is:

$$\bar{v}_o = \bar{v}_{o\,\alpha\beta} e^{-j\theta} \tag{5.33}$$

Combining (5.32) with (5.33) leads to (5.34), where $\Delta\theta = \theta - \tilde{\theta}$

$$\bar{v}_{o\,\tilde{d}\tilde{q}} = e^{j\Delta\theta} \cdot \bar{v}_{o\,dq} \tag{5.34}$$

The angular difference $\Delta\theta = \theta - \tilde{\theta}$ is determined by the dynamics of the PLL, which aligns the control frame $\tilde{d}\tilde{q}$ to the synchronous one dq. Considering the PLL-SRF structure introduced in Appendix B, the following set of algebraic-differential equations (5.35)-(5.37) allows to determine the control angle $\tilde{\theta}$.

$$\tilde{\omega} = (K_{p\,\mathrm{PLL}} \cdot v_{o\,\tilde{q}} + K_{i\,\mathrm{PLL}} \cdot E_{\tilde{q}\,\mathrm{PLL}} + \omega^*) \tag{5.35}$$

$$pE_{\tilde{q}\,\mathrm{PLL}} = v_{o\,\tilde{q}} \tag{5.36}$$

$$p\tilde{\theta} = \omega_b\,\tilde{\omega} \tag{5.37}$$

On the other hand, the synchronous angle θ can be expressed according to the grid state-space model obtainable from (5.10): this allows to represent network dynamics by

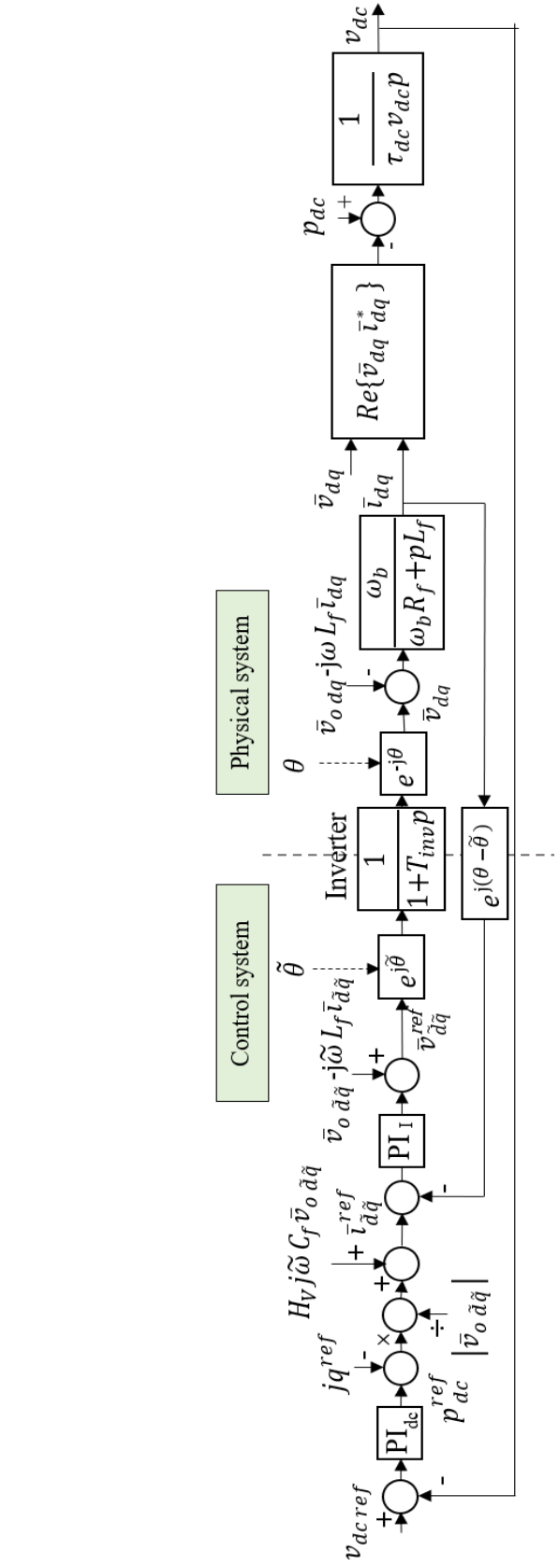

FIGURE 5.7: Non-linear scheme associated to the converter under PQ regulation, including the effect of the angle estimation performed by the PLL. The architecture is composed by two control loops, for the current and DC voltage regulation respectively, while PLL algorithm determines the difference between estimated angle $\tilde{\theta}$ and synchronous one θ, analogously to the estimated frequency $\tilde{\omega}$ and the real one ω.

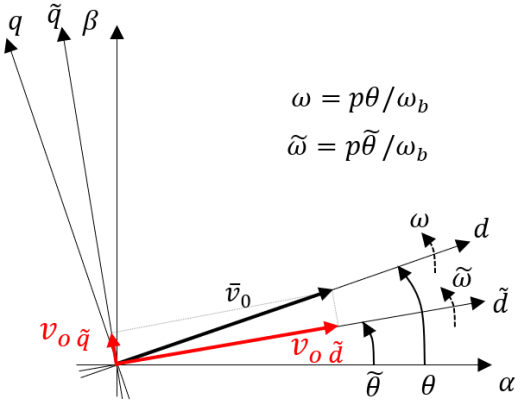

FIGURE 5.8: Definition of the synchronous dq and control $\tilde{d}\tilde{q}$ frames. Synchronous frame is associated to the angular frequency ω of the external grid, while the control frame is characterized by the angular frequency $\tilde{\omega}$. Even though at steady state the two angular frequencies coincide, transient behaviour is affected by the non-ideal response time of the PLL algorithm, which determines the difference in the angular frequencies.

means of the following set of equations:

$$p\theta = \omega_b\,\omega \quad \rightarrow \quad p\Delta\theta = \omega_b \cdot (\omega - \tilde{\omega}) \tag{5.38}$$

$$p\omega = \alpha \tag{5.39}$$

$$p\alpha = \frac{1}{T_a\tau} \cdot (-T_a\alpha - K_{\text{reg}} \cdot (\omega - \omega_{gn}) + \tau \cdot (p\,p_g + p\,p_{conv}) + (p_g + p_{conv})) \tag{5.40}$$

where T_a, τ and K_{reg} are the grid regulation parameters according to Table 5.2; p_g is the independent accelerating power of the network and p_{conv} is the active injection from the PQ unit.

The same angular error introduced by the PLL for the acquisition of the voltage $\bar{v}_o$ is also associated to the other measured AC state variables, like filter current $\bar{i}$. In particular, this can be obtained considering complex power invariance with respect to the rotation of the reference frame; thus, considering (5.34):

$$\bar{s}_o = \bar{v}_{o\,dq} \cdot \bar{i}^*_{dq} = \bar{v}_{o\,\tilde{d}\tilde{q}} \cdot \bar{i}^*_{\tilde{d}\tilde{q}} \tag{5.41}$$

$$\bar{v}_{o\,dq} \cdot \bar{i}^*_{dq} = e^{j\Delta\theta} \cdot \bar{v}_{o\,dq} \cdot \bar{i}^*_{\tilde{d}\tilde{q}} \tag{5.42}$$

$$\bar{i}^*_{o\,dq} = e^{j\Delta\theta} \cdot \bar{i}^*_{\tilde{d}\tilde{q}} \tag{5.43}$$

$$\bar{i}_{\tilde{d}\tilde{q}} = \left(e^{-j\Delta\theta} \cdot \bar{i}^*_{dq}\right)^* = e^{j\Delta\theta} \cdot \bar{i}_{dq} \tag{5.44}$$

As regards the output of the control, on the other hand, the wrong estimation of the angular position leads to a phase delay of the actual applied voltage $\bar{v}_{dq}$ with respect to the reference one imposed as input of the modulator $\bar{v}^{ref}_{\tilde{d}\tilde{q}}$ (Fig. 5.7). Thus:

$$\bar{v}_{dq} = e^{-j\Delta\theta} \cdot \bar{v}^{ref}_{\tilde{d}\tilde{q}} \tag{5.45}$$

These considerations can be generalized:

- the measured quantities are perceived, from the control perspective, affected by a rotation term $e^{j\Delta\theta}$ with respect to the synchronous ones;
- outputs of the control algorithm are subjected to a phase delay equal to $e^{-j\Delta\theta}$

Introducing in (5.45) the internal delay of the modulator expressed by (5.46), it is possible to derive:

$$\bar{v}_{dq} = \frac{e^{-j\Delta\theta}}{1 + p \cdot T_{inv}} \cdot \bar{v}^{ref}_{\tilde{dq}} \tag{5.46}$$

The complete non-linear system in state-space form is reported in Appendix A. The state space model, that includes all the dynamics of the system, will be used to evaluate the correctness of the simplified design procedures proposed in the following.

5.8 Linearised system

The system in Figure 5.7 can be linearised in order to obtain a simplified design model for DC bus control and, later, inertia support design. The following hypotheses are introduced in the derivation:

- given the typically low value of the angular difference $\theta - \tilde{\theta} \cong 0$, the transitory error introduced by the phase estimation algorithm is neglected. Thus it is possible to assume a single rotating frame dq with angular frequency ω and consider $\tilde{dq} = dq$.
- The converter output voltage $\bar{v}$ is close to the filter one $\bar{v}_o$, both in terms of magnitude and characteristic angle. The hypothesis is reasonable considering a small voltage drop on the filter inductor and the converter far from the transmission limit associated to the load angle δ. Hence $\left|\bar{V}_o\right| = V_{od} = \left|\bar{V}\right|$ and $v_{o\,q} = v_q = 0$.
- As the dissipative elements of the filter are characterized by a low value, lossless behaviour is assumed for the LCL filter. Thus the power balance can be expressed as $Re\left[\bar{v}_{dq} \cdot \bar{i}^*_{dq}\right] \cong p_{conv} = Re\left[\bar{v}_{o\,dq} \cdot \bar{i}^*_{o\,dq}\right]$.

From (5.20), the dynamic equation associated to the DC bus can be linearised resorting to the small variations method:

$$(V_{dc}+\Delta v_{dc})\cdot(I_{dc}+\Delta i_{dc})-(V_{od}+\Delta v_{od})\cdot(I_d+\Delta i_d) = \tau_{dc}\cdot(V_{dc}+\Delta v_{dc})\cdot p(V_{dc}+\Delta v_{dc}) \tag{5.47}$$

The time derivative of steady state solution is zero and also second order differentials can be neglected in (5.47), leading to:

$$V_{dc}I_{dc} + V_{dc}\Delta i_{dc} + I_{dc}\Delta v_{dc} - (V_{od}I_d + \Delta v_{od}I_d + V_{od}\Delta i_d) = \tau_{dc}V_{dc}p\,\Delta v_{dc} \tag{5.48}$$

The power balance at steady state can be expressed as $V_{dc}I_{dc} = V_dI_d$. Moreover, the variation of the voltage Δv_d is negligible with respect to other quantities as the voltage drop on the filter remains limited. Considering all these simplifications, the final linear model in the Laplace domain can be obtained.

$$\Delta v_{dc} = \frac{V_{od}}{I_{dc} - \tau_{dc}V_{dc}s} \cdot \Delta i_d - \frac{V_{dc}}{I_{dc} - \tau_{dc}V_{dc}s} \cdot \Delta i_{dc} = \tag{5.49}$$

$$= \frac{1}{I_{dc} - \tau_{dc}V_{dc}s} \cdot (V_{od}\Delta i_d - V_{dc}\Delta i_{dc}) \tag{5.50}$$

Equation (5.50) shows that the linearisation of the DC bus dynamics introduces a positive-real-part pole into the system, whose position depends on the value of the steady state DC current produced by the primary source I_{dc}, on the rectified voltage V_{dc} and on the time constant τ_{dc} (which includes the value of the available capacitance).

Additionally, a disturbance term proportional to the variation of the primary source current Δi_{dc} is present. Generally this term is characterized by slow dynamics, typically associated to the change of the physical conditions of the primary generator (e.g. photovoltaic or wind unit), thus it does not significantly affect DC bus voltage loop stability.

Figure 5.9(a) and 5.9(b) include the linearised models for the direct and quadrature systems, respectively; as the PLL system imposes $v_{oq} \cong 0$, the two linearised models are respectively responsible for the control of active and reactive powers injected into the grid.

5.9 DC bus control

The main objective of the DC bus regulator is to define the reference active power to be sent to the direct current control and maintain equal balance between production and injection. Moreover, the definition of a stabilizing controller for the DC bus is more critical than the one associated with current control as the linearised system in (5.50) shows a pole with positive real part, whose position depends on the actual injection from the primary source, on the physical installed DC bus capacitance and on the steady-state value of the DC bus voltage.

In order to define suitable parameters associated to the regulator, it is important to determine the characteristics of the equivalent load in the voltage loop. Consider the loop $L_{dc}(s)$ reported in Figure 5.10, used for the regulator design; the following hypotheses are introduced:

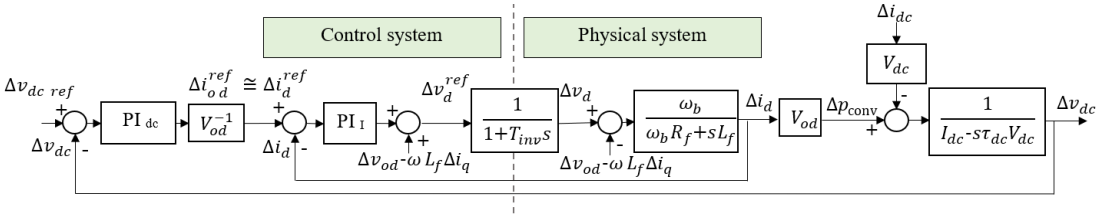

(a)

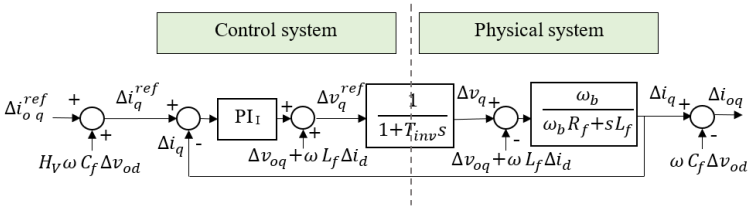

(b)

FIGURE 5.9: Linearised direct (a) and quadrature (b) components of the control system. As the PLL imposes $v_{oq} \cong 0$, direct and quadrature current components allow to independently control active /reactive network injections at the point of common connection, provided that a compensation term $H_V \simeq 1$ is introduced in the quadrature scheme and the filter capacitance value C_f is known with sufficient accuracy.

- internal current loop has been approximated as a first order transfer function according to Appendix B, where ω_{cI} is the current cut-off angular frequency.

$$K_I(s) = \frac{1}{1 + s/\omega_{cI}}. \tag{5.51}$$

- Steady-state DC current from the primary source I_{dc} can vary in the range $I_{dc} \in [0; 1]p.u.$
- Time constant $\tau_{dc} = C_{dc} \cdot V_{b\,dc}^2/A_b$ keeps into account the DC bus characteristics.
- Following steady state values are assumed: $V_{dc} = V_{dc\,\mathrm{ref}} = 1.2\,p.u.$ and $V_{od} = 1\,p.u.$.

From Fig. 5.10, the equivalent load function can be identified (5.52): it is composed by the high-frequency current control pole in ω_{cI} and by the linearised model of the DC bus as calculated in (5.50), which produces a slow pole whose angular frequency depends on the current injected from the primary source I_{dc}.

$$G_{dc}(s) = K_I(s) \cdot \frac{V_{od}}{I_{dc} - \tau_{dc} V_{dc} s} = \frac{1}{1 + s/\omega_{cI}} \cdot \frac{V_{od}/I_{dc}}{1 - \tau_{dc} V_{dc} s/I_{dc}} \tag{5.52}$$

Additionally, Fig. 5.10 shows the presence of the current disturbance $\frac{V_{dc}}{V_{od}}\Delta i_{dc}$ generated by the variation of the primary source current: in general, the variation Δi_{dc} is associated to slow dynamics and thus its effect is negligible, provided that an integral effect is included in the voltage loop [23].

Figure 5.10 shows the effect associated to the variation of the slow pole with respect to the primary source current I_{dc}: if $I_{dc} = 0$ the equivalent load function includes a natural integral associated to the capacitor dynamics. Thus in this case it would be possible to control the system with a simple proportional regulator, obtaining null steady state error thanks to the natural integrating effect of the capacitor. Intuitively, the case with $I_{dc} = 1$ is the most critical as the magnitude of the equivalent load function decreases with the current: thus for increasing injections, a stronger controller is necessary to obtain the desired pass-band and stability margins. In order to stabilise the voltage loop, different structures are considered for the controller:

- a proportional regulator with negative coefficient $k_{p\,dc}$;
- a proportional integral structure designed according to the Nyquist stability criterion of the loop L_{dc}.

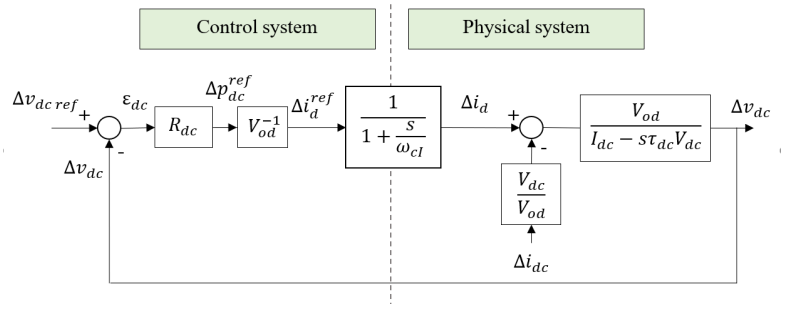

FIGURE 5.10: General model associated to the DC voltage control. Internal current loop is approximated as a first order transfer function.

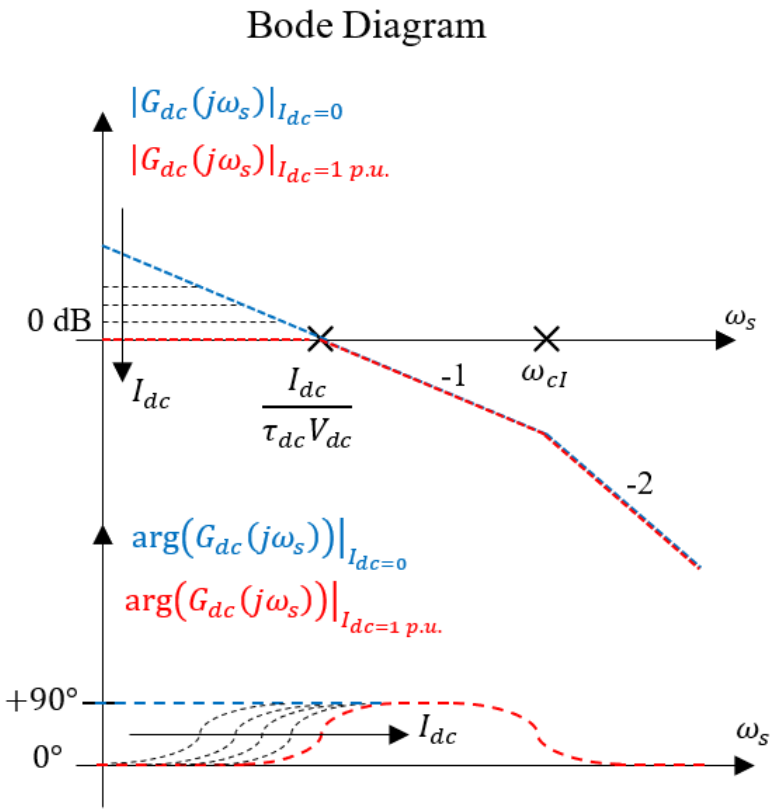

FIGURE 5.11: Equivalent load function associated to the voltage control. The low frequency pole included into the model depends on the current injected from the primary source.

5.9.1 Proportional regulator

A first approach to the DC bus regulation consists in introducing a simple proportional regulator into the voltage loop, thus referring to the following loop function:

$$L_{dc}(s) = k_{p\,dc} \cdot \frac{1}{1 + s/\omega_{cI}} \cdot \frac{1}{I_{dc} - \tau_{dc} V_{dc} s} \tag{5.53}$$

The design of the proportional regulator can be carried out considering direct and inverse root-locus for the closed-loop function, as obtained in Fig.5.12 and derived according to the tracing guidelines provided in [23].

From Fig. 5.12 it is evident the need to consider a negative proportional coefficient $k_{p\,dc} < 0$ for the voltage regulator to stabilise both closed-loop function poles. This is reasonable from the physical point of view if we consider the control structure as reported in Fig.5.10: when the actual voltage of the DC side is higher than its nominal value, $\varepsilon_{dc} = \Delta v_{dc\,\mathrm{ref}} - \Delta v_{dc} < 0$, the converter has to inject more active power into the grid in order to compensate the mismatch on the DC voltage. Hence a positive reference $p_{dc}^{ref} > 0$ should be considered and the proportional regulator $R_{dc} = k_{p\,dc} = \frac{p_{dc}^{ref}}{\varepsilon_{dc}}$, must be negative.

Moreover, the mathematical modelling of the system allows to clearly define the minimum value (in magnitude) that should be considered for the proportional regulator to obtain stability. In fact, starting from the loop function expressed in (5.53), it is

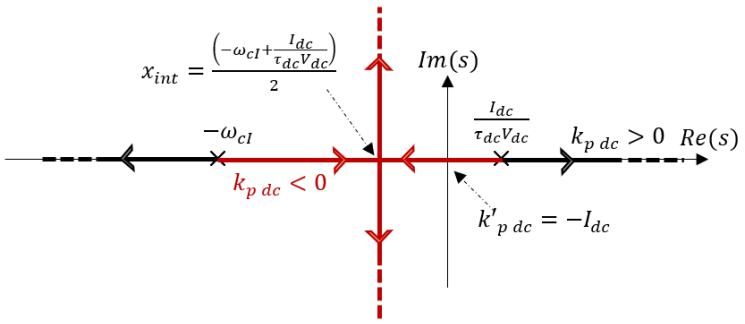

FIGURE 5.12: Root locus of the DC bus loop with proportional regulator. In black bold it is reported the direct locus, in red the inverse one.

possible to identify the closed-loop system poles given by (5.55).

$$L_{dc}(s, k_{p\,dc}) = \frac{N(s, k_{p\,dc})}{D(s)} \rightarrow K_{dc}(s) = \frac{L_{dc}}{1 + L_{dc}} \tag{5.54}$$

$$K_{dc}(s) = \frac{N(s, k_{p\,dc})}{N(s, k_{p\,dc}) + D(s)} \tag{5.55}$$

whose characteristic equation is:

$$s^2 \cdot (-V_{dc}\tau_{dc}/\omega_{cI}) + s \cdot (I_{dc}/\omega_{cI} - V_{dc}\tau_{dc}) + (I_{dc} + k_{p\,dc}) = 0 \tag{5.56}$$

The minimum value (in magnitude) for $k_{p\,dc}$ is obtained when the unstable closed-loop pole is in the origin. Thus from $(I_{dc} + k_{p\,dc}) = 0$, the maximum value k'_p that guarantees the stability equals $k'_{p\,dc} = -I_{dc}$ (Figure 5.12), where $I_{dc} = 1$ p.u. represents the most critical condition for the system.

Moreover, the position of the rightmost pole, once stabilized, determines the cut-off angular frequency $\omega_{c\,dc}$ associated to the voltage control loop. This can be imposed from the loop function (5.53):

$$|L_{dc}(j\omega_{c\,dc})| = |k_{p\,dc}| \cdot |G_{dc}(j\omega_{c\,dc})| = 1 \tag{5.57}$$

$$|k_{p\,dc}| = \frac{1}{|G_{dc}(j\omega_{c\,dc})|} = \sqrt{1 + \left(\frac{\omega_{cI}}{\omega_{c\,dc}}\right)^2} \cdot \sqrt{I_{dc}^2 + \omega_{c\,dc}^2 \tau_{dc}^2 V_{dc}^2} \tag{5.58}$$

Typically the voltage cut-off angular frequency $\omega_{c\,dc}$ should be chosen lower than the current-loop one ω_{cI}, thus avoiding mutual interferences of the two controls during regulation. Under this condition, (5.58) exclusively depends on the capacitor characteristics:

$$k_{p\,dc} = -\sqrt{I_{dc}^2 + \omega_{c\,dc}^2 \tau_{dc}^2 V_{dc}^2} \tag{5.59}$$

Furthermore, in case the DC voltage cut-off angular frequency $\omega_{c\,dc}$ is chosen higher than $\omega_{c\,dc} > \frac{I_{dc}}{\tau_{dc} V_{dc}}$, expression (5.59) simplifies to:

$$k_{p\,dc} = -\omega_{c\,dc}\tau_{dc} V_{dc} \tag{5.60}$$

The Bode and Nyquist diagrams associated to this case are reported in Fig. 5.13. The system is asymptotically stable provided that $k_{p\,dc} < -I_{dc}$: in fact the loop function

shows a positive real-part pole ($N_p = 1$), which is compensated by a single counter-clockwise turn of the frequency response around the point $(-1; 0)$ in the Nyquist diagram ($N_g = 1$). Thus the system is asymptotically stable according to the Nyquist criterion.

Consider the values of the DC bus reported in Tab.5.1, with a desired cut-off angular frequency $\omega_{c\,dc} = 2\pi \cdot 3.5$ rad/s; worst-case conditions are introduced for the current $I_{dc} = 1$ p.u., while nominal grid value $V_{od} = 1$ p.u. and DC bus reference equal to $V_{dc\,\mathrm{ref}} = 1.2$ per-unit are assumed. The approximated expression of the proportional coefficient $k_{p\,dc}$ as obtained in (5.60) leads to the coefficients in Table 5.4, compared to the exact ones obtained from the load function inversion (5.58).

The advantage of the approximate coefficient $k_{p\,dc}$ calculation is mainly associated to its independence with respect to the actual production I_{dc} from the primary source. Moreover also considering the numeric open and closed-loop transfer function of the voltage control loop (Fig. 5.14) under the primary source current I_{dc} variation ($I_{dc} \in [0, 1]$ per-unit), it is possible to see a small sensitivity of the angular cut-off frequency under different injections.

The choice to introduce a simple proportional regulator in the voltage loop allows an easy design of the control parameters, but introduces as a drawback the dependence of the steady-state voltage value on the actual level of injected DC current I_{dc}: the reason lies in the absence of integral action in the loop L_{dc} when $I_{dc} \neq 0$: the gain of the transfer function L_{dc} is finite for $s \to 0$ and the control is not able to guarantee null error at steady state, even for constant voltage references.

Consider a step change of the reference $\Delta v_{dc\,\mathrm{ref}}$; actual steady-state voltage variation can be obtained from the Laplace final value theorem applied to the closed-loop transfer

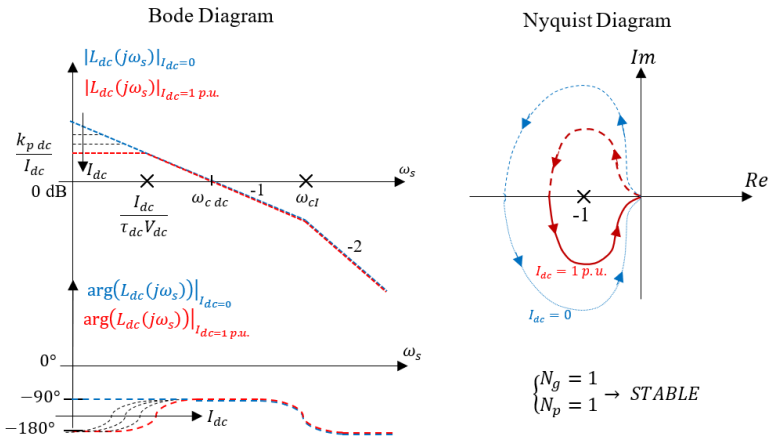

FIGURE 5.13: Bode diagram associated to the voltage loop under proportional control. The system is stable provided that $k_{p\,dc} < -I_{dc}$ as the positive-real-part pole of the loop ($N_p = 1$) is compensated by the counter-clockwise turn of the frequency response around the point $(-1; 0)$ in the Nyquist diagram ($N_g = 1$).

TABLE 5.4: Proportional DC regulator

Parameter	*Value*
Approximated (5.60)	$k_{p\,dc} = -7.03$ p.u.
Exact (5.58)	$k_{p\,dc} = -7.10$ p.u.

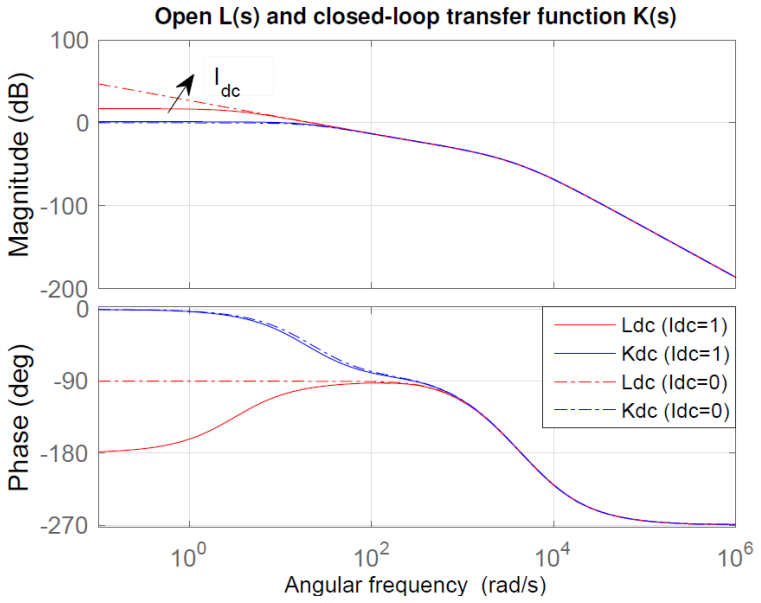

FIGURE 5.14: Numerical Bode diagram for the DC bus control - Proportional regulator.

function $K_{dc}(s)$.

$$\Delta v_{dc}(t \to \infty) = \lim_{s \to 0} \left(s \cdot K_{dc}(s) \cdot \frac{\Delta v_{dc\,\mathrm{ref}}}{s} \right) = K_{dc}(0) \cdot \Delta v_{dc\,\mathrm{ref}} = \\ = \frac{L_{dc}(0)}{1 + L_{dc}(0)} \cdot \Delta v_{dc\,\mathrm{ref}} = \frac{k_{p\,dc}}{I_{dc} + k_{p\,dc}} \cdot \Delta v_{dc\,\mathrm{ref}} \tag{5.61}$$

Equation (5.61) shows that the actual change in the voltage matches the reference variation only if $I_{dc} = 0$; in case of full current $I_{dc} = 1$p.u. and with the calculated regulator $k_{p\,dc} = -7.03$ the expected steady-state DC from (5.61) under unitary reference change would be equal to $\Delta v_{dc\,s.s.} = 1.16$p.u., compatible with the step response in Fig. 5.15.

5.9.2 Proportional-Integral regulator

A different option for DC bus controller design consists in introducing a proportional-integral regulator in the scheme already reported in Fig. 5.10. The loop function $L_{dc}(s)$ is given by (5.62), where $T_R = \frac{k_{p\,dc}}{k_{i\,dc}}$ is the integral time of the PI controller. The following procedure will be carried out to determine the conditions associated to the sign of the control coefficients:

- as already mentioned, unitary primary source current $I_{dc} = 1$ p.u. is the outmost critical condition for loop stability. Thus, the design will be carried adopting the conservative hypothesis $I_{dc} = 1$p.u. , subsequently verifying that stability is maintained also for $I_{dc} = 0$.
- Four different cases corresponding to the combinations of the coefficients sign will be considered according to Table 5.5: Bode and Nyquist diagrams associated to each case are reported in Fig. 5.17.

$$L_{dc}(s) = k_{i\,dc} \cdot \frac{1 + sT_R}{s} \cdot \frac{1}{1 + s/\omega_{cI}} \cdot \frac{V_{od}}{I_{dc} - \tau_{dc} V_{dc} s} \tag{5.62}$$

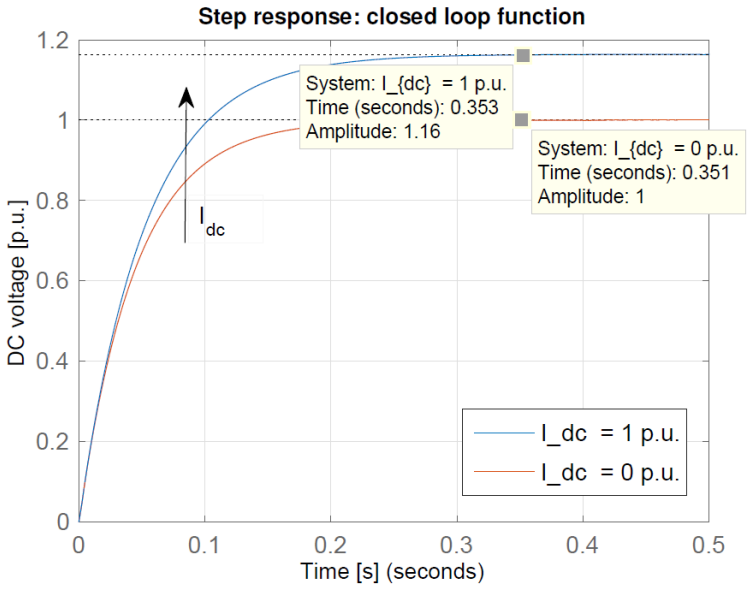

FIGURE 5.15: Step response for the DC bus control - Proportional regulator.

TABLE 5.5: PI controller for DC bus voltage - Case definition

Case	*Integral coeff.* $k_{i\,dc}$	*Time constant* T_R
1	> 0	> 0
2	> 0	< 0
3	< 0	> 0
4	< 0	< 0

The structure in (5.62) shows two degrees of freedom respectively associated to the proportional and integral coefficients. The design can be carried out imposing suitable cut-off angular frequency $\omega_{c\,dc}$ and phase margin ϕ_m for the open-loop L_{dc}. The system in (5.62) is characterized by a negative real-part zero in $\omega_z = \frac{1}{T_R}$, a slow positive-real-part pole $\omega_{p1} = \frac{I_{dc}}{V_{dc}\tau_{dc}}$ and a fast negative-real-part pole in $\omega_{p2} = \omega_{cI}$.

Consider the four cases reported in Fig. 5.17. Even though all of them are characterized by the same magnitude profile, phase profiles differ as consequence of the sign of the parameters $k_{i\,dc}$ and T_R.

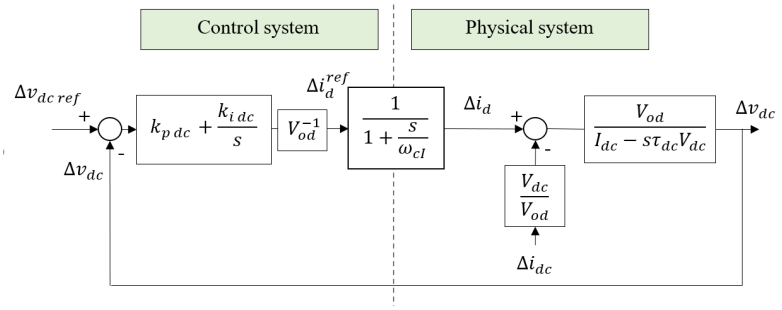

FIGURE 5.16: System block diagram with proportional integral regulator. The closed-loop stability for all the possible combinations of the coefficients sign has to be analysed.

- cases A, B and D are unstable for all the possible absolute values of the coefficients, as they do not meet Nyquist stability conditions.
- Case C is the only one which could lead to a stable closed-loop behaviour, provided that the real axis intersection in the Nyquist diagram occurs left-ward with respect to point $(-1;0)$. This condition holds only if the magnitude diagram intersection with the 0 dB axis occurs after the zero in $\omega_z = \frac{1}{T_R}$ in the corresponding Bode diagram.

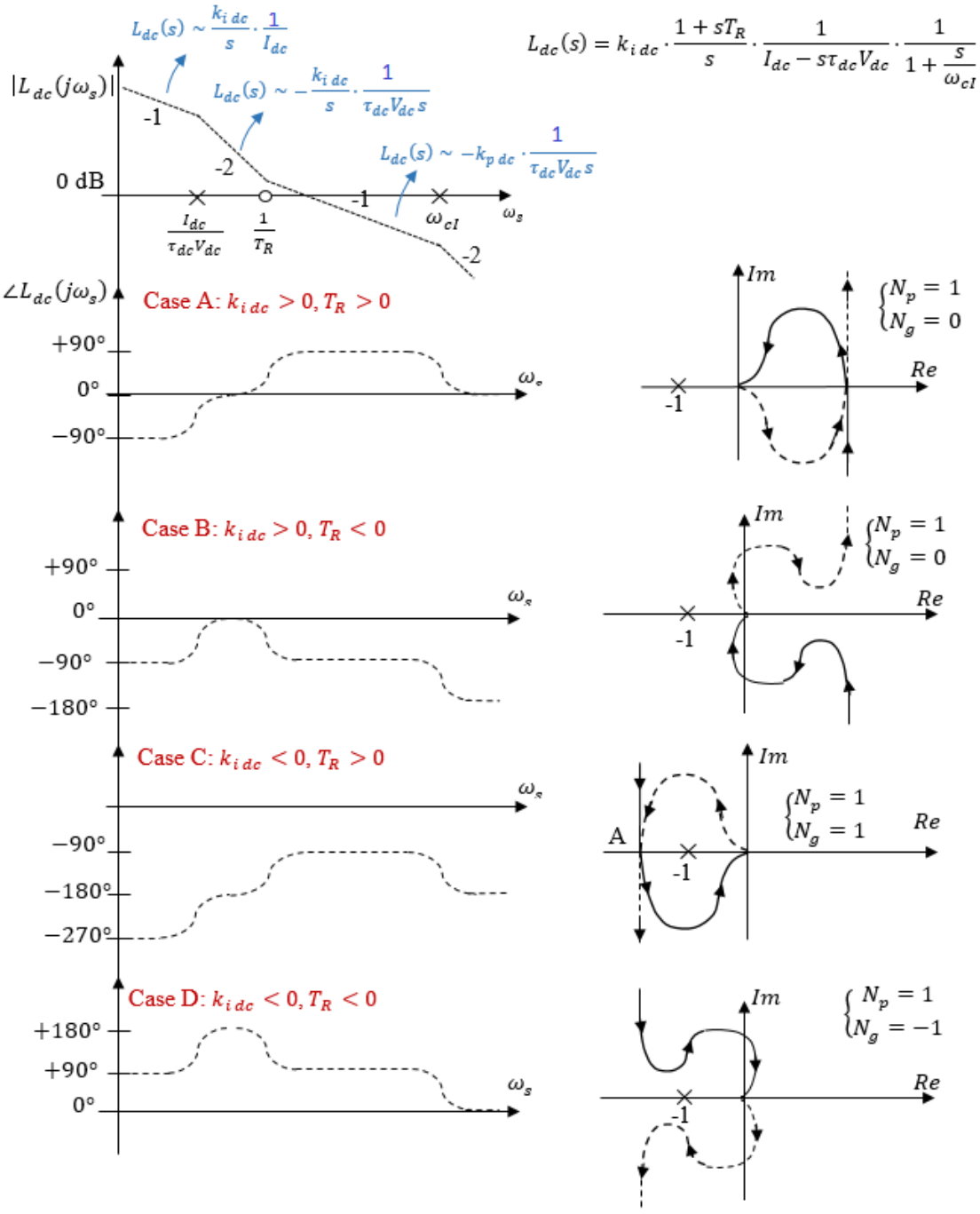

FIGURE 5.17: Stability analysis of the voltage controller with different signs for the control coefficients. Considering Nyquist stability criterion, only case C shows a stable behaviour, which corresponds to $k_{i\,dc} < 0$ and $T_R > 0$.

Thus the following condition can be derived for the controller, under the constraints imposed by the case C:

$$\left|\frac{1}{T_R}\right| < \omega_{c\,dc} \tag{5.63}$$

$$k_{i\,dc} < 0 \qquad T_R > 0 \qquad \text{(thus it must be } k_{p\,dc} < 0) \tag{5.64}$$

Provided that (5.63) is verified, the asymptotic behaviour of the DC voltage open-loop function $L_{dc}(s)$ close to the cut-off angular frequency $\omega_{c\,dc}$ is given by (5.65); in the calculation it is assumed that the voltage loop cut-off angular frequency $\omega_{c\,dc}$ is lower than the current loop one ω_{cI}, as correctly imposed by the nested-loop structure of the control architecture.

$$L_{dc}(s) = -\frac{k_{p\,dc} V_d}{\tau_{dc} V_{dc} s} \quad \text{for} \quad \left|\frac{1}{T_R}\right| < \omega < \omega_{cI} \tag{5.65}$$

Once defined the desired cut-off angular frequency $\omega_{c\,dc}$, the proportional coefficient is determined by (5.67).

$$|L_{dc}(j\omega_{c\,dc})| = \frac{|k_{p\,dc}|\, V_d}{\tau_{dc} V_{dc} \omega_{c\,dc}} = 1 \tag{5.66}$$

$$|k_{p\,dc}| = \frac{\tau_{dc}\, V_{dc}\, \omega_{c\,dc}}{V_{od}} \tag{5.67}$$

Once verified that (5.63) - (5.65) lead to stable operations for the voltage loop when primary source current is maximum $I_{dc} = 1\,p.u.$, the verification of the stability in low-production case should be evaluated. This can be done considering the constraints (5.63) - (5.65) applied to the load function reported in Fig. 5.11 when $I_{dc} = 0$. Bode and Nyquist diagrams in this case are reported in Fig. 5.18.

In these case studies, DC bus capacitance is chosen equal to $C_{dc} = 8$ mF (with maximum voltage $400\,V$) and, at this stage, it is assumed as an input of the problem. Later in the analysis it will be shown how it is possible to correlate the available capacitance with the maximum regulation performances of the inertia loop, focusing not only on energetic considerations, but also on the inherent stability of the global system. The numeric values referred to case study derived from Table 5.3 are reported in Table 5.6.

The numeric behaviour of the controller in terms of step change and frequency response is reported in Fig. 5.19 and 5.20 respectively; Fig. 5.19 in particular shows

Table 5.6: PI DC regulator

Parameter	*Symbol*	*Value*
DC bus capacitance	C_{dc}	$8mF$ (@ $400\,V$)
Time constant	$\tau_{dc} = C_{dc} \cdot V_{dc\ b}^2 / A_b$	$0.267\,s$
Max. pole position	$\frac{I_{dc}}{\tau_{dc} V_{dc}}$ with $I_{dc} = 1$ p.u.	$\cong 3.1$ rad/s
Desired cut-off angular freq.	$\omega_{c\,dc}$	$2\pi \cdot 2.5 \cong 15.7$ rad/s
Proportional coeff. (5.66)	$k_{p\,dc}$	-5.02 p.u.
Controller integral time (5.64)	T_R^{-1}	6 rad/s

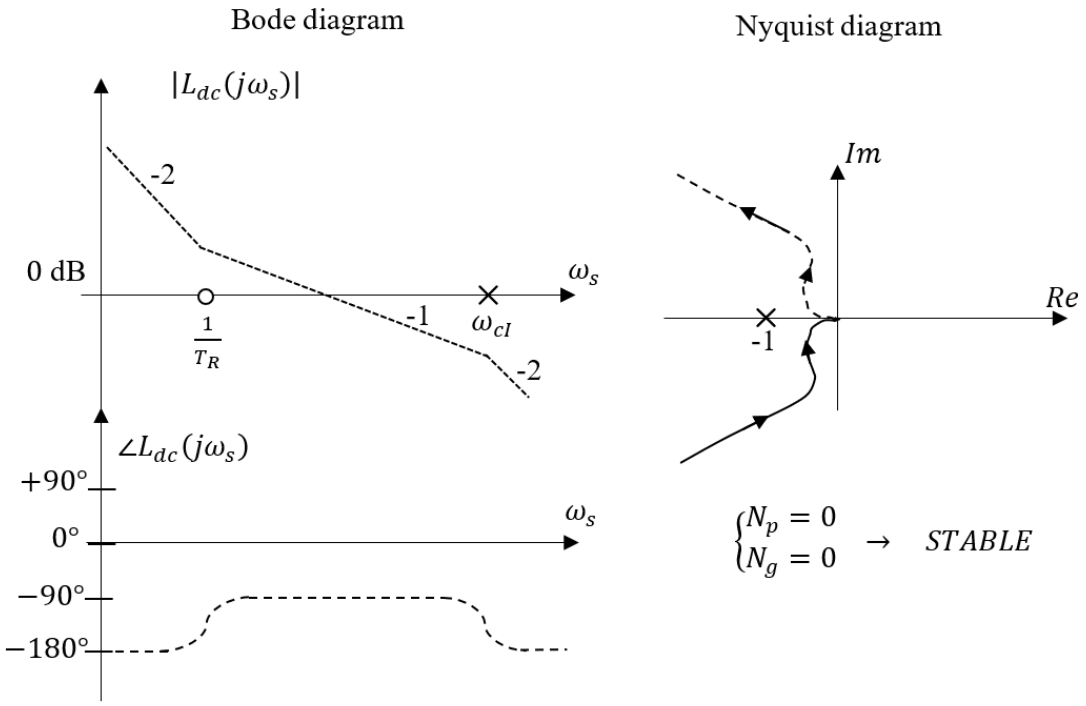

FIGURE 5.18: Verification of the voltage loop stability under low production. Conditions derived in (5.63) - (5.65) have been applied to the case with $I_{dc} = 0$.

the over-shoot due to a unitary step of the voltage reference Δv_{dcref}, caused by the contemporaneous action of the positive real-part pole $\frac{I_{dc}}{\tau_{dc} V_{dc}}$ associated to the DC bus dynamics and the slow zero T_R^{-1} introduced by the regulator. Even though the overshoot may be significant especially for high values of the DC current, the unitary change of the reference is practically not meaningful under nominal operations of the converter.

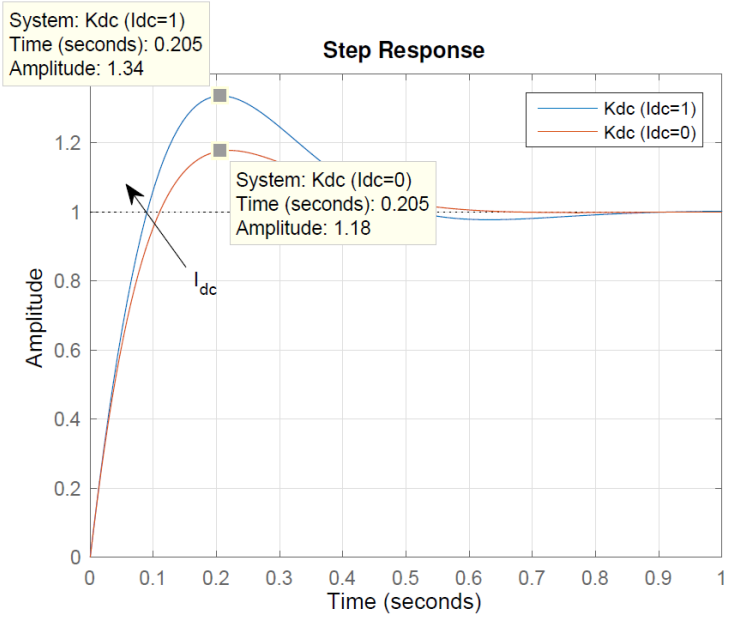

FIGURE 5.19: Step response for the DC bus control - Proportional-integral regulator.

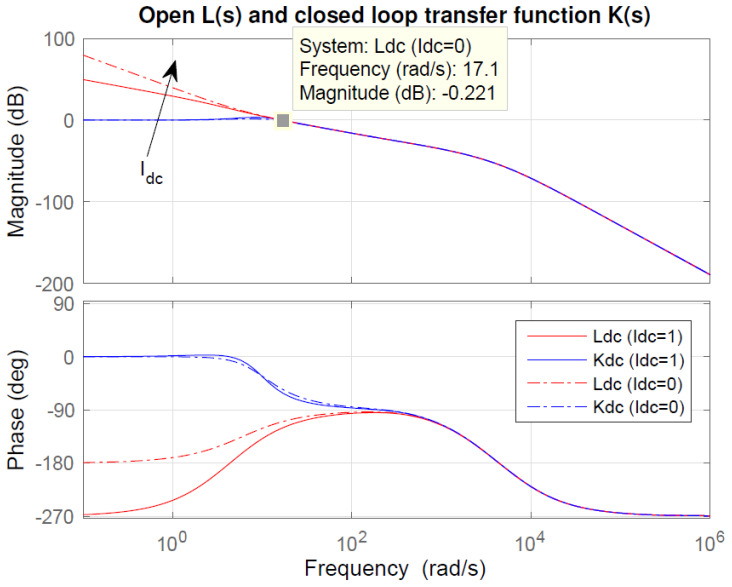

FIGURE 5.20: Bode diagrams for the DC bus control - Proportional-integral regulator. Physical and control values refer to Table 5.6.

5.10 Inertia models

The schemes reported in Fig. 5.21(a) and Fig. 5.21(b) represent the two developed architectures for the provision of inertia support to the grid: both the schemes are derived from the grid-following topology presented in Fig.5.7. Moreover the typical PQ configuration is modified with an additional feedback that introduces a dependence of the injected power on the balancing state on the network, reducing the excursion of frequency transients.

The two architectures can be interpreted considering the energetic behaviour of the system. Firstly consider the current-controlled model (Fig. 5.21(a)): the inertia feedback introduces an active power reference proportional to the frequency derivative, thus the converter emulates the behaviour of a physical inertial body (5.5). Thanks to its derivative nature, it does not affect the behaviour of the unit at steady state and can be applied also to non-dispatchable sources. Intuitively the power reference p_{in} should be positive under negative values of the derivative, coherently to (5.5).

The decision to introduce the inertia signal as an additional power reference obviously allows to obtain very fast regulation and a straightforward design of the control parameters, as all the internal dynamics show high cut-off frequencies and significant robustness. Moreover it is evident the difficulty to extract the derivative of the signal frequency from a set of voltages affected by disturbances. Thus in the next chapter it will be shown how to improve the estimation of the fundamental angular frequency derivative even under distorted network conditions.

Moving to the voltage-controlled model (Fig. 5.21(b)), the emulation contribution can be obtained acting on the DC bus voltage reference. Here it may be more difficult to define the characteristics of the controller that has to be used to provide inertia regulation. Consider a proportional behaviour between the DC bus voltage reference Δv_{dcref} and the differential angular frequency $\Delta\omega$. Chapter 8 will show that a proportional dependency between the actual frequency variation $\Delta\omega$ and the DC bus voltage reference has the same effect of an active power injection activated by the frequency derivative; this formal equivalence can be maintained provided that a positive angular

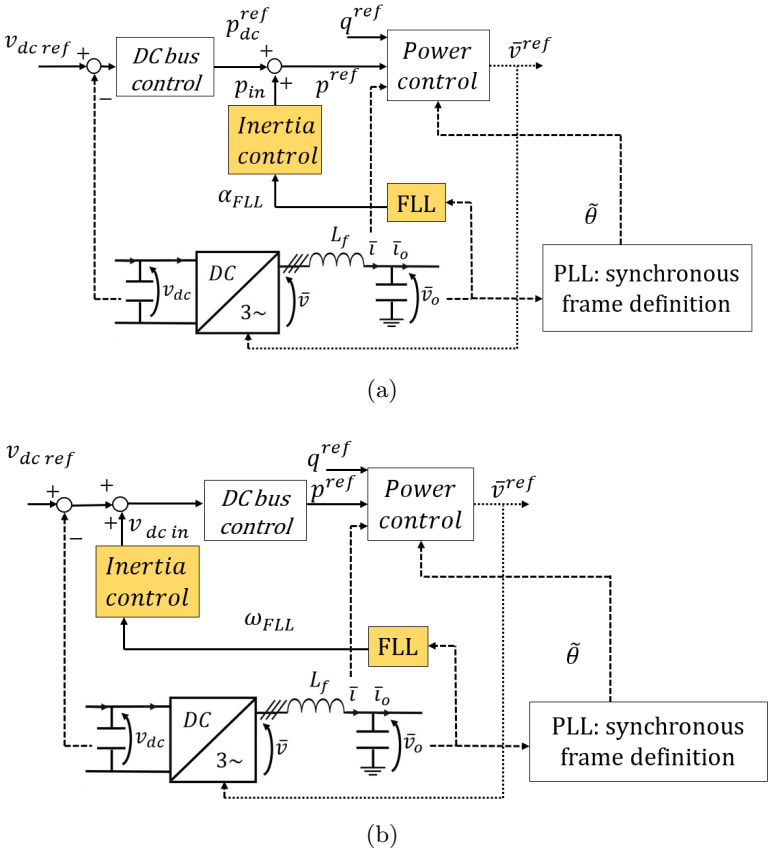

FIGURE 5.21: Control architectures for inertia support. In (a) the additional feedback comprises a derivative estimator and a power reference (current-controlled model), while in (b) the direct estimation of the system frequency produces a DC voltage reference signal (voltage-controlled model).

frequency change $\Delta\omega > 0$ is counterbalanced by an increase of the DC bus voltage reference $\Delta v_{dc\,in} > 0$.

5.11 Conclusion

In this chapter the main architecture associated to the PQ control has been introduced starting from the definition of the complete non linear model of the system: the followed approach is based on the derivation of a set of analytical equations from each element included into the system. After that, all the subsets have been combined in order to derive a model able to take into account different aspects of the control: current and voltage loops, phase estimation by means of the PLL. Analytical guidelines for the design of the internal control loops have also been provided.

Most of the concepts addressed in this chapter are known in literature, still their importance lies in the definition of a common background for the synthetic inertia analysis that will be carried out in the following. In particular, the analytical equivalence between the droop scheme and the primary frequency regulation (even though intuitively reasonable from the energetic point of view) allows to highlight the role played by each control parameter during system regulation.

Chapter 6

Angular quantities estimation for the provision of inertia services

6.1 Introduction

A key aspect to be taken into account during the provision of transitory inertia service regards the possibility to estimate the physical angular quantities in a fast and clean way from the available voltage measurements. In particular, the presence of harmonics and unbalanced components may cause a poor quality of the reconstructed signal; on the other hand, a strong filtering effect may lead to a better signal-to-noise ratio, even though slows down the reconstruction of angular variables, reducing the equivalent phase margin of the interaction between dispatchable and non-dispatchable units.

In this chapter, a comparison between some angular quantity estimators will be carried out. Moreover, a novel scheme based on the inverse sequence compensation will be proposed and it will be shown experimentally how its performances represent a good trade-off between fast estimation and high Signal-to-Noise ratio.

6.2 SOGI-FLL architecture

6.2.1 Description of the SOGI

Consider the architecture typically referred in literature as Second Order Generalized Integrator (SOGI) [26], as introduced in [27] - [28] and [29] for the extraction of the fundamental sinusoidal harmonic component ω from the input signal $v(t)$. Typical graphical representation of the SOGI is reported in Fig.6.1 in the Laplace domain.

Moreover, if we consider the analytical resolution of the feedbacks reported in Figure 6.1, it is easy to find out that the combination of all the control loops corresponds to the application of two digital resonant filters $D(s)$ and $Q(s)$ to the input signal. The

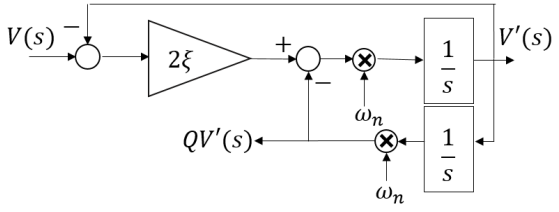

FIGURE 6.1: Architectures of the Second Order Generalized Integrator (SOGI) in the frequency domain

expressions of the transfer functions $\frac{V'(s)}{V(s)} = D(s)$ and $\frac{QV'(s)}{V(s)} = Q(s)$ are given by:

$$D(s) = 2\xi \cdot \frac{s/\omega_n}{(s/\omega_n)^2 + 2\xi(s/\omega_n) + 1} \tag{6.1}$$

$$Q(s) = 2\xi \cdot \frac{1}{(s/\omega_n)^2 + 2\xi(s/\omega_n) + 1} \tag{6.2}$$

The following notation is used:

- ω_n: resonant angular frequency;
- ξ damping factor;
- ω: network fundamental angular frequency;
- $s = j\omega_s$: Laplace operator and symbolic frequency response variable.

The filtering properties of the two transfer functions can be imposed simply acting on the equivalent damping $\xi = \frac{k_{\text{SOGI}}}{2}$ and resonance angular frequency ω_n; the magnitude and phase diagrams of the transfer functions in (6.1) and (6.2) are reported in Fig.6.2. Both functions show a unitary gain at the resonance frequency ω_n, while the phase delay is respectively equal to $0°$ and $-90°$ for $D(s)$ and $Q(s)$ in correspondence to the resonance frequency ω_n.

The physical interpretation of the output signals $V'(s)$ and $QV'(s)$ is straightforward once determined the characteristics of the transfer function $D(s)$ and $Q(s)$ from Fig. 6.2: in case ω_n coincides with the fundamental angular frequency ω, $V'(s)$ coincides with the Laplace transform of the fundamental sinusoidal component of the system voltage, while $QV'(s)$ stands for the same signal delayed by a quarter of a period.

6.2.2 Interaction of the SOGI with the FLL loop

In this section the interaction of the SOGI with the Frequency Locked Loop (FLL) will be analysed. The typical configuration is shown in the control diagram of Figure 6.3-6.4.

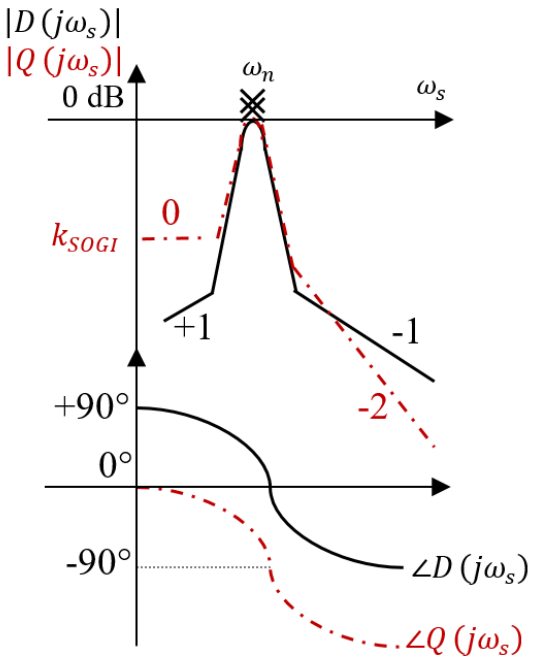

FIGURE 6.2: Bode diagrams of the transfer functions $D(s)$ and $Q(s)$.

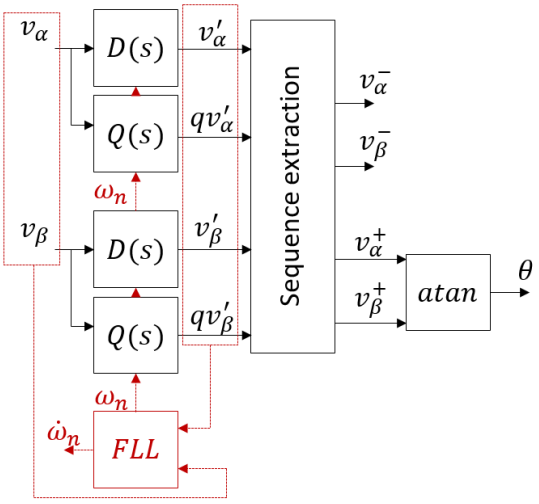

FIGURE 6.3: Equivalent control diagram of the SOGI-FLL algorithm

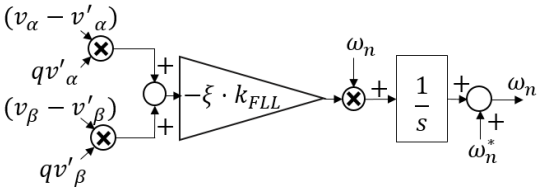

FIGURE 6.4: Representation of the FLL scheme for the SOGI architecture

In order to analyse the coordination of the SOGI scheme with the FLL algorithm, consider the response associated to the transfer functions $D(s)$ and $Q(s)$. Assume a normalized sinusoidal input signal v_α with angular frequency ω (6.3), the output signals v'_α and qv'_α from the resonant filters $D(s)$ and $Q(s)$ are given by (6.4) and (6.5); the frequency response of v'_α and qv'_α at steady state shows that the two sinusoids are always in quadrature with respect to each other, independently of the values of the input angular frequency ω and the resonance one ω_n.

$$v_\alpha(t) = cos(\omega t) \tag{6.3}$$

$$v'_\alpha(t) = \left| \frac{j2\xi\omega\omega_n}{\sqrt{(\omega_n^2 - \omega^2)^2 + (2\xi\omega\omega_n)^2}} \right| \cdot cos(\omega t + \pi/2 - \phi_d(j\omega)) \tag{6.4}$$

$$qv'_\alpha(t) = \left| \frac{j2\xi\omega\omega_n}{\sqrt{(\omega_n^2 - \omega^2)^2 + (2\xi\omega\omega_n)^2}} \right| \cdot \frac{\omega_n}{\omega} \cdot cos(\omega t - \phi_d(j\omega)) \tag{6.5}$$

where $\phi_d(j\omega) = atan(\frac{2\xi\omega\omega_n}{\omega_n^2 - \omega^2})$. The difference $\epsilon_\alpha = v_\alpha - v'_\alpha$ can be expressed by means of the transfer function $E(s) = V_\alpha(s) \cdot (1 - D(s))$.

$$E(s) = \frac{s^2 + \omega_n^2}{s^2 + 2\xi\omega_n s + \omega_n^2} V_\alpha(s) \tag{6.6}$$

Likewise (6.4), the steady state condition for the error is obtainable as:

$$\epsilon_\alpha(t) = \frac{\omega_n^2 - \omega^2}{\sqrt{\left(\omega_n^2 - \omega^2\right)^2 + \left(2\xi\omega\omega_n\right)^2}} \cdot cos(\omega t - \phi_d(j\omega)) \tag{6.7}$$

It is possible to linearise (6.7) around the equilibrium $\omega \cong \omega_n$. Thus the numerator of (6.7) becomes $\omega_n^2 - \omega^2 = (\omega_n + \omega)\cdot(\omega_n - \omega) \cong 2\omega_n \cdot (\omega_n - \omega)$; under the same condition $\omega \cong \omega_n$, the denominator can be approximated as in (6.8) provided that $\omega_n - \omega < \xi\omega$: this condition represents an index of the robustness of the linearised model with respect to the non-linear one. Nevertheless, considering the typical limited excursion of the grid angular frequency, this condition is generally verified.

$$\epsilon_\alpha(t) \cong \frac{2\omega_n \cdot (\omega_n - \omega)}{2\xi\omega\omega_n} \cdot cos(\omega t - \phi_d(j\omega)) \tag{6.8}$$

According to the FLL scheme reported in [28] and in Fig. 6.4, the product $\epsilon_\alpha(t) \cdot qv_\alpha(t)$ is proportional to the angular frequency difference $\omega_n - \omega$; this can be seen considering that the magnitude of the transfer function $|D(j\omega)|$ is almost unitary for $\omega \cong \omega_n$:

$$\epsilon_\alpha(t) \cdot qv'_\alpha(t) \cong \frac{2\omega_n \cdot (\omega_n - \omega)}{2\xi\omega\omega_n} \cdot |D(j\omega)| \cdot \frac{\omega_n}{\omega} \cdot cos^2(\omega t - \phi_d(j\omega)) \cong \tag{6.9}$$

$$= \frac{(\omega_n - \omega)}{\xi\omega_n} \cdot \frac{1}{2} \cdot [1 + cos(2\omega t - 2\phi_d(j\omega))] \quad \text{as } \omega \cong \omega_n \tag{6.10}$$

where the asymptotic behaviour $\omega \cong \omega_n$ has been used for the coefficients simplification; this allows to have a simpler control structure of the FLL, with a single input ω. The quantity defined in (6.10) can be used to tune the resonance peak of the SOGI filters on the fundamental component of the system. In a three-phase case like the one reported in Fig. 6.4 and 6.3, the actual input of the FLL is given by the average between the equivalent errors associated to the axes α and β, which is used as an input signal for the frequency tuning. Assuming pure sinusoidal inputs, the same calculation performed on the β axis gives (6.11); thus considering the sum of the two quantities as input of the FLL allows to remove the component at two times the fundamental. Predictably, this does not happen for the single phase case as reported in [16], where the pass-band of the FLL should be chosen low enough to filter out the component at 2ω.

$$\epsilon_\beta(t) \cdot qv'_\beta(t) \cong \frac{(\omega_n - \omega)}{\xi\omega_n} \cdot \frac{1}{2} \cdot [1 - \cos(2\omega t - 2\phi_d(j\omega))] \tag{6.11}$$

Thus:

$$\epsilon_\alpha(t) \cdot qv'_\alpha(t) + \epsilon_\beta(t) \cdot qv'_\beta(t) = \frac{\omega_n - \omega}{\xi\omega_n} \tag{6.12}$$

Typically, a pure integral controller k_{FLL}/s guarantees the absence of any steady-state error between the fundamental angular frequency ω and the resonant one ω_n. The introduction of normalizing coefficients (ξ, k_{FLL}) reported in Fig. 6.4 allows to define the equivalent loop used for the tuning of the FLL parameter k_{FLL}, obtainable from Fig.6.5; a feed-forward compensation of the nominal angular frequency $\omega_n^* = 1 \quad p.u.$ is also introduced to speed up the convergence of the algorithm.

The equivalent closed-loop transfer function of the FLL (6.13) shows how the parameter k_{FLL} actually coincides with the FLL pass-band, provided that the correct normalization coefficients are introduced in Fig.6.5. The linearised relation between the actual ω and estimated ω_n system angular frequencies can be expressed by (6.13), which has the typical form of a first-order low-pass filter with a known pass-band.

$$CL_{FLL}(s) = \frac{\omega_n}{\omega} = \frac{1}{1 + s/k_{FLL}} = \frac{1}{1 + s\,\tau_{FLL}} \tag{6.13}$$

Figure 6.5 shows that the input of the FLL integral can be regarded as a good estimate of the approximated angular frequency derivative associated to the fundamental system component. In the perspective of inertia service provision, this is a crucial point: it allows to have at disposal not only the information on the network balancing state (represented by the angular frequency), but also an estimate of its time evolution given by the derivative. This enables the design of fast control actions during transitory condition of the network but null at steady state and thus compatible with the undispatchable nature of the PQ units. Moreover, the natural presence of the angular system derivative in the FLL loop allows to avoid the introduction of any numerical derivation process that would bring to a poor Signal-to Noise ratio for the reconstructed signal.

From Fig.6.5, the closed loop function associated to the actual derivative estimation becomes (6.14); this can be used as an estimate of the actual angular frequency derivative of the network.

$$\dot{\omega}_n = \frac{s}{1 + s/k_{FLL}}\omega = \frac{s}{1 + s\tau_{FLL}}\omega \tag{6.14}$$

6.2.3 Design of SOGI-FLL control parameters

The design of the control coefficients ξ and $k_{FLL} = \tau_{FLL}^{-1}$ can be done considering the mutual internal dynamics of the SOGI and FLL; the expected convergence time of the resonant controllers included into the SOGI can be obtained studying the time evolution of the free motion of the system. From explicit calculation reported in Appendix C.1, the estimated settlement time of the free response of the system is given by:

$$T_{set} = \frac{4.6}{\xi\omega_n} \tag{6.15}$$

Typically the cut-off angular frequency of the external loop (the FLL in this case) should be in the same order of magnitude of the settlement time of the SOGI, so as to guarantee

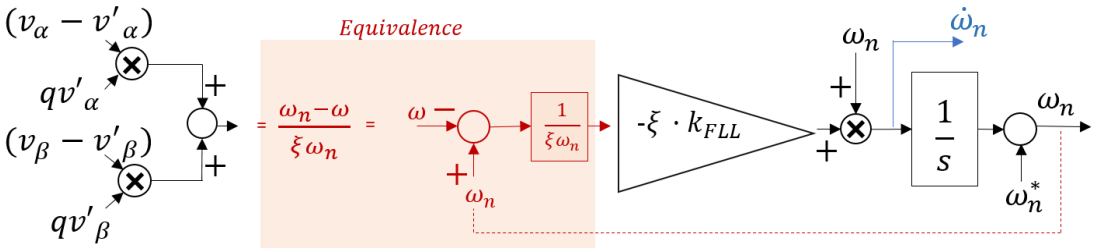

FIGURE 6.5: Derivation of the equivalent transfer function between system angular frequency ω and ω_n for the SOGI-FLL structure.

that the inner dynamics are already at steady state when the external control starts to operate: $k_{FLL}^{-1} = \tau_{FLL} \cong T_{set}$.

This produces a necessary trade-off between the desired filtering properties of the SOGI and the estimation convergence speed: a reduction of the damping coefficient ξ gives higher filtering properties but, on the other side, the settlement time will increase according to (6.15). Nevertheless, if we are able to provide a clean input signal, the internal dynamics of the SOGI and FLL can evolve contemporaneously and it will be possible to extend the fastness of the estimation keeping a good Signal-to-Noise ratio.

To compare the available SOGI architecture with newly introduced schemes, two alternative designs are considered even though only the first one is mathematically compliant with the condition expressed by (6.15). With a nominal angular frequency of the fundamental component $\omega_n = 2\pi \cdot 50$ rad/s and a damping factor $\xi = 0.2$, cases in Table 6.1 can be identified.

6.2.4 Sequence extraction

Fig. 6.3 highlights how it is possible to exploit the SOGI scheme for the identification of phase angle θ associated to the first-order positive sequence component from the determination of its space vector $\alpha\beta$ components. Even though the obtained formulas are available in literature, their derivation is often not provided in a formal way. Nevertheless, it is possible to obtain them straightforwardly.

Consider a general complex signal $v_\alpha(t) + jv_\beta(t)$ in the Park domain, obtained from the superposition of rotating vectors at positive and negative sequences.

$$(v_\alpha + jv_\beta) = \left(\sum_{h=1}^{N+} \bar{V}_h^+ \cdot e^{jh\omega t} + \sum_{h=1}^{N-} \bar{V}_h^- \cdot e^{-jh\omega t} \right) \tag{6.16}$$

$$v_\alpha = v_\alpha^+ + v_\alpha^- \tag{6.17}$$

$$v_\beta = v_\beta^+ + v_\beta^- \tag{6.18}$$

Equations (6.17)-(6.18) define four independent time-signals, which are respectively the α and β components of the separate positive and negative sequences: v_α^+, v_β^+, v_α^- and v_β^-, given by (6.19)-(6.20).

$$v_\alpha^+ = \sum_{h=1}^{N+} Re\left\{ \bar{V}_h^+ \cdot e^{jh\omega t} \right\} \qquad v_\beta^+ = \sum_{h=1}^{N+} Im\left\{ \bar{V}_h^+ \cdot e^{jh\omega t} \right\} \tag{6.19}$$

$$v_\alpha^- = \sum_{h=1}^{N-} Re\left\{ \bar{V}_h^- \cdot e^{-jh\omega t} \right\} \qquad v_\beta^- = \sum_{h=1}^{N-} Im\left\{ \bar{V}_h^- \cdot e^{-jh\omega t} \right\} \tag{6.20}$$

TABLE 6.1: Design alternatives definitions for the SOGI algorithm

Case	ξ	Design criterion	k_{FLL}
Slow SOGI	0.2	(6.15)	8.0 rad/s
Fast SOGI	0.2	Fast estimation	80 rad/s

Thus:

$$v_\alpha^+ = \sum_{h=1}^{N+} \left\{ |\bar{V}_h^+| \cdot \cos\left(h\omega t + \phi_h^+\right) \right\} \qquad v_\beta^+ = \sum_{h=1}^{N+} \left\{ |\bar{V}_h^+| \cdot \sin\left(h\omega t + \phi_h^+\right) \right\} \tag{6.21}$$

$$v_\alpha^- = \sum_{h=1}^{N-} \left\{ |\bar{V}_h^-| \cdot \cos\left(-h\omega t + \phi_h^-\right) \right\} \qquad v_\beta^- = \sum_{h=1}^{N-} \left\{ |\bar{V}_h^-| \cdot \sin\left(-h\omega t + \phi_h^-\right) \right\} \tag{6.22}$$

where ϕ_h^+ and ϕ_h^- are the arguments of the positive and negative phasors $\bar{V}_h^+$ and $\bar{V}_h^-$, while V_h^+ and V_h^- are their corresponding magnitudes.

Consider now a new set of voltages $qv_\alpha(t) + jqv_\beta(t)$, characterized by two constraints::

- the corresponding phase displacements in $qv_\alpha(t) + jqv_\beta(t)$ lag the ones of $v_\alpha + jv_\beta$ by $\pi/2$ for the positive sequence components , while lead by the same quantity for negative sequences.
- The magnitude of $qv_\alpha(t) + jqv_\beta(t)$ matches the one associated to $v_\alpha + jv_\beta$ for each harmonic component, both at the direct and negative sequences.

As already pointed out in the previous analysis, resonant controllers in the SOGI produce a $-90°$ delay of the quadrature signal with respect to the direct one independently of the angular frequency, provided that it is positive; for negative angular frequencies, the outputs of $Q(s)$ will lead by $90°$ the one associated to $D(s)$ (Fig.6.6): thus the first constraint is met. As regards the equal magnitude condition, the functions $D(s)$ and $Q(s)$ do not show from a rigorous point of view the same magnitude profile: as a consequence, the exploitation of $D(s)$ and $Q(s)$ for the positive and negative sequence extraction is affected by an intrinsic error, even though numerically limited. Still this is acceptable considering that in correspondence to the resonance frequency the equal magnitude constraint is met and, out from the resonance, the mismatch is attenuated by the significant filtering action introduced by the functions.

Thus if (6.21) and (6.22) are the output of transfer function $D(s)$ according to the scheme reported in Fig. 6.3, the quadrature signals will be given by (6.23)-(6.24), which

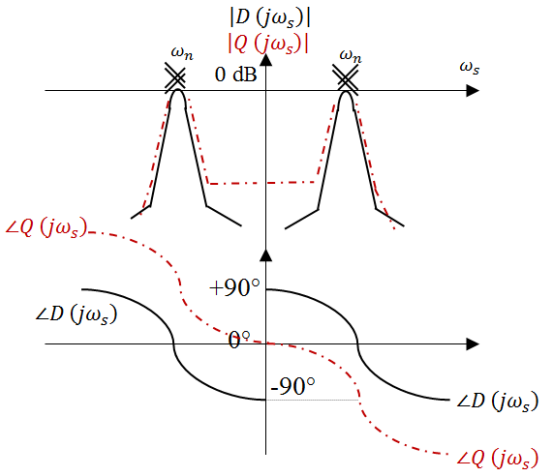

FIGURE 6.6: Extension of the transfer function $D(s)$ to the negative frequency range.

are approximatively equal to the output of $Q(s)$.

$$qv_{\alpha}^{+} = \sum_{h=1}^{N+} \left\{ |\bar{V}_h^{+}| \cdot \cos\left(h\omega t + \phi_h^{+} - \pi/2\right) \right\} \qquad qv_{\beta}^{+} = \sum_{h=1}^{N+} \left\{ |\bar{V}_h^{+}| \cdot \sin\left(h\omega t + \phi_h^{+} - \pi/2\right) \right\} \tag{6.23}$$

$$qv_{\alpha}^{-} = \sum_{h=1}^{N-} \left\{ |\bar{V}_h^{-}| \cdot \cos\left(-h\omega t + \phi_h^{-} + \pi/2\right) \right\} \qquad qv_{\beta}^{-} = \sum_{h=1}^{N-} \left\{ |\bar{V}_h^{-}| \cdot \sin\left(-h\omega t + \phi_h^{-} + \pi/2\right) \right\} \tag{6.24}$$

The application of easy trigonometric equalities to (6.23) and (6.24), combined with the definition in (6.21) and (6.22), leads to the following definitions:

$$qv_{\alpha}^{+} = v_{\beta}^{+} \qquad qv_{\alpha}^{-} = -v_{\beta}^{-} \qquad qv_{\beta}^{+} = -v_{\alpha}^{-} \qquad qv_{\beta}^{-} = v_{\alpha}^{+} \tag{6.25}$$

Thus:

$$qv'_{\alpha} = qv_{\alpha}^{+} + qv_{\alpha}^{-} = v_{\beta}^{+} - v_{\beta}^{-} \tag{6.26}$$

$$qv'_{\beta} = qv_{\beta}^{+} + qv_{\beta}^{-} = -v_{\alpha}^{+} + v_{\alpha}^{-} \tag{6.27}$$

The goal is now to derive the positive sequence components from the available signals (v'_{α},v'_{β},qv'_{α} and qv'_{β}); equations (6.17)-(6.18) and (6.26)-(6.27) define a 4^{th} order determined linear system that can easily lead to the expressions of positive and negative sequences from available signals.

$$v_{\alpha}^{+} = \frac{v_{\alpha} - qv_{\beta}}{2} \qquad v_{\beta}^{+} = \frac{qv_{\alpha} + v_{\beta}}{2} \tag{6.28}$$

$$v_{\alpha}^{-} = \frac{v_{\alpha} + qv_{\beta}}{2} \qquad v_{\beta}^{-} = \frac{-qv_{\alpha} + v_{\beta}}{2} \tag{6.29}$$

Equations (6.28)-(6.29) correspond to the block "Sequence extraction" reported in Fig. 6.3. The quantities v_{α}^{+} and v_{β}^{+} practically retain all the informations of the positive sequence component and thus can be used for the identification of the synchronization angle, obtained as $\theta = \arctan\left(\frac{v_{\beta}^{+}}{v_{\alpha}^{+}}\right)$. Regardless the widespread use of the SOGI scheme as converter synchronizer, in this work it is exclusively adopted for the identification of the angular frequency and its derivative, in the perspective of the synthetic inertia provision. Still the derivation of the sequence extraction formulas (6.28)-(6.29) will be used to modify the frequency locked loop algorithm in the proposed estimation scheme, that will be introduced in the next section: the combination of the highly disturbance-rejective SOSOGI architecture, combined with the sequence extraction from (6.28)-(6.29) and an additional compensation loop for the first-order negative component, will be the base for the development of a robust and noise-free estimator.

6.3 Second-Order Second-Order Generalized Integrator with inverse-sequence decoupling

Even though the SOGI architecture shows good filtering performances for high-order harmonic components that may be present in the grid, in order to estimate the angular frequency derivative with a good signal-to-noise ratio and in a fast way it is necessary to extend the above presented architecture in order to solve several issues associated to

the SOGI scheme. According to [30], the major critical point is the poor rejection of low-frequency components for the transfer function $Q(s)$, as the components with an angular frequency lower than the resonance one ω_n are only partially filtered by the factor $k_{sogi} = 2\xi$.

What it is generally not reported in literature regards the poor SOGI behaviour when a first-order inverse sequence component is included into the input voltages. If we refer to the Bode diagram extension in the negative frequency range (Fig.6.6), it is easy to recognize that the SOGI treats the first-order negative sequence in the same way as the fundamental one and does not provide any inner filtering effect for this component.

In this perspective, the architecture associated to the frequency-derivative estimator has to be modified in order to make it insensitive with respect to possible negative sequence components in the input voltage $\bar{v}_o$: the developed scheme is derived starting from the architecture proposed in [30] to reduce the issues related to low-harmonics and DC component rejection, with the addition of a negative-sequence compensation cell that allows to reconstruct the angular frequency of the input signal $\bar{v}_o$ in a robust and fast way. The proposed control is developed to provide pure sinusoidal direct-sequence signals to the FLL, thus allowing the extension of its internal pass-band and, by consequence, an improved response-speed of the estimation process.

Consider the scheme reported in Fig. 6.7 and the corresponding FLL architecture (Fig.6.8).

In the proposed architecture, the quadrature component qv'_α is previously filtered by $D(s)$ before entering into the block associated to the quadrature generator $Q(s)$, thus giving higher rejections for disturbance terms both at low and high frequency.

The evaluation of the SOSOGI architecture is taken into account under distorted grid conditions, in order to highlight the effects of the improvements with respect to the simple SOGI scheme. Consider as input of the system a generalized three-phase voltage

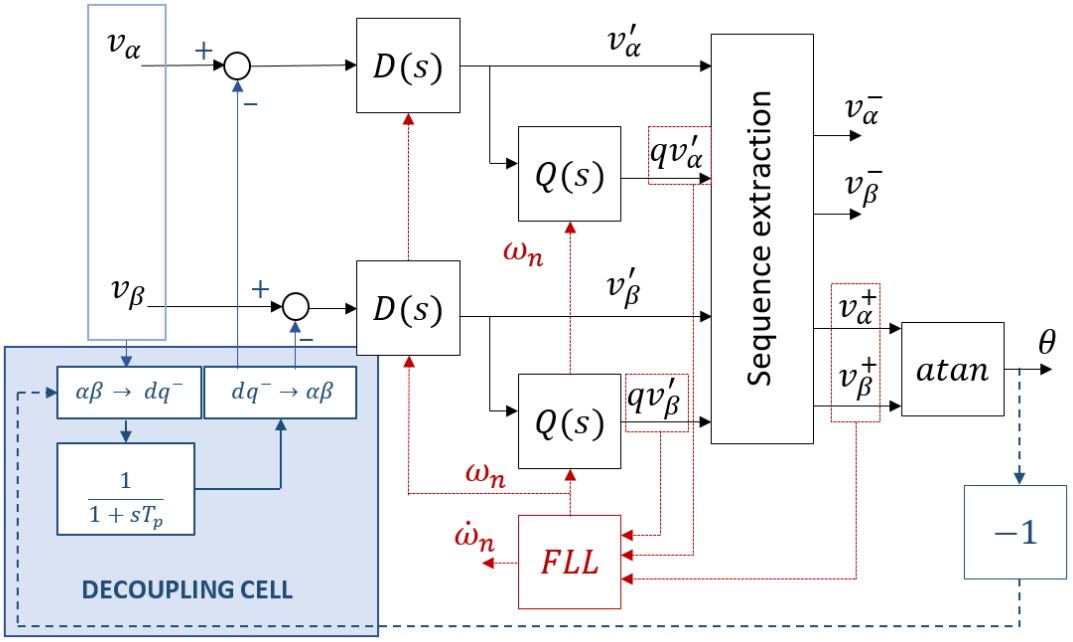

FIGURE 6.7: Proposed architecture for the extraction of angular frequency scheme: Second-Order/Second-Order Generalized Integrator with negative-sequence decoupling cell.

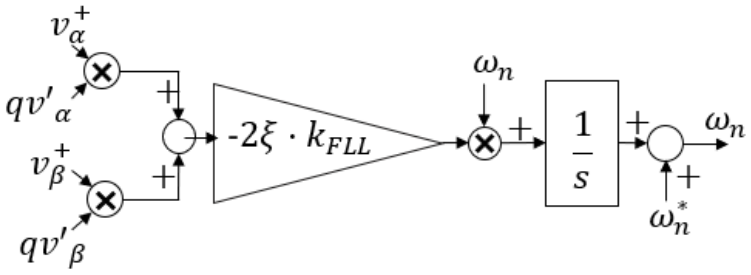

FIGURE 6.8: Representation of the FLL scheme, compliant with the SOSOGI architecture reported in Figure 6.7.

set in the Park domain, that can be expressed by the space vector $v_\alpha + jv_\beta$. The effect of the in-phase filter $D(s)$ defines the voltage set $v'_\alpha + jv'_\beta$, while the subsequent application of $Q(s)$ produces $qv'_\alpha + jqv'_\beta$

$$v_\alpha + jv_\beta = \sum_{h=1}^{N+} \bar{V}_h^+ \cdot e^{jh\omega t} + \sum_{h=1}^{N-} \bar{V}_h^- \cdot e^{-jh\omega t} \tag{6.30}$$

$$\begin{aligned} v'_\alpha + jv'_\beta = &\sum_{h=1}^{N+} \bar{V}_h^+ \cdot |D(jh\omega)|\, e^{jh\omega t + \measuredangle D(jh\omega)} + \\ &+ \sum_{h=1}^{N-} \bar{V}_h^- \cdot |D(jh\omega)|\, e^{-jh\omega t - \measuredangle D(jh\omega)} \end{aligned} \tag{6.31}$$

$$\begin{aligned} qv'_\alpha + jqv'_\beta = &\sum_{h=1}^{N+} \bar{V}_h^+ \cdot |Q(jh\omega)|\, |D(jh\omega)|\, e^{jh\omega t + \measuredangle D(jh\omega) + \measuredangle Q(jh\omega)} + \\ &+ \sum_{h=1}^{N-} \bar{V}_h^- \cdot |Q(jh\omega)|\, |D(jh\omega)|\, e^{-jh\omega t - \measuredangle D(jh\omega) - \measuredangle Q(jh\omega)} \end{aligned} \tag{6.32}$$

where the generalized frequency response magnitudes and phase displacements are given by:

$$|D(j\omega_s)| = \left| \frac{j2\xi\omega_s\omega_n}{\sqrt{(\omega_n^2 - \omega_s^2)^2 + (2\xi\omega_s\omega_n)^2}} \right| \tag{6.33}$$

$$|Q(j\omega_s)| = |D(j\omega_s)| \cdot \frac{\omega_n}{\omega_s} \tag{6.34}$$

$$\measuredangle D(j\omega_s) = \arctan \frac{\omega_n^2 - \omega_s^2}{2\xi\omega_s\omega_n} \tag{6.35}$$

$$\measuredangle Q(j\omega_s) = \arctan \frac{\omega_n^2 - \omega_s^2}{2\xi\omega_s\omega_n} - \frac{\pi}{2} \tag{6.36}$$

Unlike the traditional SOGI case, the relative angular displacement between each harmonic component of $v'_\alpha + jv'_\beta$ and $qv'_\alpha + jqv'_\beta$ is not fixed, as it is given by the angle $\measuredangle Q(j\omega)$. The combination of the filtering properties coming from the series connection of $D(s)$ and $Q(s)$ guarantees the almost complete absence of disturbance terms at the

FLL input, thus (6.31)-(6.32) simplify:

$$v'_\alpha + jv'_\beta \cong \bar{V}_1^+ \cdot |D(j\omega)|\, e^{j\omega t + \measuredangle D(j\omega)} + \\ + \bar{V}_1^- \cdot |D(j\omega)|\, e^{-j\omega t - \measuredangle D(j\omega)} \tag{6.37}$$

$$qv'_\alpha + jqv'_\beta \cong \bar{V}_1^+ \cdot |Q(j\omega)|\,|D(j\omega)|\, e^{j\omega t + \measuredangle D(j\omega) + \measuredangle Q(j\omega)} + \\ + \bar{V}_1^- \cdot |Q(j\omega)|\,|D(j\omega)|\, e^{-j\omega t - \measuredangle D(j\omega) - \measuredangle Q(j\omega)} \tag{6.38}$$

The representation of the signal inputs to the FLL is reported in Fig.6.8. According to this scheme, the sequence extraction formulas introduced in (6.28)-(6.29) are exploited to attenuate the effect of the remaining negative sequence component on the FLL dynamics; thus expressions (6.37)-(6.38) are substituted in (6.28)-(6.29) to reconstruct the $\alpha\beta$ components of the positive and negative sequences separately. Some easy trigonometric manipulations are applied during the substitution; furthermore, to simplify the procedure, it is assumed $|D(j\omega)| = |Q(j\omega)| = 1$. This is reasonable considering the transfer functions shapes and the fact that the FLL adapts the resonance frequency ω_n to be close to the fundamental ω. Nevertheless, the information related to the phase displacements ($\measuredangle D(j\omega)$ and $\measuredangle Q(j\omega)$) is retained as it represents the quantity associated to the resonance adaptation process in the FLL loop. The following expressions are thus derived:

$$v_\alpha^+ \cong V_1^+ \cos(\omega t + \frac{3}{2}\measuredangle D(j\omega) + \phi_1^+)\, \cos(\frac{\measuredangle D(j\omega)}{2}) + \\ - V_1^- \sin(\omega t + \frac{3}{2}\measuredangle D(j\omega) + \phi_1^-) \sin(\frac{\measuredangle D(j\omega)}{2}) \tag{6.39}$$

$$v_\beta^+ \cong V_1^+ \sin(\omega t + \frac{3}{2}\measuredangle D(j\omega) + \phi_1^+)\, \cos(\frac{\measuredangle D(j\omega)}{2}) + \\ + V_1^- \cos(\omega t + \frac{3}{2}\measuredangle D(j\omega) + \phi_1^-) \sin(\frac{\measuredangle D(j\omega)}{2}) \tag{6.40}$$

$$v_\alpha^- \cong - V_1^+ \sin(\omega t + \frac{3}{2}\measuredangle D(j\omega) + \phi_1^+)\, \sin(\frac{\measuredangle D(j\omega)}{2}) + \\ - V_1^- \cos(\omega t + \frac{3}{2}\measuredangle D(j\omega) + \phi_1^-) \cos(\frac{\measuredangle D(j\omega)}{2}) \tag{6.41}$$

$$v_\beta^- \cong - V_1^+ \cos(\omega t + \frac{3}{2}\measuredangle D(j\omega) + \phi_1^+)\, \sin(\frac{\measuredangle D(j\omega)}{2}) + \\ - V_1^- \sin(\omega t + \frac{3}{2}\measuredangle D(j\omega) + \phi_1^-) \cos(\frac{\measuredangle D(j\omega)}{2}) \tag{6.42}$$

If the input signal is distorted, v_α^+ retains the positive-sequence information included in $v_\alpha^{'}$, which are the ones of interest. Thus it is possible to use the signal v_α^+ instead of $v_\alpha^{'}$ as input of the FLL, to reduce the algorithm sensitivity with respect to negative sequence terms. According to the proposed scheme reproduced in Fig.6.8, the input of the FLL is obtained as $(v_\alpha^+ \cdot qv'_\alpha + v_\beta^+ \cdot qv'_\beta)$. Under the typical condition ${V_1}^+ >> {V_1}^-$,

the calculation leads to the following expressions for the FLL input:

$$v_\alpha^+ \cdot qv'_\alpha \cong \frac{V_1^{+2}}{2} \cdot \cos\left(\frac{\measuredangle D(j\omega)}{2}\right) \cdot \left[\sin\left(\frac{\measuredangle D(j\omega)}{2}\right) + \sin\left(2\omega t + \frac{7}{2}\measuredangle D(j\omega) + 2\phi_1^+\right)\right] \tag{6.43}$$

$$v_\beta^+ \cdot qv'_\beta \cong \frac{V_1^{+2}}{2} \cdot \cos\left(\frac{\measuredangle D(j\omega)}{2}\right) \cdot \left[\sin\left(\frac{\measuredangle D(j\omega)}{2}\right) + \sin\left(2\omega t - \frac{7}{2}\measuredangle D(j\omega) + 2\phi_1^+\right)\right] \tag{6.44}$$

$$(v_\alpha^+ \cdot qv'_\alpha + v_\beta^+ \cdot qv'_\beta) = V_1^{+2} \cdot \cos\left(\frac{\measuredangle D(j\omega)}{2}\right) \cdot \sin\left(\frac{\measuredangle D(j\omega)}{2}\right) \tag{6.45}$$

Provided that the resonance frequency ω_n is close to the fundamental one ω, the displacement angle $\measuredangle D(j\omega)$ is close to zero, thus it is possible to substitute the first order asymptotic behaviour for the trigonometric functions in (6.45):

$$(v_\alpha^+ \cdot qv'_\alpha + v_\beta^+ \cdot qv'_\beta) \cong V_1^{+2} \cdot \frac{1}{2}\measuredangle D(j\omega) \cong \frac{V_1^{+2}}{2} \cdot \arctan\left(\frac{{\omega_n}^2 - \omega^2}{2\xi\omega_n\omega}\right) \tag{6.46}$$

As the FLL itself imposes $\omega_n \cong \omega$, the asymptotic behaviour for the inverse tangent function leads to (6.47), where almost unitary amplitude of the fundamental positive-sequence Park voltage is assumed (in per-unit).

$$(v_\alpha^+ \cdot qv'_\alpha + v_\beta^+ \cdot qv'_\beta) \cong \frac{\arctan\left(\frac{{\omega_n}^2 - \omega^2}{2\xi\omega_n\omega}\right)}{2} \cong \frac{{\omega_n}^2 - \omega^2}{4\xi\omega_n\omega} \tag{6.47}$$

$$(v_\alpha^+ \cdot qv'_\alpha + v_\beta^+ \cdot qv'_\beta) \cong \frac{(\omega_n - \omega)(\omega_n + \omega)}{4\xi\omega_n\omega} \cong \frac{2\omega(\omega_n - \omega)}{4\xi\omega_n\omega} = \frac{\omega_n - \omega}{2\xi\omega_n} \tag{6.48}$$

The linearised expression (6.48) is exploited in order to tune the normalization coefficients in the loop, which is reported in Fig.6.9; the normalization coefficients allow to make the cut-off angular frequency of the FLL loop exclusively dependant on the design parameter $k_{FLL} = \tau_{FLL}^{-1}$.

As the FLL input exclusively depends on the filtered quantities (v^+ , qv'), the estimation is less sensitive to the external disturbances in the input voltage. This makes the proposed configuration much better than the traditional SOGI-FLL scheme presented in the previous section. Moreover, as it is possible to see from Fig. 6.7, it is also introduced a decoupling network for the reduction of inverse sequence effect.

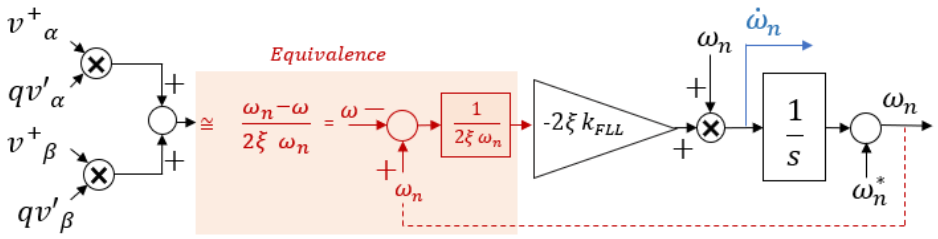

FIGURE 6.9: Linearised system for the SOSOGI-FLL architecture used for the regulation coefficient definition.

The previous analysis has shown that the main concern of the SOGI-FLL structure is associated to its inability in discriminating positive and negative sequences at the fundamental: the decoupling network allows to remove the inverse sequence by means of a feed-forward compensation scheme, avoiding any delay in the main control branch. The decoupling cell extracts the negative sequence from the input signal by means of an inverse angular rotation from the reference frame $\alpha\beta$ to dq^-. Subsequently, the inverse sequence is removed from the input signal to the SOSOGI architecture; the filter cut-off angular frequency T_p^{-1} is chosen ($T_p^{-1} << 2\omega_b$, $T_p^{-1} = 10$ rad/s), as to avoid interferences of the decoupling cell with the positive sequence component.

Under the conditions identified by the block diagram in Fig.6.9, the relation between the actual angular frequency ω and the estimated derivative $\dot{\omega}_n$ is given by:

$$\dot{\omega}_n = \frac{s}{1 + s/k_{FLL}} \cdot \omega = \frac{s}{1 + s\tau_{FLL}} \cdot \omega \tag{6.49}$$

Case studies in Table 6.2 are identified to test the algorithms performances.

6.4 Experimental results associated to the estimation of the angular frequency derivative

This section carries out an experimental comparison of the above presented estimation techniques on a real test environment. The general representation of the physical layout is provided in Appendix D, even though here the peculiar characteristics of this test will be explained (Fig. 6.11).

Two independent converters are operated in island, supplying a high resistive load. The first converter is operated in Grid-forming mode (Fig. 1.1(a)): according to this control architecture, the unit imposes whichever voltage profile at its AC terminals (both in amplitude and frequency), independently of the network conditions. The DC bus of this converter is connected to an external infinite-power source which provides the necessary capability for the system supply: in this case, the ideal source is obtained from the rectification of a three-phase voltage set from the public network, according to the scheme in Fig.6.11 (which is further explained in Fig.D.1). As in this case the entire microgrid operates at no-load, the supplied power is practically null at steady-state.

The second unit is operated in PQ mode (Fig. 5.7): as its DC bus is not supplied by any external source, at steady-state the reference active power is practically set equal to zero by the DC bus regulation, except for the tiny internal losses of the converter (${p^{ref}}_{dc} = 0$, in Fig. 5.7). The reactive reference is manually set to $q^{ref} = 0$. As no current is flowing in any of the microgrid branches, the voltage profile is practically equal in any position of the isolated network and it is exclusively determined by the grid-forming unit (Converter 1).

Once all these conditions are set, the tests can be performed. The microgrid is operated around the fundamental frequency (50 Hz) at almost unitary per-unit voltage.

Table 6.2: Design alternatives definitions for the SOSOGI algorithm

Case	ξ	Design criterion	$k_{FLL} = \tau_{FLL}^{-1}$
Slow SOSOGI	0.2	(6.15)	8.0 rad/s
Fast SOSOGI	0.2	Fast estimation	80 rad/s
Fast SOSOGI + dec. cell	0.2	Fast estimation	80 rad/s

Even though the microgrid voltages are ideally sinusoidal, the unbalances of the physical elements induce a tiny negative sequence component, whose amplitude is close to 2% of the fundamental. Furthermore, the non-linearities naturally present in any set-up produce other harmonic components (e.g. 5^{th} order negative sequence component, 7^{th} order positive sequence component). The three-phase voltage spectra associated to the steady-state microgrid voltages are reproduced in 6.10, respectively obtained from the measurements of the grid-forming converter (on the left) and of the grid-following one (on the right).

Two different conditions are tested. In the first one, the grid-forming converter imposes a constant angular frequency close to the nominal: these results are identified as *steady state* ones. In the second typology, the grid-forming converter imposes a non-constant frequency reference on the microgrid, according to a second-order oscillatory behaviour that exemplifies the typical transients experienced in power networks. The proposed algorithms are evaluated at steady state to analyse the disturbance rejection capabilities and during a frequency transient imposed by the grid-forming converter to assess the convergence performances; the comparison is carried out considering the estimated angular frequency, its derivative and the relative spectra.

It worth to highlight that no communication is established between the units; the grid-forming converter simply imposes a pre-determined voltage profile on the network, which is physically measured by the grid-following unit (Converter 2): as practically no current is flowing in the system, there is no consistent difference in the voltage profiles at the terminals of the two units.

The ideal angular frequency profile imposed by the first converter is known, as is set by the grid-forming control. The second converter, on the other hand, simply measures the quantities at its terminals (affected by the natural disturbances of the physical

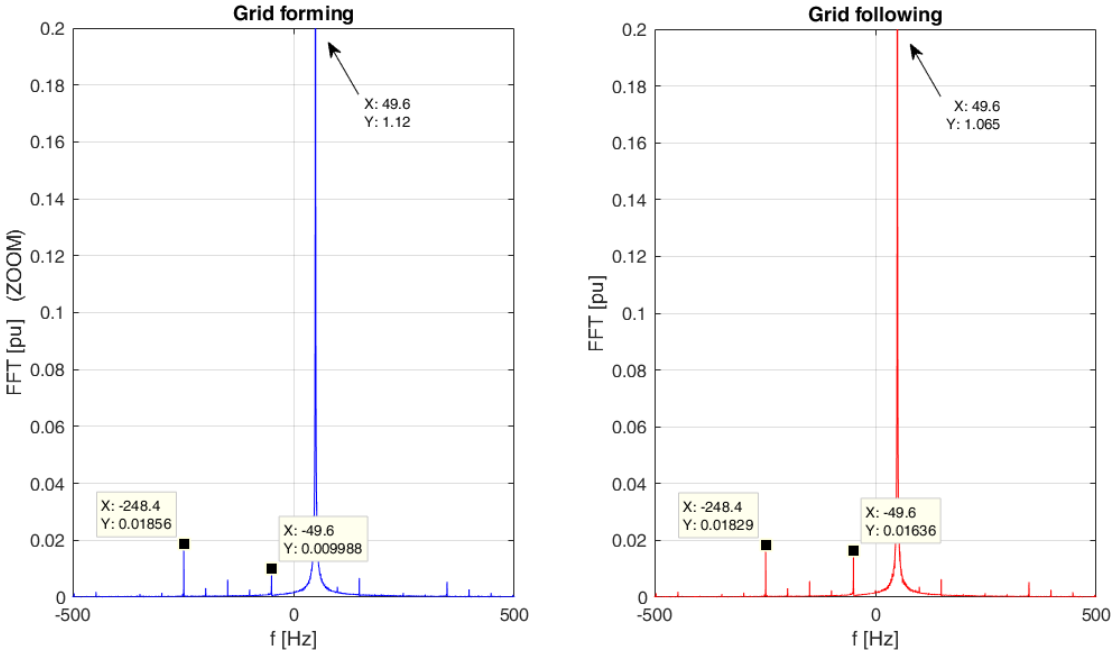

FIGURE 6.10: Spectrum associated to the set of three-phase voltages at steady state. Positive frequencies stand for the direct sequence components (space vectors in counter-clockwise direction), negative ones are the inverse sequences (clockwise direction). The left-side graph refers to the quantities as measured by the grid-forming converter, while the right-side one elaborates the measurements from the grid-following unit.

interface network) and reconstructs the angular quantities exploiting the above-presented estimators. Thus each graph shows two different time-series: the plot labelled as *real* corresponds to the ideal quantity imposed by the grid-forming unit, while *measured* stands for the reconstruction as seen by the grid-following converter.

The second unit is active (even though practically at no-load, $p^{ref}{}_{dc} = 0$ - $q^{ref} = 0$) and it is synchronized to the system by means of a traditional PLL; thus the estimation performed by means of the proposed SOGI / SOSOGI schemes does not influence its stability performances. This allows to carry out an equal and fair comparison between the techniques.

In the following subsections, the results of the experimental tests will be reported. The comments to the proposed results are included all together in Sect. 6.4.6; the considered control parameters are the ones in Tables 6.1 and 6.2.

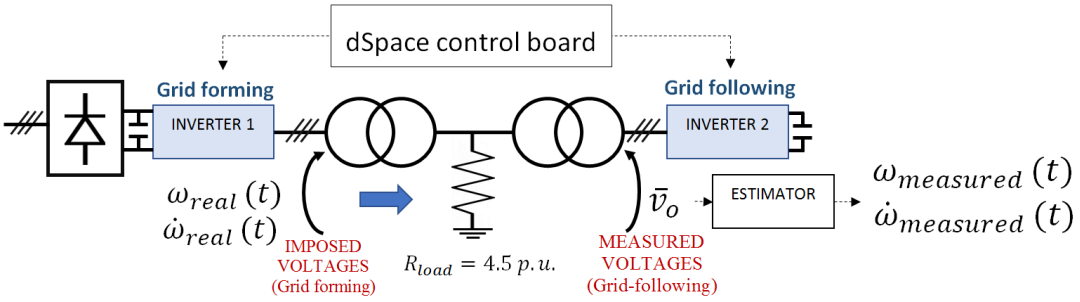

FIGURE 6.11: Scheme of the experimental set-up used for angular estimators comparison.

6.4.1 Slow SOGI ($K_{FLL} = 8.0 rad/s$)

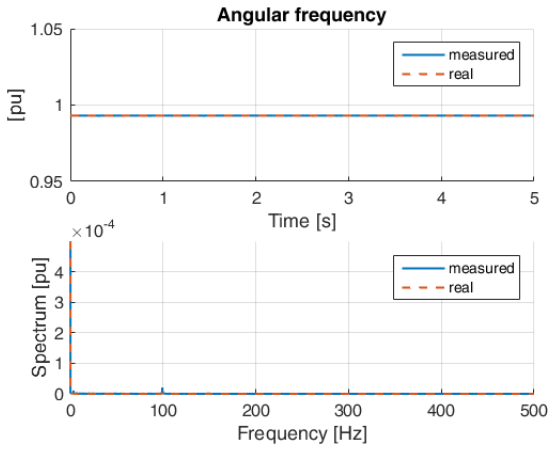

(a) Steady state ang. frequency

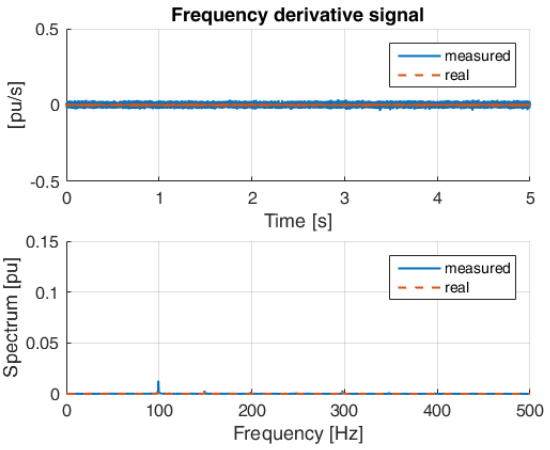

(b) Steady state ang. derivative

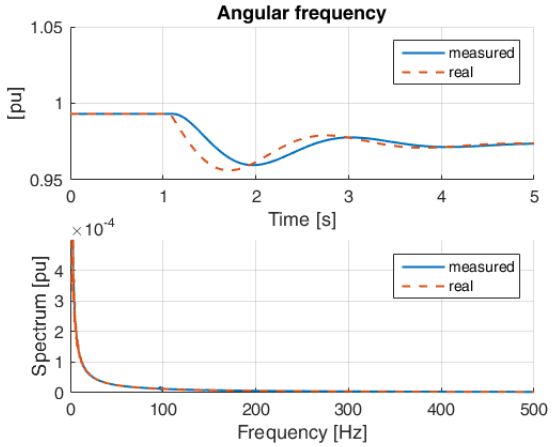

(c) Transient ang. frequency

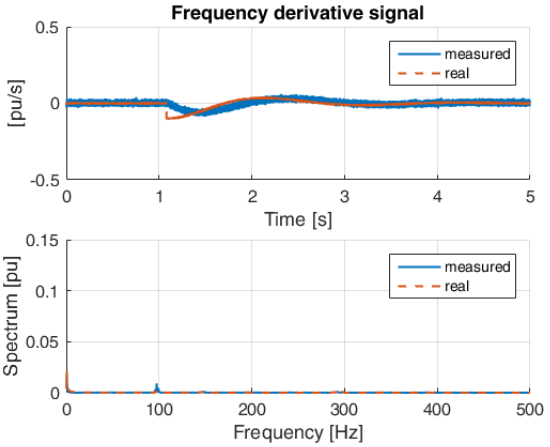

(d) Transient ang. derivative

FIGURE 6.12: Angular quantities for SOGI architecture with slow FLL. Plots report the comparison between the state imposed by the grid-forming unit (real) and the one measured by the grid-following converter. In (a) and (b) it is possible to see that the steady-state quantities are characterized by low harmonic disturbances, even though the estimation is slow during the transients (c)-(d).

6.4.2 Fast SOGI ($K_{FLL} = 80 rad/s$)

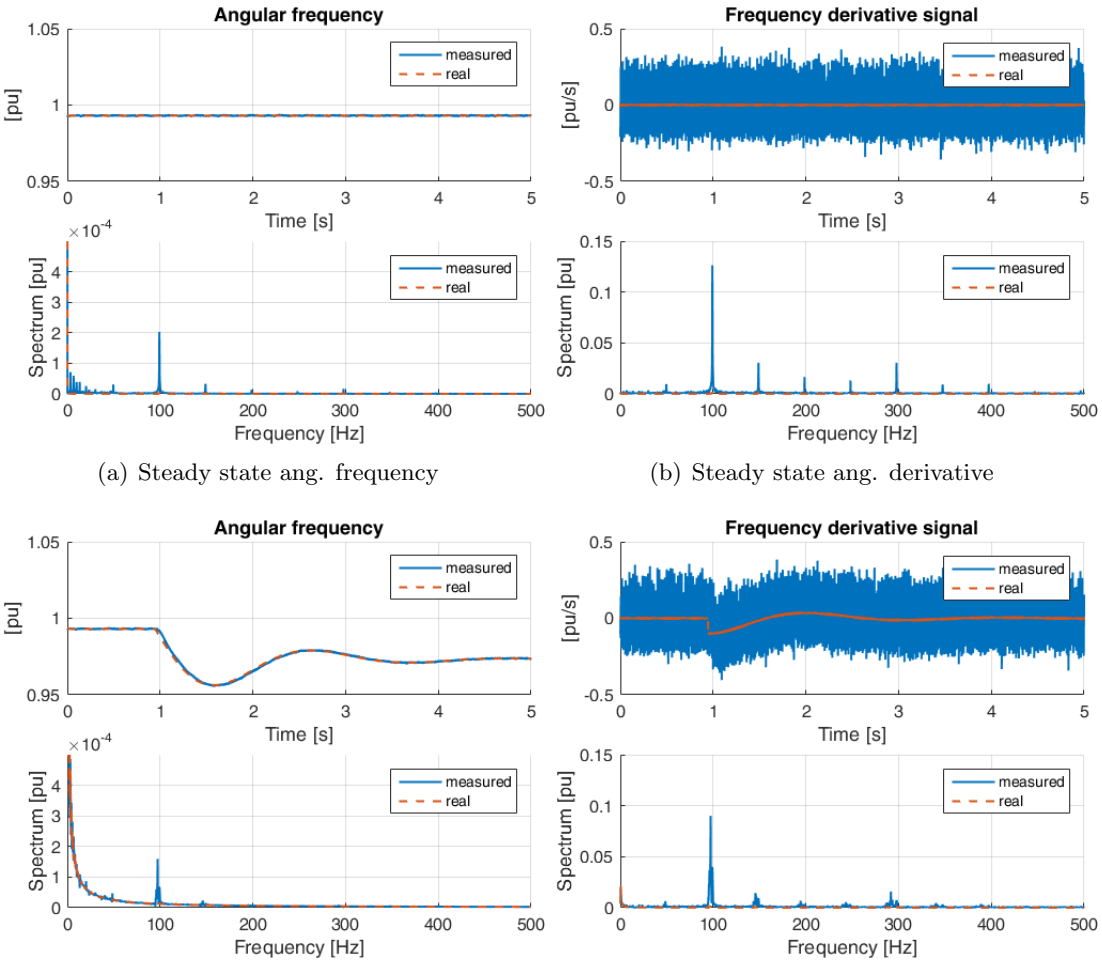

(a) Steady state ang. frequency

(b) Steady state ang. derivative

(c) Transient ang. frequency

(d) Transient ang. derivative

FIGURE 6.13: Angular quantities for SOGI architecture with fast FLL. Plots report the comparison between the state imposed by the grid-forming unit (real) and the one measured by the grid-following converter. The harmonic content of the estimation is particularly poor especially for the angular frequency derivative (b)-(d); nevertheless, the estimation is fast also during transients (c).

6.4.3 Slow SOSOGI ($K_{FLL} = 8.0 rad/s$)

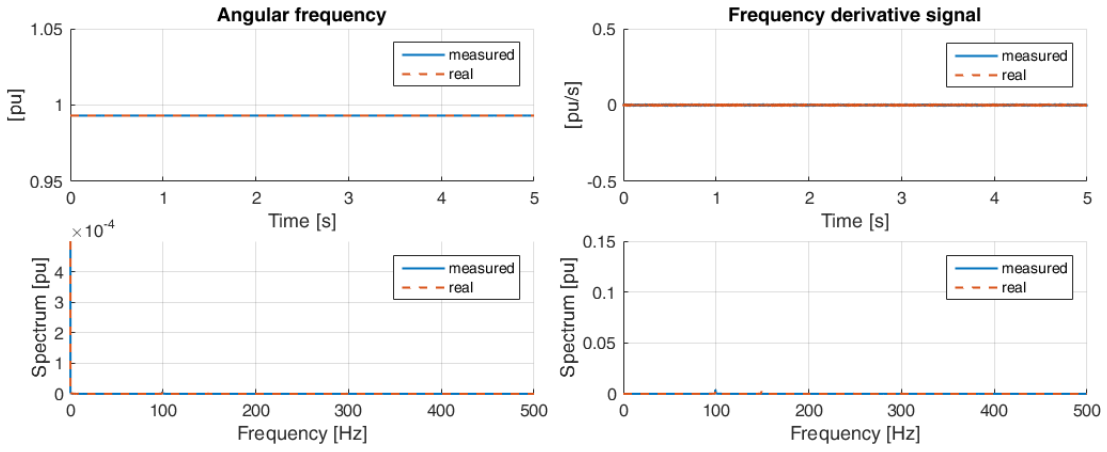

(a) Steady state ang. frequency

(b) Steady state ang. derivative

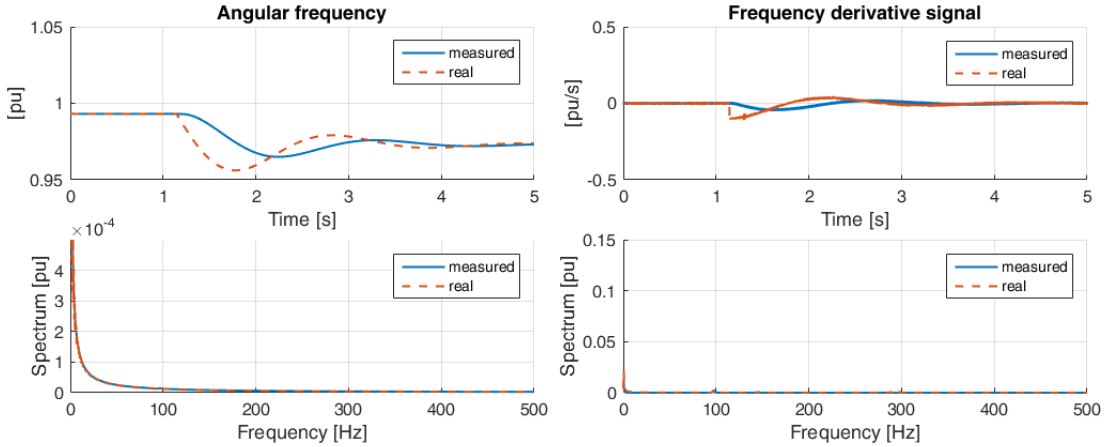

(c) Transient ang. frequency

(d) Transient ang. derivative

FIGURE 6.14: Angular quantities for SOSOGI architecture with slow FLL. Plots report the comparison between the state imposed by the grid-forming unit (real) and the one measured by the grid-following converter. In (a) and (c) it is possible to see that the steady-state quantities are characterized by low harmonic disturbances, even though the estimation is slow during the transients (b)-(d).

6.4.4 Fast SOSOGI ($K_{FLL} = 80 rad/s$)

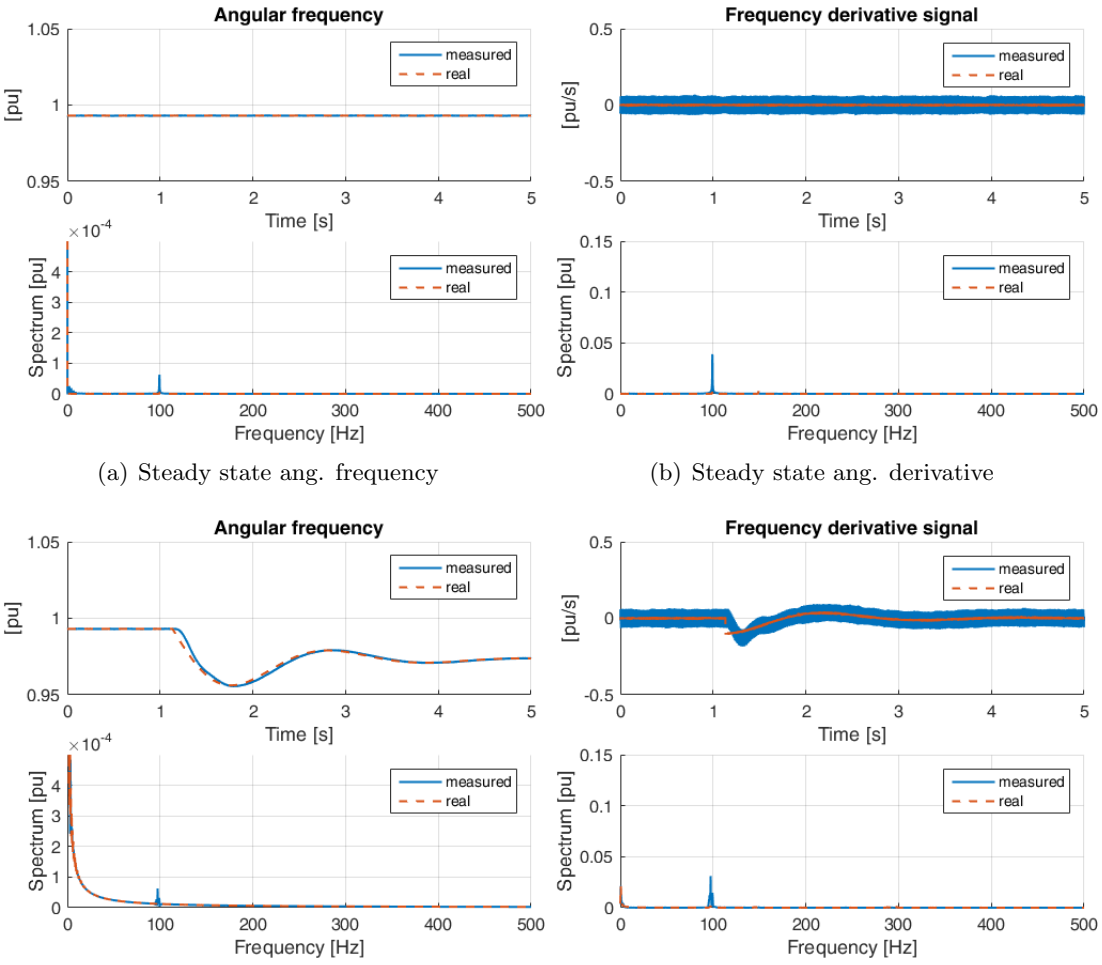

(a) Steady state ang. frequency

(b) Steady state ang. derivative

(c) Transient ang. frequency

(d) Transient ang. derivative

FIGURE 6.15: Angular quantities for SOSOGI architecture with fast FLL. Plots report the comparison between the state imposed by the grid-forming unit (real) and the one measured by the grid-following converter. Even though high-order harmonics are cancelled, still the effect of the negative sequence produces a disturbance at 100 Hz, both at steady-state (a)-(b) and during transients (c)-(d).

6.4.5 Fast SOSOGI with decoupling cell ($K_{FLL} = 80 rad/s$)

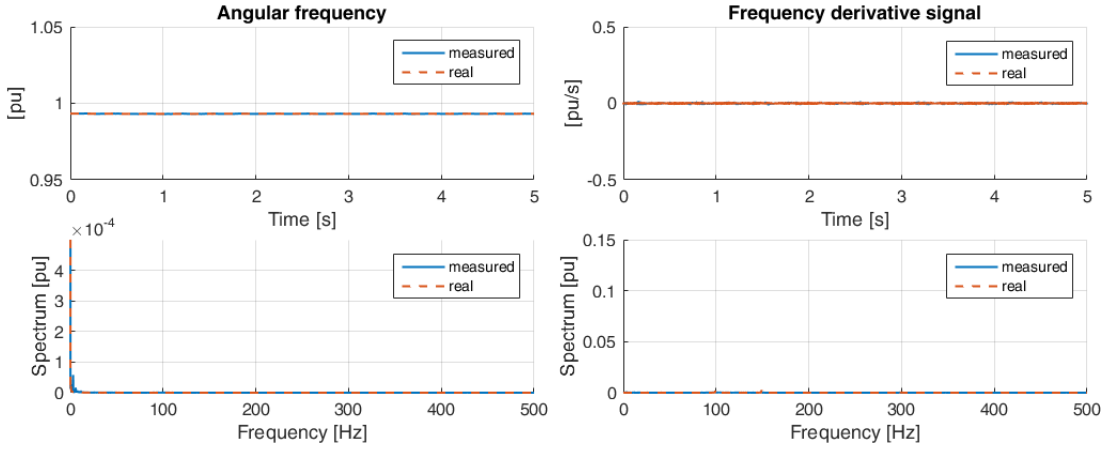

(a) Steady state ang. frequency

(b) Steady state ang. derivative

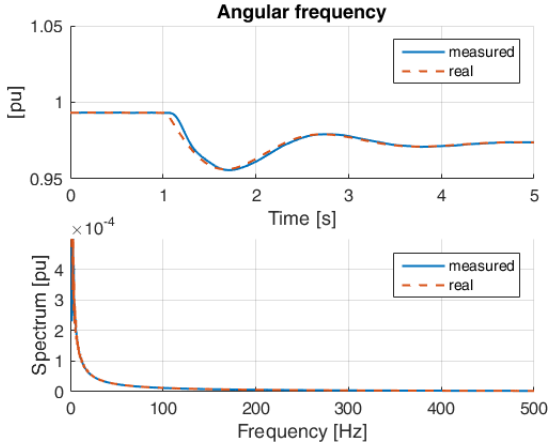

(c) Transient ang. frequency

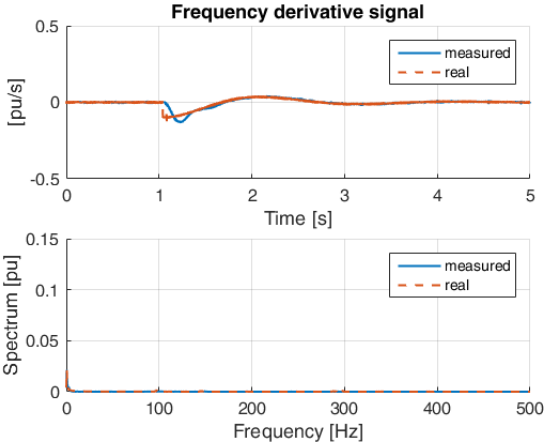

(d) Transient ang. derivative

FIGURE 6.16: Angular quantities for SOSOGI architecture with fast FLL and decoupling cell for the inverse sequence component. Plots report the comparison between the state imposed by the grid-forming unit (real) and the one measured by the grid-following converter. The proposed topology over-perform with respect to other techniques: the real and measured quantities are almost coincident in all the tested conditions.

6.4.6 Analysis of the results

The steady state and transitory behaviour reported in Fig. 6.12-6.16 show the time profiles and spectrum associated to the estimation techniques under test, both at steady-state and during a known network frequency transient imposed by the grid forming unit. The goal is to guarantee the best possible combination of noise rejection and convergence speed: this ensures a good signal-to-noise ratio for the reconstruction, while limiting the equivalent delay associated to the estimation.

Figure 6.12 refers to the case of a SOGI scheme, with slow FLL algorithm. Looking at the steady state profiles of the angular quantities in Fig.6.12(a)-6.12(b), it is easy to see that the algorithm guarantees a good rejection from system disturbances; nonetheless its performances significantly deteriorate during the frequency transients imposed on the network, as the slow pass-band of the FLL introduces a significant delay in the estimation of system derivative. From a dynamical point of view this aspect should be taken into

account carefully during the introduction of synthetic inertia, as a too high delay may reduce the phase margin associated to the control. Thus it is reasonable to investigate the possibility to a faster reconstruction of the derivative signal.

A first attempt reported in Fig.6.13 consists in the increase of the band-pass of the FLL. As regards the angular frequency, both at steady-state Fig.6.13(a) and during transients Fig.6.13(c), the SOGI algorithm performs well; on the other hand, the corresponding angular frequency derivative has a poor signal-to-noise characteristic 6.13(b)-6.13(d). The analysis of the spectrum in Fig. 6.13(b) allows to identify major disturbance components. The main criticality regards the presence of a strong inverse sequence: with respect to the synchronous angular frequency, the inverse sequence appears as an equivalent disturbance at $2f_n = 100\,\text{Hz}$, which produces a highly-distorted behaviour on the derivative signal. Furthermore, the spectrum in Fig. 6.13(b) highlights the presence of a higher-frequency disturbance located in correspondence to 300 Hz: this is the effect of the 5^{th} and 7^{th} components introduced by the physical non-linearities of the converter interface, as seen by the rotating synchronous frame. Even though the convergence time is acceptable, the reconstruction results ineffective because of the poor signal-to-noise ratio.

Figure 6.14 shows the reconstruction carried out by the SOSOGI, with slow FLL pass-band. Its noise rejection properties are good but the convergence time is characterized by the same unacceptable delay already identified in Fig. 6.12: as a consequence of its slow dynamic, it would induce a significant degradation of the phase margin in all the controls it would be exploited in.

On the other hand, the pass-band increase results inapplicable in terms of signal-to-noise ratio (Figure 6.15): if we compare the spectra with respect to the SOGI ones in Fig.6.13 characterized by the same regulation parameters, it is possible to observe a reduction of the disturbance terms at 300 Hz as a consequence of the higher filtering properties of the SOSOGI architecture. Nevertheless, this scheme it is still not able to completely cancel the impact of the first order negative sequence.

On the contrary, the introduction of the decoupling cell as proposed in Fig.6.7 guarantees a fast estimation of the angular quantities and an effective noise insensitivity: not only it provides good rejection with respect to the disturbance at 300 Hz, it almost completely cancel the effect of the negative sequence on the angular derivative estimation. Furthermore, its convergence time is comparable to the one of the SOGI scheme in Fig.6.12, even though it is possible to highlight the presence of a small oscillatory transient in the estimation. This is due to the more complicated interactions of the internal dynamics of the algorithm.

As a global consideration, it is possible to highlight that all the techniques guarantee an acceptable estimation of the angular frequency: still, as soon as they are evaluated in terms of frequency derivative, significant changes occur between the algorithms.

In order to assess in a numerical way the performances of the schemes, it is possible to define some numerical performance indexes associated to the curves above. According to the definitions, the higher it is the performance indexes, the better the system behaviour: the subscript "0" in the definition of the performance index indicates the average value of the estimation, which is physically obtained in correspondence of the DC component of the spectrum.

- Inverse of the Total harmonic distortion (THD) of the angular frequency signal (up to 500 Hz, at steady state); ω_0 is the value of the average fundamental component,

as seen from the synchronous frame.

$$PI_1^{-1} = THD_{\omega_g} = \frac{\sqrt{\sum_{h\neq 0}\omega_h^2 - \omega_0^2}}{\omega_0} \tag{6.50}$$

- Inverse of the harmonic content (HC) of the derivative signal (up to 500 Hz, at steady state)

$$PI_2^{-1} = HC_{\dot{\omega}_g} = \sqrt{\sum_{h\neq 0}^{500}\dot{\omega}_h^2} \tag{6.51}$$

- Inverse of the cumulative integral error between actual and estimated angular frequency:

$$PI_3^{-1} = \sum_{t=0}^{\mathrm{T}=5\ \mathrm{s}} |\omega_{\mathrm{real}}(t) - \omega_{\mathrm{measured}}(t)| \tag{6.52}$$

- Cumulative integral error between actual and estimated derivative:

$$PI_4^{-1} = \sum_{t=0}^{\mathrm{T}=5\ \mathrm{s}} |\dot{\omega}_{\mathrm{real}}(t) - \dot{\omega}_{\mathrm{measured}}(t)| \tag{6.53}$$

Table 6.3 shows the comparison of performance indexes between tested algorithms, highlighting how the developed technique is able to produce a fast and accurate estimate of the desired angular quantities. It is possible to see that the proposed algorithm is characterized by better performances in almost all the indexes: this means that the reconstructed quantities are almost identical to the ones imposed by the grid-forming converter and thus the estimation is minimally affected by physical disturbances.

Figure 6.17 shows the normalized performances indexes for each considered estimation technique; a global index PI_g, obtained from the arithmetic average of the single indexes for each tested algorithm, is introduced for synthetic evaluation. The higher value of this global indicator for the SOSOGI-N highlights the out-performances of the proposed strategy: both in terms of response speed and disturbance rejection, the developed scheme behaves better with respect to the available techniques reported in literature. In this perspective, the possibility to estimate in a fast and reliable way the evolution of the network represents the key enabling factor for the experimental validation of the inertia schemes that will be proposed in the following.

TABLE 6.3: Numerical comparison between angular quantities estimation techniques.

Estimator	PI_1 (6.50)	PI_2 (6.51)	PI_3 (6.52)	PI_4 (6.53)
Slow SOGI	$1.0 \cdot 10^4$	$5.2 \cdot 10^1$	$3.3 \cdot 10^{-2}$	$5.5 \cdot 10^{-3}$
Fast SOGI	$3.0 \cdot 10^4$	$5.3 \cdot 10^0$	$2.2 \cdot 10^{-1}$	$9.1 \cdot 10^{-4}$
Slow SOSOGI	$1.0 \cdot 10^4$	$1.7 \cdot 10^2$	$2.2 \cdot 10^{-2}$	$5.9 \cdot 10^{-3}$
Fast SOSOGI	$9.1 \cdot 10^3$	$1.7 \cdot 10^1$	$1.3 \cdot 10^{-1}$	$2.6 \cdot 10^{-3}$
Fast SOSOGI + dec. cell	$1.0 \cdot 10^4$	$2.3 \cdot 10^2$	$1.3 \cdot 10^{-1}$	$1.4 \cdot 10^{-2}$

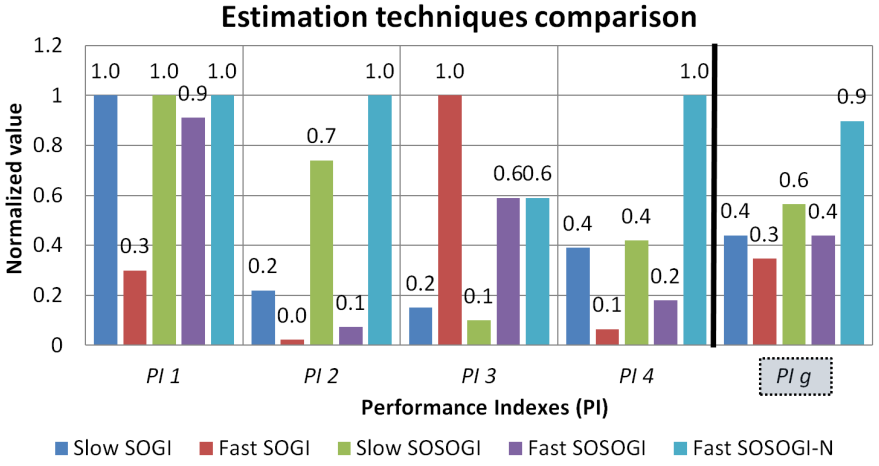

FIGURE 6.17: Normalized performance indexes for the tested estimators.

6.5 Voltage amplitude variation

In this section, the robustness of the developed algorithm against changes of the voltage amplitude (like the ones caused by short circuits and voltage sags) is analysed. In order to decouple the estimation of the fundamental angular frequency from the variation of input voltage amplitude, it is necessary to adopt the normalization scheme reported in Fig.6.18. This allows also to make the dynamical performances of the algorithms exclusively determined by the control parameters and not by the nominal voltage level.

Consider the set of three-phase voltages as acquired by the converter control system; at $t = 1\,sec.$ (Fig.6.19), a voltage sag equal to 50% of the nominal occurs. In order to prove the robustness of the estimation algorithm, a negative sequence component equal to 2% of the fundamental is added to the voltage profile, as well as 5^{th} and 7^{th} harmonics, with an amplitude of 2%. Additionally, a zero-sequence DC component of 1 V is added, in order to simulate voltage bias on the sensors, and a Gaussian noise with standards deviation $\sigma = 2.5\,V$ models the random non-biased errors in the acquisition process. The profile of the acquired three-phase voltages is reported in Fig. 6.19.

In Fig.6.20(a) the system is simulated without on-line normalization; it is possible to see that as soon as the voltage sag occurs, an undesired transient is measured both on the angular frequency ω and on its derivative $\dot{\omega} = \alpha$. This leads to misinterpretation of the

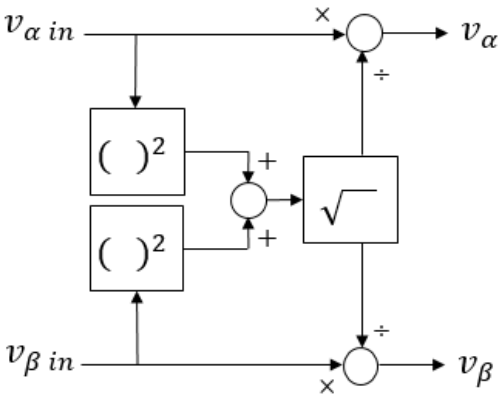

FIGURE 6.18: Normalization scheme for input voltages.

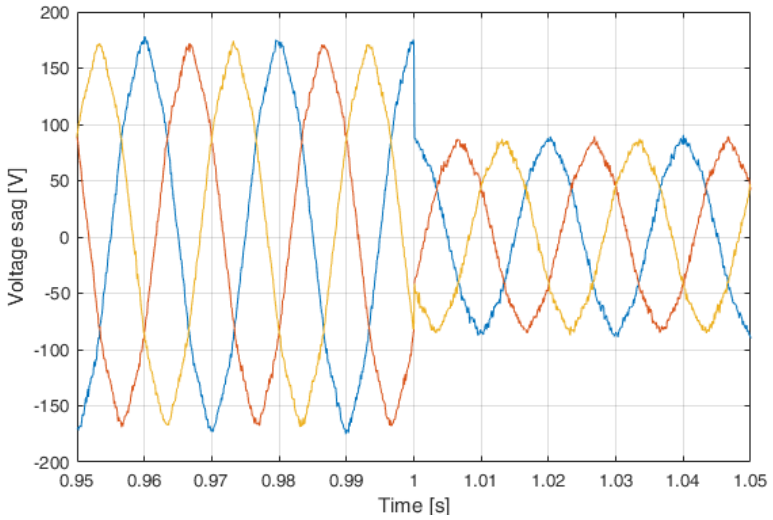

FIGURE 6.19: Actual zoomed profile of the three-phase voltages.

actual network status and to possible instability for the inertia provision. On the other hand, the introduction of the normalization scheme (Fig. 6.18), makes the estimation practically insensitive with respect to changes in the input voltage amplitude, allowing the reconstruction of the real system state 6.20(b).

6.6 Conclusion

In this chapter, several alternatives have been considered for the estimation of the system angular quantities; the analysis has been primarily focused on Generalized Integrators schemes [27] combined with a Frequency Locked Loop algorithm: this schemes are generally recognized as good solutions for angular quantities estimation as they do not require numerical derivation processes. Several alternatives have been taken into account, comparing their performances in terms of convergence speed and rejection of the disturbances (coming from the negative sequence and the harmonics naturally present in the network); moreover, it is shown that the combination of a SOSOGI scheme with a negative-sequence decoupling cell allows a very good reconstruction of the desired system states. Analytical procedures for the control parameters design have been reported in all the considered cases.

The proposed estimation scheme based on negative sequence compensation together with the changes carried out in the FLL loop to properly adapt to the SOSOGI scheme are new and unpublished. Furthermore, the representation of generalized integrators schemes as resonant controllers allows an easy tuning of all the control parameters involved in the estimation.

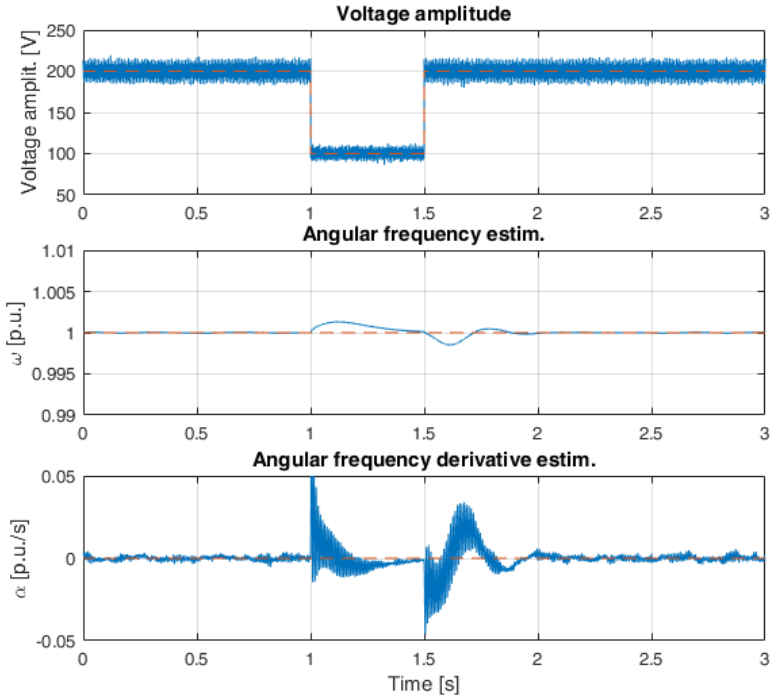

(a) Without on-line normalization of the input

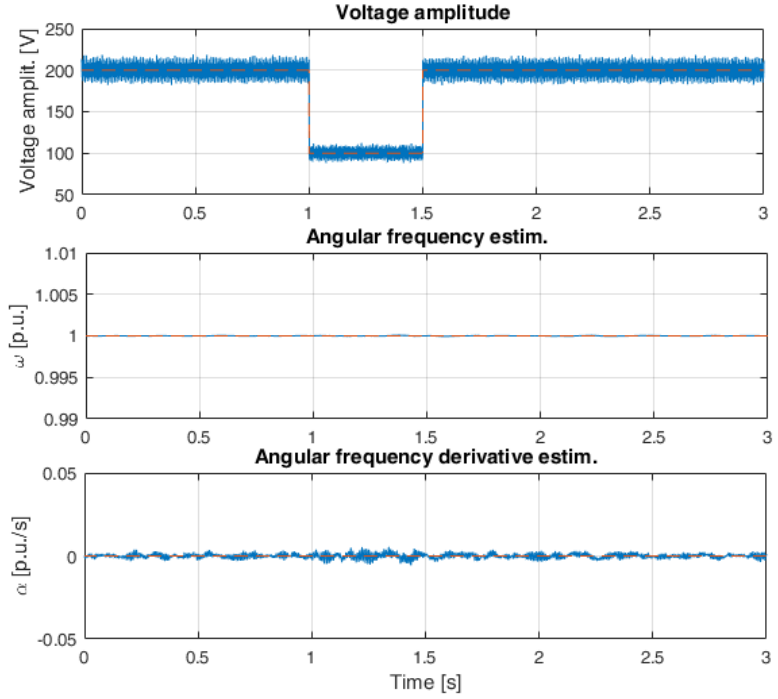

(b) With on-line normalization of the input

FIGURE 6.20: Comparison between estimated and real angular quantities without (a) and with (b) the proposed normalization scheme. A 50% voltage sag is applied to the voltages, to test the algorithm robustness.

Chapter 7

Current-controlled inertia

7.1 Introduction

In this chapter the control structure that provides inertia service to the system by means of a current-controlled injection will be analysed. The non-linear model of the system will be developed and design methods for the control coefficients will be presented.

7.2 Non-linear model of the converter under current-controlled inertia

Synthetic inertia function can be realised introducing an additional loop between the evolving dynamical state of the system, represented by the derivative of the angular frequency, and the injected power, as introduced in Sec. 5.10 (an reported again in Fig. (7.1) for clarity).

This creates a mutual dependence between the converter and the external grid: especially in case of comparable nominal power of the units, a wrong design of control parameters may lead to instability for the global system. Thus it is necessary to define a rigorous analytical model, able to predict the stability properties and design regulation parameters correctly.

Starting from the non-linear system of the PQ converter as developed in Fig.5.7, current-controlled inertia can be modelled as in Fig.7.2, where the additional feedback includes the external grid dynamics by means of the transfer function (5.10), expressed in the state-space form already introduced in (5.37) - (5.40).

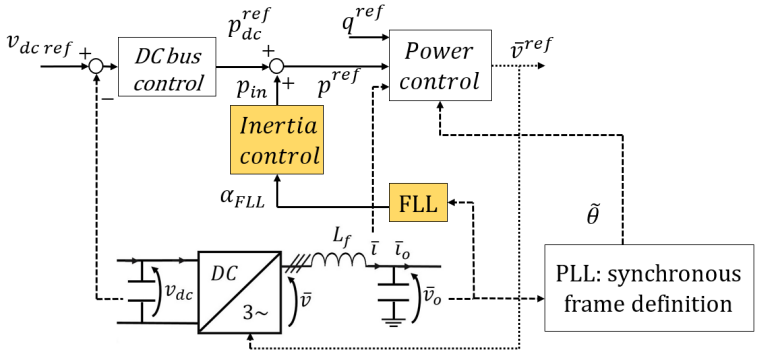

FIGURE 7.1: Control architectures for inertia support: current-controlled mode.

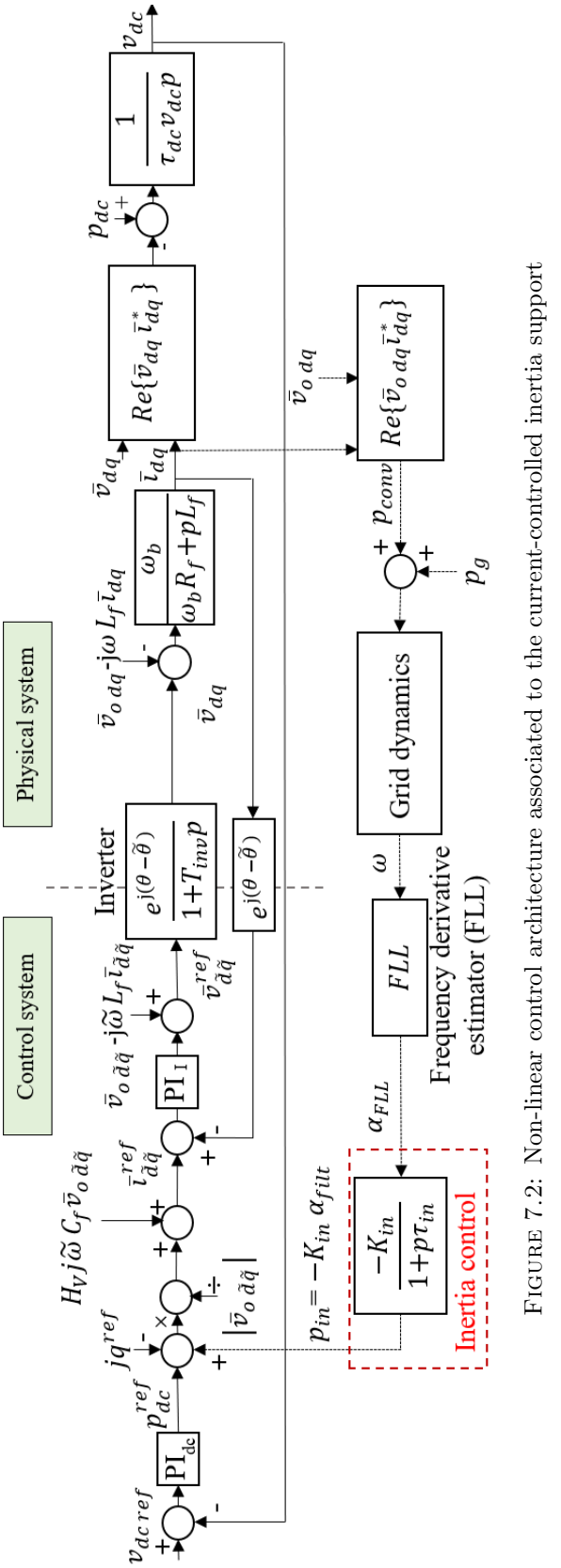

FIGURE 7.2: Non-linear control architecture associated to the current-controlled inertia support

The inertia control acts as an additional power reference p_{in}, proportional to the angular frequency derivative as estimated by the FLL algorithm introduced in Chapter 6; a first order low-pass filter with time constant τ_{in} defines the operational frequency range of the inertia support. The dynamical properties of the synthetic inertia loop are expressed by:

$$p_{in} = -K_{in} \cdot \alpha_{filt} \tag{7.1}$$

$$p\alpha_{\text{filt}} = \frac{1}{\tau_{in}} \cdot (\alpha_{FLL} - \alpha_{filt}) \tag{7.2}$$

$$p\alpha_{\text{FLL}} = \tau_{FLL} \cdot (\alpha - \alpha_{FLL}) \tag{7.3}$$

where the FLL behaviour in estimating the angular frequency derivative has been modelled according to (6.49), as shown in Chapter 6. The filtered derivative of the grid angular frequency, as estimated by the SOSOGI-FLL algorithm, represents the input signal for the inertia regulator. The decision to refer to the SOSOGI-FLL algorithm (Chapter 6) for the angular frequency estimation, instead of the available PLL used for converter synchronization, allows to keep independent dynamics between the inertia loop and the rotating control system.

Reference signals for the internal current loop are obtained, in the control frame $\tilde{dq}$.

$$i_{o\tilde{d}}^{ref} = \frac{p_{dc}^{ref} + p_{in}}{\left|\bar{v}_{o\,\tilde{dq}}\right|} \tag{7.4}$$

$$i_{o\tilde{q}}^{ref} = -\frac{q^{ref}}{\left|\bar{v}_{o\,\tilde{dq}}\right|} \tag{7.5}$$

Combining equations (7.1) - (7.5) with the state-space model introduced in Section 5.7, it is possible to analytically obtain the non-linear dynamical state-space model of the global system reported in Appendix A. This can be used for the identification of the equilibrium states, internal dynamics and participation factors associated to the control: in particular, it will be exploited to validate the approximated design models of the inertia loops, guaranteeing that the introduced simplifications are consistent from the dynamical perspective.

In Fig. 7.3 are shown the equivalent eigenvalues associated to the dynamical model of the system for case study 1 (Fast primary regulation - Tab. 5.1): numeric values associated to Fig. 7.3 are also reported in Table 7.1.

The determination of the dynamical dependence inside the system is crucial as it allows to identify which states can be neglected in the design process of the inertia

Table 7.1: Eigenvalues calculation without synthetic inertia introduction, CASE STUDY 1 with $K_{in} = 0$.

Eig. identifier	Numeric value $\left[s^{-1}\right]$	Eig. identifier	Numeric value $\left[s^{-1}\right]$
λ_1	-5.14	λ_2	-5.81
λ_3	-16.2	λ_4	-50.0
λ_5	-80.0	λ_6	-195
λ_{7-8}	$-405 \pm 5.30i$	λ_{9-10}	$-661 \pm 671i$
λ_{11-12}	$-2520 \pm 2150i$	λ_{13-14}	$-3210 \pm 2630i$
λ_{15-16}	$-6890 \pm 5260i$	λ_{17-18}	$-6900 \pm 5700i$

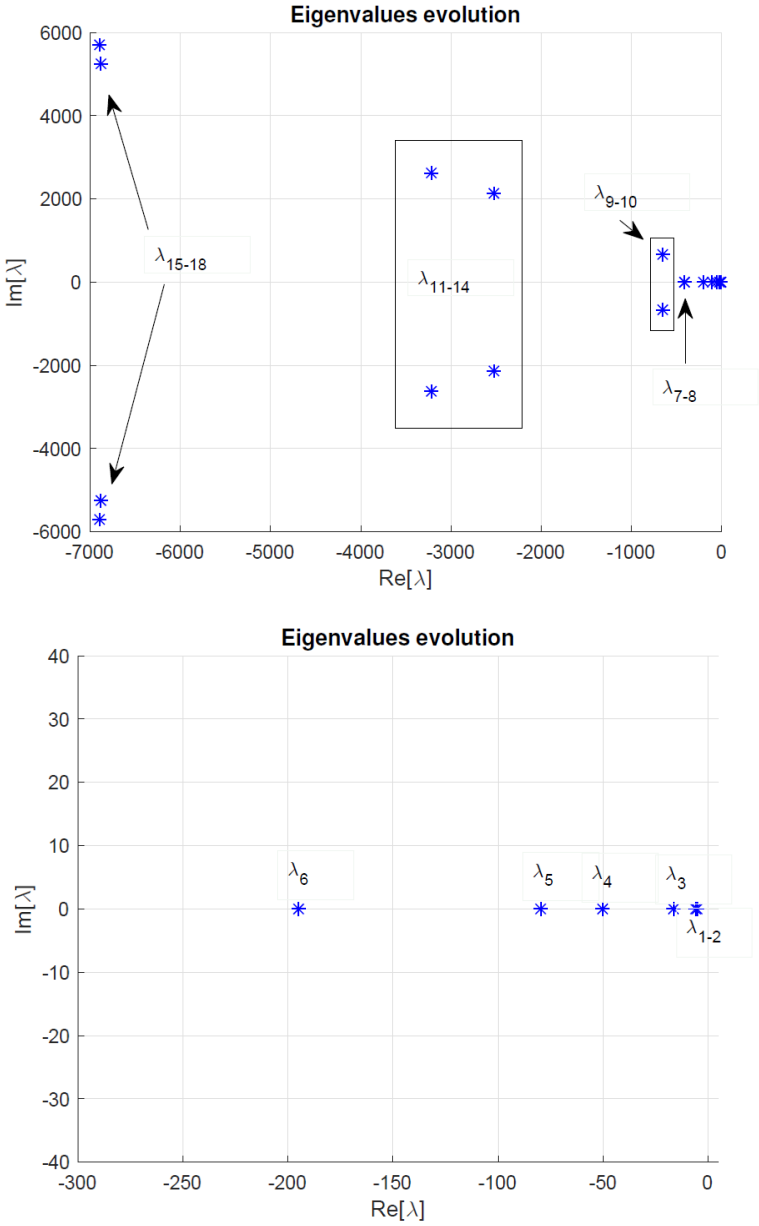

FIGURE 7.3: Eigenvalues position for CASE STUDY 1, without inertia ($K_{in} = 0$). The zoomed view around the origin is reported in (b), for a better identification of the slow dynamics.

regulation and which, on the other hand, should be taken into account. This can be done referring to the participation factors calculation, according to the procedure reported in [22]: results associated to the eigenvalues in Fig. 7.3 are reported in Fig. 7.4.

Three main time scales that can be studied independently of one another:

- Dominant eigenvalues (λ_{1-6}) principally depend on the internal dynamics associated to the grid swing equation (α, ω), to DC bus regulation (v_{dc}, E_{dc}) and synthetic inertia control (represented by the estimated angular frequency derivative from the FLL α_{FLL} and its filtered version α_{filt}).
- A second group of eigenvalues (λ_{7-10}) identifies the effects of the internal current regulator and of the synchronous angle definition by means of the PLL.

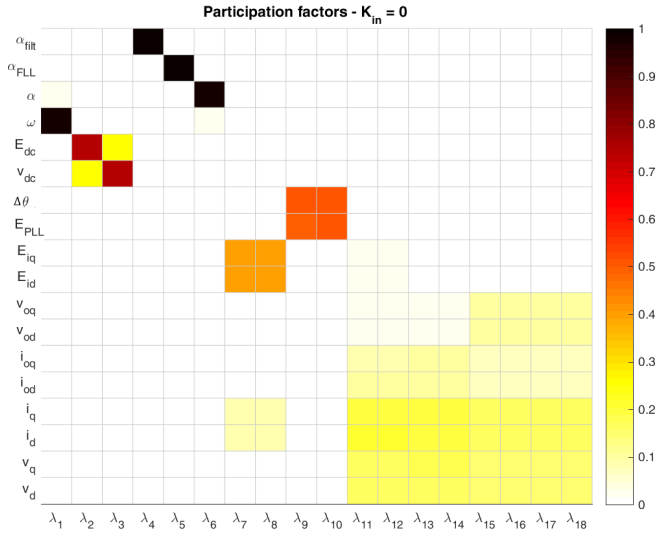

FIGURE 7.4: Participation factors for CASE STUDY 1, without inertia ($K_{in} = 0$). Null production from the primary source is considered: $I_{dc} = 0$.

- Fastest eigenvalues (λ_{11-18}) include high-frequency transients associated to the physical circuit of the system. Even though they show significant mutual influence caused by the physical circuit coupling, they are practically independent of the other parts into the system.

This allows to define a simplified design model which includes only the dominant dynamics identified by means of the reported participation factors analysis. Moreover, it is worth noting the validity of the proposed approach independently of the actual injection from the primary source: performing a similar analysis under maximum production from the primary source ($I_{dc} = 1$ p.u.), the pattern reported in Fig. 7.5 can be obtained. Even though the dependence with respect to state variables differs from the no-load case in Fig. 7.4, still it is possible to reduce the analysis of the problem to the dominant eigenvalues $\lambda_1 - \lambda_6$.

All the considerations introduced up to now remain valid also for CASE STUDY 2 (where the regulation unit is a traditional synchronous generator, Tab. 5.2), considering the values in Fig. 7.6 and Tab. 7.2. The participation factor analysis in Fig.7.7 reveals the maintained dynamical conditions highlighted for case study 1, with three state variable subsets associated to almost-independent ranges of the frequency spectrum. Moreover even though eigenvalues λ_1 and λ_6 remain the ones connected to the internal dynamics of the grid, they show a different nature with respect to the ones in CASE STUDY 1. In particular Table 7.2 highlights the presence of a slow couple of complex-conjugate dynamics associated to the grid state (λ_{1-6}).

Even though the equivalent nature of the grid is different, it is reasonable to derive the simplified linearised model of the system associated to the current-controlled inertia as reported in Fig. 7.8 for the direct component (the one related to the active power balance). The introduced simplifying assumptions are consistent in the perspective of the participation factor analysis reported before:

- the internal dynamics of the PLL and the damping filter ones have been neglected, as they typically act in the high-frequency range of the spectrum.

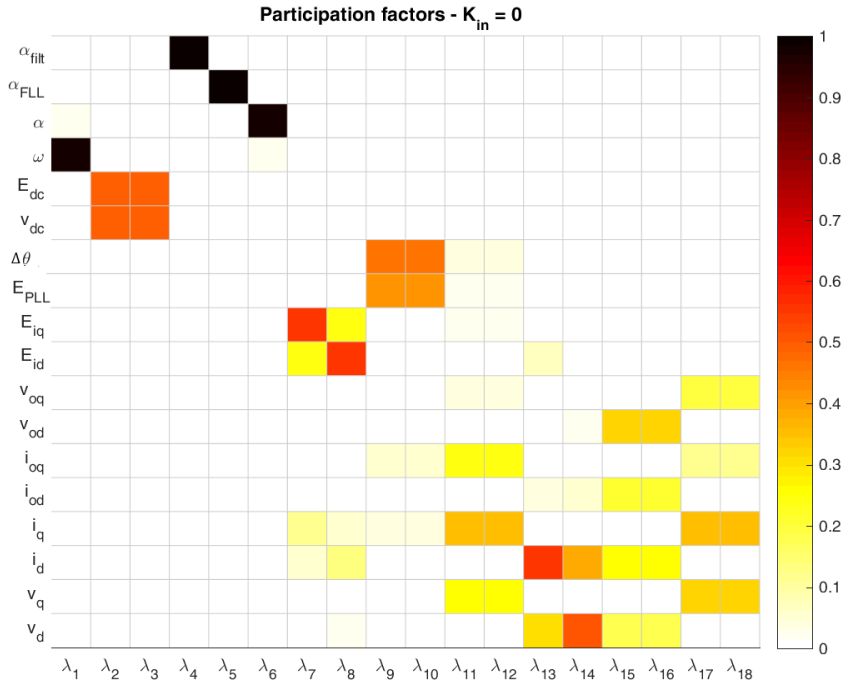

FIGURE 7.5: Participation factors for CASE STUDY 1 (Fast primary reg., Tab. 5.1), without inertia ($K_{in} = 0$). Maximum production from the primary source is considered: $I_{dc} = 1$ p.u.; even though the participation pattern is different from the one reported in Fig. 7.4, the independence of the slow grid dynamics with respect to the production level I_{dc} persists.

TABLE 7.2: Eigenvalues calculation without inertia introduction, CASE STUDY 2 with $K_{in} = 0$ ($I_{dc} = 0$).

Eig. identifier	Numeric value $[s^{-1}]$	Eig. identifier	Numeric value $[s^{-1}]$
λ_{1-6}	$-1.0 \pm 3.1i$	λ_2	-5.8
λ_3	-16	λ_4	-50
λ_5	-80		
λ_{7-8}	$-400 \pm 5.3i$	λ_{9-10}	$-660 \pm 670i$
λ_{11-12}	$-2.5 \cdot 10^3 \pm 2.2 \cdot 10^3\, i$	λ_{13-14}	$-3.2 \cdot 10^3 \pm 2.6 \cdot 10^3\, i$
λ_{15-16}	$-6.9 \cdot 10^3 \pm 5.2 \cdot 10^3\, i$	λ_{17-18}	$-6.9 \cdot 10^3 \pm 5.7 \cdot 10^3\, i$

- Internal current loop is approximated as a first order transfer function, with pole pulsation equal to the cut-off angular frequency ω_{cI} of the current loop.

$$K_I(s) = \frac{1}{1 + s/\omega_{cI}} \tag{7.6}$$

- The internal dynamics of the SOGI-FLL are represented as an approximated derivative, according to the model reported in (6.49). Thus the procedure to extract the angular frequency derivative α_{FLL} can be expressed by:

$$K_{FLL}(s) = \frac{\alpha_{FLL}}{\omega} = \frac{s}{1 + s\,\tau_{FLL}} \tag{7.7}$$

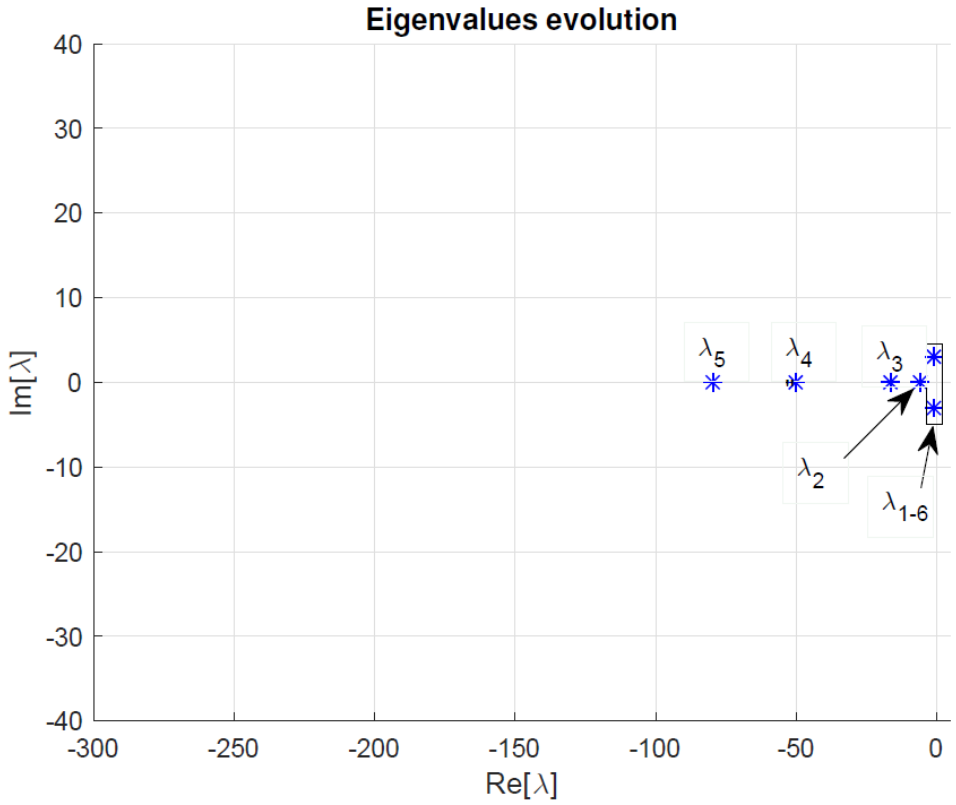

FIGURE 7.6: Eigenvalues position for CASE STUDY 2 (Slow primary reg., Tab. 5.2), without inertia ($K_{in} = 0$). The significant delay introduced by the primary frequency regulation units produces a couple of low-damped complex conjugate eigenvalues at low frequency; high pulsation dynamics are not reported as they are coincident with the ones already plotted in Fig.7.3-(a).

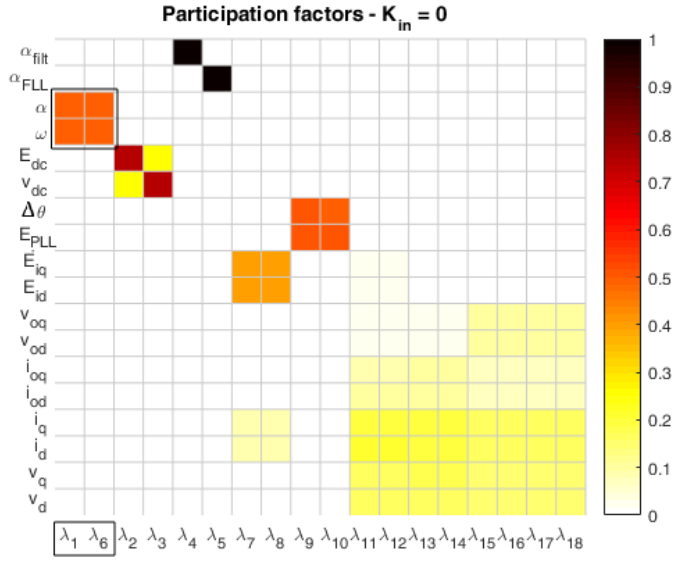

FIGURE 7.7: Participation factors for CASE STUDY 2, without inertia ($K_{in} = 0$). Null production from the primary source is considered: $I_{dc} = 0$.

- Grid dynamics are represented by the equivalent transfer function (5.10), here recalled, which takes into account the primary frequency regulation effect by means of the coefficient K_{reg}, the regulation delay τ and the equivalent starting time of the system T_a, which includes the inertia properties of the network. Differently from the case with no synthetic inertia, now also the converter power Δp_{conv} contributes has an influence in the transient.

$$\Delta\omega = \frac{1 + s\,\tau}{s^2\,T_a\,\tau + s\,T_a + K_{reg}} \cdot (\Delta p_g + \Delta p_{conv}) = K_g(s) \cdot (\Delta p_g + \Delta p_{conv}) \tag{7.8}$$

Once the linearised model is derived, the design of the inertia loop is carried out considering the mutual interaction of the dynamics included in the model of Figure 7.8, which can be simplified as in Figure 7.9. Open-loop function $L_{in}(s)$ can thus be determined as:

$$L_{in}(s) = K_I(s) \cdot K_g(s) \cdot \frac{K_{in}}{1 + s\tau_{in}} \cdot K_{FLL}(s) = \tag{7.9}$$

$$= \frac{1}{1 + s/\omega_{cI}} \cdot \frac{1 + s\,\tau}{s^2\,T_a\,\tau + s\,T_a + K_{reg}} \cdot \frac{K_{in}}{1 + s\tau_{in}} \cdot \frac{s}{1 + s\,\tau_{FLL}} \tag{7.10}$$

The model in (7.10) will be analysed for the case of inertia support in a fast-regulating microgrid for slow primary regulation, highlighting the frequency transients improvements obtained with the introduction of synthetic inertia. Moreover, a new equivalent transfer function $K'_g(s)$ will be derived, which represents the modified grid dynamics after the introduction of the emulated inertia.

Asymptotic stability conditions will be derived analytically from the dynamical model of the system: in this case, it is possible to design the inertia loop taking into account the characteristics of the external network in a robust and straightforward way.

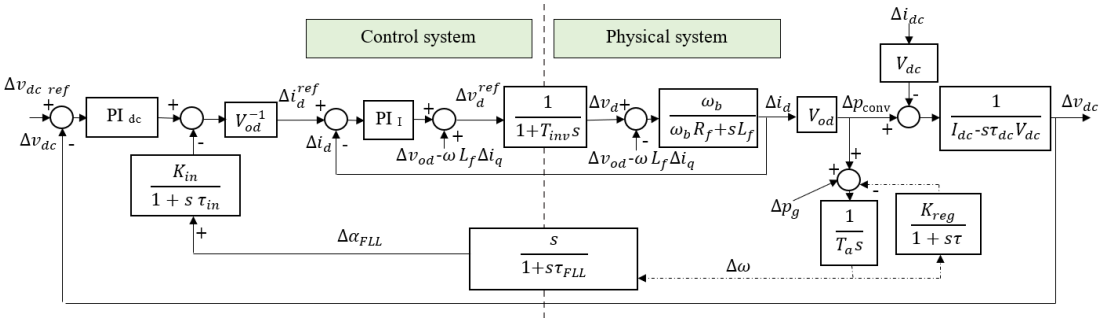

FIGURE 7.8: Current-controlled inertia: linearised models for direct axis.

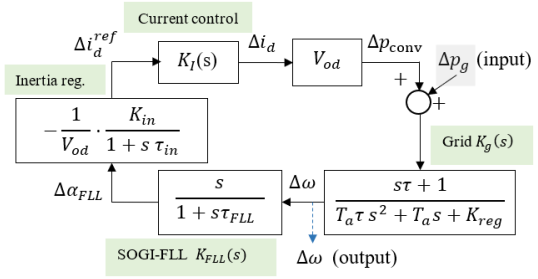

FIGURE 7.9: Simplified model for the design of the current controlled inertia loop: only the direct axis is associated to the stability of the frequency support

7.3 CASE STUDY 1: mathematical model

As already highlighted from the analysis of the participation factors for case study 1 reported in 7.4, both the eigenvalues λ_1 and λ_6 show a strong dependence on the grid state variables (α, ω), even though their numeric values show different order of magnitude. This behaviour can be easily explained considering the approximated singularities of transfer function (7.8), combined with the equivalence in (5.18) and with the numerical values associated to case study 1 (Tab. 5.1). Given the limited value of the equivalent delay τ associated to the external balancing of the network, a pole-zero simplification occurs in the dynamical model of the grid at high-frequencies. Asymptotic expression of the poles under condition $\tau << \frac{T_a}{4\,K_{reg}}$ leads to (7.11).

$$p_{1,2} = -\frac{1}{2\tau} \cdot \left(1 \pm \sqrt{1 - \frac{4\,K_{reg}\tau}{T_a}}\right) \cong -\frac{1}{2\tau} \cdot \left[1 \pm \left(1 - \frac{2\,K_{reg}\tau}{T_a}\right)\right] = \begin{cases} p_1 = -\frac{K_{reg}}{T_a} \\ p_2 = -\frac{1}{\tau} \end{cases} \tag{7.11}$$

The equivalent grid function can be approximated as a first order system, with a time constant determined by the primary regulation coefficient K_{reg} and the internal inertia of the system defined by the starting time T_a. Thus, for $\tau << \frac{T_a}{4\,K_{reg}}$, the grid function becomes:

$$K_g(s) \cong \frac{1}{s\,T_a + K_{reg}} \tag{7.12}$$

Thus it is possible to define a design model able to determine simplified stability conditions for the inertia-controlled loop under fast primary regulation. The equivalent loop function changes from (7.10) to (7.13), where also the effect of internal current loop is neglected.

$$L_{in}(s) = \frac{1}{s\,T_a + K_{reg}} \cdot \frac{K_{in}}{1 + s\tau_{in}} \cdot \frac{s}{1 + s\,\tau_{FLL}} \tag{7.13}$$

The modified grid function $K'_g(s)$ is obtained considering the closed-loop dynamics between the variation of the system accelerating power Δp_g and the angular frequency $\Delta\omega$. Thus from Fig. 7.9 one can obtain:

$$K'_g(s) = \frac{\Delta\omega}{\Delta p_g} = \frac{K_g(s)}{1 + L_{in}(s)} \cong \frac{1}{(T_a + K_{in})s + K_{reg}} \tag{7.14}$$

Figure 7.10 shows the effect associated to the introduction of inertia emulation on the equivalent grid function $K'_g(s)$, compared to the original one $K_g(s)$. Increasing the coefficient K_{in} moves the equivalent pole of the grid to a slower angular frequency (Fig. 7.10), contributing to the reduction of frequency transients derivative on the network.

Pole $\omega_p = \frac{K_{reg}}{T_a}$ associated to the grid model moves to the pulsation $\omega'_p = \frac{K_{reg}}{T_a + K_{in}}$, reducing the equivalent characteristic time constant associated to the frequency transient (Fig. 7.10-(a)).

Moreover the identification of the asymptotic transfer function in Fig. 7.10-(b) allows to define a set of design constraints for the system under study. The followed approach is based on the inclusion of equivalent grid parameters into the model definition. In fact, these are typically affected by a low variability during normal operations of the system.

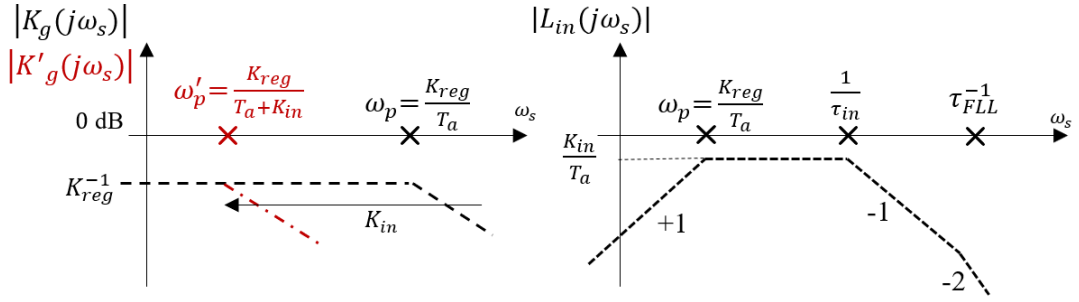

FIGURE 7.10: Asymptotic behaviour for the current-controlled inertia loop functions in case study 1. In (a) the initial and modified grid dynamics are reported, represented by $K_g(s)$ and $K'_g(s)$ respectively; in (b), the open-loop function $L_{in}(s)$ allows to identify the stability conditions for the control.

7.3.1 Design approach A

A too conservative approach for the design of maximum inertia coefficient K_{in} would be based on the small-gain theorem: imposing the magnitude of the loop function $|L_{in}(s)|$ lower than one in its maximum value, asymptotic stability of the feedback loop is guaranteed by the absence of $0\,dB$ intersections of the loop function $L_{in}(s)$. From the asymptotic behaviour reported in Fig. 7.10-(b), it is easy to recognize that the maximum magnitude for the loop function $L_{in}(s)$ is obtained when the two poles associated to the FLL and inertia time constant τ_{in} are located at a higher frequency with respect to the grid singularity.

Thus a maximizer of the open-loop function magnitude in $\left[\omega_p; \frac{1}{\tau_{in}}\right]$ can be easily derived:

$$L_{in}(j\omega_s) \cong \frac{K_{in}}{T_a} \qquad \text{for } \omega_s \in \left[\frac{K_{reg}}{T_a}; \frac{1}{\tau_{in}}\right] \tag{7.15}$$

Approximation (7.15) determines the following criterion for the coefficient K_{in} design:

$$|L_{in}(s)| < 1 \quad \forall \omega_s \quad \rightarrow \quad K_{in} < T_a \tag{7.16}$$

Equation (7.16) clearly corresponds to a sufficient condition for the stability and thus leads to a much conservative design of the maximum inertia gain K_{in}. Moreover as τ_{in}^{-1} approaches τ_{FLL}^{-1}, the sufficient condition evolves toward a necessary one, to avoid $0\,dB$ intersection of the magnitude function with slope -2, according to the Bode stability condition.

7.3.2 Design approach B

A less conservative definition of the maximum inertia coefficient K_{in} can be derived considering the asymptotic behaviour of the open-loop function $L_{in}(s)$. In particular:

- from (7.12), the grid function $K_g(s)$ shows a single pole at the pulsation $\omega_p = \frac{K_{reg}}{T_a}$. Typically this is the slowest singularity in (7.10).
- The pole associated to the inertia regulator should be chosen lower than the one of the equivalent FLL function, thus:

$$\tau_{in}^{-1} < \tau_{FLL}^{-1} \tag{7.17}$$

Depending on the desired fastness of the inertia intervention, τ_{in} can determine the maximum frequency range where synthetic inertia actively contributes to the damping of the system dynamics. Moreover, in case of undesired disturbances introduced in the derivative estimation from the FLL algorithm, a slower value of the pulsation $\frac{1}{\tau_{in}}$ can introduce a stronger filtering effect.

Under condition (7.17), the maximum value associated to the inertia coefficient can be obtained imposing an intersection of $L_{in}(s)$ with the $0\,dB$ axis with a maximum slope equal to -2. Considering the asymptotic behaviour of the open-loop function, the inertia coefficient K_{in} is obtained as:

$$K_{in} \cong T_a \cdot \sqrt{1 + \left(\tau_{FLL}^{-1}\tau_{in}\right)^2} \tag{7.18}$$

Considering $\tau_{FLL}^{-1} = 80$ rad/s as reported in Tab.5.3, a reasonable design of the inertia time constant τ_{in} is $\tau_{in} = 1/50$ [s]. Under these conditions, the maximum inertia coefficient K_{in} can be obtained from (7.18) as $K_{in} \cong 1.9\,T_a$. The proposed approach has been numerically validated considering the complete transfer function associated to the loop and the eigenvalues model already introduced in the previous sections.

7.3.3 Numerical validation of the design approaches

Figure 7.11 shows the exact phase margin of the transfer function $L_{in}(s)$ under different values of the synthetic inertia coefficient K_{in}: even a limited increase of the coefficient leads to a significant reduction of the phase margin associated to the open-loop function. Dominant eigenvalues of the system are plotted in Fig.7.12 where it is possible to highlight the dynamical effects related to the inertia coefficient K_{in} increase.

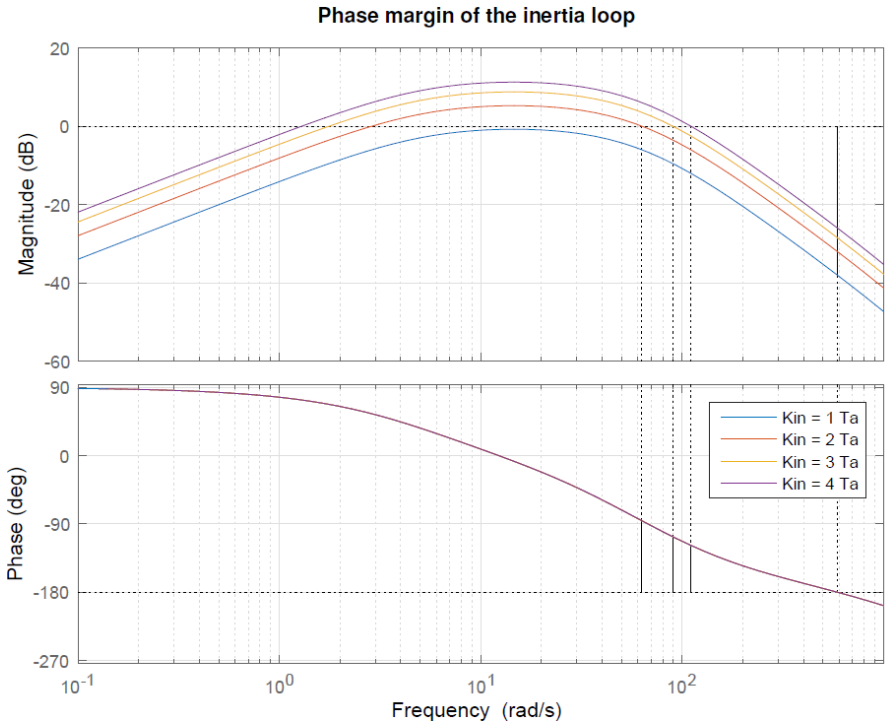

FIGURE 7.11: Numeric Bode diagram associated to the current-controlled inertia loop $L_{in}(s)$.

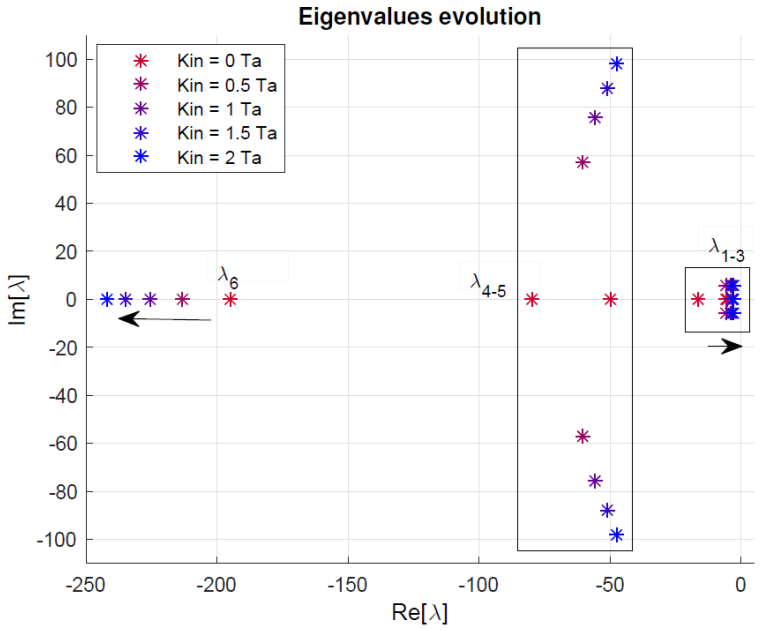

FIGURE 7.12: Current-controlled scheme: evolution of eigenvalues under variation of the inertia coefficient K_{in}. Eigenvalues positions move from red to blue as the inertia coefficient K_{in} increases.

Figure 7.12 confirms the validity of asymptotic behaviour reported in Fig.7.10: the coefficient K_{in} increase moves the slow grid pole λ_1 towards lower pulsations, while the λ_6 evolves in the opposite direction. This further confirms the validity of the simplifying assumption introduced in (7.12), making the single-pole model of the grid even more consistent for increasing values of the inertia coefficient K_{in}. Figure 7.12 allows also to identify the evolution of other singularities into the system: as far as concerns poles λ_{4-5}, they evolve to complex conjugate values and towards instability. The result is coherent with the proposed design method (7.18), in which the maximum allowable inertia coefficient K_{in} has been correlated with the FLL characteristics and angular frequency filter by means of τ_{FLL} and τ_{in}. Even though the analytical design model in (7.18) seems to be more conservative than the numeric one expressed by Fig.7.12, still in practical applications the effects of model uncertainties lead to prefer the most conservative solution.

7.3.4 Dynamical model verification: simulated results

In this section the characteristics of the resulting frequency transients after synthetic inertia introduction are analytically derived in terms of maximum measurable angular frequency derivative. Theoretical results will be compared with experimental ones for the validation of the model. The correctness of the dynamical model has been verified by means of a Matlab/Simulink based simulation model. The C-code used for the laboratory test has been exactly imported in the Matlab environment, thus to replicate the same exact control dynamics. Reported results are also published in [31]. Figure 7.13 shows the transients associated to the microgrid with different values of the inertia coefficient K_{in}, under a unitary step reduction of the system accelerating power $\Delta p_g = -1$ per-unit. The parameters used in the simulations are the ones reported in Tab.5.1 and the numerical comparison is carried out in Table 7.3.

The analysis of the values in Table 7.3 serves to verify the adherence of simulation environment with the theoretical model, thus it represents an initial benchmark for the correctness of the proposed analytical approach. For each considered case, two data series (theoretical and simulated) are compared in terms of steady-state frequency deviation and correspondence of maximum derivative measured from the FLL. The reason of this choice lies in the measurement ease associated to these parameters; as regards the maximum theoretic derivative case, the internal dynamic of the FLL is included in the analytical model according to the procedure reported in Appendix C.2: this enables a fair comparison between the theoretical results and the actual signal processed by the FLL algorithm.

As regards the steady state behaviour, the difference between the theoretical model and the simulated one is practically null; this validates the general behaviour of the system as well as the correct implementation of the regulation settings for the dispatchable generator: the network frequency shows a steady state deviation that can be easily predicted from the final value theorem applied to the modified regulation transfer function (7.14).

A more interesting comparison regards the maximum derivative measured by the FLL, as this term is directly influenced by the transitory inertia provided by the undispatchable PQ converter; nevertheless, because of the fast evolving dynamics that characterize the system, the expected theoretical model needs to contemporaneously take into account the system regulation (obtained from the mutual interaction of the dispatchable and undispatchable system) and the convergence time of the angular estimator (FLL). This can be easily obtained referring to the simple calculation reported in Appendix C.2, whose final expression (C.18) is used in Tab.5.1 for the comparison with the simulated case.

The limited values of the comparison errors (normalized with respect to the theoretical value) confirm the general correctness of the dynamical representation: furthermore it is possible to highlight that the higher residual is associated to the case in which no inertia support is provided by the undispatchable converter. This is reasonable as this case is the one characterized by the fastest rate of change: under this condition the role of the fast system dynamics (neglected during the analytical derivation) becomes more significant and the model accuracy reduces.

7.4 CASE STUDY 2: Mathematical model

Similar consideration introduced for the case study of fast primary regulation can be done also in the case of slow primary regulation typically performed by a traditional

TABLE 7.3: Model validation for current-controlled inertia in CASE STUDY 1: comparison of dynamical quantities. Both the reported transients refer to the measurements as acquired by the FLL.

Parameter	Expression	K_{in}/T_a	Theoretic value	Simulated result	Error
Freq. deviation	$\Delta\omega = \Delta p_g/K_{reg}$	$\{0, 0.4, 0.8\}$	-0.020	-0.020	$< 1\%$
Maximum		0	-0.10	-0.086	14%
derivative	(C.18)	0.4	-0.071	-0.067	5%
(FLL)		0.8	-0.056	-0.058	3.5%

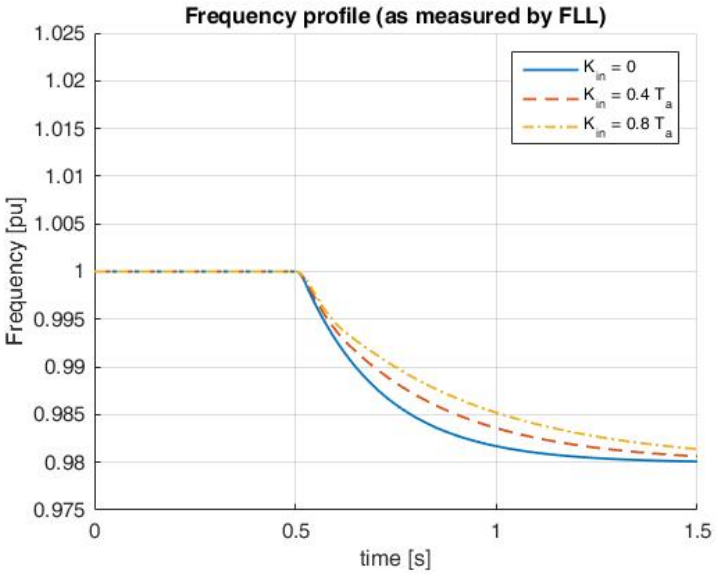

(a)

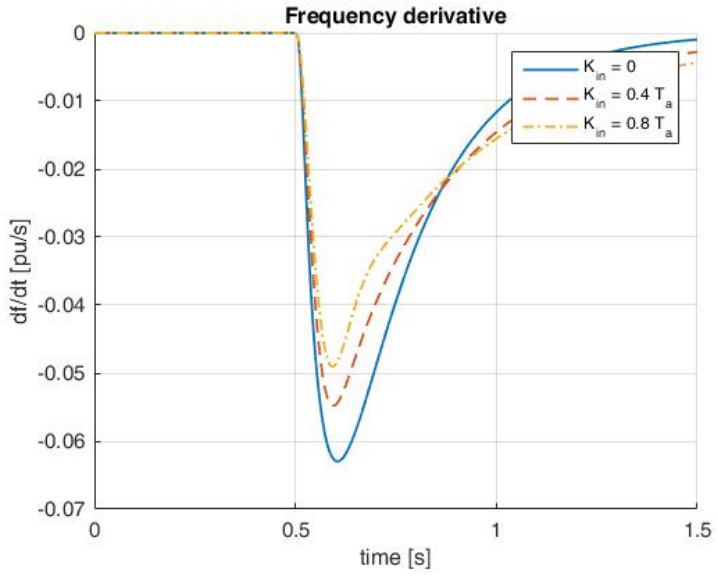

(b)

FIGURE 7.13: Transients associated to frequency regulation in CASE STUDY 1. The synthetic inertia introduction changes the derivative of the fundamental frequency, even though the modification is affected by the finite pass-band of the FLL.

synchronous machine. The numeric values are the ones associated to CASE STUDY 2 in Table 5.2. In these conditions, the complete system shows a couple of complex conjugate weakly-damped poles located at the natural frequency of the system. Additionally, synthetic inertia becomes particularly effective as the dynamical characteristics of the frequency transients are exclusively determined by the physical (and thus not-modifiable) construction parameters of the synchronous machine. Thus the interaction of the PQ converter with the rest of the system may significantly improve transitory frequency oscillations into the network.

From the mathematical point of view, the transfer function associated to the frequency regulation $K_g(s)$ shows a couple of complex conjugate poles with natural frequency and damping given by (7.19) and (7.20) respectively.

$$\omega_n = \sqrt{\frac{K_{\text{reg}}}{T_a \tau}} \tag{7.19}$$

$$\xi = 0.5 \cdot \sqrt{\frac{T_a}{\tau K_{\text{reg}}}} \tag{7.20}$$

In case $\tau > \frac{T_a}{2 \cdot K_{\text{reg}}}$ ($\xi < \frac{1}{\sqrt{2}}$), the Bode diagram associated to the system shows a resonance peak in correspondence of the grid natural frequency ω_n (7.19) and the active power transients on the system show a marked oscillatory behaviour. The model reported in Fig. 7.9 again allows to retrieve the characteristics of the modified grid function after inertia introduction. Approximated behaviour for $\omega_s < 1/\tau_{in}$ is represented by (7.21).

$$K'_g(s) = \frac{1 + \tau s}{s^2 \left(T_a \tau + K_{in} \tau\right) + s \left(T_a + K_{in}\right) + K_{reg}} \qquad \text{for } \omega_s < 1/\tau_{in} \tag{7.21}$$

which is characterized by a natural frequency and damping factor equal to:

$$\omega'_n = \sqrt{\frac{K_{\text{reg}}}{T_a \tau + K_{in} \tau}} \tag{7.22}$$

$$\xi' = 0.5 \cdot \sqrt{\frac{T_a + K_{in}}{\tau K_{\text{reg}}}} \tag{7.23}$$

The introduction of inertia support by means of the coefficient K_{in} reduces both the amplitude and the natural frequency of the resonance peak associated to the grid dynamics, as shown in Figure 7.14. Moreover the definition of the loop function as reported in 7.14 allows to determine the stability condition associated to the dynamical interaction of the PQ converter with the grid supporting unit and to correlate the design of the control parameters to the stability of the feedback. A very conservative design in (7.21) can be obtained imposing the resonance peak amplitude lower than one, thus avoiding intersections with the $0\,dB$ axis. As the resonance peak in the open loop function occurs close to the natural frequency of grid dynamic ($\omega_p \cong \omega_n$), the above condition $|L_{in}(j\omega_p)| < 1$ corresponds to (7.24).

$$\frac{K_{in}}{T_a} < \sqrt{\frac{T_a}{K_{reg} \tau}} \tag{7.24}$$

As for the time constant τ_{in} associated to the inertia, it determines the spectral range of the angular frequency derivative signal where inertia is active and can be designed

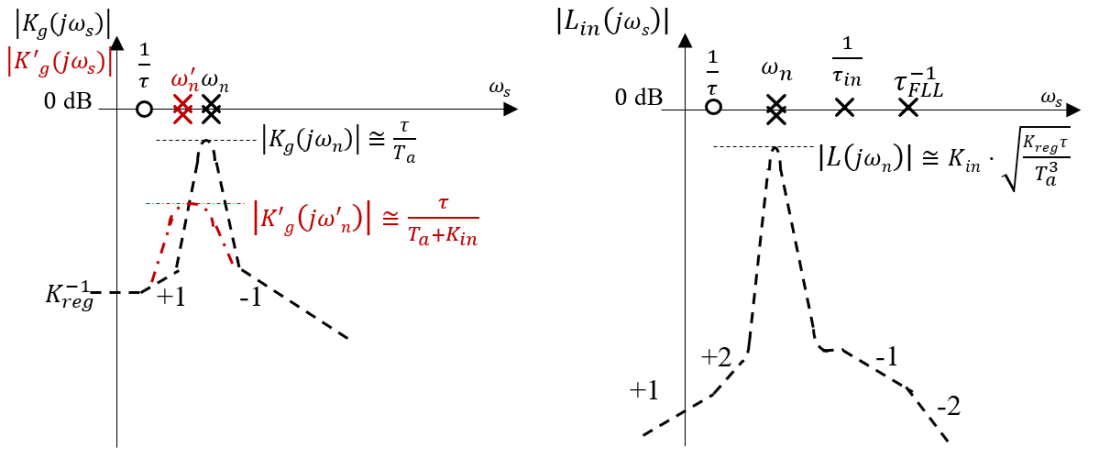

FIGURE 7.14: Asymptotic behaviour for the current-controlled inertia loop functions in case study 2. In (a) the initial and modified grid dynamics are reported, represented by $K_g(s)$ and $K'_g(s)$ respectively; in (b) the open-loop function $L_{in}(s)$ is depicted. The introduction of inertia support by means of the PQ converter damps the resonance peak associated to the couple of complex conjugate poles of the system.

according ot the same procedure illustrated in section 7.3.2. In order to verify the correctness of the predicted dynamical model, the properties of simulated transients are compared with the analytical ones in Table 7.4, under a unitary step decrease of the accelerating power $\Delta p_g = -1$ per-unit; the simulated transients values associated to table 7.4 are reported in Fig. 7.15.

Similarly to what was done in Sect. 7.3.4, the comparison is carried out considering some macroscopic quantities linked to the dynamical model of the network: beside the steady state value, the transient oscillation period and its associated overshoot are analysed; the direct analytical derivation of these macroscopic quantities from the expected transfer function of the network regulation is reported in Appendix C.3. The obtained final expressions (C.28)-(C.30)-(C.31) are then exploited for the comparison in Tab. 7.4.

The analysis of Tab. (7.4) reveals a close correspondence of the theoretical model with the simulated one: as regards the oscillation period, the correspondence between simulated and theoretical models remains robust in all the considered cases. As for the overshoot, the analysis reveals a higher sensitivity of the model with respect to the high-order dynamics neglected during the derivation phase, especially for the case where the transitory inertia support from the undispatchable unit is minimum ($K_{in} = 0$). It is worth also to underline that in the last simulated case ($K_{in} = 2\,T_a$) the error results significant mainly because of the normalization with respect to the low theoretical result: the actual difference between the simulated and analytical overshoot remains limited.

Once assessed the correctness of the dynamical mode from the simulation perspective, the reproducibility of the same dynamical behaviour on an experimental set-up needs to be tackled: thus in the next section, after an initial explanation of the operational test conditions, the validation of the proposed inertia model and its effectiveness on a small-scale network will be analysed.

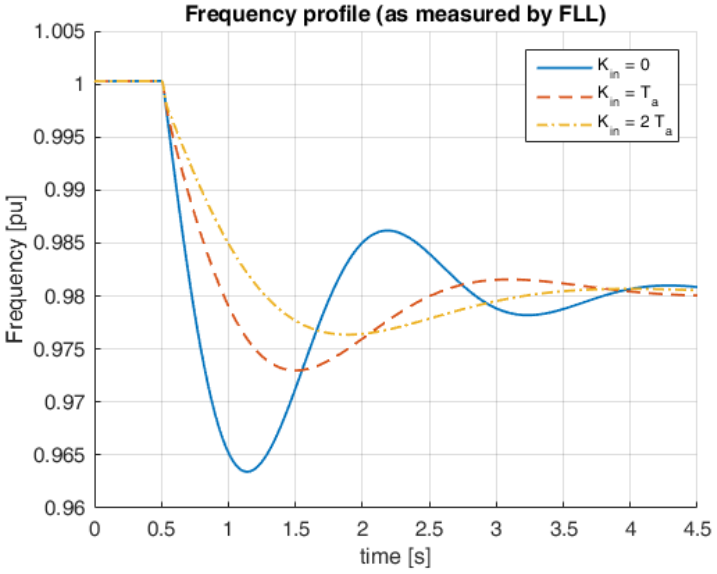

(a)

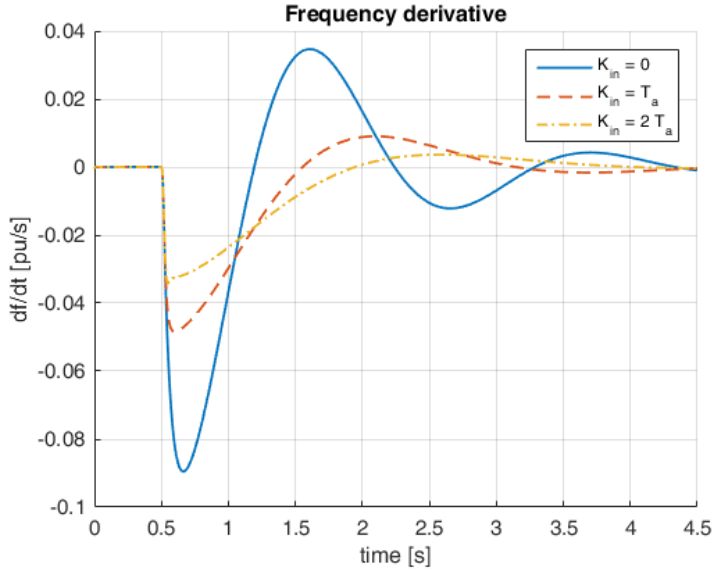

(b)

FIGURE 7.15: Transients associated to the a unitary step change of absorbed power ($\Delta p_g = -1$ p.u.) in case study 2, for slow primary frequency regulation.

TABLE 7.4: Model validation for current-controlled inertia in CASE STUDY 2: comparison of transients characteristic.

Parameter	Expression	K_{in}/T_a [s/s]	Theoretic	Simulated	Error
Steady state	$\omega^* = \omega_o + \Delta p_g / K_{reg}$	$\{0, 1, 2\}$	0.98 p.u.	0.98 p.u.	$< 1.0\%$
Expected natural frequency	ω'_n (7.22)	0	3.16 rad/s	-	-
		1	2.23 rad/s	-	-
		2	1.82 rad/s	-	-
Expected damping factor	ξ' (7.23)	0	0.31	-	-
		1	0.44	-	-
		2	0.54	-	-
Period of oscillation	$T = \frac{2\pi}{\omega'_n \cdot \sqrt{1-\xi'^2}}$ (C.28)	0	2.09 s	2.13 s	2.0%
		1	3.14 s	3.07 s	2.3%
		2	4.12 s	4.21 s	2.2%
Overshoot	(C.30)-(C.31)	0	79%	85%	7.6%
		1	36%	35%	2.4%
		2	18%	15%	18%

7.5 Experimental implementation of the current-controlled synthetic inertia

7.5.1 Experimental set-up and protection scheme

One of the major criticality issues related to the experimental testing of the transitory inertia schemes regards the possibility to obtain measurable and repeatable frequency events and, thus, verify the response of the converter to the disturbance. This constraint excludes the possibility to exploit public network transients, as a consequence of their intrinsic non-repeatability and due to the impossibility to measure the impact of the single small-scale unit on the network regulation. Thus the natural environment for the verification of the synthetic inertia performances is represented by a small-scale microgrid operated in island and supplied by stand-alone units: this allows to induce controlled and repeatable frequency transients on the network and, consequently, to analyse the additional damping provided by the undispatchable units after a network event. Appendix D provides a general description of the test set-up , as well as of the acquisition and control architecture: still it is useful to point out some of the characteristics of the synthetic inertia tests.

Consider the scheme reported in Figure 7.16: two converters are connected in parallel to a high-impedance load. The first converter is operated in grid-forming mode and imposes to the system a symmetrical set of voltages with an angular frequency ω. The ω evolves according to the frequency regulation law equivalent to the one provided by the dispatchable unit: this converter is supplied by a infinite-power source able to impose a constant voltage between its DC-bus terminals. The regulation strategy provided by this unit needs to take into account:

- the dynamical characteristics of the primary regulation (T_a, K_{reg}, τ);
- the value of the independent accelerating power Δp_g;

- the instantaneous response of the PQ converter Δp_{conv} in case the synthetic inertia control is activated, in order to correctly emulate the dynamical interaction between the two units.

The second converter is operated in grid-following mode: in case no synthetic inertia control is implemented, its injected active power is constant. Once the inertia support is introduced, the unit responds to the system transient by modulating its active injection profile Δp_{conv} according to the characteristics of the inertia regulator. Its control is thus identical to the one that would have in grid-connected mode: this allows to operate the converter in the same conditions of dynamical damping provision to a public power network.

Instead of recurring to a physical load connection / disconnection, the control of the grid-forming converter (inverter 1) has been designed to create a frequency transient on the network: as the converter is operated in grid-forming mode, it is able to impose any constant (or time-variable) profile to the network frequency, as the high-power source at its DC side guarantees the necessary regulation capability. In order to derive homogeneous comparison with the previously-simulated transients, the imposed frequency profile follows the dynamical model already introduced in (7.8), suitably discretized with the bilinear transform ($k = T_c/2$ stands for the Tustin discretization coefficient).

The following elements determine the transient characteristics (Fig. 7.16):

- a fictitious change of the accelerating power $\Delta\tilde{p}_g$ is introduced into the control system of the grid-forming converter (inverter 1), which responds imposing a network frequency ω transient determined by (7.8). The time behaviour of the network angular frequency ω would be the same of a physical active load $\Delta\tilde{p}_g$ connection / disconnection.
- The grid-following unit (inverter 2) identifies the transient by means of the frequency estimation algorithm explained in Chapter 5 (FLL) by measuring the voltages at the interface and modulates its power injection Δp_{conv} (provided that a non-null inertia coefficient K_{in} is introduced). This second converter is blind with respect to the original nature of the frequency transient: it exactly behaves as if it were connected to a public power network.
- The response of the grid-following converter Δp_{conv} affects the angular frequency ω transient as a consequence of the (real) power balance on the circuit. This highlights the synthetic inertia effect on the equivalent network. In practice the grid-forming units is controlled as a grid-emulator device, able to impose whichever dynamical evolution (within its power capability) to its controlled network.

This architecture allows to identify the effect of the synthetic inertia under any possible system unbalance $\Delta\tilde{p}_g$ without the need of a physical load connection / disconnection, as the transient excitation quantity $\Delta\tilde{p}_g$ is a fictitious control term rather than a real power.

Furthermore, the presence of a limited available capacitance on the DC side of the grid-following converter has to be taken into account, in order to avoid damage to the installed components during the test evaluation. The scheme reported in Fig.7.17 allows to inhibit the inertia contribution once the operational limits are reached. Even though this protection scheme is quite simple, still it has a primary importance as it allows to perform inertia services independently of the physical available capacitance: the grid-following converter contributes to the regulation with the available energy stored on its DC bus up to the safety thresholds represented by $V_{dc\,min}$ and $V_{dc\,Max}$.

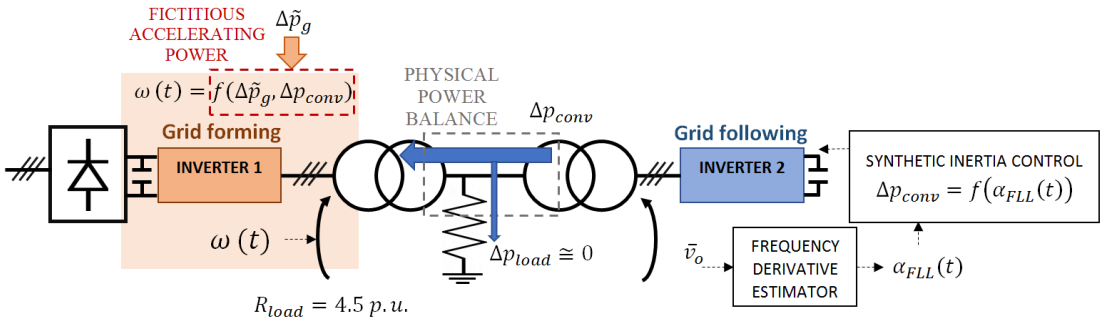

FIGURE 7.16: Structure of the experimental set-up used for the testing.

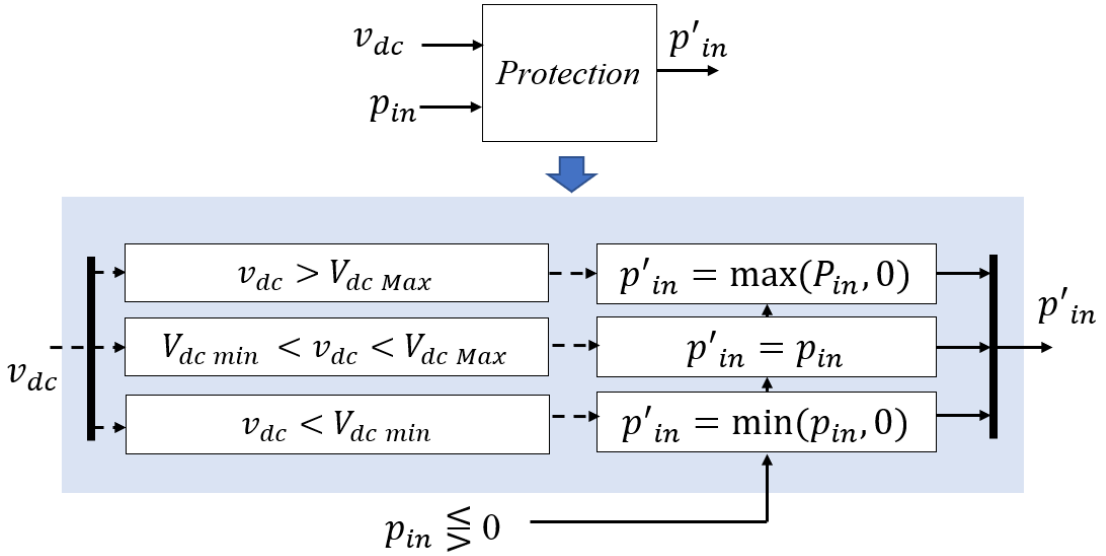

FIGURE 7.17: Algorithm for DC bus protection under current-controlled inertia support.

7.5.2 Experimental results

In this section the experimental results related to the simulation of the frequency transients modification after synthetic inertia introduction are reported. In particular, the numeric values of the case study associated to the traditional network (slow primary regulation, Tab. 5.2) have been considered: this is the case in which the additional converter-provided inertia is more useful, as the grid dynamic shows an under-damped behaviour: synthetic inertia introduction contributes to increase the equivalent system damping (7.23) and reduces angular frequency excursion during the transient, avoiding possible intervention of the over / under frequency protections of the power network.

The considered numeric values are reported here in Tab. 7.5, as a recall.

TABLE 7.5: Emulated-grid characteristics used for the experimental test.

Parameter	*Symbol*	*Numeric value*
Starting time	T_a	10 s
Regulating energy	K_{reg}	50 p.u.
Time constant of the internal regulation delay	τ	500 ms

Similarly to the simulated cases, the consistency of the theoretical and experimental results is assessed, referring to the steady-state conditions, the measured transitory oscillation period and the corresponding overshoot: again, the evaluation of the theoretical response characteristics refers to the analytical procedure reported in Appendix C.3, especially as regards the oscillation (C.28) period and overshoot (C.30)-(C.31). The experimental profiles associated to an equivalent accelerating power $\Delta p_g = 1$ p.u. are reported in Fig.7.18 for different values of the inertia coefficient K_{in}, while in Tab.7.6 and Fig.7.19 the comparison between the theoretical and analytical model is carried out.

The residuals between the experimental test and the analytical derivation are reported in Fig.7.19 (normalized with respect to the theoretical model). Differently from the simulated result, the residuals interpretation is more critical as it involves both the physical uncertainty associated to the real set-up elements and the numerical approximation in the simplified model derivation. Nevertheless it is possible to derive the following considerations.

- From the energetic perspective, the system behaves as expected: an increase of the inertia coefficient K_{in} provides transitory damping to the system, reducing the network frequency overshoot. This property represents the key advantage of the inertia regulation: without affecting the steady-state behaviour of the system, it is possible to reduce the amplitude of the frequency transient and thus avoid possible intervention of the network protection relays by means of a zero-net-energy control.

TABLE 7.6: Experimental validation of the current-controlled inertia in CASE STUDY 2.

Parameter	Expression	K_{in}/T_a	Theoretic	Experim.
Steady state dev.	$\Delta\omega^* = \Delta p_g / K_{reg}$	$\{0, 0.3, 0.6\}$	0.020 p.u.	0.020 p.u.
Natural frequency	ω'_n (7.22)	0	3.16 rad/s	-
		0.3	2.77 rad/s	-
		0.4	2.67 rad/s	-
		0.6	2.50 rad/s	-
Damping factor	ξ' (7.23)	0	0.31	-
		0.3	0.36	-
		0.4	0.37	-
		0.6	0.40	-
Period of oscillation	$T = \frac{2\pi}{\omega'_n \cdot \sqrt{1-\xi'^2}}$ (C.28)	0	2.09 s	2.04 s
		0.3	2.43 s	1.98 s
		0.4	2.67 s	2.07 s
		0.6	2.74 s	2.34 s
Overshoot	(C.30)-(C.31)	0	79%	87%
		0.3	61%	82%
		0.6	56%	77%
		0.6	48%	67%

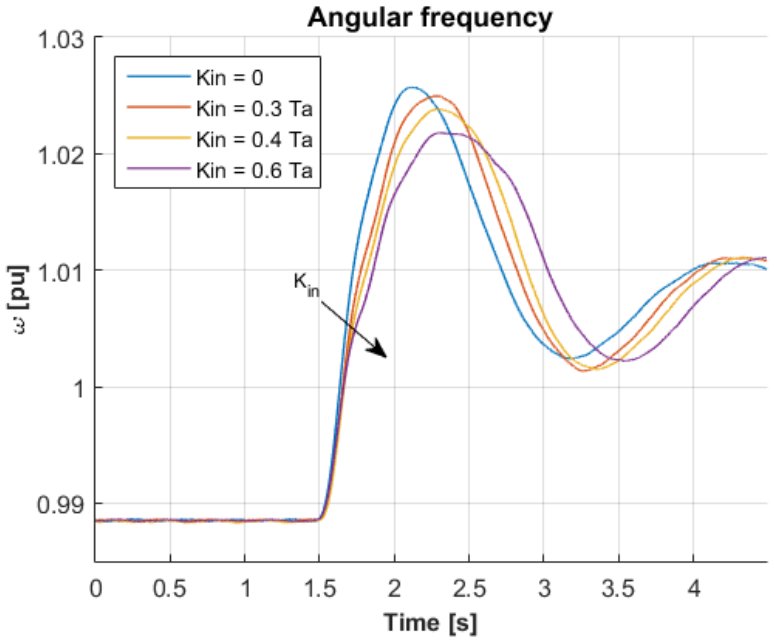

FIGURE 7.18: Angular frequency profile under different values of the synthetic inertia. An increasing of the regulation coefficient K_{in} provides additional damping to the system, thus reducing the transient overshoot.

- Independently of the considered case, the normalized errors result limited and they highlight the consistency and robustness of the proposed approach.
- Figure 7.20 reproduces the profile of the estimated angular frequency derivative during the transient, as estimated by the FLL algorithm; this signal, once filtered according to the scheme reported in Fig. 7.2, represents the input of the inertia loop. The experimental tests show the reduction of maximum derivative (often referred as Rate Of Change Of Frequency) as a consequence of the additional damping provided by the undispatchable converter. Furthermore, the acceptable signal-to-noise resolution of the derivative signal remarks the effectiveness of the developed angular estimator (Chapter 6) even under disturbed network conditions.

Figures 7.22 and 7.21 show, respectively, the profile of the DC bus voltage and the injected power from the grid-following converter in the three analysed cases. When the inertia control is deactivated ($K_{in} = 0$) these quantities remain constant during the transient of the grid frequency. Nevertheless, for $K_{in} \neq 0$, the converter absorbs power from the network to counterbalance the frequency increase (Fig. 7.21); this causes an increase of the DC voltage (Fig. 7.22). At steady state, after the extinction of the transient, both the active power and the DC bus voltage recovers their nominal values: synthetic inertia configures as an energy-invariant control and thus it is suitable also for converters supplied by non-dispatchable units.

Beside the uncertainty associated to the physical set-up parasitic losses and the analytical exemplification introduced in the dynamical model derivation, a further source of mismatch is clearly represented by the presence of a limited DC bus in the experimental setup. In particular, observing the power profile in Fig.7.21, it is possible to highlight the presence of incipient oscillatory terms with a lower period with respect to the network oscillations.

This is, indeed, one of the concerns generally considered for current-controlled inertia regulation, that is the absence of easy-to-use analytical dependency between the DC bus

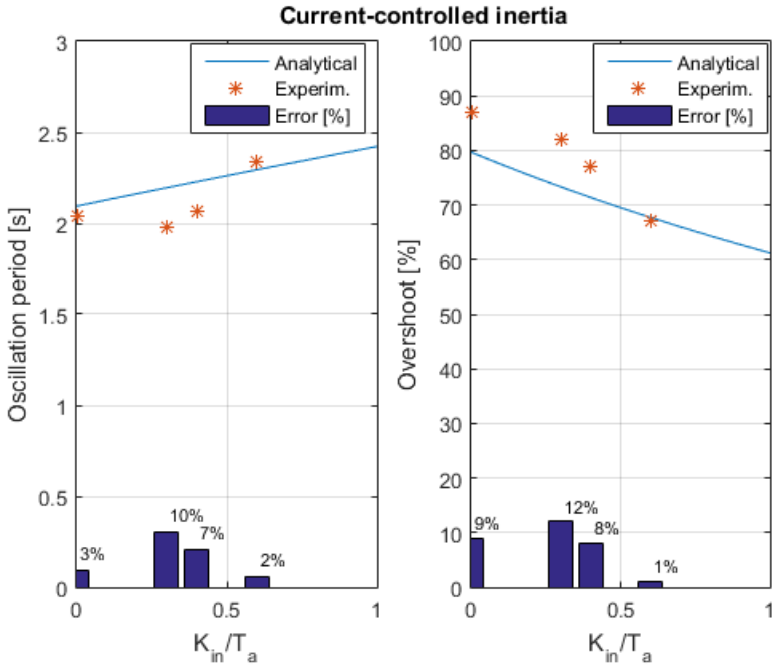

FIGURE 7.19: Comparison between the derived analytical model and the experimental one for the current-controlled inertia scheme. The limited value of the errors guarantees the correctness of the proposed dynamical model.

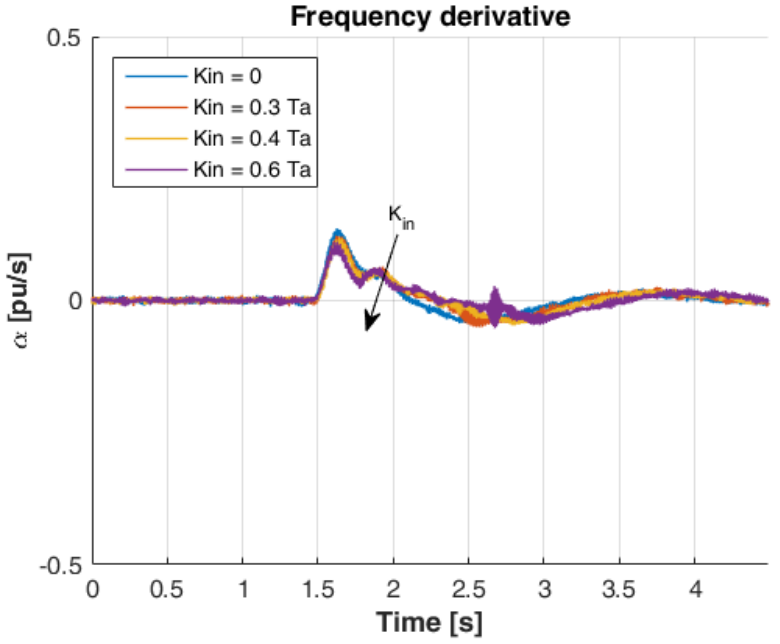

FIGURE 7.20: Angular frequency derivative (as estimated by the FLL) under different values of the synthetic inertia. The peak derivative reduces under increasing values of K_{in}.

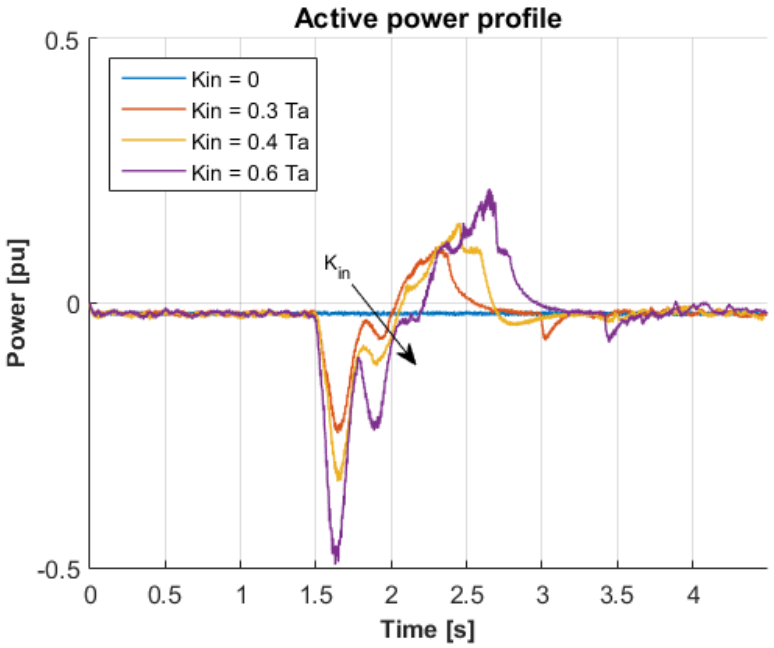

FIGURE 7.21: Injected power under different values of the synthetic inertia. The sign of the injected power is opposite with respect to the estimated angular frequency derivative α_{FLL}: under this condition, the converter behaves as a physical controllable inertia.

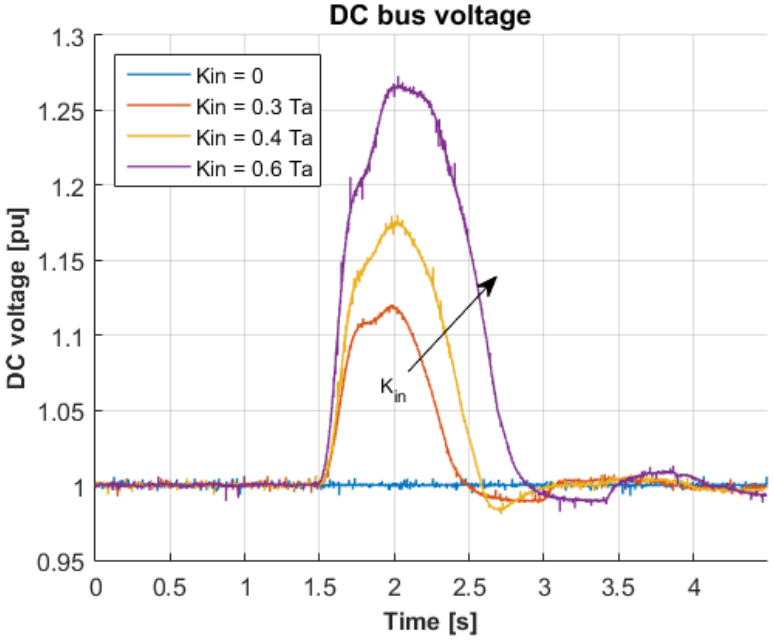

FIGURE 7.22: DC bus voltage under different values of the synthetic inertia. The DC bus behaves as an energy buffer.

voltage variation and the imposed inertia provision coefficient K_{in}: even though some approximated expressions are derivable from the resolution of the complete feedback in Fig.7.9, still the heavy analytical derivation of these expressions often discourages from their application. The actual problem is not related to the low predictability of the maximum voltage peak (as this can be easily solved with simple protection schemes like the one in Fig. 7.17), but rather the possible dynamical coupling between the external DC voltage regulation loop and the inertia provision algorithm. This aspect may be the base for future extensions of the model.

7.6 Conclusion

In this chapter, the model of the current-controlled synthetic inertia has been introduced. The complete model of the system has been analysed in the initial part of the chapter referring to eigenvalues and participation-factors analysis. Once identified the dominant dynamics, a reduced order linear system has been developed: this allows to derive simpler design models for the inertia parameters and to highlight the intrinsic dynamical behaviour of the system. Experimental verification of the method feasibility has been provided at the end.

The method used for the stability identification of the synthetic inertia is the main novelty introduced by this chapter: the typical approach followed in literature addresses this control as an open-loop reference signal, whose stability is exclusively determined by the regulation properties of the PQ internal loop. In reality, the analysis highlights the significant impact associated to the mutual dynamical interaction between the primary regulation (performed by dispatchable units) and the transitory frequency support provided by PQ generators: even though for public network this represents a minor concern due to their high regulation capability, for small-scale microgrids the effect becomes predominant and could easily lead to un-damped mutual power oscillations between the parallel connected units.

Furthermore, the experimental tests carried out on a small-scale microgrid reveal the actual possibility to carry out derivative-based inertia schemes, provided that a sufficiently elaborated angular estimator (like the one proposed in Chapter 6) is implemented.

Chapter 8

Voltage-controlled inertia

8.1 Introduction

This final chapter will take into account the provision of inertia services by means of the regulation of the DC bus voltage in a PQ converter (non-dispatchable unit is Fig. 5.3); the results associated with this control strategy will be compared with the ones obtained for the current scheme. Experimental validation of the proposed method is also provided.

8.2 Non-linear model of the converter under voltage-controlled inertia

Starting from the architecture already presented in Fig. 5.21(b) (reported again in Fig. 8.1 for clarity), consider the control scheme in Fig.8.2, which takes into account the contribution of the inertia regulation performed by means of an additional DC bus voltage reference proportional to the angular frequency displacement.

As regards the internal current and voltage regulation loops, the system is equal to the one already introduced in Fig. 7.2; nevertheless, it is possible to highlight the presence of an additional feedback between the estimated angular frequency of the system ω_{FLL} and the DC bus voltage reference. This feedback takes into account the DC bus capacitor power balance, as well as the characteristic dynamics of the network, which determine the evolution of the angular frequency ω. The introduction of the inertia regulator produces an additional voltage $v_{dc\,in}$ function of the grid frequency.

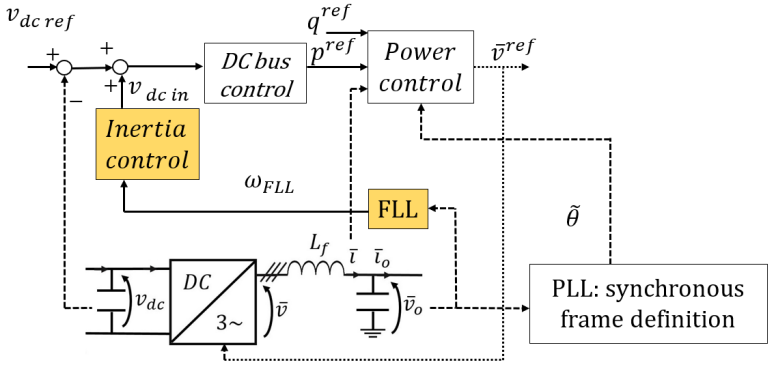

FIGURE 8.1: Synthetic inertia by means of the DC bus voltage control.

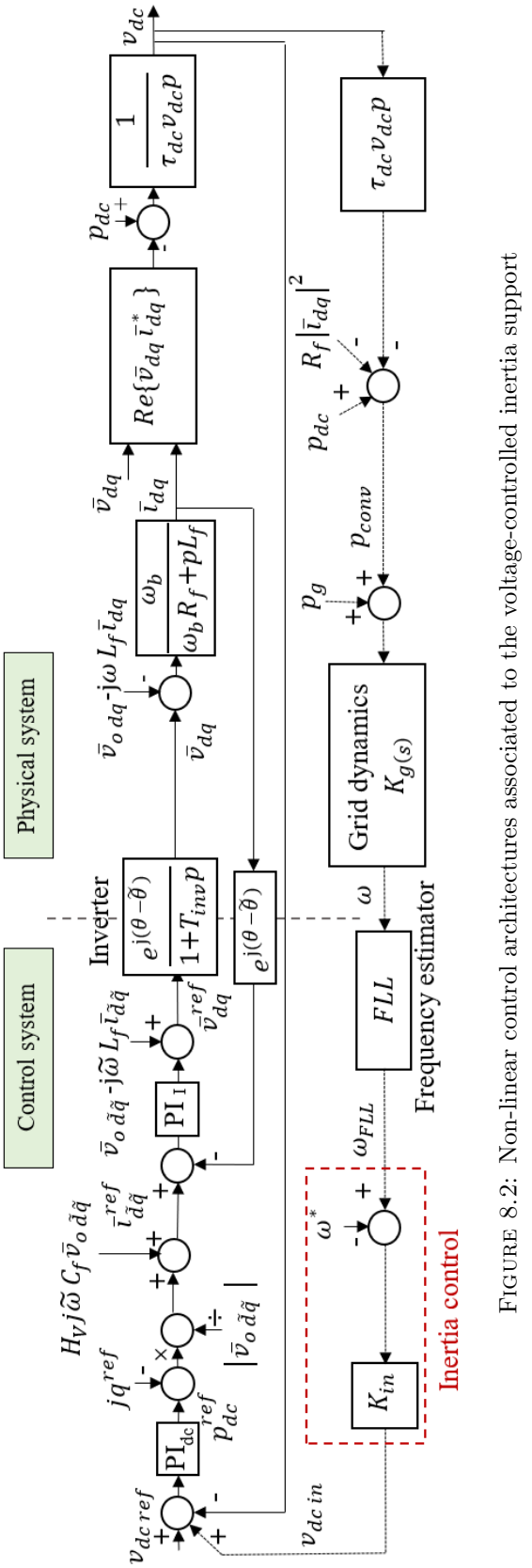

FIGURE 8.2: Non-linear control architectures associated to the voltage-controlled inertia support

The non-linear set of equations that describe the system behaviour can be identified from Fig. 8.2; as the equations related to the internal current control and to the physical systems have already been identified Sec. 5.7, in the following only the changes with respect to the previous model will be highlighted. Nevertheless, the complete dynamical model in state-space form is reported in Appendix A.

Consider, as a recall, the non-linear dynamic of the DC bus voltage (8.1) (recalled from (5.21)). Once the inertia loop in voltage-controlled mode is introduced, the definition of the integral error associated to the DC bus regulator is given by (8.2): the additional reference $v_{dc\,in}$ determines the inertia contribution from the converter.

$$pv_{dc} = \frac{1}{\tau_{dc} v_{dc}} \cdot (i_{dc} v_{dc} - (v_d i_d + v_q i_q)) \tag{8.1}$$

$$pE_{dc} = (v_{dc\,ref} + v_{dc\,in} - v_{dc}) \tag{8.2}$$

$$p_{dc}^{ref} = [k_{p\,dc} \cdot (v_{dc\,ref} + v_{dc\,in} - v_{dc}) + k_{i\,dc} \cdot E_{dc}] \tag{8.3}$$

The inertia signal is determined by the difference between the estimated system angular frequency ω_{FLL} and the nominal one ω^*. Differently from the current-based scheme, in which the input of the control was the angular frequency derivative, the voltage-based scheme performs a proportional regulation; as the frequency estimation shows a much better signal-to-noise ratio with respect to the derivative one, here it is not included any additional low-pass filter effect. The estimated angular frequency can be linked to the actual one by means of the FLL dynamics, expressed as a first order system according to the scheme proposed in Chapter 6.

$$v_{dc\,in} = K_{in} \cdot (\omega_{FLL} - \omega^*) \tag{8.4}$$

Direct and quadrature current references are expressed as:

$$i_{o\,\tilde{d}}^{ref} = \frac{p_{dc}^{ref}}{\left|\bar{v}_{o\,\tilde{d}\tilde{q}}\right|} \tag{8.5}$$

$$i_{o\,\tilde{q}}^{ref} = -\frac{q^{ref}}{\left|\bar{v}_{o\,\tilde{d}\tilde{q}}\right|} \tag{8.6}$$

The non linear model reported in Fig.8.2 also includes the losses associated to the filter; the representation of the power balance contribution is taken from Fig.5.2.

8.3 Linearised model

From the complete non-linear system reported in Fig.8.2, it is possible to derive a linearised-version of the system, useful to identify the design constraints for the control parameters.

Referring to the scheme if Fig. 5.3, the following hypotheses are considered:

- a loss-less behaviour is taken into account both for the converter and for the interface filter;
- it is assumed a constant power p_{dc} from the primary sources, thus $\Delta p_{dc} = 0$;
- the control of the DC bus voltage is modelled as a first-order unitary gain system, with a cut-off angular frequency equal to $\omega_{c\,dc} = 2\pi \cdot 2.5$ rad/s (Tab. 5.6).

$$K_{dc}(s) = \frac{v_{dc}}{v_{dc\,ref}} = \frac{1}{1 + s/\omega_{d\,dc}} \tag{8.7}$$

The behaviour of the DC bus voltage is linearised as follows:

$$p_{conv} \cong p_{dc} - \tau_{dc}\, v_{dc}\, p v_{dc} \tag{8.8}$$

$$\Delta p_{conv} \cong \Delta p_{dc} - \tau_{dc}\, V_{dc}\, p\Delta v_{dc} \cong -\tau_{dc}\, V_{dc}\, p\Delta v_{dc} \tag{8.9}$$

Moving to the Laplace domain, it is possible to obtain the equivalent loop system reported in Fig. 8.3. This representation is particularly useful to identify the predominant effect of each term on the system stability, as it includes: the characteristics of the external grid $K_g(s)$, the physical available energy on the DC bus voltage (related to $\tau_{dc}V_{dc}\Delta v_{dc}$), the synthetic inertia coefficient K_{in} and the characteristics of the DC bus voltage regulation expressed by $K_{dc}(s)$.

From the reported diagram, it becomes evident the choice to introduce a proportional regulator on the voltage feedback instead of a derivative one (differently from the current oriented scheme): the linearisation of the DC bus dynamics highlights a natural derivative effect that plays the same role of the numerical one introduced in the current-oriented scheme reported in Fig.7.2.

Once identified the open-loop function associated to the inertia provision $L_{in}(s)$,

$$L_{in}(s) = K_{in} \cdot \frac{1}{1 + s/\omega_{c\,dc}} \cdot (s\,\tau_{dc}V_{dc}) \cdot \frac{1 + s\tau}{T_a\tau s^2 + T_a s + K_{reg}} \cdot \frac{1}{1 + s\tau_{FLL}} \tag{8.10}$$

the closed-loop function between the accelerating power Δp_g and the angular frequency variation $\Delta\omega$ is described by (8.11). The minus sign associated to the DC bus voltage has not been included in the open-loop function $L_{in}(s)$ (8.10) as it compensates the positive feedback of the inertia.

$$K'_g(s) = \frac{\Delta\omega}{\Delta p_g} = \frac{K_g(s)}{1 + L_{in}(s)} \tag{8.11}$$

Even though the stability definition only depends on the loop function $L_{in}(s)$ and the grid characteristic changes the modified grid function $K'_g(s)$, still it is interesting to correlate the accelerating power Δp_g with the one injected by the converter Δp_{conv}, as well as with the DC bus voltage variation Δv_{dc}.

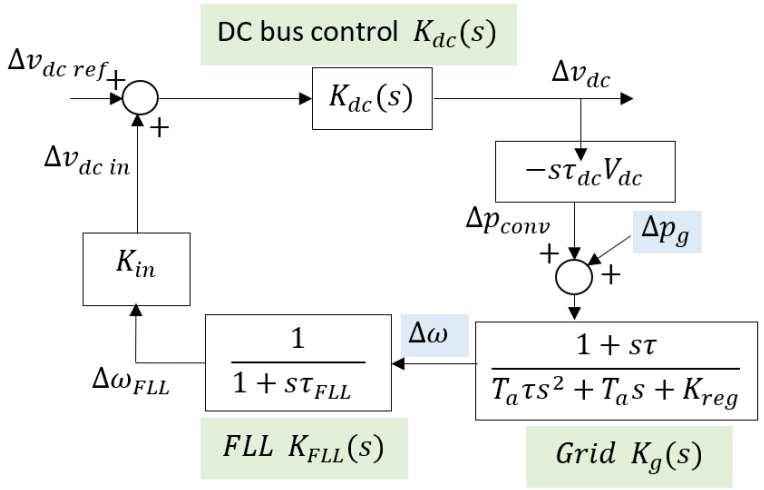

FIGURE 8.3: Simplified model for the design of the voltage-controlled inertia loop.

$$\frac{\Delta p_{conv}}{\Delta p_g} = \frac{-L_{in}(s)}{1 + L_{in}(s)} \tag{8.12}$$

$$\frac{\Delta v_{dc}}{\Delta p_g} = K_{in}\, K_g(s)\, K_{FLL}(s)\, K_{dc}(s) \cdot \frac{1}{1 + L_{in}(s)} \tag{8.13}$$

The steady-state condition of the state variables under a step-change of the accelerating power can be reconstructed from the Laplace final value theorem applied to (8.12) and (8.13).

According to the definition of the loop function provided in (8.10), the relation between the accelerating power and the converter injection under a step-change Δp_g^* becomes:

$$\Delta p_{conv}(\infty) = \lim_{s \to 0}\, s \cdot \frac{-L_{in}(s)}{1 + L_{in}(s)} \cdot \frac{\Delta p_g^*}{s} = 0 \tag{8.14}$$

At steady state, the power injected by the converter results to be independent of the excitation Δp_g, guaranteeing the applicability of the technique for undispatchable units. The same analysis can be applied to link the output converter power Δp_{conv} under a step change of the angular frequency variation $\Delta\omega$:

$$\Delta p_{conv}(\infty) = \lim_{s \to 0}\, s \cdot \frac{-s\, \tau_{dc}\, V_{dc}\, K_{in}\, K_{dc}(s)\, K_{FLL}(s)}{1 + L_{in}(s)} \cdot \frac{\Delta\omega^*}{s} \cong \lim_{s \to 0} s K_{in} \tau_{dc} V_{dc} \Delta\omega^* = 0 \tag{8.15}$$

From (8.15) it becomes evident the natural derivative effect introduced by the DC bus dynamic; even though a proportional controller K_{in} is applied, still the relation between the injected power Δp_{out} and the angular frequency variation $\Delta\omega$ retains a derivative nature, similar to the one of a physical rotating mass. Thus, at steady state, the injection from the converter results to be independent of the actual grid frequency $\Delta\omega$, coherently with (8.14).

Now it is possible to consider the inertia effect on the DC bus voltage Δv_{dc}. The steady-state conditions are derived from (8.13).

$$\Delta v_{dc}(\infty) = \lim_{s \to 0} s\, K_{in}\, K_g(s)\, K_{FLL}(s)\, K_{dc}(s)\, \frac{1}{1 + L_{in}(s)} \cdot \frac{\Delta p_g^*}{s} = \tag{8.16}$$

$$= K_{in}\, K_g(0)\, K_{FLL}(0)\, K_{dc}(0) \cdot \Delta p_g^* = \frac{K_{in}}{K_{reg}}\, \Delta p_g^* = K_{in} \cdot \Delta\omega_{ss} \tag{8.17}$$

From (8.16), the dependency of the DC bus voltage from the steady state angular frequency $\Delta\omega_{ss}$ becomes evident, even though the injection remains exclusively determined by the un-dispatchable primary source. Thus, when the converter is operated in island, the DC bus voltage converges to different values depending on the system state; this may be acceptable or not depending on the primary source nature and on the hardware constraints associated to the converter.

As regards stability analysis, two study cases can be identified according to the definition already provided for the dispatchable unit: droop-controlled microgrid (Tab. 5.1) and traditional synchronous machine regulation (Tab. 5.2), according to Fig. 5.1

8.4 CASE STUDY 1 (droop-controlled microgrid): mathematical model

Figure 8.4 represents the linearised simplified model of the converter used for the design of the inertia coefficient. Under the hypothesis of a limited value of the regulation delay $\tau << \frac{T_a}{4K_{reg}}$ (same condition derived in Sec.7.3), the grid dynamics $K_g(s)$ can be represented as a single-pole function as already developed for the current-controlled inertia. Thus:

$$K_g(s) = \frac{1}{T_a\, s + K_{reg}} \tag{8.18}$$

and the open-loop function becomes:

$$L_{in}(s) \cong K_{in} \cdot \frac{1}{1 + s/\omega_{c\,dc}} \cdot (s\,\tau_{dc} V_{dc}) \cdot \frac{1}{T_a s + K_{reg}} \cdot \frac{1}{1 + s\tau_{FLL}} \tag{8.19}$$

Graph (b) in Fig. 8.4 represents the open-loop inertia function $L_{in}(s)$ under this hypothesis and allows to derive sufficient stability conditions for the feedback. Imposing the magnitude of the loop function less than 0 dB, it is possible to obtain the following sufficient stability limit, obtained from the asymptotic function behaviour expressed in Fig. 8.4-(b):

$$K_{in} < \frac{T_a}{\tau_{dc} V_{dc}} \tag{8.20}$$

Fig. 8.4-(a) depicts the modification introduced in the equivalent closed-loop grid transfer function $K'_g(s)$ (8.11) after the introduction of the voltage-controlled inertia support. This can be obtained from them asymptotic approximation of $L_{in}(s)$ in the low-frequency range. For $\omega_s \leq \omega_{c\,dc}$,

$$L_{in}(s) \cong K_{in} \cdot (s\tau_{dc} V_{dc}) \cdot \frac{1}{T_a s + K_{reg}} \tag{8.21}$$

The modified closed-loop function then becomes:

$$K'_g(s) = \frac{K_g(s)}{1 + L_{in}(s)} \cong \frac{1}{}(T_a + K_{in}\tau_{dc} V_{dc}) \cdot s + K_{reg} \tag{8.22}$$

In particular, limiting the analysis to $\omega_s < \omega_{c\,dc}$ it is possible to observe that the equivalent starting time of the system changes according to (8.23); thus the equivalent cut-off angular frequency of the DC-voltage control loop determines the spectrum range where synthetic inertia has an effect.

$$T'_a = T_a + K_{in}\tau_{dc} V_{dc} \tag{8.23}$$

8.5 CASE STUDY 2: mathematical model

Figure 8.5 reports the asymptotic diagrams of the closed $K'_g(s)$ (a) and open-loop $L_{in}(s)$ (b) transfer functions associated to the voltage-controlled inertia applied to a network with slow primary regulation $\tau \geq \frac{T_a}{4K_{reg}}$ (as derived in Sec.7.3). Similarly to the

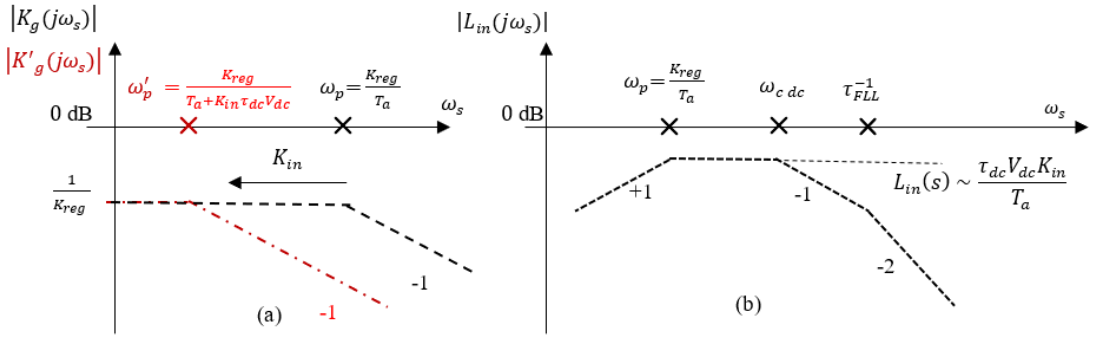

FIGURE 8.4: Bode diagram associated to the synthetic inertia loop in CASE STUDY 1. $K_g(s)$ and $K'_g(s)$ are the grid function before and after inertia insertion, while $L_{in}(s)$ is the open-loop function associated to the voltage-controlled scheme.

analysis reported in Section 7.4, the system shows a couple of complex conjugate poles whose damping depends on the relative magnitude of the grid regulation parameters.

The closed-loop transfer function $K'_g(s)$ in Fig.8.3 is obtainable from (8.11). In the frequency range $\omega_s < \omega_{c\,dc}$ the open $L_{in}(s)$ and closed-loop functions $K'_g(s)$ are given by:

$$L_{in}(s) \cong K_{in}\tau_{dc}V_{dc}\, s \cdot \frac{1 + s\tau}{s^2 T_a \tau + sT_a + K_{reg}} \tag{8.24}$$

$$K'_g(s) = \frac{K_g(s)}{1 + L_{in}(s)} \cong \frac{1 + s\tau}{s^2\left(T_a + K_{in}\tau_{dc}V_{dc}\right)\tau + \left(T_a + K_{in}\tau_{dc}V_{dc}\right)s + K_{reg}} \tag{8.25}$$

The natural frequency and damping factor of (8.25) are respectively given by:

$$\omega'_n = \sqrt{\frac{K_{reg}}{\tau\left(T_a + K_{in}\tau_{dc}V_{dc}\right)}} \tag{8.26}$$

$$\xi' = 0.5 \cdot \sqrt{\frac{\left(T_a + K_{in}\tau_{dc}V_{dc}\right)}{K_{reg}\,\tau}} \tag{8.27}$$

An increase of the inertia coefficient K_{in} reduces the natural angular frequency ω'_n associated to the transfer function $K'_g(s)$ and increases its equivalent damping ξ': in this way it contributes to the reduction of the angular frequency oscillations on the power network.

Furthermore, in order to have a positive impact on the system, the cut-off angular frequency of the DC bus regulation $\omega_{c\,dc}$ should be higher than the natural frequency of the grid without synthetic inertia ω_n. Thus, the following condition determines synthetic inertia effectiveness:

$$\omega_n = \sqrt{\frac{K_{reg}}{T_a\tau}} < \omega_{c\,dc} \tag{8.28}$$

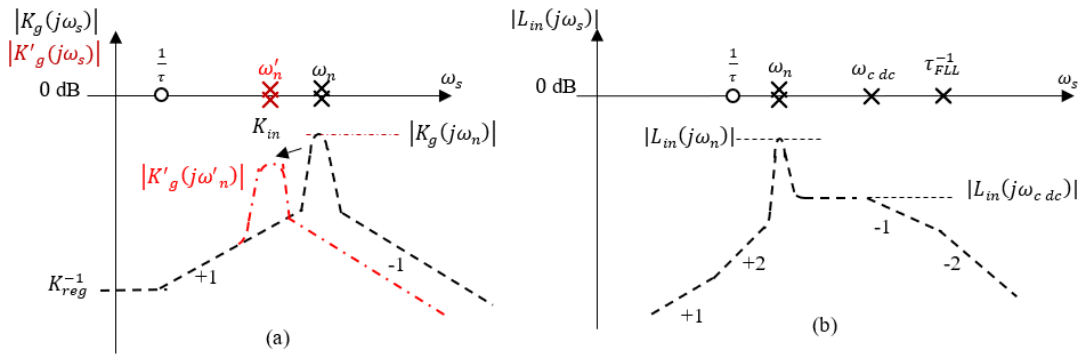

FIGURE 8.5: Bode diagram associated to the synthetic inertia loops in CASE STUDY 2. $K_g(s)$ and $K'_g(s)$ are the grid function before and after inertia insertion, while $L_{in}(s)$ is the open-loop function associated to the voltage-controlled scheme.

8.6 DC bus voltage proportional inertia: experimental results

In this section, the results associated to the comparison of the experimental waveforms with the analytical ones are reported. In order to verify the effectiveness of the inertia service provision, the experimental set-up already introduced in Section 7.5 has been considered. A broader explanation of the physical layout (as well as of the acquisition and control architectures) is reported in Appendix D.

Similarly to what was done for the current-controlled inertia, it is necessary to define a suitable protection scheme for the converter DC-bus to avoid possible damage to the installed capacitors. Nonetheless, in this case it is easier to coordinate the inertia provision with the acceptable operating ranges, as the control directly acts on the state variable under protection v_{dc}; thus the simple saturation scheme proposed in Fig. 8.6 can be adopted, where $V_{dc\,min} = 1.05$ p.u. and $V_{dc\,Max} = 1.35$ p.u.

The comparison between the derived analytical model and the experimental tests is carried out considering some macroscopic characteristics of the network frequency and DC bus voltage transients; the following aspects have been taken into account for the comparison: grid and DC voltage steady-state condition, natural oscillation period for the network frequency transient and its corresponding overshoot. As regards the DC bus steady state voltage, the comparison verifies the general energetic correctness of the set-up and provides a numeric indication of the DC bus variability associated to a network event. On the other hand, the procedure in Appendix C.3 correlates the macroscopic transient index with the expected natural frequency and damping as expressed by (8.26)-(8.27).

Consider the numeric results reported in Tab.8.1 and the experimental curves for the network frequency and DC bus transient under different level of the inertial support

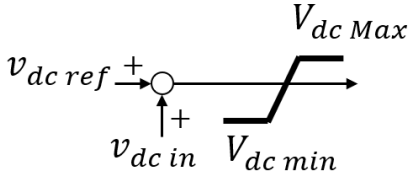

FIGURE 8.6: DC bus voltage protection scheme based on reference saturation.

K_{in}, respectively reported in Fig. 8.7 and Fig.8.9, under a unitary step-change of the accelerating power ($\Delta p_g = 1$ per-unit).

The following consideration can be derived from the analysis of the results:

- comparing Fig.8.7 with the corresponding one of the current-controlled inertia (Fig.7.18), it is evident that, from the network perspective, the two inertia schemes are practically equivalent. The change introduced by the proportional DC bus reference variability provides an equivalent damping behaviour equal to the one associated to the current-controlled inertia: this can be observed from the reduction of the network oscillation overshoot and from the increase of the transient period.
- The mismatch analysis between the proposed analytical derivation and the experimental tests (Fig.8.8) highlights the general robustness of the developed model: the correspondence represents a valuable result especially considering that synthetic inertia techniques have been rarely verified on a real test-bench, even though its simulated features have been extensively validated.
- The correctness of the simplified dynamical mode reported in Fig.8.3 (and verified through the comparison of the transients characteristics - Fig.8.8) allows to derive easy-to-use analytical relations between all the state variables that appear in the dynamical representation of the system, both in terms of the steady-state behaviour and as regards the stability margins. The provided mathematical description of the system highlights the intrinsic feedback between the dispatchable generation (modelled through K_{reg}, T_s and τ) and the transient support K_{in} from the undispatchable units: as a results, the physical power exchanges between system elements can be modelled in an analytical form, without recurring to complex numerical models.
- Figure 8.9 highlights the DC bus voltage profiles during inertia support; the major difference with respect to the current-controlled inertia regards the DC bus voltage level after the transient extinction. Differently from Fig. 7.22, the voltage-controlled scheme does not guarantee nominal steady-state behaviour for the DC bus, coherently with the model reported in equation (8.17) and with the numerical comparison carried out in Tab.8.8. Independently of the acceptability of a non-nominal DC voltage level, it is clear the higher impact of this regulation scheme on other system elements that may be connected in parallel to the converter bus (e.g. a controlled rectifier in a double-stage conversion system or a physical generator in single-stage photovoltaic interface): the modelling of these possible mutual effects may be the topic for further prosecutions of the work.
- Figure 8.10 reproduces the power injection from the converter p_{conv} under inertia service provision. Beside the proportional characteristics of this architecture with respect to DC-side quantities, as regards the AC side of the converter the control maintains an intrinsic derivative nature, and thus a global null-net-energy behaviour. This can be seen considering that the null power injection at steady state is not influenced by the inertia application, coherently with the model expressed by (8.14).

As a final remark, Figure 8.11 highlights the behaviour associated to the DC bus voltage protection under different inertia strength; in (a) the required DC bus voltage reference v_{dc}^{ref} does not exceed the predetermined thresholds, while in (b) the saturation limits the reference to avoid dangerous operating conditions. In (b) it is also possible to observe the over-shoot produced by the DC bus regulation, even though at steady state the actual voltage v_{dc} coincides with the reference one. Even if the non-linear behaviour associated to the implemented saturation scheme produces a mismatch between the

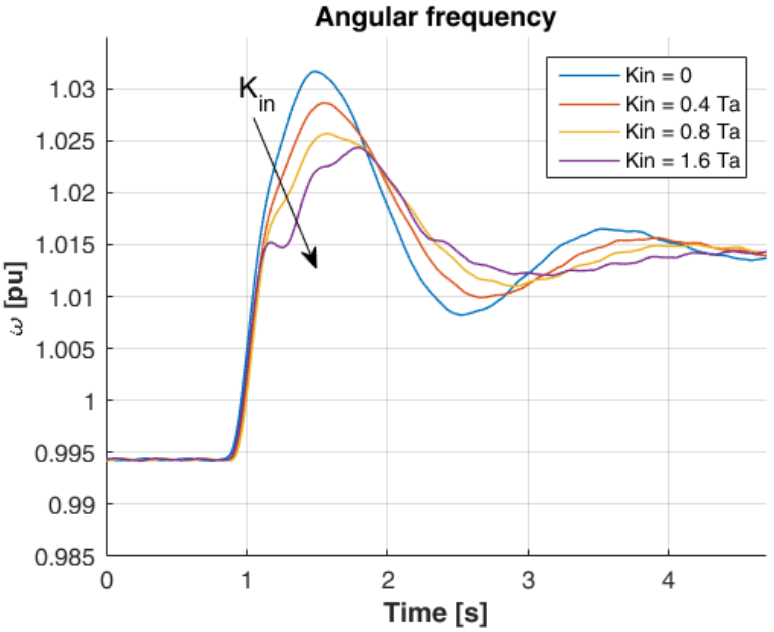

FIGURE 8.7: Angular frequency profile under different values of the synthetic inertia. The increase of the regulation coefficient K_{in} reduces the amplitude of the angular frequency overshoot.

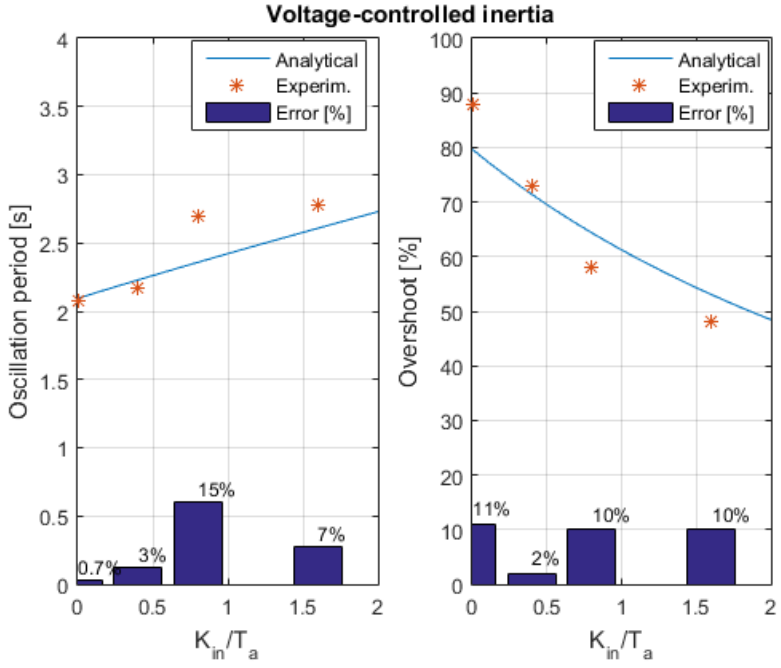

FIGURE 8.8: Representation of the residuals associated to the voltage-controlled inertia regulation.

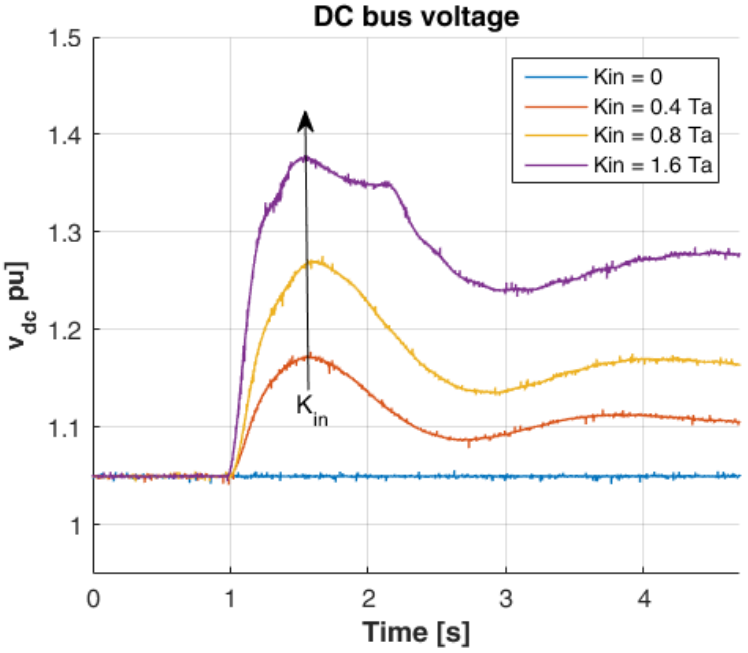

FIGURE 8.9: DC bus voltage under synthetic inertia control. The steady-state level of the DC bus differs from the nominal one, especially for high values of the coefficient K_{in}.

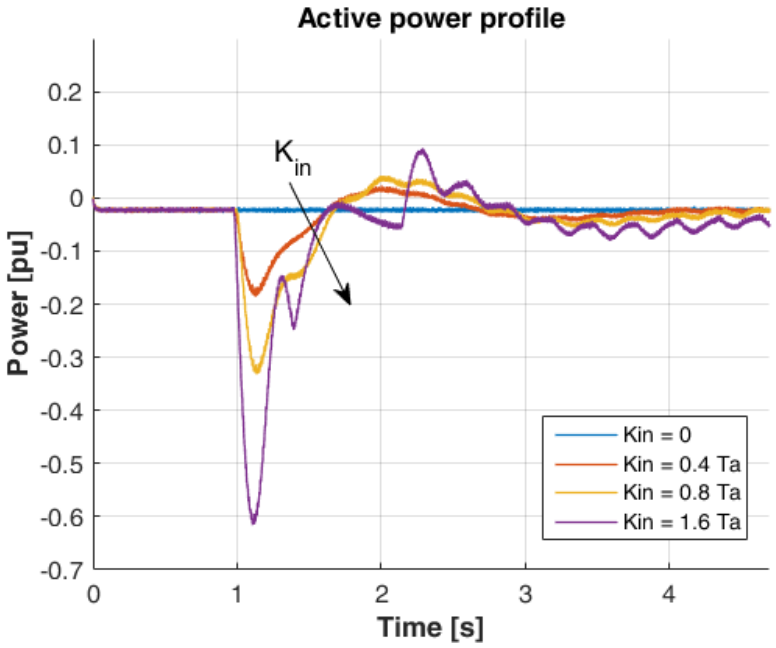

FIGURE 8.10: Injected power under different values of the synthetic inertia. The experimental system shows a lower phase margin with respect to the theoretical one, as it is possible to see from the oscillation in the power injection for high values of K_{in}. This is mainly due to the approximations carried out in the analytical development of the model.

TABLE 8.1: Model validation for voltage-controlled inertia in CASE STUDY 2: comparison of transients characteristic.

Parameter	Expression	K_{in}/T_a	Theoretic	Experim.
Steady state dev.	$\Delta\omega(\infty) = \Delta p_g / K_{reg}$	$\{0, 0.4, 0.8, 1.6\}$	0.020 p.u.	0.0195 p.u.
DC bus voltage steady-state variation	$\Delta v_{dc}(\infty)$ (see (8.17))	0	0	0
		0.4	0.080 p.u.	0.051 p.u.
		0.8	0.160 p.u.	0.103 p.u.
		1.6	0.320 p.u.	0.230 p.u.
Natural frequency	ω'_n (8.26)	0	3.16 rad/s	-
		0.4	3.01 rad/s	-
		0.8	2.87 rad/s	-
		1.6	2.64 rad/s	-
Damping factor	ξ' (8.27)	0	0.32	-
		0.4	0.33	-
		0.8	0.35	-
		1.6	0.38	-
Period of oscillation	$T = \frac{2\pi}{\omega'_n \cdot \sqrt{1-\xi'^2}}$	0	2.09 s	2.08 s
		0.4	2.19 s	2.17 s
		0.8	2.35 s	2.70 s
		1.6	2.61 s	2.78 s
Overshoot	see (C.30)-(C.31)	0	80%	88%
		0.4	73%	73%
		0.8	64%	58%
		1.6	53%	48%

theoretical and experimental models, still it allows to exploit the maximum available energy buffer for the provision of grid regulation service in a safe and reliable way.

8.7 Comparison between current-controlled and voltage-controlled inertia loops

In this final section, the main differences between the current-controlled and the voltage-controlled inertia loops will be pointed out.

From the energetic point of view, both the techniques are clearly equivalent, as they both exploit a physical energy buffer on the DC side. The experimental tests have proved the correspondence of the two algorithms as regards the energetic impact of the network damping: both the schemes provide a controlled transitory frequency support, reduce the overshoot experienced by the system and avoid the possible undesired intervention of the network over-frequency relays.

Both the techniques can be analytically modelled by means of a coupling loop between the dispatchable generation and the PQ converter: this representation allows to

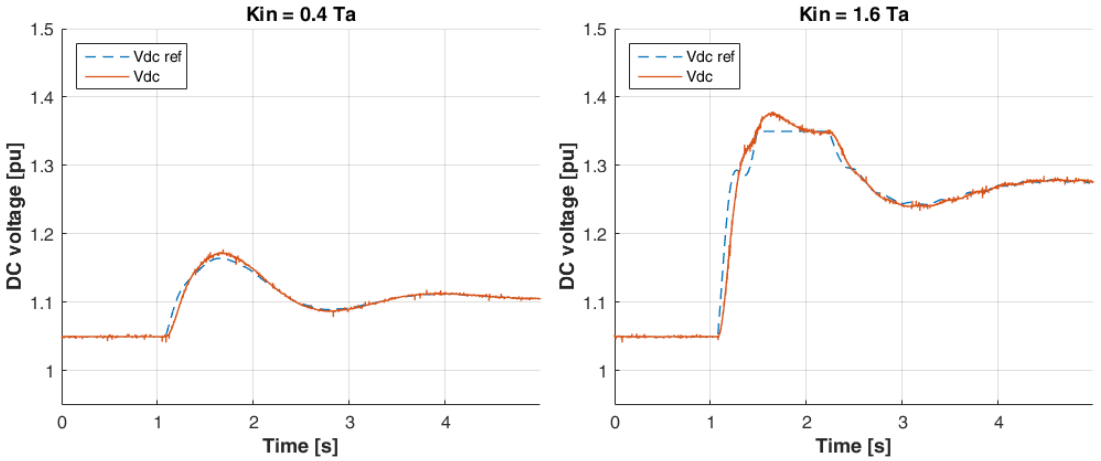

(a) Linear regulation conditions

(b) Saturated regulation conditions

FIGURE 8.11: Comparison between reference and actual voltage under inertia support. The protection scheme in Fig. 8.6 limits the maximum voltage reference, thus to protect the converter.

predict the stability properties of the regulated network, as well as to predict the equivalent natural frequency and damping of the resulting system. Some experimental tests have been carried out verify the correctness of the developed analytical model in both the configurations.

Even though from the AC side perspective the techniques are equivalent and both characterized by a null average energetic contribution (apart from the intrinsic parasitic losses experienced during the service provision), still from the DC side point of view the voltage-controlled approach does not guarantee the mathematical convergence of the DC bus to its nominal value after the transient extinction. This can give rise to possible unwanted interactions with other elements of the system: these aspects will be studied in further researches.

As proved by the experimental tests, the concern related to the fast and robust angular frequency derivative estimation for the current-controlled scheme can be easily solved recurring to sufficiently structured angular estimation techniques, like the one presented in Chapter 6: the development of structured synchronization algorithm represents a general trend in the control of grid-interfaced power converters (also confirmed by the increasing interest in Phasor Measurement Units, which combine the local angular quantities estimation with a global GPS synchronization for phase angle reconstruction).

Often the nature of the system itself imposes one architecture over the other. If we consider an electrochemical storage unit under PQ control with a single stage conversion system, the current-controlled scheme turns out to be the only feasible option as a consequence of the impossibility to directly control the DC bus voltage. In other applications (e.g. super-capacitor installations or HVDC links), both the analysed schemes are feasible and the choice of one architecture over the other mainly depends on the required intervention fastness. In this perspective the identification of the mathematical models as carried out in this thesis assumes an important role as it provides a technology-neutral representation of the system, that can be later exploited for a vast range of engineering applications.

8.8 Conclusion

In this last chapter of the thesis, the synthetic inertia provision by means of a proportional regulator acting between the grid angular frequency and the DC bus voltage has been taken into account. The changes in the complete model of the converters have been identified with respect to the current-controlled inertia scheme; later, some simplified design models have been developed for the stability assessment. Finally, the dynamical properties associated to the proposed inertia scheme have been validated experimentally.

As done for the previous chapter, the novelty introduced by the inertia representation as an equivalent closed-loop scheme lies in the possibility to predict the modified global regulation properties after inertia introduction, as well as its stability limits. In the considered proportional voltage scheme, the identification of dynamical coupling between the inertia provided by PQ converter and the dispatchable network frequency regulation allows to correctly predict the steady state voltage deviation as a function of the physical and control parameters.

References - part II

[1] ENTSO-E, ENTSO-E guidance document for national implementation for Network Codes on grid connection, *"Need for synthetic inertia (SI) for frequency regulation"*, 2016.

[2] J. Van De Vyver, J. De Kooning, B. Meersman, L. Vandevelde, and T. Vandoorn, "Droop control as an alternative inertial response strategy for the synthetic inertia on wind turbines," *IEEE Transactions on Power Systems*, vol. 31, no. 2, pp. 1129–1138, 2016. cited By 56.

[3] S. Nanou, A. Papakonstantinou, and S. Papathanassiou, "A generic model of two-stage grid-connected pv systems with primary frequency response and inertia emulation," *Electric Power Systems Research*, vol. 127, pp. 186–196, 2015. cited By 17.

[4] L. Castillo, A. Lazaro, I. Quesada, and A. Barrado, "Auto-design simulation set up of pv vsc with grid supporting functions," 2014. cited By 2.

[5] A. Hoke, E. Muljadi, and D. Maksimovic, "Real-time photovoltaic plant maximum power point estimation for use in grid frequency stabilization," 2015. cited By 17.

[6] Terna, *"Allegato A70 - Regolazione Tecnica dei requisiti di sistema della Generazione Distribuita" (Italian grid code)*. Available at: www.terna.it, 2012. Attachment to the Italian grid code.

[7] S. Nanou and S. Papathanassiou, "Modeling of a pv system with grid code compatibility," *Electric Power Systems Research*, vol. 116, pp. 301–310, 2014. cited By 27.

[8] P. Zarina, S. Mishra, and P. Sekhar, "Exploring frequency control capability of a pv system in a hybrid pv-rotating machine-without storage system," *International Journal of Electrical Power and Energy Systems*, vol. 60, pp. 258–267, 2014. cited By 29.

[9] P. Kundur, J. Paserba, V. Ajjarapu, G. Andersson, A. Bose, C. Canizares, N. Hatziargyriou, D. Hill, A. Stankovic, C. Taylor, T. Van Cursem, and V. Vittal, "Definition and classification of power system stability," *IEEE Transactions on Power Systems*, vol. 19, no. 3, pp. 1387–1401, 2004. cited By 1646.

[10] M. F. M. Arani and E. F. El-Saadany, "Implementing virtual inertia in dfig-based wind power generation," *IEEE Transactions on Power Systems*, vol. 28, pp. 1373–1384, May 2013.

[11] W. He, X. Yuan, and J. Hu, "Inertia provision and estimation of pll-based dfig wind turbines," *IEEE Transactions on Power Systems*, vol. 32, pp. 510–521, Jan 2017.

[12] S. Nanou, A. Spetsiotis, and S. Papathanassiou, "Provision of primary frequency support and inertia emulation by offshore wind farms connected through multi-terminal vsc-hvdc links," pp. 170–173, 2015. cited By 0.

[13] Y. Li, Z. Xu, J. Østergaard, and D. Hill, "Coordinated control strategies for offshore wind farm integration via vsc-hvdc for system frequency support," *IEEE Transactions on Energy Conversion*, vol. 32, no. 3, pp. 843–856, 2017. cited By 11.

[14] M. Zhang, X. Yuan, and J. Hu, "Inertia and primary frequency provisions of pll-synchronized vsc hvdc when attached to islanded ac system," *IEEE Transactions on Power Systems*, vol. 33, pp. 4179–4188, July 2018.

[15] Y. Li, Z. Zhang, Y. Yang, Y. Li, H. Chen, and Z. Xu, "Coordinated control of wind farm and vsc-hvdc system using capacitor energy and kinetic energy to improve inertia level of power systems," *International Journal of Electrical Power and Energy Systems*, vol. 59, pp. 79–92, 2014. cited By 32.

[16] J. Fang, R. Zhang, H. Li, and Y. Tang, "Frequency derivative-based inertia enhancement by grid-connected power converters with a frequency-locked-loop," *IEEE Transactions on Smart Grid*, pp. 1–1, 2018.

[17] J. Fang, H. Li, Y. Tang, and F. Blaabjerg, "Distributed power system virtual inertia implemented by grid-connected power converters," *IEEE Transactions on Power Electronics*, vol. 33, no. 10, pp. 8488–8499, 2018. cited By 1.

[18] Terna, *"Allegato A15 - Partecipazione alla Regolazione di Frequenza e Frequenza-Potenza" (Italian grid code)*. Available at: www.terna.it, 2008. Attachment to the Italian grid code.

[19] R. Marin and M. Valtorta, *"Trasmissione ed Interconnessione"*. CEDAM, 1973.

[20] F. Iliceto, *Impianti elettrici*. Patron Editore, 1981.

[21] N. Faletti and P. Chizzolini, *Trasmissione e distribuzione dell'energia elettrica (parte I e part II)*. Patron Editore, 1987.

[22] P. Kundur, *"Power system stability and control"*. Mc. Graw Hill, 1993.

[23] P. Bolzern, R. Scattolini, and N. Schiavoni, *"Fondamenti di controlli automatici"*. McGraw-Hill, 2008.

[24] R. Teodorescu, M.Liserre, and P.Rodriguez, *"Grid converters for photovoltaic and wind power systems"*. Wiley and Sons, 2010.

[25] A. Yazdani, A. Di Fazio, H. Ghoddami, M. Russo, M. Kazerani, J. Jatskevich, K. Strunz, S. Leva, and J. Martinez, "Modeling guidelines and a benchmark for power system simulation studies of three-phase single-stage photovoltaic systems," *IEEE Transactions on Power Delivery*, vol. 26, no. 2, pp. 1247–1264, 2011. cited By 178.

[26] M. Mojiri, M. Karimi-Ghartemani, and A. Bakhshai, "Time-domain signal analysis using adaptive notch filter," *IEEE Transactions on Signal Processing*, vol. 55, pp. 85–93, Jan 2007.

[27] P. Rodríguez, R. Teodorescu, I. Candela, A. V. Timbus, M. Liserre, and F. Blaabjerg, "New positive-sequence voltage detector for grid synchronization of power converters under faulty grid conditions," in *2006 37th IEEE Power Electronics Specialists Conference*, pp. 1–7, June 2006.

[28] P. Rodriguez, A. Luna, I. Candela, R. Mujal, R. Teodorescu, and F. Blaabjerg, "Multiresonant frequency-locked loop for grid synchronization of power converters under distorted grid conditions," *IEEE Transactions on Industrial Electronics*, vol. 58, pp. 127–138, Jan 2011.

[29] M. Ciobotaru, R. Teodorescu, and F. Blaabjerg, "A new single-phase pll structure based on second order generalized integrator," in *2006 37th IEEE Power Electronics Specialists Conference*, pp. 1–6, June 2006.

[30] Z. Xin, X. Wang, Z. Qin, M. Lu, P. C. Loh, and F. Blaabjerg, "An improved second-order generalized integrator based quadrature signal generator," *IEEE Transactions on Power Electronics*, vol. 31, pp. 8068–8073, Dec 2016.

[31] A. Bolzoni, C. Terlizzi, and R. Perini, "Analytical design and modelling of power converters equipped with synthetic inertia control," in *2018 20th European Conf. on Power Electronics and Applications (EPE'18 ECCE)*, pp. P.1–P.9, Sept 2018.

Conclusions

In this thesis, the main control strategies for power converters in microgrids applications have been analysed and developed, starting from the main architecture illustrated in the first chapter, which also provided a description of the general normative context.

In the first part of the thesis the droop scheme has been analysed; starting from the traditional regulation architecture reported in literature, the dynamical model of the converter has been developed. This allows to determine the contribution of each control element on the converter stability: in particular, the chapter has analysed the effect of the feed-forward compensation in the voltage loop and the influence of derivative droop terms. The adopted methodology is based on the development of simplified design methods: the attempt is to highlight the intrinsic converter dynamics.

The second chapter has been focused on the analysis of the virtual impedance control; a new design method based on closed-loop stability has been developed and experimentally tested, both in grid-connected and island mode. The analysis has revealed a strong influence of the external converter impedance on the system stability; nevertheless, the effectiveness of the virtual impedance as regards balancing of island-operated parallel converter has been assessed, as well as its positive impact on active / reactive decoupling, both in grid-connected and island mode.

Clearly the impact of the external output impedance on system stability is a critical task for the development of control system with fully-determined dynamical properties; in this perspective, the possibility to exploit natural system harmonics has been analysed, to estimate the network state and thus to reconstruct the equivalent interface impedance. Several alternatives have been analysed and experimentally tested, even though the external network state reconstruction is still an open task in literature: clearly the proposed approach based on single-harmonics control is characterized by a limited reconstruction capability, nonetheless it can be easily implemented on low-computational-power controllers and allows a synthetic characterization of the system.

Even though the coordination of all the system sub-controls requires further analysis, still the identification of the major dynamical characteristics of each sub-algorithm represents a significant step towards the development of a more advanced (and adaptive) architecture able to maintain constant dynamical properties independently of the external system characteristics.

The second part of the thesis has been entirely devoted to the analysis of the synthetic inertia control. This algorithm configures as a regulation technique able to provide transitory system support during frequency events; its derivative nature enables its implementation also for un-dispatchable units, provided that they are equipped with a small energy buffer.

A key aspect in the provision of inertia support regards the possibility to estimate in a clean and fast way the angular quantities (angular frequency and its derivative) associated to the network voltages, especially under disturbed and unideal operating

conditions. Thus an advanced resonant-based estimation technique has been developed, which allows the compensation of the disturbance terms inside the control; a comparison between the proposed method and other algorithms available in literature has been developed on an experimental base.

The final chapters of the thesis have analysed two possible architectures for the synthetic inertia provision: the first one acts on the current-control loop and exploits a derivative-based controller, the second produces a DC-voltage reference proportional to the frequency deviation with respect to the nominal conditions. The current-based approach is suitable when the internal grid dynamics are fast, but it requires a better estimation of the angular quantities and it is more susceptible of possible un-compensated disturbances. On the other hand, the DC-voltage-based architecture guarantees a higher robustness against angular quantities estimation uncertainties but is typically characterized by a lower equivalent pass-band.

The methodology followed in the thesis deserves a final consideration: often the design of the regulation algorithms for the control of power converters is performed on a numerical base or resorting to simulations. In this thesis, the author's attempt has been to develop the design procedures on an analytical base. On one side, a drawback of this approach is the necessary introduction of simplifying hypotheses that produce, sometimes, differences between the prospected results and the obtained ones. Nevertheless, the advantages of this methodology are evident: it highlights the main dynamical relations inside the system, allows the determination of simplified design constraints and, more important, provides an intuitive but rigorous understanding of the physical behaviour of the controllers. It keeps complicated things easy: this was, at least, the attempt.

Appendix A

State space models

In this Appendix, the complete expressions of the dynamical models of the converter under different regulation schemes are reported. It does not configure as a stand-alone analysis: rather it is an extensive representation of the state-space models proposed in the main chapters and allows to identify the actual set of equations numerically implemented in the Matlab environment. For a physical interpretation of the included quantities, the reader is invited to refer to the main chapters in which each dynamical model is reported.

The combination of the physical and control elements determine a non-linear set of equations, which include that stability properties of the converter. Typically the system can be described by a set of differential-algebraic equations; direct substitution of the algebraic equalities in the differential equations allows to obtain a model in state-space form[1]:

$$\dot{x}(t) = f\left(x(t), u(t), t\right) \tag{A.1}$$

where x is the state-vector and u are the inputs of the system. In the following, time-invariant models are considered, so as to remove the direct dependency from time in (A.1). The operator p is used to indicate the time derivative of a state variable, $p = \frac{d}{dt}$. The reported state-space models can be used for equilibrium identification, eigenvalues calculation and participation factors analysis; the solution of the non-linear numeric system for the identification of the equilibrium point has been performed by means of the Newton-Raphson algorithm.

A.1 Droop-controlled converter in grid-connected mode

State variables:

$$x = [\ P_o\ Q_o\ E_{v\,d}\ E_{v\,q}\ E_{i\,d}\ E_{i\,q}\ i_d\ i_q\ v_{o\,d}\ v_{o\,q}\ i_{o\,d}\ i_{o\,q}\ \delta\ ]^T \tag{A.2}$$

External conditions and inputs:

$$u = [\ \omega_{pcc}\ V_{pcc}\ \omega^*\ V^*\ ] \tag{A.3}$$

[1] P. Bolzern, R. Scattolini, N. Schiavoni, *"Fondamenti di controlli automatici"*, McGraw-Hill 2008

State model:

$$pP_o = \frac{1}{T_p} \cdot (v_{od}\, i_{od} + v_{oq}\, i_{oq} - P_o) \tag{A.4}$$

$$pQ_o = \frac{1}{T_p} \cdot (v_{oq}\, i_{od} - v_{od}\, i_{oq} - Q_o) \tag{A.5}$$

$$pE_{v\,d} = \left(v_{od}^{ref} - v_{od}\right) \tag{A.6}$$

$$pE_{v\,q} = \left(v_{oq}^{ref} - v_{oq}\right) \tag{A.7}$$

$$pE_{i\,d} = \left(i_{d}^{ref} - i_{d}\right) \tag{A.8}$$

$$pE_{i\,q} = \left(i_{q}^{ref} - i_{q}\right) \tag{A.9}$$

$$pi_d = \frac{\omega_b}{L_f} \cdot (v_d - v_{od} + \omega L_f i_q - R_f i_d) \tag{A.10}$$

$$pi_q = \frac{\omega_b}{L_f} \cdot (v_q - v_{oq} - \omega L_f i_d - R_f i_q) \tag{A.11}$$

$$pi_{od} = \frac{\omega_b}{L_g} \cdot (v_{od} - V_{pcc} \cdot \cos(\delta) + \omega L_g i_{oq} - R_g i_{od}) \tag{A.12}$$

$$pi_{oq} = \frac{\omega_b}{L_g} \cdot (v_{oq} - V_{pcc} \cdot \sin(\delta) - \omega L_g i_{od} - R_g i_{oq}) \tag{A.13}$$

$$pv_{od} = \frac{\omega_b}{C_f} \cdot (i_d - i_{od} - \omega C_f R_d \cdot (i_q - i_{oq}) + C_f R_d/\omega_b \cdot (pi_d - pi_{od}) + \omega C_f v_{oq}) \tag{A.14}$$

$$pv_{oq} = \frac{\omega_b}{C_f} \cdot (i_q - i_{oq} + \omega C_f R_d \cdot (i_d - i_{od}) + C_f R_d/\omega_b \cdot (pi_q - pi_{oq}) - \omega C_f v_{od}) \tag{A.15}$$

$$p\delta = \omega_b \cdot (\omega_{pcc} - \omega) \tag{A.16}$$

where the converter output voltage $\bar{v}_{dq} \cong \bar{v}_{dq\,ref}$ can be expressed as function of the regulators equations:

$$v_{d\,ref} = k_{pI} \cdot \left(i_{d}^{ref} - i_{d}\right) + k_{iI} \cdot E_{i\,d} + v_{od} - \omega L_f i_q \tag{A.17}$$

$$v_{q\,ref} = k_{pI} \cdot \left(i_{q}^{ref} - i_{q}\right) + k_{iI} \cdot E_{i\,q} + v_{oq} + \omega L_f i_d \tag{A.18}$$

$$i_{d\,ref} = k_{pV} \cdot \left(v_{od}^{ref} - v_{od}\right) + k_{iV} \cdot E_{v\,d} + H_I i_{od} + \omega C_f H_V v_{oq} \tag{A.19}$$

$$i_{q\,ref} = k_{pV} \cdot \left(v_{oq}^{ref} - v_{oq}\right) + k_{iV} \cdot E_{v\,q} + H_I i_{oq} - \omega C_f H_V v_{od} \tag{A.20}$$

Moreover the following algebraic equalities associated to the droop hold:

$$\omega = \omega^* - m\, P_o - m_d \cdot pP_o \tag{A.21}$$

$$v_{od}^{ref} = V^* - n\, Q_o - n_d \cdot pQ_o \tag{A.22}$$

$$v_{oq}^{ref} = 0 \tag{A.23}$$

A.2 PQ-controlled converter with synthetic inertia

The dynamical model of the converter under PQ regulation is introduced and commented in Sec.5.7 and later extended for the current and voltage-controlled inertia schemes, respectively in Sec.7.2 and Sec.8.2.

State variables:

$$x = [\ v_d\ v_q\ i_d\ i_q\ i_{od}\ i_{oq}\ v_{od}\ v_{oq}\ E_{id}\ E_{iq}\ E_{PLL}\ \Delta\theta\ v_{dc}\ E_{dc}\ \omega\ \alpha_{FLL}\ \alpha_{filt}\ ]^T \tag{A.24}$$

External conditions and inputs:

$$u = \left[p_g\ p_{dc}\ v_{dcref}\ q^{ref}\ K_{in}\ \right] \tag{A.25}$$

State model:

$$pv_d = \frac{1}{T_{inv}} \cdot \left(+\cos(\Delta\theta)\ v_{\tilde{d}}^{ref} + \sin(\Delta\theta)\ v_{\tilde{q}}^{ref} - v_d\right) \tag{A.26}$$

$$pv_q = \frac{1}{T_{inv}} \cdot \left(-\sin(\Delta\theta)\ v_{\tilde{d}}^{ref} + \cos(\Delta\theta)\ v_{\tilde{q}}^{ref} - v_q\right) \tag{A.27}$$

$$pi_d = \frac{\omega_b}{L_f} \cdot (v_d - v_{od} + \omega L_f i_q - R_f i_d) \tag{A.28}$$

$$pi_q = \frac{\omega_b}{L_f} \cdot (v_q - v_{oq} - \omega L_f i_d - R_f i_q) \tag{A.29}$$

$$pi_{od} = \frac{\omega_b}{L_g} \cdot (v_{od} - V_g \cdot \cos(0)\ + \omega L_g i_{oq} - R_g i_{od}) \tag{A.30}$$

$$pi_{oq} = \frac{\omega_b}{L_g} \cdot (v_{oq} - V_g \cdot \sin(0)\ - \omega L_g i_{od} - R_g i_{oq}) \tag{A.31}$$

$$pv_{od} = \frac{\omega_b}{C_f} \cdot (i_d - i_{od} - \omega C_f R_d \cdot (i_q - i_{oq}) + C_f R_d/\omega_b \cdot (pi_d - pi_{od}) + \omega C_f v_{oq}) \tag{A.32}$$

$$pv_{oq} = \frac{\omega_b}{C_f} \cdot (i_q - i_{oq} + \omega C_f R_d \cdot (i_d - i_{od}) + C_f R_d/\omega_b \cdot (pi_q - pi_{oq}) - \omega C_f v_{od}) \tag{A.33}$$

$$pE_{id} = \left(i_{\tilde{d}ref} - i_{\tilde{d}}\right) \tag{A.34}$$

$$pE_{iq} = (i_{\tilde{q}ref} - i_{\tilde{q}}) \tag{A.35}$$

$$pE_{PLL} = v_{o\tilde{q}} \tag{A.36}$$

$$p\Delta\theta = \omega_b \cdot (\omega - \tilde{\omega}) \tag{A.37}$$

$$pv_{dc} = \frac{1}{\tau_{dc} v_{dc}} \cdot (I_{dc} v_{dc} - (v_d i_d + v_q i_q)) \tag{A.38}$$

$$pE_{dc} = (v_{dcref} - v_{dc} - v_{dcin}) \tag{A.39}$$

$$p\omega = \alpha \tag{A.40}$$

$$p\alpha \cong \frac{1}{T_a \tau} \cdot (-T_a \alpha - K_{reg} \cdot (\omega - \omega^*) + p_g + p_{conv} + \tau\,(p\,p_g + p\,p_{conv})) \tag{A.41}$$

$$p\alpha_{FLL} = \frac{1}{\tau_{FLL}} \cdot (\alpha - \alpha_{FLL}) \tag{A.42}$$

$$p\alpha_{filt} = \frac{1}{\tau_{in}} \cdot (\alpha_{FLL} - \alpha_{filt}) \tag{A.43}$$

where:

$$p_{conv} = (v_{od} i_{od} + v_{oq} i_{oq}) \tag{A.44}$$

The converter reference output voltage $\bar{v}^{ref}_{\tilde{d}\tilde{q}}$ can be expressed as a function of the current regulators equations:

$$v^{ref}_{\tilde{d}} = k_{pI} \cdot \left(i^{ref}_{\tilde{d}} - i_{\tilde{d}} \right) + k_{iI} \cdot E_{i\,d} + v_{o\,\tilde{d}} - \tilde{\omega} L_f i_{\tilde{q}} \tag{A.45}$$

$$v^{ref}_{\tilde{q}} = k_{pI} \cdot \left(i^{ref}_{\tilde{q}} - i_{\tilde{q}} \right) + k_{iI} \cdot E_{i\,q} + v_{o\,\tilde{q}} + \tilde{\omega} L_f i_{\tilde{d}} \tag{A.46}$$

The current reference $\bar{i}^{ref}_{\tilde{d}\tilde{q}}$ is determined by the DC-bus control, reactive feed-forward compensation and synthetic inertia signals.

$$i^{ref}_{o\,\tilde{d}} = \frac{p^{ref}_{dc} + p_{in}}{\sqrt{v^2_{o\,\tilde{d}} + v^2_{o\,\tilde{q}}}} \tag{A.47}$$

$$i^{ref}_{o\,\tilde{q}} = -\frac{q_{ref}}{\sqrt{v^2_{o\,\tilde{d}} + v^2_{o\,\tilde{q}}}} \tag{A.48}$$

$$p^{ref}_{dc} = (k_{p\,dc} \cdot (v_{dc\,ref} - v_{dc} + v_{dc\,in}) + k_{i\,dc}\, E_{dc}) \qquad i^{ref}_{\tilde{d}} = i^{ref}_{o\,\tilde{d}} - H_V C_f \tilde{\omega} v_{o\,\tilde{q}} \tag{A.49}$$

$$i^{ref}_{\tilde{q}} = i^{ref}_{o\,\tilde{q}} + H_V C_f \tilde{\omega} v_{o\,\tilde{d}} \tag{A.50}$$

As regards the **current-controlled inertia**, the following relations hold:

$$\begin{cases} p_{in} = -K_{in} \cdot \alpha_{filt} \\ v_{dc\,in} = 0 \end{cases} \tag{A.51}$$

while for the **voltage-controlled inertia** the references are determined as:

$$\begin{cases} p_{in} = 0 \\ v_{dc\,in} = K_{in} \cdot (\omega - \omega^*_n) \end{cases} \tag{A.52}$$

The rotating control angular frequency $\tilde{\omega}$ is determined by the PLL dynamics. The PLL also determines the relationship between acquired and real quantities from the perspective of the synchronous control, according to (A.54)-(A.57).

$$\tilde{\omega} = k_{pPLL} v_{o\,\tilde{q}} + k_{iPLL} E_{PLL} + \omega^*_n \tag{A.53}$$

$$i_{\tilde{d}} = (+i_d \cos(\Delta\theta) - i_q \sin(\Delta\theta)) \tag{A.54}$$

$$i_{\tilde{q}} = (+i_d \sin(\Delta\theta) + i_q \cos(\Delta\theta)) \tag{A.55}$$

$$v_{o\,\tilde{d}} = (+v_{o\,d} \cos(\Delta\theta) - v_{o\,q} \sin(\Delta\theta)) \tag{A.56}$$

$$v_{o\,\tilde{q}} = (+v_{o\,d} \sin(\Delta\theta) + v_{o\,q} \cos(\Delta\theta)) \tag{A.57}$$

Appendix B

Current regulator and Phase-Locked Loop (PLL) design

B.1 Current regulator

In this Appendix the complete procedure for the determination of the current loop regulators is performed, as addressed in Sec. 2.6 and Sec.5.7.

The design of the regulator for internal filter current $\bar{i}$ is based on the definition of the equivalent phase margin and cut-off frequency for the closed-loop system. Consider the base system and the physical parameters for the filter as reported in Table B.1.

Consider the equivalent structure of the feedback as reported in Fig. B.1(a). In order to control the filter current, a traditional PI regulator is adopted; the presence of the control integrator in the loop guarantees null error at steady-state in dq frame. A unitary feed-forward compensation is introduced both as regards the capacitor voltage $\bar{v}_o$ and the inductor coupling term. The modulator of the converter is taken into account by means of an equivalent time delay in the Laplace domain.

The equivalent transfer function associated to the modulator depends on the discretization carried out by the digital control system of the converter. A typical model consists in the introduction of an equivalent time delay that takes into account the type of modulation carried out by the converter (SPWM or PWM), the elaboration time of the microelectronic controller and the signal acquisition method implemented by the ADC converter.

The modulator introduces a highly non linear behaviour associated to the discrete state of the controllable switch; anyway, from the perspective of slower control loops, it is very common to model it as a time delay equal to half of the switching period $\frac{T_{sw}}{2}$.

As for the control and acquisition system, the equivalent delay depends on the discretization technique of the ADC converter: typically, most of the acquisition systems

Table B.1: Parameters for filter current loop design

Quantity	*Symbol*	*Value*
Base system	V_b [V], A_b [kVA], ω_b [rad/s]	200; 2.4; 2π 50
Filter inductor param.	R_f, L_f [p.u.]	0.0073, 0.045
Desired cut-off ang. freq.	ω_{cI}	$2\pi \cdot 350$ rad/s
Desired phase margin	ϕ_{mI}	60 ang. degrees

are designed based on a Sample&Hold approach which, from the mathematical perspective, is a Zero-Order-Holder; generally this can be simplified as a pure delay equal to half of the acquisition / elaboration time $\frac{T_{sampling}}{2}$ [1].

Combining the effect of the modulator with the ones of the acquisition system, a pure time delay $T_{inv} = \frac{T_{sampling}}{2} + \frac{T_{sw}}{2}$ is obtained. Referring to the characteristics of the experimental set-up, the following values are considered: $T_{sw} = T_{sampling} = 100\mu s$. Thus the effect of the whole modulation process acts as a global delay of around $T_{inv} = 100\mu s$.

$$F(s) = e^{-s\,T_{inv}} \tag{B.1}$$

Instead of (B.1), the first-order ratio form corresponding to the Padè approximation is typically exploited. In practice, as $T_{inv} \cong 0$, the first order asymptotic equivalences reported in (B.2) hold.

$$F(s) = e^{-sT_{inv}} \cong 1 - s \cdot T_{inv} \cong \frac{1}{1 + s \cdot T_{inv}} \tag{B.2}$$

Thus the linearised model associated to the current regulator can be obtained as in Fig. B.1(b). The structures of the regulator and of the equivalent load are given by:

$$R_I(s) = k_{pI} + \frac{k_{iI}}{s} = k_{iI} \cdot \frac{1 + sT_{iI}}{s} \tag{B.3}$$

$$G_I(s) = \frac{1}{\left(\dfrac{s}{\omega_b} L_f + R_f\right) \cdot (1 + s\,T_{inv})} \tag{B.4}$$

B.1.1 Analytical expressions for the regulator parameters

After defining the desired cut-off angular frequency ω_{cI} and phase margin ϕ_{mI}, the parameters of the controller $R_I(s)$ are obtained analytically. Given the desired control performances, the open-loop function $L_I(s) = R_I(s) \cdot G_I(s)$ has the following characteristics:

$$|L_I(j\omega_{cI})| = 1 \tag{B.5}$$

$$\phi_{mI} = \pi + arg\, L_I(j\omega_{cI}) \tag{B.6}$$

Thus:

$$L_I(j\omega_c) = 1\angle(-\pi + \phi_{mI}) \tag{B.7}$$

Considering magnitude and angle separately, it is possible to obtain:

$$|G_I(j\omega_{cI})||R_I(j\omega_{cI})| = 1 \tag{B.8}$$

$$\arg(G_I(j\omega_{cI})) + \arg(R_I(j\omega_{cI})) = -\pi + \phi_m \tag{B.9}$$

[1] P. Bolzern, R. Scattolini, N. Schiavoni, *"Fondamenti di controlli automatici"*, McGraw-Hill 2008

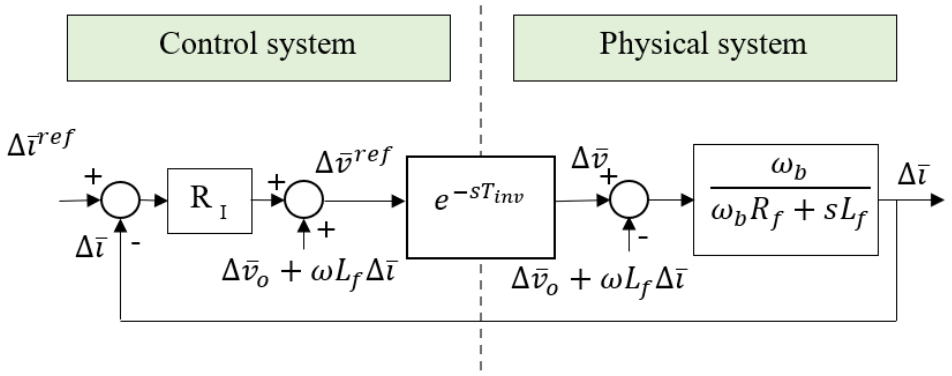

(a) Structure of the current control scheme

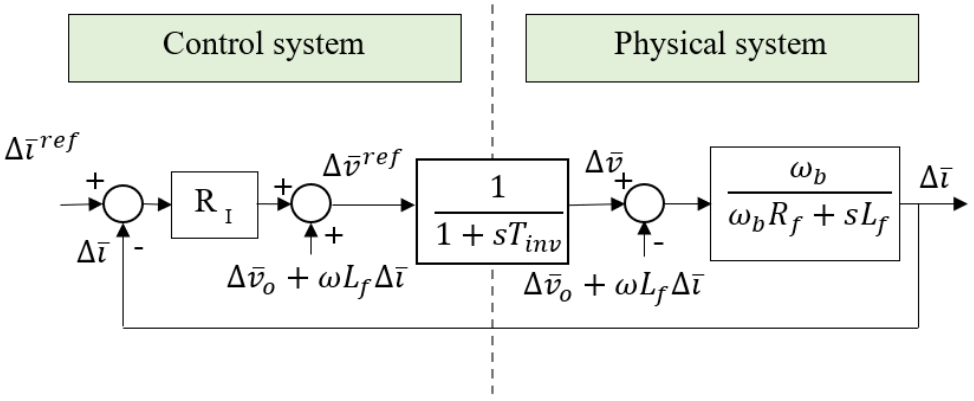

(b) Linearized model of the current control scheme

FIGURE B.1: Design of the filter current $\bar{i}$ regulator.

From (B.9):

$$|R_I(j\omega_{cI})| = \frac{1}{|G_I(j\omega_{cI})|} \tag{B.10}$$

$$\arg(R_I(j\omega_{cI})) = -\arg(G_I(j\omega_{cI})) - \pi + \phi_{mI} \tag{B.11}$$

$$R_I(j\omega_{cI}) = \frac{1}{|G_I(j\omega_{cI})|}\cos(-\arg(G_I(j\omega_{cI})) - \pi + \phi_{mI}) + \\ + j\frac{1}{|G_I(j\omega_{cI})|}\sin(-\arg(G_I(j\omega_{cI})) - \pi + \phi_{mI}) \tag{B.12}$$

The complex equality of (B.12) with (B.3) leads to the following expression for the coefficients:

$$k_{pI} = \frac{\cos(-\arg(G_I(j\omega_{cI})) - \pi + \phi_{mI})}{|G_I(j\omega_{cI})|} \tag{B.13}$$

$$k_{iI} = -\omega_{cI}\frac{\sin(-\arg(G_I(j\omega_{cI})) - \pi + \phi_{mI})}{|G_I(j\omega_{cI})|} \tag{B.14}$$

All the angles in (B.13) and (B.14) are expressed in radians.

B.1.2 Current regulator: results

As regards the design of the current regulator the following values have been assumed:
$\omega_{cI} = 2200\,\text{rad/s}$
$\phi_{mI} = 70°$
obtaining the following values for the parameters
$k_{pI} = 0.30\,pu$
$k_{iI} = 110\,pu/s$

Once determined the parameters of the open-loop transfer function $L_I(s)$, the corresponding closed-loop dynamic $K_I(s)$ is easily obtainable as:

$$K_I(s) = \frac{L_I(s)}{1 + L_I(s)} \tag{B.15}$$

Asymptotic Bode diagram of the open and closed loop transfer functions associated to the current controller are reported in Figure B.2. The controller zero introduces a leading effect in the loop, increasing the phase margin at the intersection; thus a sufficient condition for a stable operation of the current loop is the following:

$$\frac{1}{T_{iI}} < \omega_{cI} < \frac{1}{T_{inv}} \tag{B.16}$$

In the frequency range $\omega_s << \omega_{cI}$ (typically $\omega_s < \frac{\omega_{cI}}{7}$) it is possible to approximate the closed-loop behaviour as a single-pole function:

$$\bar{i} = K_I(s) \cdot \bar{i}_{ref} = \frac{1}{1 + s/\omega_{cI}} \cdot \bar{i}_{ref} \tag{B.17}$$

$$\Delta\bar{i} = K_I(s) \cdot \bar{i}_{ref} = \frac{1}{1 + s/\omega_{cI}} \cdot \Delta\bar{i}_{ref} \tag{B.18}$$

B.2 Phase-Locked loop (PLL) design

Consider the typical structure of a Phase-Locked loop architecture, combined with an internal first-order filter used for high frequency damping. The representation of the control algorithm is provided in the upper part of Fig.B.3.

The linearisation of Park transform leads to the simplified design model reported in the lower part of Fig.B.3 [2]. The design of the control system can be performed referring to the symmetrical optimum conditions, used for dynamical systems with two poles in the origin: keeping equal the ratios $\frac{\omega_{c\,PLL}}{T_{i\,PLL}^{-1}} = \frac{\omega_f}{\omega_{c\,PLL}}$ allows to maximise the phase margin under a certain desired cut-off angular frequency $\omega_{c\,PLL}$ (Fig. B.4). Consider the equivalent open-loop function $L_{PLL}(s)$:

$$L_{PLL}(s) = k_{i\,PLL}\frac{1 + sT_{i\,PLL}}{s} \cdot \frac{\omega_b}{s} \cdot \frac{1}{1 + s/\omega_f} \tag{B.19}$$

[2] R. Teodorescu, M. Liserre, P.Rodriguez, *"Grid converters for photovoltaic and wind power systems"*, Wiley and Sons, 2010

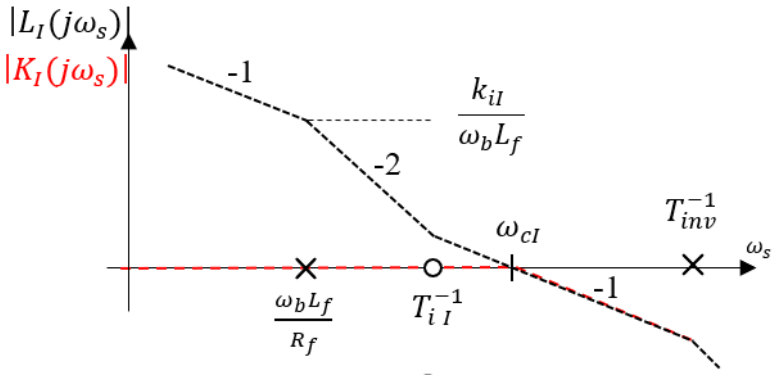

(a) Asymptotic behaviour

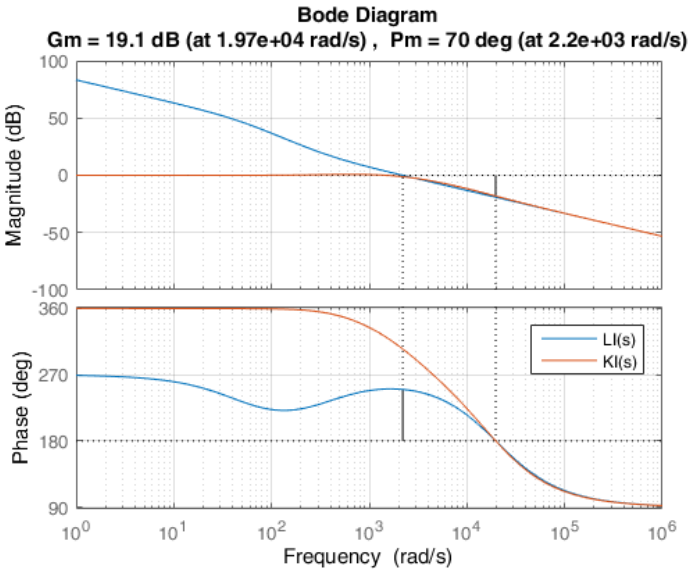

(b) Real behaviour (MATLAB)

FIGURE B.2: Bode diagram of the open $L_I(s)$ and closed $K_I(s)$ transfer functions.

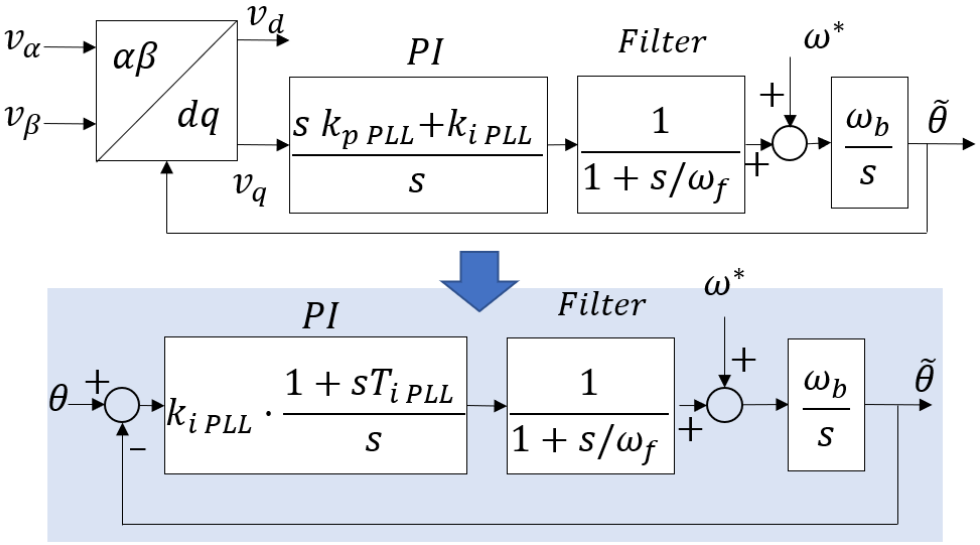

FIGURE B.3: Phase-Locked loop scheme, with internal first order filter.

The design can be performed considering that:

$$g = \omega_{c\,PLL} \cdot T_{i\,PLL} = \frac{\omega_f}{\omega_{c\,PLL}} \tag{B.20}$$

$$\omega_{c\,PLL} = \left(\sqrt{T_f T_{i\,PLL}}\right)^{-1} \tag{B.21}$$

$$\varphi_m = \pi + \angle\left(L_{PLL}(j\omega_{c\,PLL})\right) = \arctan\left(\omega_{c\,PLL}\, T_{i\,PLL}\right) - \arctan\left(\frac{\omega_{c\,PLL}}{\omega_f}\right) = \tag{B.22}$$

$$= \arctan(g) - \arctan\left(\frac{1}{g}\right) = \arctan\left(\frac{g^2-1}{2g}\right) \tag{B.23}$$

$$\tan(\varphi_m) = \frac{g^2-1}{2g} \tag{B.24}$$

$$g = \tan(\varphi_m) + \sqrt{\tan^2(\varphi_m) + 1} \tag{B.25}$$

From (B.23), it is possible to observe that the actual phase margin of the system exclusively depends on the parameter g. Thus (B.25) allows to determine the value of g starting from the desired phase margin.

As regards the cut-off angular frequency, it can be obtained as:

$$|L_{PLL}(j\omega_{c\,PLL})| = 1 \tag{B.26}$$

$$\frac{\omega_b}{\omega_{c\,PLL}^2} \cdot k_{i\,PLL} \cdot \sqrt{1+g^2} \cdot \frac{\omega_f}{\omega_{c\,PLL}\sqrt{1+g^2}} = 1 \tag{B.27}$$

$$\frac{\omega_b \cdot k_{p\,PLL} \cdot \omega_f}{T_{i\,PLL} \cdot \omega_{c\,PLL}^3} = 1 \tag{B.28}$$

Considering the condition in (B.20), (B.28) becomes:

$$\omega_{c\,PLL} = k_{p\,PLL} \cdot \omega_b \tag{B.29}$$

The condition reported in Table B.2 has been chosen for the design of the PLL:

Table B.2: Design parameters for the PLL loop

Quantity	*Symbol*	*Value*
Cut-off ang. frequency	$\omega_{c\,PLL}$	$2\pi \cdot 40$ rad/s
Phase margin	φ_m	60 deg.
Margin coeff.	g	$\cong 4$ p.u. (from (B.25))
Proportional coeff.	$k_{p\,PLL} = \omega_{c\,PLL}/\omega_b$	0.8 p.u.
Regulator integral time	$T_{i\,PLL} = g/\omega_{c\,PLL}$	$(2\pi \cdot 10)^{-1}$ s
Filter cut-off ang. frequency	$\omega_f = g \cdot \omega_{c\,PLL}$	$2\pi \cdot 160$ rad/s

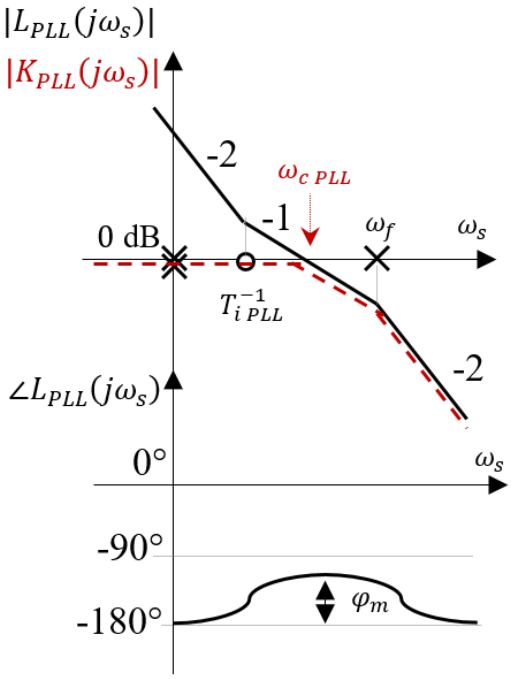

FIGURE B.4: Bode diagram of the PLL dynamical model.

Appendix C

Time-response evaluation of system dynamics

C.1 Resonant controllers: settlement time

This appendix analytically derives the convergence time value of a resonant second order system, used for the coordination of the SOGI scheme with the FLL algorithm (Sec. 6.2.3).

Two typical structures are considered for resonant controllers; the first one $D(s)$ introduces a null phase delay at the resonance frequency ω_n, while the second $Q(s)$ produces a delay equal to ninety angular degrees.

$$D(S) = K_r \cdot 2\xi \cdot \frac{s/\omega_n}{(s/\omega_n)^2 + 2\xi(s/\omega_n) + 1} \tag{C.1}$$

$$Q(S) = K_r \cdot 2\xi \cdot \frac{1}{(s/\omega_n)^2 + 2\xi(s/\omega_n) + 1} \tag{C.2}$$

The properties of these transfer functions are determined by three parameters:

- the coefficient K_r determines the vertical translation of the function;
- the damping factor ξ defines the extension of the resonance peak;
- ω_n determines the angular position of the peak.

The Bode diagrams associated to the resonant controllers are reported in Fig. C.1.

Consider the Laplace expression associated to $D(s)$ under sinusoidal input signal. Assume for simplicity that the angular frequency of the input matches the resonance one in the controller. The Laplace transform of the output under co-sinusoidal input is given by (C.3).

$$Y(s) = D(s) \cdot U(s) = K_r \cdot \frac{2\xi\omega_n s}{s^2 + 2\xi\omega_n s + \omega_n^2} \cdot \frac{s}{s^2 + \omega_n^2} \tag{C.3}$$

By applying the Heaviside decomposition method to (C.3) it is possible to obtain:

$$K_r \cdot \frac{2\xi\omega_n s}{s^2 + 2\xi\omega_n s + \omega_n^2} \cdot \frac{s}{s^2 + \omega_n^2} = \frac{A\,s}{s^2 + 2\xi\omega_n s + \omega_n^2} + \frac{B\,s}{s^2 + \omega_n^2} \tag{C.4}$$

$$K_r \cdot 2\xi\omega_n s^2 = (A\,s) \cdot \left(s^2 + \omega_n^2\right) + (B\,s) \cdot \left(s^2 + 2\xi\omega_n s + \omega_n^2\right) \tag{C.5}$$

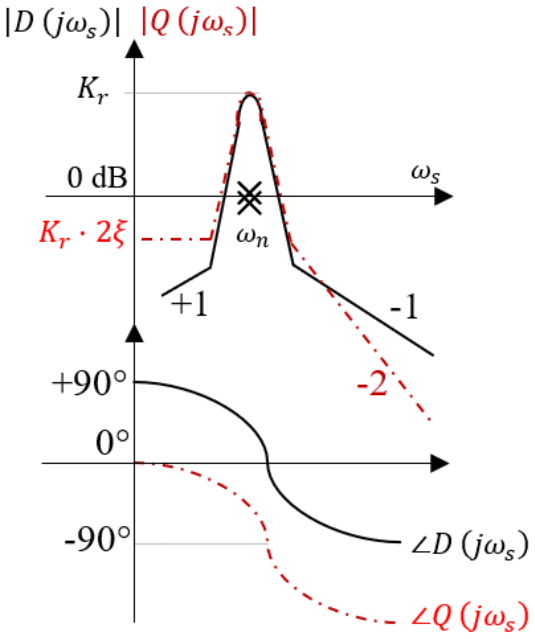

FIGURE C.1: Bode diagram of the transfer functions $D(s)$ and $Q(s)$.

Equating the polynomials at the two sides, it is easy to derive that condition (C.5) is verified provided that $A = -K_r$ and $B = K_r$. Thus:

$$K_r \cdot \frac{2\xi\omega_n s}{s^2 + 2\xi\omega_n s + \omega_n^2} \cdot \frac{s}{s^2 + \omega_n^2} = \frac{-K_r\, s}{s^2 + 2\xi\omega_n s + \omega_n^2} + \frac{K_r\, s}{s^2 + \omega_n^2} \tag{C.6}$$

The time response of the system is given by (C.7), where the first term represents the periodic steady-state condition and the second one describes the transient behaviour associated to the resonant response.

$$y(t) = \mathscr{L}^{-1}\{Y(s)\} = K_r \cos(\omega_n t) - \mathscr{L}^{-1}\left[\frac{K_r\, s}{s^2 + 2\xi\omega_n s + \omega_n^2}\right] \tag{C.7}$$

The first term in equation (C.7) corresponds to the frequency response of the system, while the second determines its transitory properties; in this analysis the focus is on this last element as it determines the convergence time of the system.

If we refer to the Laplace inverse transform definition [1], the following equalities hold:

$$\mathscr{L}^{-1}\left[\frac{s + \xi\omega_n}{s^2 + 2\xi\omega_n s + \omega_n^2}\right] = e^{-\xi\omega_n t} \cdot \cos\left(\sqrt{1-\xi^2}\omega_n t\right) \cdot step(t) \tag{C.8}$$

$$\mathscr{L}^{-1}\left[\frac{\sqrt{1-\xi^2}\,\omega_n}{s^2 + 2\xi\omega_n s + \omega_n^2}\right] = e^{-\xi\omega_n t} \cdot \sin\left(\sqrt{1-\xi^2}\omega_n t\right) \cdot step(t) \tag{C.9}$$

[1] P. Bolzern, R. Scattolini, N. Schiavoni, *"Fondamenti di controlli automatici"*, McGraw-Hill 2008

It is possible to perform some simple analytical substitutions to obtain the inverse Laplace transform in (C.7) from (C.8)-(C.9).

$$\mathscr{L}^{-1}\left[\frac{K_r\, s}{s^2+2\xi\omega_n s+\omega_n^2}\right] = K_r \cdot \mathscr{L}^{-1}\left[\frac{s+\xi\omega_n}{s^2+2\xi\omega_n s+\omega_n^2} - \frac{\xi}{\sqrt{1-\xi^2}}\cdot\frac{\sqrt{1-\xi^2}\,\omega_n}{s^2+2\xi\omega_n s+\omega_n^2}\right] = \tag{C.10}$$

$$= e^{-\xi\omega_n t}\cdot K_r\left[\cos\left(\sqrt{1-\xi^2}\omega_n t\right) - \frac{\xi}{\sqrt{1-\xi^2}}\cdot\sin\left(\sqrt{1-\xi^2}\omega_n t\right)\right] \tag{C.11}$$

The properties of the transients are mainly determined by the exponential, which defines the convergence of the time response. If we refer to literature, a settlement time of $T_{set} = \frac{4.6}{\xi\omega_n}$ is generally indicated; thus the value of the exponential at $t = T_{set}$ is:

$$e^{-\xi\omega_n T_{set}} = e^{-4.6} < 1\% \tag{C.12}$$

Nevertheless, the reported calculation is useful as it allows to verify the typically assumed condition $T_{set} = \frac{4.6}{\xi\omega_n}$ and to calculate the complete time-domain response of the system as:

$$y(t) \cong K_r\cos(\omega_n t) - K_r\, e^{-\xi\omega_n t}\cdot K_r\left[\cos\left(\sqrt{1-\xi^2}\omega_n t\right) - \frac{\xi}{\sqrt{1-\xi^2}}\cdot\sin\left(\sqrt{1-\xi^2}\omega_n t\right)\right] \tag{C.13}$$

C.2 Convergence time of the FLL

If we consider the most simplified model of the modified grid function under fast primary regulation in (7.14),

$$K'_g(s) = \frac{1}{(T_a+K_{in})s+K_{reg}} \tag{C.14}$$

it is easy to derive the characteristics of the resulting frequency transient under a step variation of the system accelerating power Δp_g^* in terms of maximum angular frequency. Applying the inverse Laplace transform to (C.14), a simple first order transient is derived (C.15); maximum derivative modified by the inertia introduction is given by (C.17) and it is inversely proportional to the inertia coefficient K_{in}.

$$\omega(t) = \omega_o + \left(1 - e^{-\frac{K_{reg}}{T_a+K_{in}}t}\right)\cdot\frac{\Delta p_g^*}{K_{reg}} \tag{C.15}$$

$$p\omega(t) = \alpha(t) = \frac{1}{T_a+K_{in}}\cdot e^{-\frac{K_{reg}}{T_a+K_{in}}t}\cdot\Delta p_g^* \tag{C.16}$$

$$p\omega_{max} = \alpha_{max} = \frac{1}{T_a+K_{in}}\cdot\Delta p_g^* \tag{C.17}$$

Assuming the internal dynamic of the FLL as a first order system with time constant τ_{FLL}, coherently to the model derived in (6.14), it is possible to estimate the total convergence time as $5\cdot\tau_{FLL}$; assuming uncoupled dynamics between the FLL and the network evolution, the relation between the maximum measured value from the FLL

and the actual angular frequency derivative can be expressed as (C.18).

$$\alpha_{\max\ \mathrm{FLL}} = \alpha_{\max} \cdot e^{-\frac{K_{reg}}{T_a+K_{in}} \cdot 5\,\tau_{FLL}} \rightarrow \alpha_{\max} = \alpha_{\max\ \mathrm{FLL}} \cdot e^{\frac{K_{reg}}{T_a+K_{in}} \cdot 5\,\tau_{FLL}} \tag{C.18}$$

The mathematical relation expressed by (C.18) is used to taken into account the FLL dynamics in the evaluation of the synthetic inertia effect for the microgrid case (Tab.(7.3)).

C.3 Synthetic inertia: expected dynamics of the network frequency

In this section the time response associated to the network frequency evolution during a power transient is analytically evaluated. As highlighted in (5.10), the system evolves following a second order resonant dynamic with an additional zero at the numerator, whose value depends on the delay τ associated to the primary frequency regulation. The presence of this zero plays a major role in the transient characteristics definition as it leads to a higher overshoot with respect to the one generally estimated for simple resonant dynamics: this section will derive the explicit behaviour of the network frequency as a function of time and serves as a benchmark to evaluate the correctness of the synthetic inertia dynamical models.

Consider the dynamic associated to the network angular frequency $\omega(t)$ under a step change of the accelerating input power Δp_g (5.10).

$$\omega(t) = \mathcal{L}^{-1}\left[\frac{1+s\tau}{T'_a\tau s^2 + T'_a s + K_{reg}} \cdot \frac{\Delta p_g}{s}\right] \tag{C.19}$$

The Heaviside procedure can be used for the calculation of the inverse Laplace transform. The expected steady-state value $\Delta p_g/K_{reg}$, obtained from the final value theorem, is introduced as a normalization coefficient in the Heaviside procedure to get compact expressions;

$$\frac{1+s\tau}{T'_a\tau s^2 + T'_a s + K_{reg}} \cdot \frac{\Delta p_g}{s} = \frac{\Delta p_g}{K_{reg}} \cdot \left[\frac{A}{s} + \frac{Bs+C}{s^2 + 2\xi'\omega'_n s + {\omega'_n}^2}\right] \tag{C.20}$$

The calculation of the coefficients leads to:

$$A = 1 \qquad B = -1 \qquad C = \frac{K_{reg}}{T'_a} - 2\xi'\omega'_n \tag{C.21}$$

where the natural frequency ω'_n and the damping ξ' are function of the physical network regulation characteristics (possibly modified by the synthetic inertia presence), whose expressions are here recalled:

$$\omega'_n = \sqrt{\frac{K_{reg}}{T'_a\tau}} \qquad \xi' = 0.5 \cdot \sqrt{\frac{T'_a}{K_{reg}\tau}} \tag{C.22}$$

and $T'_a = T_a + K_{in}$ (current-controlled inertia) or $T'_a = T_a + K_{in}\tau_{dc}V_{dc}$ (voltage-controlled inertia). Once obtained the coefficients, the inverse Laplace transform of (C.19) is

obtained.

$$\omega(t) = \frac{\Delta p_g}{K_{reg}} \cdot \left[1 + e^{-\xi'\,\omega'_n t} \cdot \left(B\,\cos(\sqrt{1-\xi'^2}\omega'_n t) + \frac{C - \xi'\omega'_n B}{\sqrt{1-\xi'^2}\,\omega'_n}\,\sin(\sqrt{1-\xi'^2}\,\omega'_n t)\right)\right] = \tag{C.23}$$

$$= \frac{\Delta p_g}{K_{reg}} \cdot \left[1 + e^{-\xi'\omega'_n t} \cdot \sqrt{B^2 + \frac{(C - \xi'\omega'_n B)^2}{(1-\xi'^2){\omega'_n}^2}}\,\sin\left(\sqrt{1-\xi'^2}\,\omega'_n t + atan\left(\frac{B\sqrt{1-\xi'^2}\,\omega'_n}{C - \xi'\omega'_n B}\right)\right)\right] \tag{C.24}$$

The free-response of the system shows an oscillatory sinusoidal behaviour with a period of $T = \frac{2\pi}{\sqrt{1-\xi'^2}\,\omega'_n}$ and a damped amplitude which depends on the coefficients calculated in (C.21); substituting (C.21) in (C.24), the normalized sinusoidal free-response amplitude is given by:

$$K = \sqrt{1 + \frac{(K_{reg}/T'_a - \xi'\omega'_n)^2}{(1-\xi'^2){\omega'_n}^2}} \tag{C.25}$$

The amplitude of the overshoot can thus be approximated as the product of the sinusoidal amplitude K with the decreasing exponential $e^{-\xi'\omega'_n t^*}$, where t^* is the time instant in which the sine function is maximum. Thus:

$$\sqrt{1-\xi'^2}\,\omega'_n t^* - atan\left(\frac{\sqrt{1-\xi'^2}\,\omega'_n}{K_{reg}/T'_a - \xi'\omega'_n}\right) = \frac{\pi}{2} \tag{C.26}$$

$$-\xi'\omega'_n t^* = -\frac{\xi'}{\sqrt{1-\xi'^2}} \cdot \left[\frac{\pi}{2} + atan\left(\frac{\sqrt{1-\xi'^2}\,\omega'_n}{K_{reg}/T'_a - \xi'\omega'_n}\right)\right] \tag{C.27}$$

As a recap, the network frequency evolution is modelled as a second order system with the introduction of an additional zero associated to the regulation delay. The analytical evaluation of the time response highlights the values of two macroscopic quantities which are used as benchmark for the model validation (in Table 7.6 and 8.1 for the current and voltage-controlled inertia schemes respectively):

- *Damped-oscillation period:*

$$T = \frac{2\pi}{\sqrt{1-\xi'^2}\,\omega'_n} \tag{C.28}$$

- *Overshoot normalized amplitude*

$$OS = K \cdot e^{-\xi'\omega'_n t^*} \tag{C.29}$$

where

$$K = \sqrt{1 + \frac{(K_{reg}/T'_a - \xi'\omega'_n)^2}{(1-\xi'^2){\omega'_n}^2}} \tag{C.30}$$

$$-\xi'\omega'_n t^* = -\frac{\xi'}{\sqrt{1-\xi'^2}} \cdot \left[\frac{\pi}{2} + atan\left(\frac{\sqrt{1-\xi'^2}\,\omega'_n}{K_{reg}/T'_a - \xi'\omega'_n}\right)\right] \tag{C.31}$$

Appendix D

Experimental set-up

In this appendix, the physical structure of the experimental set-up exploited for the verification of the different topics included in the thesis will be analysed. Consider the scheme reported in Fig. D.1, which depicts the major elements of the system under study; in the following, a brief description of each element will be provided.

D.1 Power circuit

Figure D.1 includes the single-line diagram of the test set-up. As already introduced in the thesis chapter, the system is composed by a couple of fully-controllable three-phase power converters interfaced to the micro-grid by means of an LC filter for high-frequency components damping. Each converter is interfaced to the system by a three-phase power transformer, whose ratings and electrical characteristics are reported in Table D.1. The presence of two transformers is fundamental in order to avoid differential mode between the two converters, with the subsequent short circuit currents involving the DC bus of the two units; this concept is explained in Fig. D.1, where several connection schemes are represented and compared. These transformers also enable the direct connection with the external 400 V public grid adapting the voltage level from the nominal 200 V phase-to-phase voltages of the converters.

The connection at the DC side determines the converter control strategy. Independently of the considered configuration, at least one unit must be operated in grid-forming or grid supporting mode to impose the network angular frequency and voltage amplitude: this role is carried out by converter 1, which is operated either in droop (grid-supporting) or in grid-forming mode depending on the specific test. In order to provide the necessary regulation capability to the unit, a constant voltage source should be placed on the converter DC side: in real power systems, this is obtained by means of high-energy storage units placed in parallel to the DC bus. In our experimental set-up, this is obtained providing an external three-phase supply from the 400 V public network, suitably rectified by a simple diode bridge; the variable autotransformer at the interface allows to obtain the desired DC side voltage level.

The switch S1 state has to be handled taking into account the typology of the control for converter number 2. In the first part of the thesis the droop converters parallel operations are analysed, thus the switch S1 is kept closed to provide infinite-energy DC bus supply also to the second unit similarly to what was done for converter number 1. In the second part of the thesis, the second unit is operated as an undispatchable system; in this configuration, the DC side of the converter is modelled as a constant current source: the unit regulation is responsible of the power balance between the DC side current generation and the AC absorption / injection. Nevertheless, the converter can

provide transitory frequency regulation (synthetic inertia) dynamically acting on the DC bus voltage level, within its acceptable operational limits; a slightly higher capacitance is installed on the second converter DC side to amplify the undispatchable system effects. This is the typical scheme adopted for renewable generators or fast-discharging supercapacitor systems. In the experimental apparatus, a null DC side current is imposed as a particular case keeping the contact S1 open.

As regards the AC side, the microgrid is realised by a local high-impedance balanced resistive load, obtained by variable resistors. The switch S2 determines the connection with the public network: in case S2 is open, the microgrid operates in island and the regulation is provided by the grid-forming / grid-supporting converters, while in case the S2 is closed the external public network defines the electrical values of the interface, both in terms of angular frequency and voltage amplitude. Grid-following and grid-supporting schemes can be interfaced to the public power network, while this is not the case for grid-forming control (not explicitly analysed in the thesis).

TABLE D.1: Test set-up

Element	*Quantity*	*Value*
Power converters	Power module	Siemens IGBT BSM 50 GD 120 DN2
	Nominal output voltage	$200\,V$
	Nominal design power	$2.4\,kVA$
	DC bus capacitance (inv. 1)	$3\,mF$
	DC bus capacitance (inv 2)	$8\,mF$
	Max DC side voltage	$400\,V$
Transformers	Nominal voltages	$200\,V$-$400\,V$
	Design power	$5\,kVA$

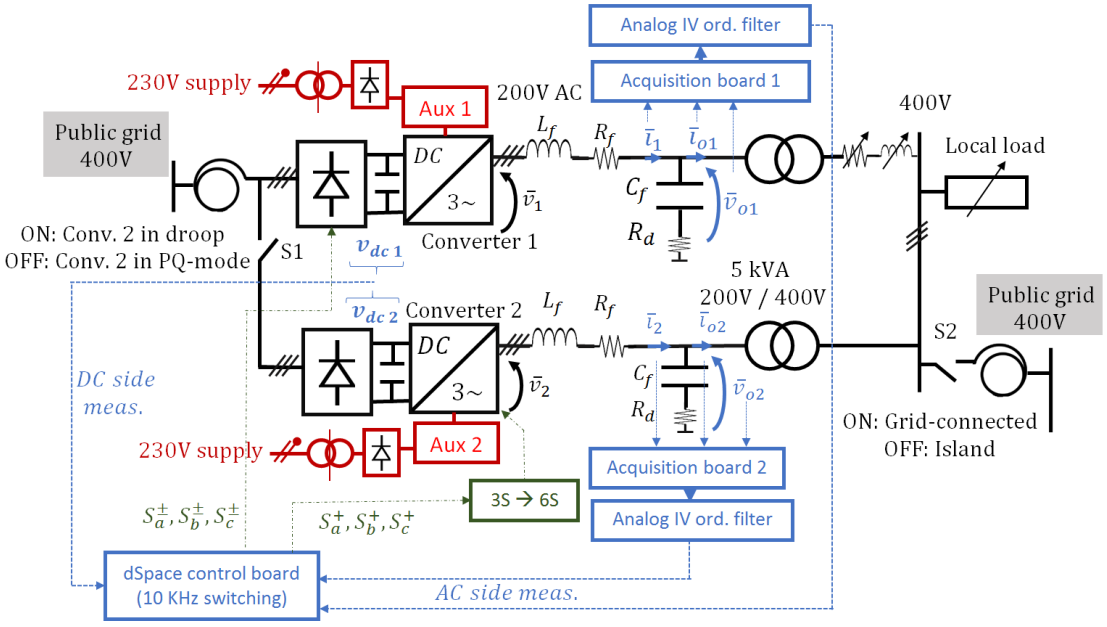

FIGURE D.1: Physical scheme of the adopted experimental setup

D.2 Acquisition system

The acquisition of the physical quantities is carried out by means of a board consisting of:

- six Hall effect transducers for the measurement of the filter inductor ($i_{abc}(t)$) and output ($i_{o\,abc}(t)$) current components; each transducer is characterized by a maximum measured current of 125 A and introduces a reduction factor of 1000:1, with an accuracy of $\pm 0.8\%$ and a frequency bandwidth up to 100 kHz. An external resistance connected to the mass guarantees the conversion of a the sensor current into a voltage signal with a maximum value suitable for the following conversion stage;
- three insulated electronic voltage transducers, with a maximum input of 10V, an accuracy of $\pm 0.5\%$ and a frequency bandwidth up to 100 kHz. A high-impedance resistive divider is introduced before the voltage input to reduce the measured quantity to an acceptable level.

Once acquired, the analog signals associated to the real states of the system are filtered by a fourth-order low pass Butterworth filter with a cut-off frequency set a 2.5 kHz, obtained by the monolithic switched-capacitor architecture TLC04/MF4A-50. These devices guarantees the absence of aliasing phenomena in the signal management, even though they may introduce significant delays in the frequency range close to the cut-off. As the filter outputs a maximum voltage of 2.5V, its input signals from the acquisition board should be scaled to this voltage level as to guarantee the absence of saturation at the filter stage. As a further consequence, the filter practically reduces the usable input range of the following ADC converter ($\pm 10V$, 10 bit), as a significant part of the acceptable input voltage range is practically unused. This worsens the acquisition accuracy, especially as regards harmonic components which are generally characterized by a limited amplitude and whose normalized level becomes closer to the ADC resolution.

D.3 Control system

The control of the system is carried out by means of the dSpace control platform. The system allows the analog to digital conversion of a maximum of 20 independent signals by means of internal ADC converters: the physical measured quantities for each conversion unit are the ones reported in Fig. D.1 (v_{dc}, i_{abc}, $v_{o\,abc}$, $i_{o\,abc}$). The dSpace platform allows the programming of the control system in a Matalab/Simulink environment, which is later compiled and synchronously executed with a sample time of $T_s = 100\mu s$. The Matlab/Simulink block-approach has been exclusively used for the Input / Output quantities management and for memory allocation during real-time operations, as to simplify the hardware-related tasks inside the computation; on the other hand, all the mathematical equations associated to the control laws have been introduced in the form of compiled C-code, recurring to the available S-Function block in Matlab, executed at any computation step T_s. The general architectures of the control exploited for the first and second parts of the thesis are depicted in Fig.D.2 - Fig.D.3 respectively.

The advantages of this approach are the following:

- the operations related to the low-level hardware-related tasks (e.g. peripherals management, synchronization and memory allocation) are automatically executed by the and set by user-friendly graphical programming blocks;
- the definition of the control rules (that is the converter "intelligence") are rigorously coded in C, taking into account the time-discretization effects by means

of the Tustin integration method for all the regulators inside the control. This guarantees robust operations for the system and a direct controllability of each computation step. Some of the exploited codes are reported as examples at the end of this appendix, in a simplified and commented form.

The C-code associated to each converter outputs the modulating signals of the three-phase AC voltages; nevertheless, the adopted control board is exclusively able to output nine PWM signals, thus it is not possible to directly control the twelve controllable valves in the network. To overcome this situation, the following solution has been adopted:

- the first converter IGBT are directly controlled by six of the available nine output signals, corresponding to the switching signals $S_a^{\pm}$-$S_b^{\pm}$-$S_c^{\pm}$; the dead time is automatically introduced by the dSpace modulator.
- The remaining three channels define the switching pattern of the second converter upper valves S_a^{+}-S_b^{+}-S_c^{+}; an intermediate custom electronic circuit, constituted by the amplifiers LM311N and the drivers IR21844, defines the lower valves states S_a^{-}-S_b^{-}-S_c^{-} and introduces a $1\mu s$ dead-time between the ON conditions for the upper and lower switches. This intermediate stage is introduced in Fig. D.1 and labelled "3S to 6S".

As regards the protections of the global system, they are obtained by an independent sub-routine with self-retained characteristics that allows to inhibit the converter

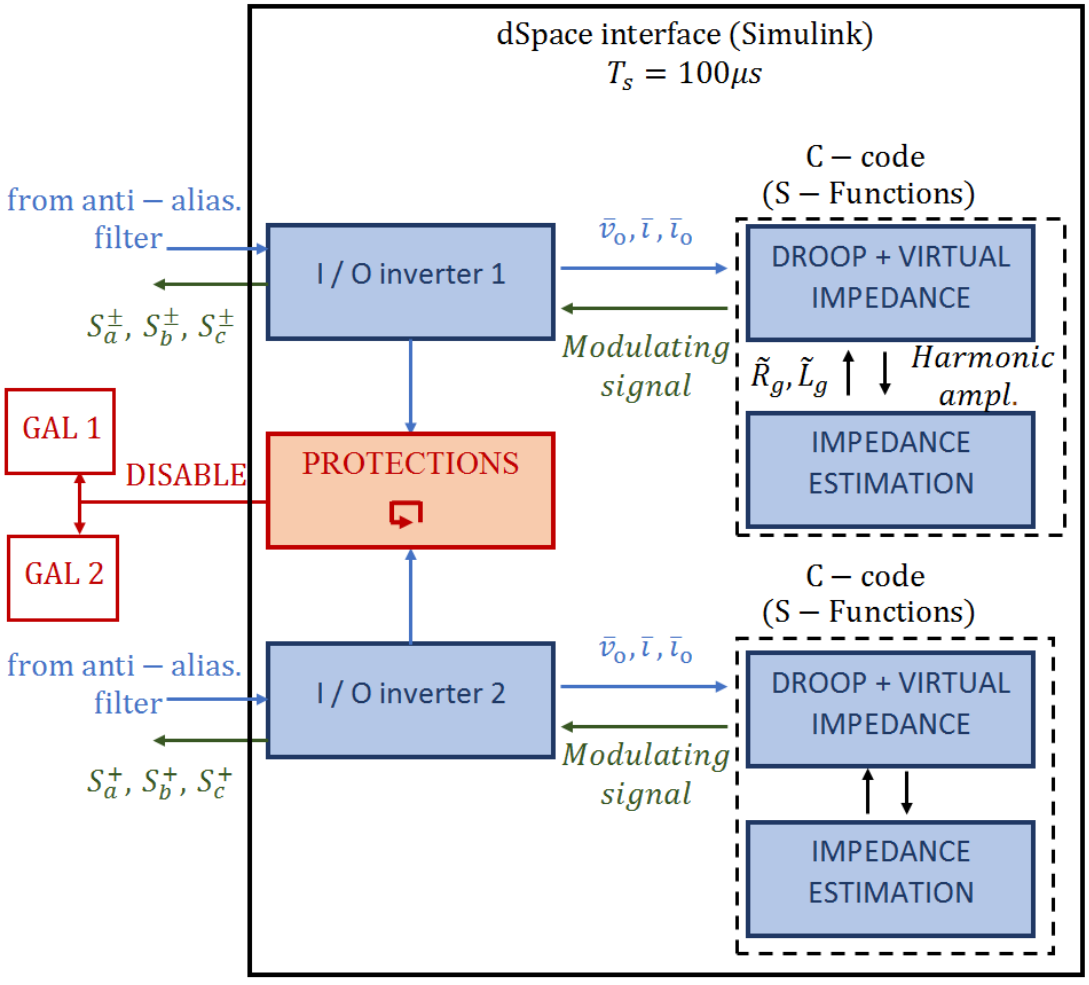

FIGURE D.2: Functional structure of the code used for the two inverters in droop operations (Part I of the thesis)

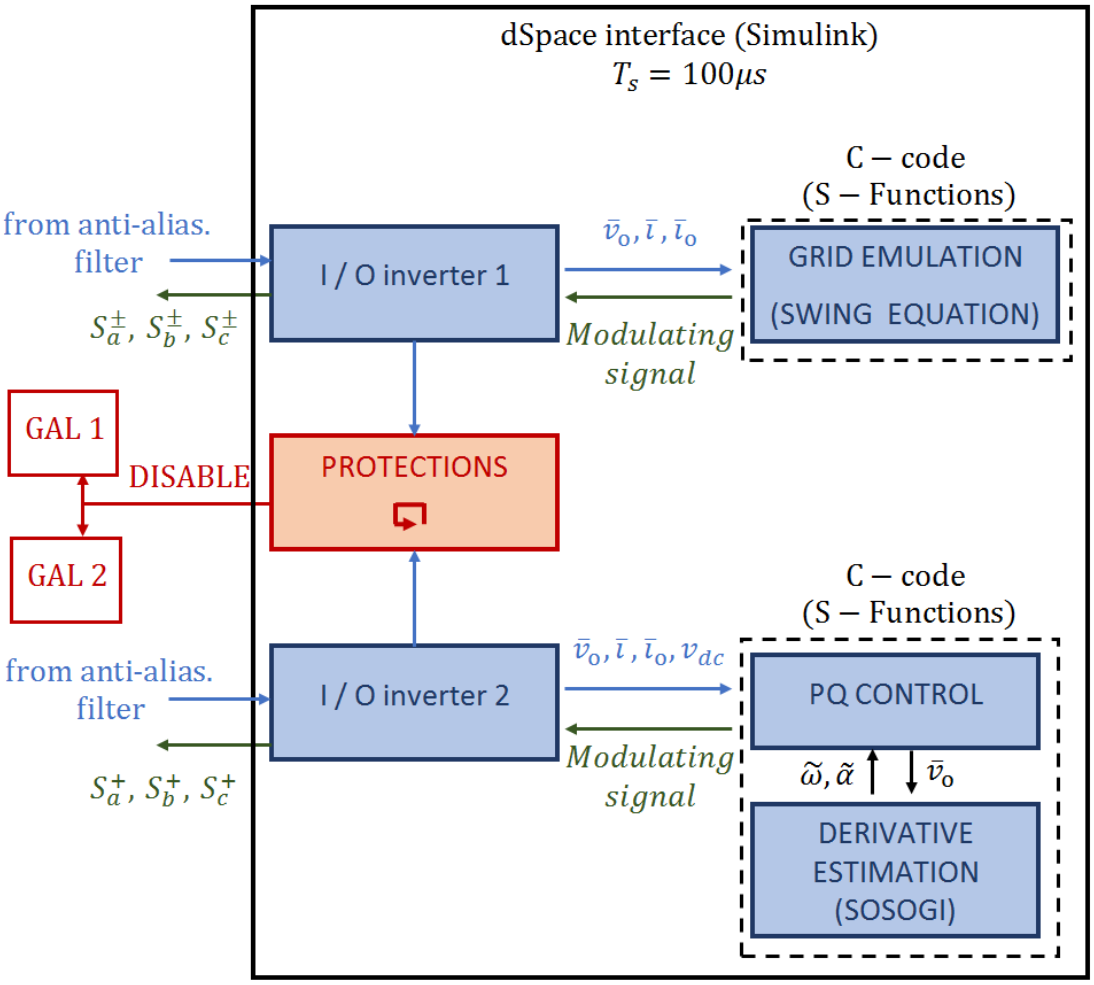

FIGURE D.3: Functional structure of the code used for the experimental testing of the synthetic inertia schemes (Part II of the thesis)

modulation as soon one of the currents / voltages in the microgrid exceeds its nominal value. The protection code controls the state of a digital output, which is directly connected to a programmable General Array Logic (GAL) element mounted on the power converter: this integrated circuit allows to implement generic boolean operations between its inputs and, it this context, it is used to disable the converters IGBTs in case of dangerous conditions on the network.